Air Force Institute of Technology
AFIT Scholar

Theses and Dissertations Student Graduate Works

9-2003

Controlled-Stress Large-Area Pulsed Laser Deposition of Yttria Stabilized Zirconia

Paul C. Rounsavall

Follow this and additional works at: https://scholar.afit.edu/etd

Part of the Semiconductor and Optical Materials Commons

Recommended Citation

Rounsavall, Paul C., "Controlled-Stress Large-Area Pulsed Laser Deposition of Yttria Stabilized Zirconia" (2003). *Theses and Dissertations*. 4132.
https://scholar.afit.edu/etd/4132

This Dissertation is brought to you for free and open access by the Student Graduate Works at AFIT Scholar. It has been accepted for inclusion in Theses and Dissertations by an authorized administrator of AFIT Scholar. For more information, please contact richard.mansfield@afit.edu.

CONTROLLED-STRESS LARGE-AREA PULSED LASER DEPOSITION OF YTTRIA STABILIZED ZIRCONIA

DISSERTATION

Paul C. Rounsavall, Captain, USAF

AFIT/DS/ENG/03-06

DEPARTMENT OF THE AIR FORCE
AIR UNIVERSITY

AIR FORCE INSTITUTE OF TECHNOLOGY

Wright-Patterson Air Force Base, Ohio

APPROVED FOR PUBLIC RELEASE; DISTRIBUTION UNLIMITED.

The views expressed in this dissertation are those of the author and do not reflect the official policy or position of the United States Air Force, the U.S. Department of Defense, or the U. S. Government.

AFIT/DS/ENG/03-06

CONTROLLED-STRESS LARGE-AREA PULSED LASER DEPOSITION OF YTTRIA STABILIZED ZIRCONIA

DISSERTATION

Presented to the Faculty

Graduate School of Engineering and Management

Air Force Institute of Technology

Air University

Air Education and Training Command

in Partial Fulfillment of the Requirements for the

Degree of Doctor of Philosophy

Paul C. Rounsavall, B.S., M.S.

Captain, USAF

1 August 2003

APPROVED FOR PUBLIC RELEASE; DISTRIBUTION UNLIMITED.

AFIT/DS/ENG/03-06

CONTROLLED-STRESS LARGE-AREA PULSED LASER DEPOSITION OF YTTRIA STABILIZED ZIRCONIA

Paul C. Rounsavall, B.S., M.S.
Captain, USAF

Approved:

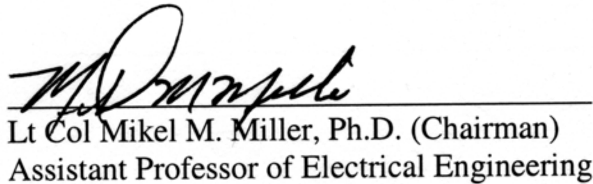

28 Aug 03

Lt Col Mikel M. Miller, Ph.D. (Chairman) — Date
Assistant Professor of Electrical Engineering

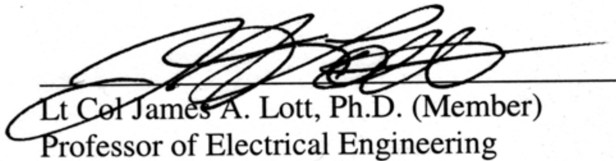

28 AUG 03

Lt Col James A. Lott, Ph.D. (Member) — Date
Professor of Electrical Engineering

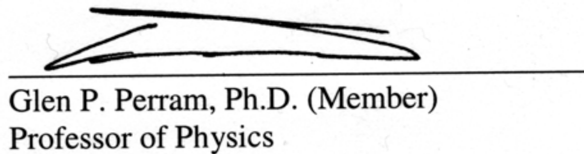

28 Aug 03

Glen P. Perram, Ph.D. (Member) — Date
Professor of Physics

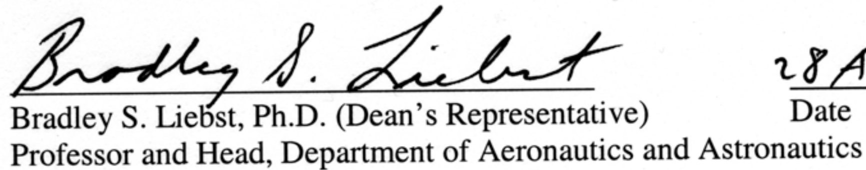

28 Aug 03

Bradley S. Liebst, Ph.D. (Dean's Representative) — Date
Professor and Head, Department of Aeronautics and Astronautics

Accepted:

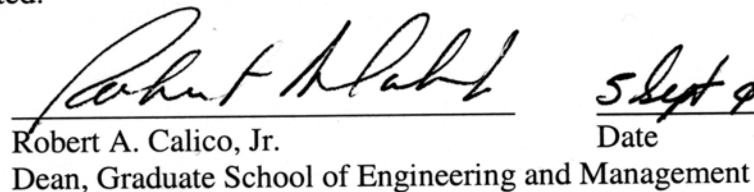

5 Sept 03

Robert A. Calico, Jr. — Date
Dean, Graduate School of Engineering and Management

Acknowledgments

This dissertation is the combined effort of many individuals, despite the fact that my name appears alone on the title page. To begin, I would like to thank my Lord and Savior, Jesus Christ for giving me the ability and time to complete this dissertation. Anything good in this research can be attributed directly to Him. I would also like to express my appreciation to Southbrook Christian Church for the wonderful spiritual, emotional, and social support that I need to endure my time at AFIT.

Secondly, I thank my mother and father for all the encouragement and love they gave to me. They have always supported me in all my endeavors. In addition, they have made many sacrifices so that I could be better equipped to succeed in life. I am also grateful for the love and support of my wife and my 'parent-in-laws'. Thank you all support.

Next, Dr. Mikel Miller deserves considerable thanks for acting as my Dissertation Advisor and providing me with continuous emotional support and encouragement during my research. My greatest technical guidance came from another committee member, Dr. Glen Perram. Thank you Dr. Perram for defocusing my perspective so that I would ask (and hopefully have answered) the right questions. In addition, I would like to thank Lt Col James Lott and Dr. Bradley Liebst for their efforts, which resulted in many improvements to this dissertation.

Finally, I would like to thank Mr. John Busbee for sponsoring my research. In addition to his financial support, he provided me with valuable direction and advice throughout my research efforts. Along with Mr. Busbee, Mr. David Dempsey, Dr. Rand

Biggers, and Dr. John Jones provided extraordinary technical help, as well as friendship and encouragement. In addition, Dave was always available with a "gizmo" for every occasion and a wealth of experience that enabled me to achieve my goals. Without John, Rand, John, and Dave, I would have accomplished very little. Thank you for all your help and hard work.

- Paul C. Rounsavall

Table of Contents

Page

Acknowledgments iv

List of Figures ix

List of Tables xvi

List of Equations xviii

Abstract xx

1 Introduction 1-1

1.1 Introduction 1-1
1.2 Problem Statement and Approach 1-3
1.3 Dissertation Organization 1-6

2 Background 2-1

2.1 Overview 2-1
2.2 Thin Film Stress 2-1
2.2.1 Thermal Stress 2-2
2.2.2 Intrinsic Stress 2-3
2.2.3 Microstructure Dependence upon Deposition Parameters 2-6
2.3 Epitaxial Deposition Overview 2-10
2.3.1 Electron Beam Evaporation 2-10
2.3.2 Sputtering Deposition 2-12
2.3.3 Ion Beam Deposition 2-20
2.3.4 Vapor Phase Epitaxy 2-23
2.4 Pulsed Laser Deposition 2-27
2.5 Thin Film Analysis Techniques 2-35
2.5.1 Light Microscopy 2-35
2.5.2 Scanning Electron Microscope 2-36
2.5.3 Transmission Electron Microscopy 2-36
2.5.4 Energy-Dispersive X-Ray Spectroscopy 2-36
2.5.5 X-Ray Diffraction 2-37
2.5.6 Auger Electron Spectroscopy 2-38
2.5.7 Mechanical and Optical Profiling 2-38
2.6 Chapter Summary 2-39

3 Experimental Setup 3-1

3.1 Overview 3-1
3.2 Excimer Laser 3-2
3.3 Laser Optic System 3-3

3.4 Target Carousel 3-5
3.5 Substrate Manipulation System 3-6
3.6 Pressure Control System 3-7
3.7 Temperature Control 3-9
3.8 Time-of-Flight Emission Sensor System 3-10
3.9 Fast-imaging Camera System 3-13
3.10 Raman Spectroscopy System 3-14
3.11 Software Control and Logging 3-15
3.12 Chapter Summary 3-16

4 Controlled-Stress Deposition of Yttria Stabilized Zirconia 4-1

4.1 Overview 4-1
4.2 Theory 4-2
4.3 Experiment 4-7
4.4 Data 4-9
4.5 Analysis 4-12
4.6 Conclusion 4-20

5 Optical Diagnostics of the Yttria Stabilized Zirconia (YSZ) Plume 5-1

5.1 Overview 5-1
5.2 Theory 5-3
5.3 Experiment 5-16
5.4 Data and Analysis 5-17
5.5 Conclusion 5-38

6 Large Area Pulsed Laser Deposition of Yttria Stabilized Zirconia 6-1

6.1 Overview 6-1
6.2 Theory 6-1
6.3 Experiment 6-5
6.4 Data and Analysis 6-10
6.5 Conclusion 6-27

7 Yttria Stabilized Zirconia Coatings for Stress-Shaped Polymer Mirrors 7-1

7.1 Overview 7-1
7.2 Experiment 7-2
7.3 Data and Analysis 7-5
7.4 Conclusion 7-12

8 Conclusion, Contributions, and Recommendations 8-1

8.1 Introduction 8-1
8.2 Conclusion and Contributions 8-1

8.3 Future Research Recommendations 8-6

Appendix A In-situ Raman Spectroscopy During the Pulsed Laser Deposition of Silicon Carbide A-1

A.1 Overview A-1
A.2 Theory A-3
A.2.1 Raman Effect Phenomenon A-4
A.2.2 Raman Spectroscopy Instrumentation A-8
A.2.2.1 Excitation Source A-9
A.2.2.2 Illumination and Collection Optics A-10
A.2.2.3 Monochromator or Spectrometer A-11
A.2.2.4 Detection A-12
A.2.3 Benefits of Raman Spectroscopy A-13
A.2.4 Silicon Raman Spectroscopy and Stress A-14
A.2.5 Silicon Carbide Raman Spectroscopy and Stress A-15
A.2.6 Vibrational Temperature from Raman Spectra A-21
A.3 Experiment A-26
A.3.1 Raman Spectroscopy System Spectral Calibration A-26
A.3.2 Raman Probe Focusing A-27
A.3.3 Simulated In-situ Raman Spectral Acquisition for Silicon Carbide A-29
A.3.4 In-situ Raman Spectral Acquisition for Silicon Carbide A-30
A.3.5 In-situ Raman Spectra Vibrational Temperature Extraction for Silicon Carbide A-31
A.4 Data and Analysis A-32
A.4.1 Simulated In-situ Raman Spectral Acquisition for Silicon Carbide A-32
A.4.2 *In-situ* Raman Spectral Acquisition for Silicon Carbide A-34
A.4.3 *In-situ* Raman Spectra Vibrational Temperature Extraction for Silicon Carbide A-38
A.4.4 Other Data and Results A-43
A.5 Conclusion A-44

Vita VITA-1

List of Figures

Figure Page

Figure 1-1. Example Satellite System [1] 1-2

Figure 1-2. Comparison Between Launch Costs and Mirror Aperture Diameter for the Three Different Mirror Types [1] 1-3

Figure 1-3. CP1 Polymer Spin-coating Schematic and Example [1] 1-4

Figure 1-4. Membrane Mirror Coating Solution [1] 1-5

Figure 2-1. Origin of Thermal Stress Diagram 2-3

Figure 2-2. Thin Film Growth Model Diagram [2] 2-4

Figure 2-3. Grain Boundary Intrinsic Stress Diagram [4] 2-4

Figure 2-4. Structure Zone Model Correlating Thin Film Microstructure with Substrate Temperature to Thin Film Material Melting Temperature Ratio [4; 10]. .. 2-7

Figure 2-5. Schematic Representation of the Thornton-Hoffman Structure Zone Model Illustrating the Influence of Argon Pressure for Cylindrical Magnetron Sputtered Coatings [4; 10] 2-7

Figure 2-6. Messier Structure Zone Model Diagram Illustrating the Influence of Surface Mobility Energy on Zone T [10] 2-8

Figure 2-7. Idealized Stress–Normalized Momentum Curve from Sputtered Thin Films [3] 2-9

Figure 2-8. Electron Beam Evaporation System Schematic [10; 16] 2-11

Figure 2-9. Physical Sputtering Process Diagram [24] 2-14

Figure 2-10. Angular Sputtering Emission Distribution Diagram [24] 2-15

Figure 2-11. DC Sputtering Deposition System Schematic [25] 2-15

Figure 2-12. Cylindrical Magnetron (Post Cathode) Sputter Deposition System Schematic [10] 2-18

Figure 2-13. Planar Magnetron Sputter Deposition System Schematic [10] 2-18

Figure 2-14. Schematic of a) Hollow Cathode Cylindrical Magnetron and b) Cylindrical Post Magnetron [24] 2-19

Figure 2-15. Ion Beam Sputtering Diagram [10] 2-21

Figure 2-16. Dual Ion Beam IBAD System Schematic [16] 2-22

Figure 2-17. Vapor Phase Epitaxial Growth Process of Arsenic-doped Silicon [15]... 2-24

Figure 2-18. Horizontal (a) and Vertical (b) Vapor Phase Epitaxy Process [38] 2-24

Figure 2-19. Horizontal Vapor Phase Epitaxy Schematic [15] 2-25

Figure 2-20. Pulsed Laser Deposition Schematic 2-29

Figure 2-21. Slot 1 (64.7 mm From the Target Surface) Time-of-Flight 470±5 nm Emissions from YSZ Plume Ablated in 75 mTorr Oxygen using 1.57 J/cm^2 Laser Pulses 2-30

Figure 2-22. Time-resolved Images of Plumes Produced by Ablating an YSZ Target in 150 mTorr Oxygen or Argon Ambient Environments using 10 J/cm^2 248-nm Laser Pulses as Recorded by a Princeton Instruments 576-RBE Fast-imaging Camera System Through 480±5 nm and 610±5 nm Optical Bandpass Filters [13] 2-32

Figure 2-23. Pulsed Laser Deposition Variables [47] 2-33

Figure 3-1. Pulsed Laser Deposition System Diagram 3-1

Figure 3-2. Optical Path Diagram 3-4

Figure 3-3. Pressure Control Vacuum Diagram 3-8

Figure 3-4. Time-of-Flight Emission Sensor System Diagram 3-12

Figure 3-5. Laser Pulse Detector and Trigger Conditioning Circuit Schematic 3-13

Figure 3-6. Raman Probe Schematic 3-15

Figure 4-1. Examples of Stress Quantitization Categories 4-9

Figure 4-2. Oxygen Pressure, Laser Fluence, and Target-to-Substrate Distance Combinations Plot of YSZ on CP1 Polymer Substrates Yielding Films Categorized as Flat 4-11

Figure 4-3. YSZ on CP1 Polymer Pressure-Distance Combinations That Produce No Curvature, Theoretical Fit, and Bowed Curvature Pressure-Distance Combinations using a 1.57 J/cm^2 Laser Fluence 4-14

Figure 4-4. Pressure and Laser Fluence Combinations (Varied by Adjusting Average Energy per Laser Pulse at a Fixed Footprint Size of 0.14 mm^2) that Produce

Substrates Exhibiting no Curvature at a Target-to-Substrate Distance of 56.7 mm.......... 4-15

Figure 5-1. Results from an YBCO Plume Dynamics Investigation using Fast Photography [8].......... 5-7

Figure 5-2. Percent Transmission of Optical Bandpass Filters Compared to the YSZ Spectra Acquired During Pulsed Laser Ablation in a 150 mTorr Oxygen Ambient Environment using a 1.57 J/cm^2 Laser Fluence. Spectral Emission Peaks are Labeled (A) through (E) for Reference.......... 5-8

Figure 5-3. Zr* 5G and 5F Atomic Energy Level Diagram [14].......... 5-9

Figure 5-4. Slot 1 (64.7 mm From the Target Surface) Time-of-Flight 470±5 nm Emissions from YSZ Plume Ablated in 75 mTorr Oxygen using 1.57 J/cm^2 Laser Pulses.......... 5-10

Figure 5-5. Slot 1 (64.7 mm From the Target Surface) Time-of-Flight 470±5 nm Emissions from an YSZ Plume Ablated in 75 mTorr Oxygen using 1.57 J/cm^2 Laser Pulses Fitted to a Shifted Center-of-Mass Maxwell-Boltzmann Velocity Distribution.......... 5-12

Figure 5-6. Example Normalized TOF Waveforms of YSZ Emissions near 470 nm When Ablating using 1.57 J/cm^2 Laser Pulses in a 75 mTorr Oxygen Ambient Environment.......... 5-18

Figure 5-7. Slot 11 (98.2 mm From the Target Surface) 470±5 nm Time-of-Flight Emissions from YSZ Plume Ablated in Oxygen using 1.57 J/cm^2 Laser Pulses.......... 5-19

Figure 5-8. Time-Resolved Normalized Images of YSZ Plume in 75 mTorr Oxygen Ablated Using 1.57 J/cm^2 and a 470±5 nm Optical Bandpass Filter.......... 5-21

Figure 5-9. Comparison of Time-of-Flight 470±10 nm Emissions from YSZ Plume Ablated in 100 mTorr Oxygen using 1.57 J/cm^2 Laser Pulse at Slot 1 (64.7 mm From the Target Surface) as Monitored Using the TOF Emission Sensor System and as Extracted from the Fast Imaging Camera System Data.......... 5-22

Figure 5-10. Comparison of Time-of-Flight 470±10 nm Emissions from YSZ Plume Ablated in 200 mTorr Oxygen using 1.57 J/cm^2 Laser Pulse at Slot 11 (98.2 mm From the Target Surface) as Monitored Using the TOF Emission Sensor System and as Extracted from the Fast Imaging Camera System Data.......... 5-23

Figure 5-11. Distance from the Target Surface Corresponding to Maximum Emission Intensity as Recorded by the Fast Imaging Camera System Through a 470±10 nm Optical Bandpass Filter When Ablating an YSZ Target in 200 mTorr Oxygen using 1.57 J/cm^2 Laser Pulse 5-26

Figure 5-12. Most Probable Time as Monitored via the 470±5 nm Time-of-Flight Emissions from the YSZ Plume Ablated in Oxygen using 1.57 J/cm^2 Laser Pulses.. 5-28

Figure 5-13. Most Probable Velocity as Monitored via the 470±5 nm Time-of-Flight Emissions from the YSZ Plume Ablated in Oxygen using 1.57 J/cm^2 Laser Pulses.. 5-29

Figure 5-14. Streaming Velocity as Monitored via the 470±10 nm Time-of-Flight Emissions from YSZ Plume Ablated in Oxygen using 1.57 J/cm^2 Laser Pulses.. 5-31

Figure 5-15. Effective Temperature as Monitored via the 470±5 nm Time-of-Flight Emissions from YSZ Plume Ablated in Oxygen using 1.57 J/cm^2 Laser Pulses.. 5-32

Figure 5-16. Streaming Velocity u and Effective Temperature T Monitored Through Slot 1 (64.7 mm From the Target Surface) as a Function of Oxygen Pressure 5-33

Figure 5-17. Normalized TOF Waveforms of YSZ Emissions near 470 nm When Ablating using 1.57 J/cm^2 Laser Pulses and No Curvature Pressure/Target-to-substrate Distance Combinations... 5-34

Figure 5-18. Comparison between the Streaming Velocities at Slot 1 (64.7 mm From the Target Surface) Measured During Diagnostic Depositions and During the Growth of YSZ of CP1 Polymer Substrates that Exhibit no Curvature using 1.57 J/cm^2 Laser Pulses.. 5-37

Figure 5-19. Comparison between the Effective Temperature at Slot 1 (64.7 mm From the Target Surface) Measured During Diagnostic Depositions and During the Growth of YSZ of CP1 Polymer Substrates that Exhibit no Curvature using 1.57 J/cm^2 Laser Pulses 5-37

Figure 6-1. "Off-Axis" and "Rotational/Translational" Large Area PLD Method Configuration [1]... 6-4

Figure 6-2. Tencor P-10 Surface Profilometer Step Height Measurement..................... 6-6

Figure 6-3. Contour Mapping and Radial Cross-Section of YSZ Film on Six-Inch Diameter Silicon Substrate Grown Using the Iteratively Derived Radial Profile that Produced the Most Uniform Thickness to Date 6-10

Figure 6-4. Initial Radial Profile and Final Radial Profile for YSZ Film on Six-Inch Diameter Silicon Substrate Grown Using the Iteratively Derived Radial Profile that Produced the Most Uniform Thickness to Date 6-11

Figure 6-5. Contour Mapping of Film Thickness of YSZ Film on Six-Inch Diameter Silicon Substrates Grown Using the Static Plume Configuration at Four Different Target Radial Positions.. 6-13

Figure 6-6. Relationship Between Laser Footprint Target Radial Position and Radial Location of Peak Film Thickness on the Substrate 6-14

Figure 6-7. Cross-Sectional Comparison of YSZ on Six-Inch Silicon Substrates Grown Using the Static Plume Configuration at Four Target Radial Positions... 6-15

Figure 6-8. Results of Static Numerical Simulations Using the Static Plume Configuration for YSZ on Six-Inch Silicon Substrates........................... 6-18

Figure 6-9. Cross-sectional View of Static Numerical Simulation Results................. 6-19

Figure 6-10. Mapping of Target Radial Location to Radial Location of Peak Simulated Film Thickness on Substrate 6-19

Figure 6-11. Contour Mapping of Film Thickness of YSZ Film on Six-Inch Diameter Silicon Substrates Grown Using the Rotation Plume Configuration 6-21

Figure 6-12. Cross-section of Film Thickness of YSZ Film on Six-Inch Diameter Silicon Substrates Grown Using the Rotation Plume Configuration 6-22

Figure 6-13. Comparison of the Static Numerical Simulation Results and Actual Growths Using the Rotation Plume Configuration for YSZ on Six-Inch Silicon Substrates 6-23

Figure 6-14. Mapping of Target Radial Location to Radial Location of the Peak Film Thickness on Substrate.. 6-24

Figure 6-15. Contour Mapping and Cross-Section of YSZ Film on Six-Inch Diameter Silicon Substrate Grown Using the Calculated Theoretical Profile Method 6-25

Figure 6-16. Comparison of the Calculated Radial Profile Designed to Produce Uniform Thickness Films and the Iterative Radial Profile 6-26

Figure 7-1. Initially Flat CP1 Polymer Substrate Suspended on an Aluminum Mounting Ring [2] 7-2

Figure 7-2. Concave Up Pyrex Mirror Mold with Cast CP1 Polymer Substrate [3] 7-4

Figure 7-3. YSZ-Coated CP1 Polymer Substrate Still Mounted to a Concave Pyrex Mirror Mold and Aluminum Ring [3] 7-5

Figure 7-4. YSZ Film Thickness on a 6-inch Diameter Silicon Substrate a) Grown using the Radial Profile b) and the Deposition Conditions Listed in Table 7-1. . 7-6

Figure 7-5. ZYGO Interferometer Images of Initially Flat CP1 Polymer Substrate Suspended on an Aluminum Mounting Ring [2] 7-7

Figure 7-6. Central 1.3-Inch Diameter Optical Path Difference Plot of the Initially Flat CP1 Polymer Substrate Suspended on an Aluminum Mounting Ring Displaying 2.51 Wavelengths (1594.2 nm) Peak-to-Valley Deviation and 0.52 Wavelengths (329.5 nm) Root Mean Square Deviation [2]............... 7-8

Figure 7-7. Image of Coated and Released CP1 Polymer Substrate Grown in Pyrex Mold and Mounted to an Aluminum Ring with Concave Surface Down [3] 7-10

Figure 7-8. Zygo Interferometer Image of an YSZ-Coated and Released CP1 Polymer Substrate Grown in Pyrex Mold and Mounted to an Aluminum Ring [3] 7-11

Figure A-1. Schematic Representation of Molecular Motion and Raman Scattering ... A-5

Figure A-2. Interaction Between a Molecule and a Photon Diagram............................ A-6

Figure A-3. Energy Levels for Normal Raman, Resonance Raman, and Fluorescence Spectra... A-7

Figure A-4. Double Monochromator Schematic [2]... A-12

Figure A-5. Typical Raman Spectrum for Bulk Crystalline Silicon Using a 514.5 nm Argon-Ion Laser Excitation Source.. A-15

Figure A-6. Stacking Order of 3C and 6H Silicon Carbide [11] A-16

Figure A-7. Stacking Order of Common Silicon Carbide Polytypes........................... A-17

Figure A-8. Raman Spectra of Several Silicon Carbide Polytypes [15]...................... A-18

Figure A-9. Absorption Coefficients as a Function of Wavelength for Bulk 3C and 6H Silicon Carbide [17] A-20

Figure A-10. Variation in Raman Wavenumber with Temperature [23]..................... A-25

Figure A-11. Relationship Between the Stokes/anti-Stokes Raman Peak Intensity Ratio and Temperature [23] A-25

Figure A-12. Typical 6H Silicon Carbide Raman Spectra and Fitted Parameters....... A-33

Figure A-13. Silicon Carbide Raman Spectra from Room Temperature to 800°C A-34

Figure A-14. Chronological In-Situ Silicon Raman Peak Wavenumber during Silicon Carbide Deposition.. A-35

Figure A-15. In-Situ Silicon Raman Peak Wavenumber as a Function of Thermocouple Output Temperature During the PLD Growth of Silicon Carbide A-36

Figure A-16. In-Situ Silicon Raman Peak Wavenumber Shift as a Function of Thermocouple Output Temperature During the PLD Growth of Silicon Carbide A-37

Figure A-17. Stokes Raman Mean Wavenumber Dependence on Temperature A-40

Figure A-18. Silicon Vibrational Temperature as a Function of Optical Pyrometer Output Temperature A-41

Figure A-19. Difference between Optical Pyrometer Temperature and Thermocouple Temperature. A-41

List of Tables

Table Page

Table 2-1. Electron Beam Evaporation Parameters for YSZ Deposition 2-12

Table 2-2. Sputtering Deposition Parameters for YSZ Deposition 2-19

Table 2-3. Dual Ion Beam IBAD Parameters for YSZ Deposition 2-22

Table 2-4. MOCVD Parameters for the Deposition of YSZ 2-26

Table 2-5. Generic PLD Parameters for the Deposition of YSZ 2-34

Table 3-1. Lambda Physik LPX® 305i Specifications [1] 3-2

Table 3-2. Distance of Photo Multiplier Tube Spatial Filters from Target 3-12

Table 4-1. YSZ on CP1 Polymer Substrates Growth Parameters Yielding Films Categorized as Flat 4-10

Table 4-2. YSZ on CP1 Polymer Substrates Growth Parameters Yielding Films with Bowed Curvature 4-12

Table 4-3. Fitting Statistics for No Curvature Pressure Distance Relationship When Ablating with a 1.57 J/cm^2 Laser Fluence 4-14

Table 4-4. Fitting Statistics for No Curvature Pressure Fluence Relationship When Ablating with a Target-to-Substrate Distance of 56.7 mm and a Laser Footprint Size of 14 mm^2 4-16

Table 4-5. Fitting Statistics for No Curvature Pressure Distance Fluence Relationship When Ablating with a 14 mm^2 Constant Laser Footprint Size 4-18

Table 5-1. Spectra Content of Plume Emissions from YSZ Ablation in an Oxygen Ambient Near 470 nm [12; 14; 15] 5-9

Table 5-2. Time-of-Flight Emissions from YSZ Plume Shifted Center-of-Mass Maxwell-Boltzmann Velocity Distribution Fitting Statistics 5-16

Table 6-1. Deposition Conditions for Uniform Film Thickness on Large Area Substrates Testing 6-7

Table 6-2. Uniform Thickness Statistics of YSZ Film on Six-Inch Diameter Silicon Substrate Grown Using the Iteratively Derived Radial Profile that Produced the Most Uniform Thickness to Date 6-10

Table 6-3. Peak Film Thickness of YSZ on Six-Inch Diameter Silicon Substrates Grown Using the Static Plume Configuration 6-15

Table 6-4. Statistics for the Normalized Cross-Sectional Film Thickness Along the X and Y Axis When Fitted to a Cosine N Distribution 6-16

Table 6-5. Uniform Thickness Statistics of YSZ Film on Six-Inch Diameter Silicon Substrate Grown Using the Calculated Radial Profile 6-26

Table 7-1. Deposition Parameters for Initially Flat CP1 Polymer Substrate Suspended on an Aluminum Mounting Ring 7-3

Table 7-2. Growth Parameters for Cast CP1 Polymer Substrate Cast in a Concave Pyrex Mirror Mold 7-4

Table 7-3. Growth Parameters for Cast CP1 Polymer Substrate Cast in a Concave Pyrex Mirror Mold 7-12

Table A-1. Stacking Order of Common Silicon Carbide Polytypes A-16

Table A-2. Raman Spectral Peaks for Common Polytypes of Silicon Carbide [15; 16] A-19

Table A-3. Growth Parameters for Silicon Carbide Thin Films on (100) Silicon Substrates A-30

List of Equations

Equation Page

(2-1).. 2-2

(2-2).. 2-37

(4-1).. 4-3

(4-2).. 4-5

(4-3).. 4-5

(4-4).. 4-6

(4-5).. 4-6

(4-6).. 4-16

(4-7).. 4-16

(4-8).. 4-17

(4-9).. 4-17

(4-10).. 4-17

(4-11).. 4-17

(5-1).. 5-4

(5-2).. 5-5

(5-3).. 5-6

(5-4).. 5-11

(5-5).. 5-11

(5-6).. 5-14

(5-7).. 5-14

(5-8).. 5-14

(5-9) ... 5-14

(5-10) ... 5-14

(5-11) ... 5-15

(5-12) ... 5-35

(5-13) ... 5-35

(5-14) ... 5-35

(6-1) ... 6-15

(A-1) ... A-7

(A-2) ... A-10

(A-3) ... A-20

(A-4) ... A-20

(A-5) ... A-20

(A-6) ... A-21

(A-7) ... A-21

(A-8) ... A-21

(A-9) ... A-22

(A-10) ... A-22

(A-11) ... A-23

(A-12) ... A-23

(A-13) ... A-24

(A-14) ... A-24

(A-15) ... A-24

AFIT/DS/ENG/03-06

Abstract

Current polymer membrane technology suffers from an inability to overcome shape deformation problems caused by intrinsic stresses from the membrane casting and mounting processes. This poses a difficult challenge to the US Air Force, which has a critical requirement for parabolic-shaped membrane mirrors for surveillance satellites. One method to overcome the shape deformation problem is to coat the membrane mirrors with a stressed coating to compensate for the shape deformations caused by the intrinsic stresses. However, previous attempts using sputtering, thermal evaporation, and electron beam evaporation met with limited success due to growth technique limitations. An innovative method to grow yttria stabilized zirconia (YSZ) thin films on CP1 polymer substrates and silicon substrates using controlled-stress large-area pulsed laser deposition (PLD) technique was developed. In addition, an optical time-of-flight (TOF) sensor system for control of the PLD process with respect to YSZ thin film stress was investigated and incorporated into the PLD process control systems. Initially, the PLD-grown YSZ film stress was controlled using a combination of deposition parameters; namely ambient pressure, laser fluence, and target-to-substrate distance. A theory was applied to describe the relationship among these deposition parameters for the conditions that produced YSZ films on CP1 polymers that exhibited no stress. All deposition parameters were held as constant as possible throughout the deposition. In addition to constant deposition parameter control, an optical TOF sensor was incorporated into the laser fluence feedback loop. A shifted center-of-mass Maxwell-Boltzmann (SCMMB) distribution was used to model the TOF data and the streaming velocity parameter from

the SCCMB distribution was extracted. This streaming velocity was indicative of the YSZ film stress and correlated well with the data obtained during the constant deposition parameter control experiments. A streaming velocity of approximately 6250 m/s was found to produce YSZ thin films on CP1 that exhibited no stress, while faster streaming velocities were found to produce compressively-stressed YSZ thin films. Likewise, slower streaming velocities produced tensiley-stressed YSZ thin films on CP1 polymer substrates. The streaming velocity was then used to control the laser fluence in order to compensate for slight variations in deposition conditions. Thus, controlling the laser fluence greatly improved the YSZ film stress run-to-run stability. Additionally, iterative and theoretical experiments produced large-area (6-inch diameter) YSZ thin films on silicon substrates with less than ten percent total thickness (typically 75-200 nm) variations. Compressively stressed YSZ thin films were grown on initially flat 6-inch diameter suspended CP1 polymer substrates using the ambient pressure, laser fluence, and target-to-substrate distance relationship theory and the large-area investigation results. The resulting growths demonstrated desirable shape modification to the polymer substrates. However, the suspended CP1 polymer substrate YSZ film growths were limited to a maximum repetition rate of 10 Hz at 1.57 J/cm^2 laser fluence to avoid substrate damage. The investigation was repeated using CP1 polymer substrates still mounted to the casting mold, which were grown at repetition rates up to 40 Hz without damage. Initial results from the YSZ thin films grown CP1 polymer substrates still mounting to the casting mold were promising. Finally Raman spectroscopy, which has the potential to be used as a non-destructive *in-situ* film stress sensor, was shown to be compatible with the PLD process during the growth of silicon carbide.

CONTROLLED-STRESS LARGE-AREA PULSED LASER DEPOSITION OF YTTRIA STABILIZED ZIRCONIA

1 Introduction

1.1 Introduction

Several directorates of the Air Force Research Laboratory (AFRL) are currently pursuing large-diameter mirror-based satellite telescopes for surveillance [1]. The project vision is to "deploy an Atlas-launched, diffraction limited, visible-to-IR telescope that will dramatically enhance current surveillance capabilities" [1]. The project, labeled the "Membrane Mirror Experiment" (MMX) [2], is of great importance to the Air Force. The 2002 Space Experiments Review Board (SERB) rated the MMX its 15th highest priority and approved the MMX project for space tests.

The MMX project encompasses a multitude of technical disciplines ranging from polymer materials to dynamic waveform correction devices. The multi-discipline aspect of the MMX project is evident in an example satellite system shown in Figure 1-1. Of the many subsystems shown in Figure 1-1, this research will focus on issues relevant to the polymer and dielectric laminate membrane mirror.

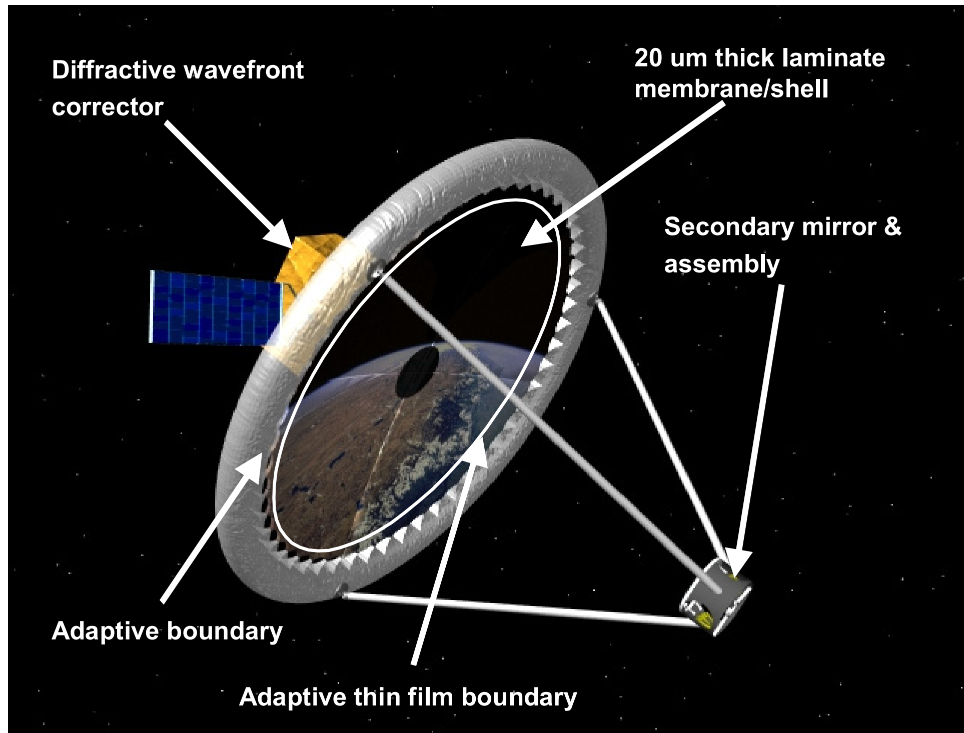

Figure 1-1. Example Satellite System [1]

Membrane mirrors comprise a crucial portion of the MMX project. In fact, advances in membrane mirrors have enabled the MMX vision to exist. According to the Scientific Advisory Board Science and Technology Review report on AFRL Directed Energy (DE) Directorate in 2000:

> *The membrane mirror work is impressive. Much progress has been made in the past two years, and apparently at low cost. … Membrane mirrors are potentially a revolutionary enabler to various space-based activities, and the Lab should get ready for space experiments.* [1]

Although membrane mirrors have several of the same advantages found with conventional monolithic mirrors, the primary motivation to use membrane mirrors is cost. The performance requirements for the MMX project demand a large 25-meter aperture mirror. The size and weight of large aperture monolithic mirrors prohibit their use in space-based applications. Figure 1-2 presents a launch cost comparison between the

systems based upon three different mirror types. Launch costs are primarily based upon mirror weight, which is proportional to the square of the aperture diameter [1]. Thus, Figure 1-2 provides strong justification for using membrane optics in large-aperture, space-based telescopes. The diameter proposed for the MMX project is 25 meters. The launch cost associated with a 25-meter membrane mirror based-system is approximately $275 million [1]. Both the 25-meter monolithic and deployable mirror-based systems are so cost prohibitive ($15.2 and $1.7 billion, respectively) that they are outside the range of the plot shown in Figure 1-2.

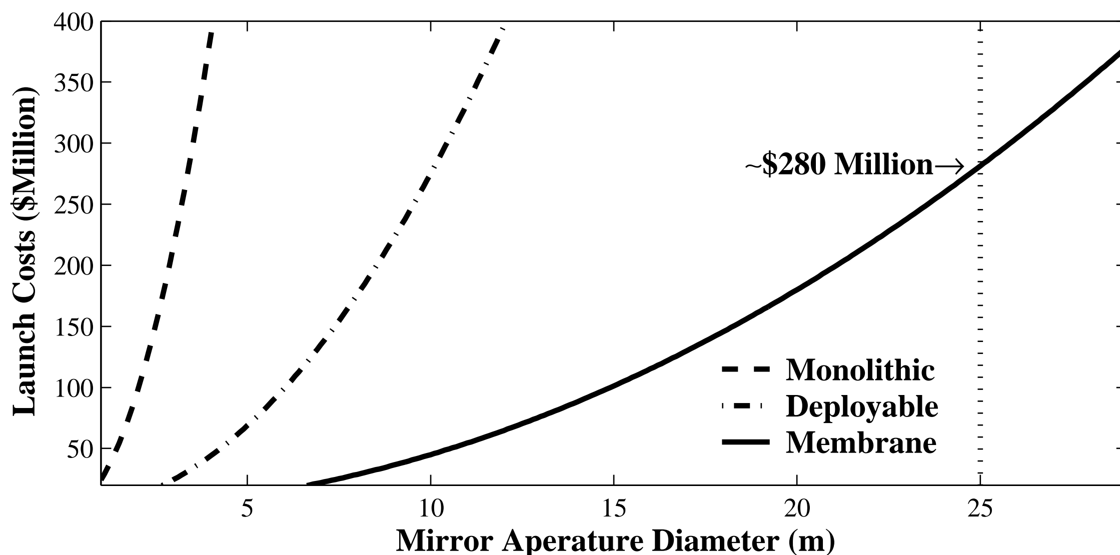

Figure 1-2. Comparison Between Launch Costs and Mirror Aperture Diameter for the Three Different Mirror Types [1]

1.2 Problem Statement and Approach

The shape and the large-area aspects of the membrane mirror comprise two of the critical issues for the MMX project, as described in Section 1.1. The polymer membranes are manufactured using a spin-coating process in which liquid polymer,

specifically a colorless, low dielectric, radiation-resistant polyimide, denoted CP1, that was developed by NASA Langley Research Center for space-based applications [4; 5; 6], is poured into a rotating Pyrex mold and then cured [3]. Figure 1-3 shows a schematic of the process and an example of a molded polymer. SRS Technologies is currently investigating the scale-up in diameter of the CP1 polymer for the MMX project, which is outside the scope of this research [1].

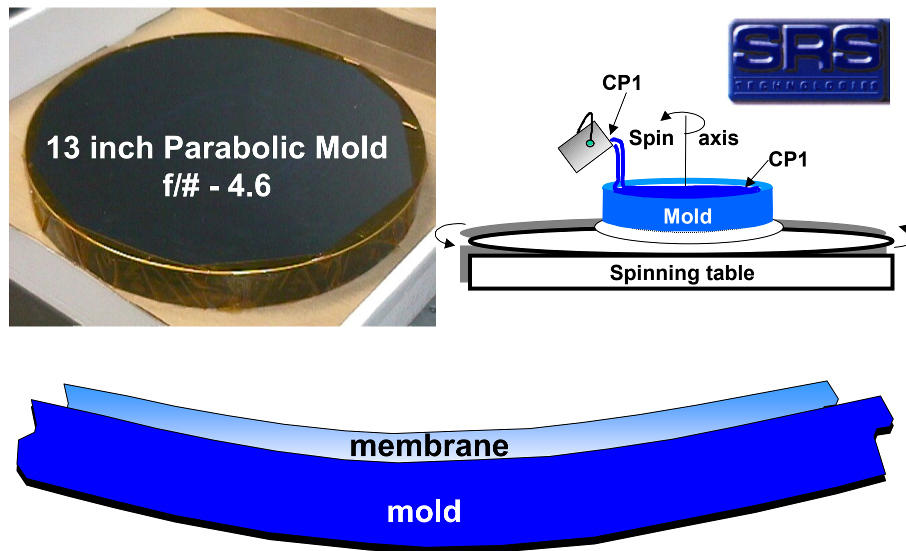

Figure 1-3. CP1 Polymer Spin-coating Schematic and Example [1]

The CP1 polymer shown in Figure 1-3 still resides inside the parabolic mold. During mounting to a mounting ring and removal of the CP1 polymer mirror from the casting mold, the mirror loses much of its shape. Thus, the resulting mirror is described as a near-net shape membrane mirror. Another process must compensate for the change in shaped due to the intrinsic stresses from membrane mirror mounting and subsequent release from the mold. One possible solution is to coat the membrane mirror, either before or after the mounting/release process, as shown in Figure 1-4. If the stress and

uniformity of such a coating can be sufficiently controlled, the shape of the mounted and released membrane mirror can be altered back to the desired net shape [1].

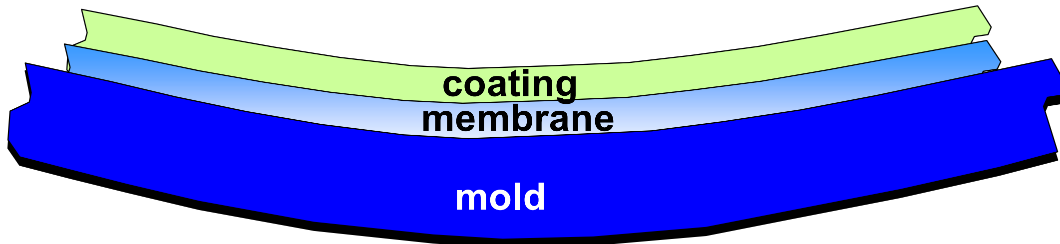

Figure 1-4. Membrane Mirror Coating Solution [1]

Attempts to deposit the coating onto the membrane mirror have been and are being investigated using a variety of deposition methods, which include: thermal evaporation, e-beam evaporation, and sputtering (both RF and DC). Ion-assisted enhancements to these deposition processes and cathodic arc deposition were also attempted. To date, these deposition processes have not produced satisfactory results. Pulsed laser deposition (PLD) has several advantages over the previously listed deposition techniques, such as the ability to produce films with high packing density and high indices of refraction [1], as described in Chapter 2. To exploit these advantages, this research focuses on studies of the deposition of membrane mirror coatings by PLD.

The goals of this research were to produce controlled-stress, large-area, pulsed-laser-deposited thin films on CP1 polymer substrates and to investigate relevant monitoring sensors and techniques for the control of the PLD process, specifically with respect to deposited thin film stress. Yttria stabilized zirconia (YSZ) was chosen as a suitable material to deposit based on the availability of experts within AFRL and

previous PLD research into the characteristics of YSZ [7; 8; 9]. The growth aspect of the research goals was accomplished through multiple growths of YSZ on both silicon substrates and CP1 polymer films using a wide range of deposition parameters. In addition to these thin film growths, the PLD plume was characterized in terms of stress-determining parameters using optical emission spectroscopy and fast-imaging photography.

1.3 Dissertation Organization

The remainder of this dissertation is divided into eight chapters. Chapter 2 presents an overview of the deposition techniques typically used to grow silicon carbide and yttria stabilized zirconia, which includes pulsed laser deposition. In addition, Chapter 2 discusses various thin film analysis techniques used in this dissertation. Following this background information, Chapter 3 details the PLD system, including both the hardware and software used for this research.

The research goals described in Section 1.2 were divided into four parts, which are split into individual chapters. Chapter 4 reports on the determination of stress-affecting deposition parameters. In addition, Chapter 4 derives a physics-based theory that describes the relationship among these stress-affecting deposition parameters. This theory allows equivalent-stress films to be deposited using an unlimited variety of relevant deposition parameters, as well as specifying the affect of each parameter on film stress. Chapter 5 expands upon this theory by determining the *in-situ* measurable plume parameters that predict the film stress. A closed-loop PLD process control scheme utilizes these parameters to improve the run-to-run stability of the film stress, as also described in Chapter 5. Independent of the stress investigations, Chapter 6 illustrates two

large-area PLD investigations and the resulting YSZ thin film growths. Then, Chapter 7 incorporates this large-area aspect into the controlled-stress aspect to produce uniform-thickness controlled-stress YSZ films on undamaged six-inch diameter CP1 polymers substrates. Finally, Chapter 8 summarizes this research, details the contributions represented here, and lists additional areas in which this research could be expanded.

In addition to the research goals listed previously, Raman spectra were acquired during the PLD growth of silicon carbide (SiC), or *in-situ*. Analysis of the Raman spectra was performed to correlate thin film stress with Raman peak wavenumber shift. Appendix A describes this investigation.

Bibliography

1. Martin, Lt Col Jeffrey B."Membrane Mirrors in Space." Unpublished Report to DARPA Program Managers, DARPA, Washington DC, 5 Feb 2002.

2. Office of the Under Secretary of the Air Force for Space Acquisition, Department of the Air Force. Memorardum. "Results of 2002 DoD Space Experiments Review Board." Washington DC, 2002.

3. Patrick, Brian. Optical Engineer, SRS Technologies, Huntsville AL. Personal Correspondence. 22 October 2002.

4. St. Clair, A. K. and St. Clair, T. L., U.S. Patent 4,595,548 to NASA June 17, 1986.

5. St. Clair, A. K. and St. Clair, T. L., U.S. Patent 4,603,061 to NASA July 29, 1986.

6. "Thin Film…Large Payoff," *Spinoff*, no vol.: 98, 1998.

7. Voevodin, Andrey A., J. G. Jones, and Jeffery S. Zabinski. "Characterization of Zro_2/Y_2O_3 Laser Ablation Plasma in Vacuum, Oxygen, and Argon Environments," *Journal of Applied Physics*, 88(2): 1088-1096, 15 July 2000.

8. -----. "Structural Modification of Single-Axis-Oriented Yttria-Stabilized-Zirconia Films under Zirconium Ion Bombardment," *Applied Physics Letters*, 78(6): 730-732, 5 February 2001.

9. Jones, J. G., A. A. Voevodin, and J. S. Zabinski. “Characterization of Plume Fluence for Laser Ablation of Yttria Stabilized Zirconia in Mixed Oxygen and Argon Environments,” *Surface and Coatings Technology*, 16: 258-262, 2001.

2 Background

2.1 Overview

This chapter provides an overview of the relationships between thin film properties and stress, several physical transport methods used to grow yttria stabilized zirconia (YSZ) thin films on various substrates, and several characterization techniques used to analyze YSZ. A basic understanding of various epitaxial growth methods provides a better understanding of the benefits pulsed laser deposition (PLD) provides over these other growth methods. In addition, conceptual knowledge of PLD is helpful to better understand the research presented in this dissertation. The remainder of this chapter describes the thin film properties/stress relationship, various epitaxial growth methods, pulsed laser deposition, and several thin film characterization techniques used in this research.

2.2 Thin Film Stress

The origins of thin films stress can be divided into two groups, thermal stress and intrinsic stress. Thermal stress is described in Section 2.2.1. Both thermal and intrinsic stress may be present in physical vapor deposited thin films. The source of intrinsic stress and the correlation with thin film microstructure is discussed in Section 2.2.2. Finally, the relationship between thin film microstructure and deposition parameters is described in Section 2.2.3.

2.2.1 Thermal Stress

Thermal stress refers to the stress caused by differential volume changes between the substrate and the thin film due to a mismatch in the thermal expansion for thin films grown at elevated growth temperatures. Thermal stresses occur when the substrate and the thin film are cooled from growth temperature to room temperature. The coefficient of thermal expansion α relates the magnitude of the material contraction to the change in temperature. Thus, the difference in the coefficient of thermal expansion between the substrate material ($\alpha_{Substrate}$) and the thin film material ($\alpha_{Thin\ Film}$) can be used to estimate the amount of thermal stress [1; 2; 3; 4; 5; 6; 7; 8; 9; 10]. Figure 2-1 illustrates the effects of thermal stress. The top row of substrates and thin films shown in Figure 2-1 reveals the substrate and the thin film relative change in volume for the each of the three possible thermal expansion coefficient combinations after cooling to room temperature from growth temperature. The bottom row illustrates the results when the thin film adheres to substrate. For the conditions in which $\alpha_{Thin\ Film}$ is not equal to $\alpha_{Substrate}$, the substrate will curve. The amount of curvature can be used to estimate the stress in the thin film through Stoney's Formula, as shown in Equation (2-1):

$$\sigma_{film} = \frac{E_s h_s^2}{6(1-\upsilon_s)h_f}\left(\frac{1}{r}\right) \quad (\text{GPa}) \tag{2-1}$$

where σ is the *film stress* in giga-Pascals (GPa), E_s is *Young's modulus of the substrate material* (GPa), h_s is the *substrate thickness* (meters), h_f is the *film thickness* (meters), υ_s is *Poisson's ratio of the substrate material* (unitless), and r is the *substrate radius of curvature* (m). Substrate curvature measurements are commonly used to estimate the net stress of thin films [2; 8]. Other measurements use post-processing techniques to produce

stress measurement structures, such as suspended cantilever beams, double clamped beams, and suspended membranes. These measurement structures are used to estimate stress on a micro scale, as compared to the macro scale or net stress wafer curvature measurement. X-ray diffraction (XRD) measurements, as described in Section 2.5.5, can also be analyzed to calculate stress [6; 7; 8; 10].

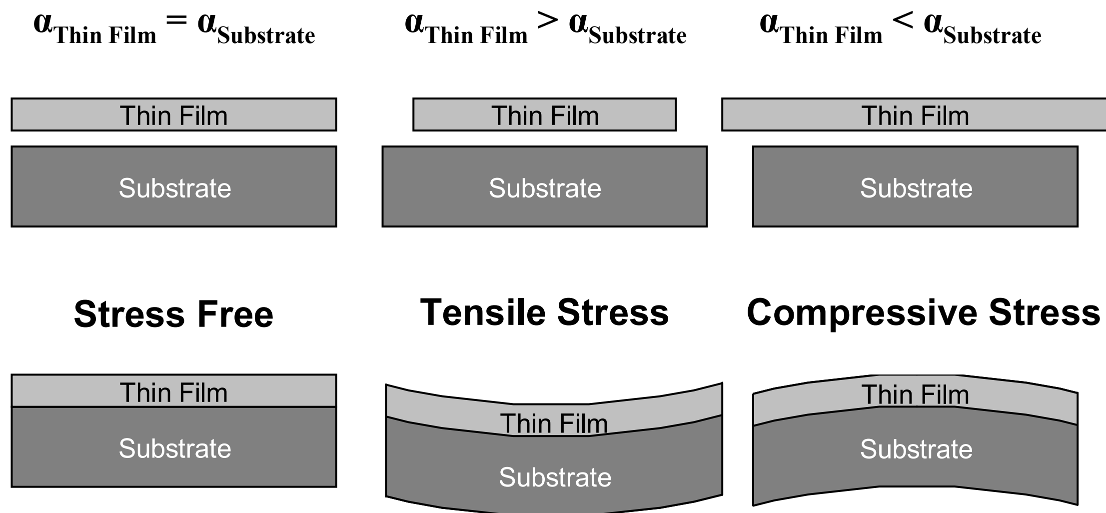

Figure 2-1. Origin of Thermal Stress Diagram

2.2.2 Intrinsic Stress

Intrinsic stress refers to the stress caused by the microstructure of the thin film. Most evaporation deposition systems produce thin films with tensile intrinsic stress caused by crystallographic flaws, microvoids in the thin film material, and/or grain boundary interfaces. Figure 2-2 illustrates the stages of thin film growth. As material arrives at the substrate, localized growth sites form and act as “seeds” for thin film growth (nucleation). As the thin film growth continues, these localized growth sites abut

other localized growth sites (island coalescence). Without a renucleation process, the thin film growth evolves into multiple adjacent growths (grain growth) with grain boundaries separating the adjacent localized growth sites (grains). Figure 2-3 depicts a thin film cross section. The grain boundaries appear as voids in the thin film. These voids create tensile stresses due to the attractive interaction of the atoms across the voids. In addition to grain boundaries, microvoids are vacancy defects in the thin film. Microvoids also produce a tensile stress in the thin film, similar to the grain boundary effects [2].

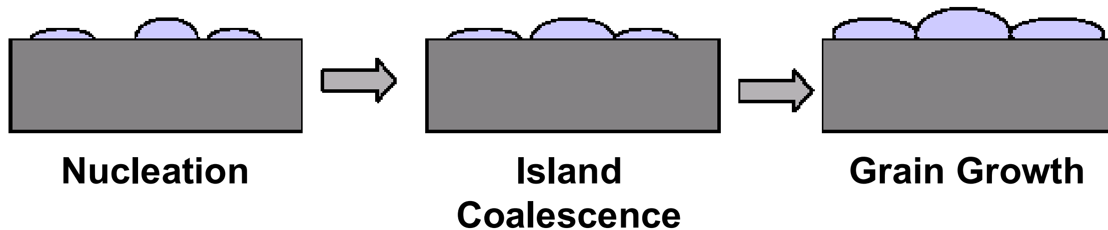

Figure 2-2. Thin Film Growth Model Diagram [2]

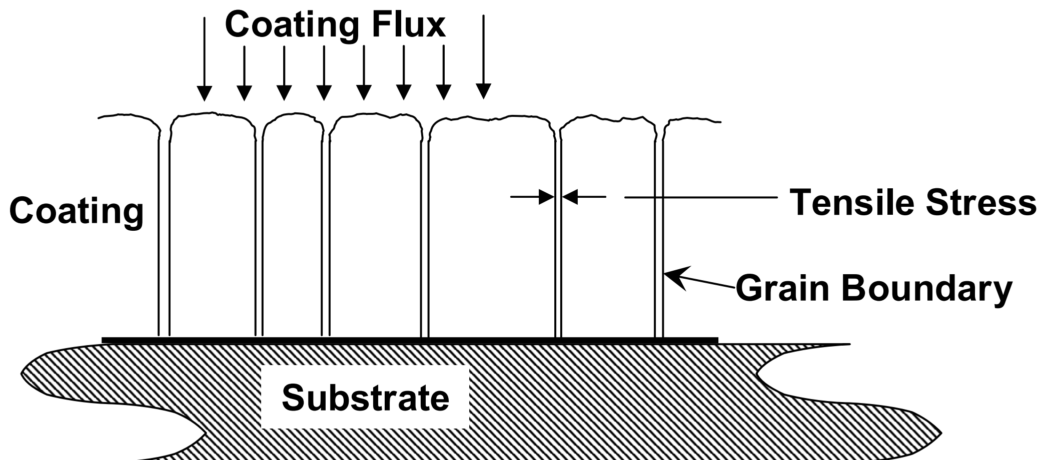

Figure 2-3. Grain Boundary Intrinsic Stress Diagram [4]

Although most evaporation deposition systems produce thin films that exhibit tensile intrinsic stress, several internal thin film processes can occur to reduce the tensile stress. Depending upon the deposition conditions, recrystallization or recovery can occur, which increases the size of the grains resulting in a reduced number of grain boundaries in the thin film. In addition, recovery can "fills in" the microvoids in the thin film. Both recrystallization and recovery reduce the tensile stress in thin films [2; 3; 4; 10].

In addition to reducing the tensile stress in the thin film, compressively-stressed thin films can be produced, given the appropriate deposition conditions. Atomic shot peening refers to the process in which the surface of the thin film is bombarded with heavy ions or energetic particles. This bombardment compacts the underlying thin films to reduce the size of or eliminate microvoids and grain boundaries, which reduces the tensile stress of the thin film. Furthermore, relatively high energy bombardment of the thin films can compact the thin films sufficiently so that the thin films will exhibit compressive stress. Besides atomic shot peening, the incorporation of impurities into the thin film can produce compressive stress, similar to the interstitial atom incorporation into a crystal lattice [1; 2; 3; 4; 8; 10].

Regardless of the source of thin film stress, all thin films are in some state of stress [2; 3; 4; 8; 10]. Forty years of research has produced a number of phenomenological models that attempt to explain the sources of residual stress [3; 7]. However, residual stress is a complex thin film behavior. As such, the only generalizations that can be made about the expected level of stress in a thin film are that the stress is highly correlated with process/deposition parameters [2; 3; 7] and that

intrinsic stress originates in the thin film microstructure [1; 2; 3; 4; 5; 6; 7; 8; 9; 10]. Therefore, Section 2.2.3 discusses the relationship between deposition parameters and the resulting thin film microstructure.

2.2.3 Microstructure Dependence upon Deposition Parameters

Movchan and Demchisin [11] first proposed a theory that related the microstructure of thin films to the relative substrate temperature during the deposition. The ratio of the substrate temperature during deposition (T_s) to the thin film material's melting temperature (T_m) was used to create three growth "zones". Zone 1 (T_s/T_m ratio less than or equal to 0.3) corresponds to porous thin films exhibiting textured and fibrous fine grains with domed tops and large defect densities. Zone 2 (T_s/T_m ranging from 0.3 to 0.5) describes thin films with columnar grains that have highly faceted tops that produce a smooth mat surface texture. Thin films grown under Zone 3 conditions (T_s/T_m ratio greater than or equal to 0.5) have columnar grains with larger grain sizes than that of Zone 2 due to increased bulk diffusion and recrystallization [4; 10]. Figure 2-4 illustrates the thin film microstructure for each of the three zones relative to the T_s/T_m ratio.

Thornton and Hoffman [4] expanded the Movchan-Demchisin structure zone model (SZM) to include sputtering pressure. In addition, the Thornton-Hoffman SZM added a new zone "T," which is a transition zone between Zone 1 and Zone 2. Zone T characterizes thin films as dense arrays of fibrous grains with voided boundaries. Zone T thin films have a smoother surface than either the Zone 1 or Zone 2 thin films. These characteristics of Zone T films have been attributed to ion bombardment during the sputtering of the thin film. The sputtering process and ion bombardment are described in

more detail in Sections 2.3.2 and 0. Figure 2-5 shows the thin film microstructure for each of the four zones in the Thornton-Hoffman SZM.

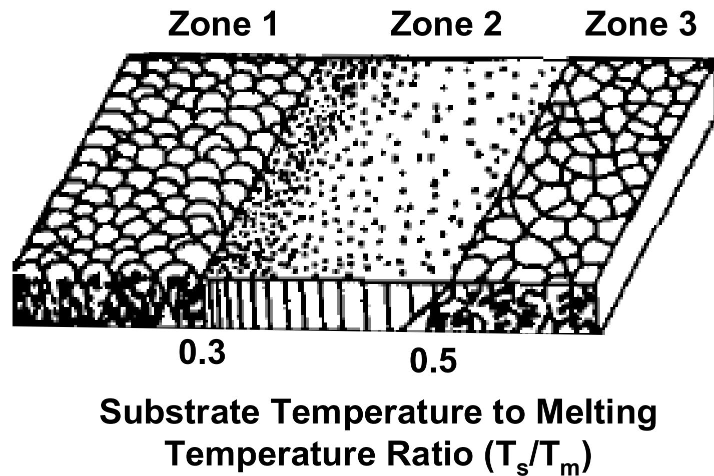

Figure 2-4. Structure Zone Model Correlating Thin Film Microstructure with Substrate Temperature to Thin Film Material Melting Temperature Ratio [4; 10].

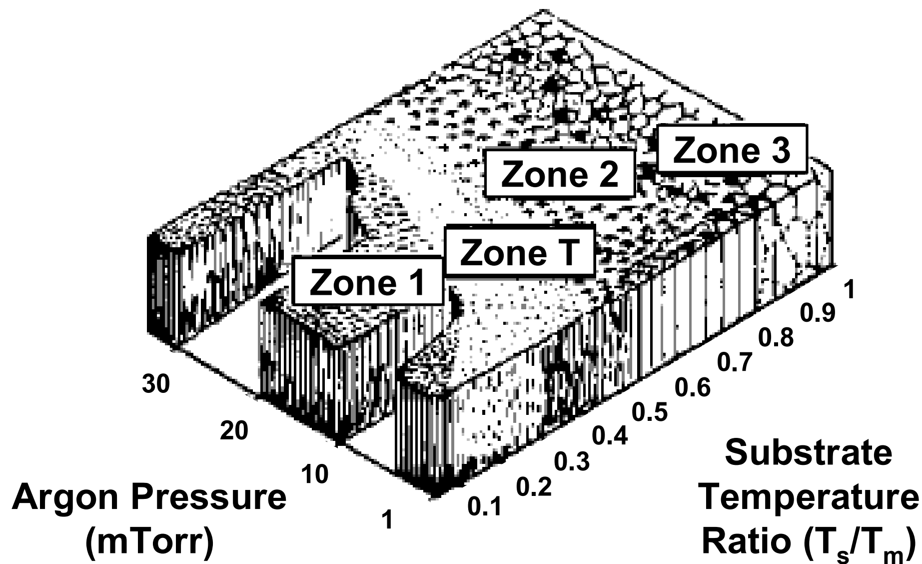

Figure 2-5. Schematic Representation of the Thornton-Hoffman Structure Zone Model Illustrating the Influence of Argon Pressure for Cylindrical Magnetron Sputtered Coatings [4; 10]

Messier, et al., also include Zone T in their SZM. However, the Messier SZM relates Zone T to bombardment-induced mobility energies at the substrate surface. As the energy increases, the Zone T width increases and the Zone 1 width decreases. Zone 2 is unaffected. The Messier SZM is in good agreement with the Thornton-Hoffman SZM since both models show Zone T increasing with sputtering particle energy.

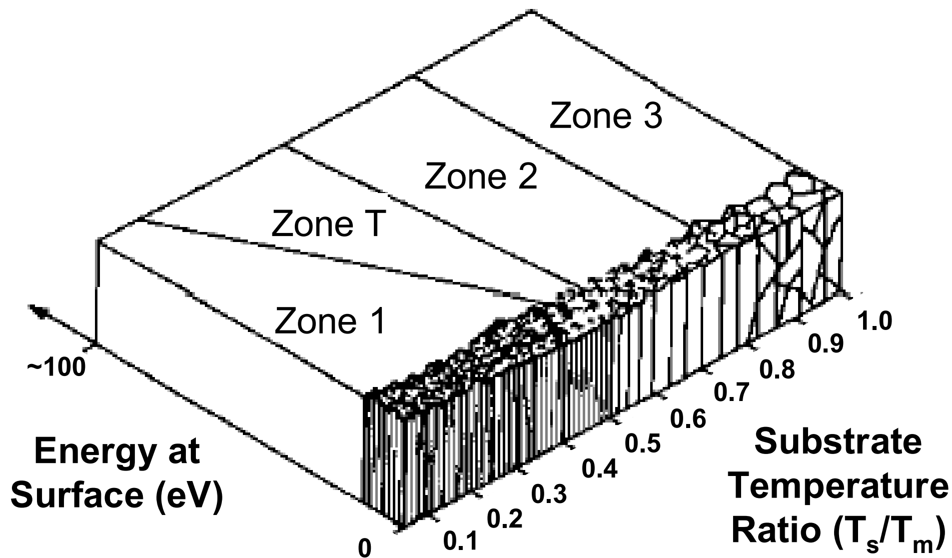

Figure 2-6. Messier Structure Zone Model Diagram Illustrating the Influence of Surface Mobility Energy on Zone T [10]

Other research has shown that the structure zone model derived from magnetron sputtered films can be generically applied to any physical vapor deposition technique that includes “super-thermal energy particles striking” the thin film surface [3]. In addition, the change in deposition conditions corresponding to the Zone 1 to Zone T transition usually includes a stress reversal from tensile to compressive stress. Initially, this stress reversal was incorrectly attributed to sputtering gas incorporation into the thin film. Further research has shown that the stress reversal is primarily due to thin film

densification caused by atomic peening, as described earlier. Thus, an idealized stress and normalized momentum relationship was found, as shown in Figure 2-7. Relatively low momentum bombardment deposition conditions produce tensilely-stressed porous thin films that are characterized as Zone 1 growths. As the normalized momentum is increased, the tensile stress reaches a maximum and is then rapidly reversed. Further increases in the normalized momentum produce Zone T compressively-stressed thin films [3]. The variation in normalized momentum can be equivalently produced by varying one or more of the following variables: the ratio of the target material's atomic mass to the atomic mass of the sputtering gas, the sputtering gas pressure, and/or the angle of the sputtering flux [3; 4].

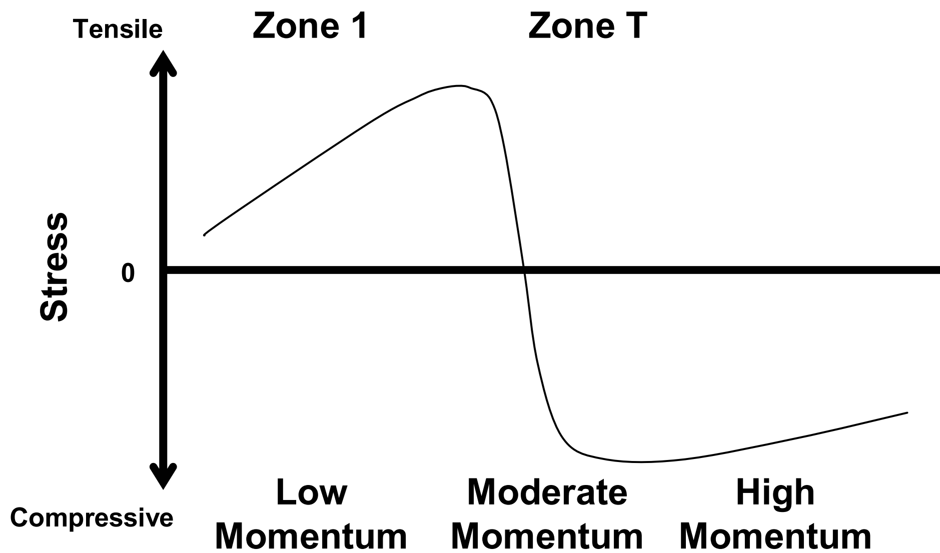

Figure 2-7. Idealized Stress–Normalized Momentum Curve from Sputtered Thin Films [3]

2.3 Epitaxial Deposition Overview

Although many methods to grow thin films exist, only a few are commonly used to grow YSZ, including: electron beam evaporation, sputtering, ion beam assisted deposition, vapor phase epitaxy, and pulsed laser deposition [12; 13; 14]. The word epitaxy originates from the Greek words “epi,” meaning on, and “taxis,” meaning arrangement [15]. During epitaxial growth, molecules of the desired elements are deposited at the proper crystallographic location to grow thin films on a compatible substrate, which is generally bulk crystalline material with a nearly equivalent lattice constant to that of the thin film. Epitaxially-grown YSZ, as well as many other materials, can be grown on substrates that are composed of a different material, such as silicon or fused quartz. For electronic application, this reduces the fabrication costs by allowing high quality material to be deposited on lower-cost substrates [15]. In addition, epitaxial growth allows alternating structural and sacrificial layers to grown on various substrates for microelectromechanical systems [16].

2.3.1 Electron Beam Evaporation

Electron beam evaporation is a high vacuum thermal deposition process in which the material to be deposited is thermally evaporated using an electron beam [10; 17; 18]. Figure 2-8 illustrates the basic components of an electron beam evaporation system: an electron beam source, electron beaming focusing and steering elements, a vacuum chamber, a vacuum pump, a source material, and substrate(s). An electron beam source produces electrons that are directed to the surface of the source (material to be deposited) by electron beam focusing and steering elements (labeled “Focusing Magnet” and

“Deflecting Magnet” in Figure 2-8). The electrons bombard the surface of the source (labeled “Ingot Rod” in Figure 2-8), which heats the source to create a “Molten Pool.” A vacuum chamber and vacuum pump produce a high vacuum in the area between the source and the substrate [10; 17]. This vacuum typically ranges from 10^{-5} to 10^{-10} Torr, which results in a large mean free path (typically 5×10^2 to 10^7 cm) relative to the distance between the source and the substrate [10; 17; 18]. Thus, evaporated atoms travel from the source to the substrate without undergoing any collisions. A crucible contains the molten pool and cools the remaining source material [10; 17; 18]. The electron beam evaporation system shown in Figure 2-8 uses an ingot rod as the source material. As material is removed from the molten pool by evaporation, the ingot rod is feed up into the crucible so that the surface of the molten pool remains at a fixed distance from the

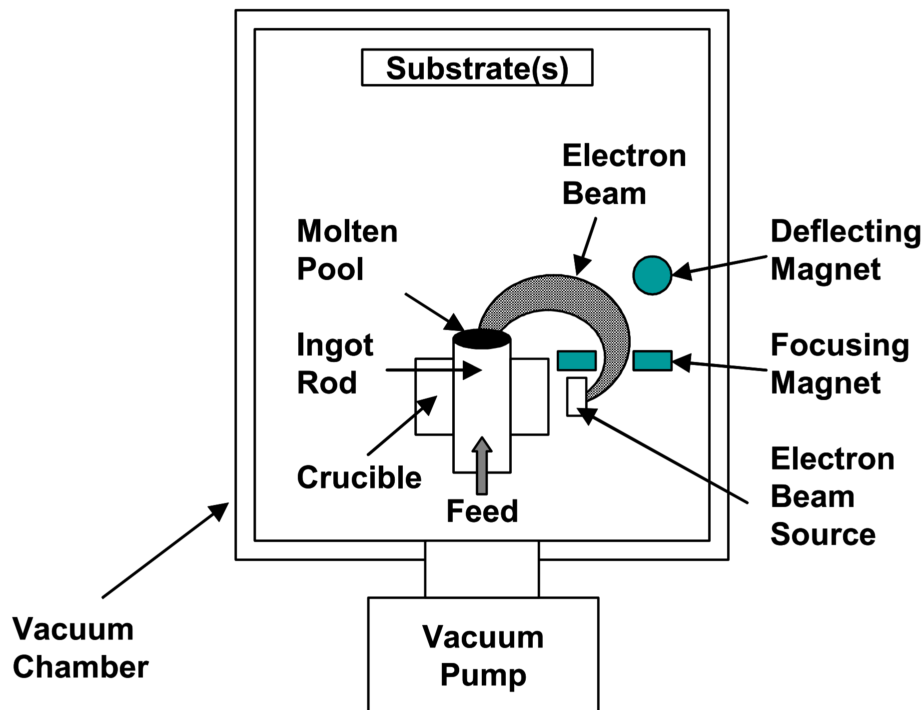

Figure 2-8. Electron Beam Evaporation System Schematic [10; 17]

substrate. Other configuration may not include such a feed mechanism. Table 2-1 lists the relevant deposition parameters used to deposit YSZ by electron beam evaporation. As listed in Table 2-1, YSZ is typically deposited onto a heated substrate, typically above 500° C. However, the current literature also describes some research that investigates depositing YSZ with the substrate at room temperature [19]. The YSZ crystalline quality is highly dependent upon the substrate temperature. As such, the YSZ films grown at room temperature were amorphous, while all the YSZ films grown with substrate temperatures greater than or equal to 500° C were crystalline.

Table 2-1. Electron Beam Evaporation Parameters for YSZ Deposition

Parameter	Values
Background gas	4% hydrogen/96% argon gas [21; 22] None [19; 20; 23]
Deposition pressure (mTorr)	10 [23] 20 [21; 22] 30 [20]
Substrate temperature (° C)	27, 700, 830 [19] 500 [20] 625 [21; 22] 800-850 [23]
Deposition rates (nm/s)	0.1 [19] 400 [20]
Film thickness (nm)	100 [19] 130-200 [21; 22] 700-2000 [23]
Source-to-substrate distance (cm)	28 [20]

2.3.2 Sputtering Deposition

Sputtering deposition is a coating process in which a liquid or solid target surface is bombarded with gas ions so that the target material is ejected from the surface and

deposited on a substrate [10; 24; 25]. The surface erosion portion of the sputtering deposition technique (sputter etching) can be compared to sandblasting at an atomic level. In fact, sputtering is often used to etch a surface for many processes, such as surface cleaning, semiconductor wafer patterning, micromachining, and depth profiling [25]. As stated previously, sputter etching removes surface atoms through a transfer of momentum from the bombarding ion to the target surface, as shown conceptual in Figure 2-9. An incident ion is generated and accelerated toward the target surface. The incident ion strikes the target surface and transfers its momentum to the target atoms. The transferred momentum is sufficient to break atomic bonds and dislodge the surface atoms [10; 24; 25]. A more conceptual description of sputtering is to consider the target atoms as billiard balls stacked together against a billiard table bumper and an incident ion as the cue ball. Thus, when the cue ball strikes one or more of the billiard balls, the cue ball's momentum is transferred into the stack of billiard balls, which causes one or more of the billiard balls at the surface to be ejected [24].

The direction in which the sputtered atoms are ejected predominantly depends upon the energy at which the ions strike the target surface (knock-on energy). A cosine distribution is often used to describe the angular distribution of sputtered particles, as shown in Figure 2-10. A cosine distribution equates the sputtered atom flux at a given angle to product of the sputtered atom flux emitted at normal incidence to the target surface and the cosine of the angle from normal incidence. An over-cosine distribution describes an angular distribution in which the sputtered atoms are grouped more closely toward normal incidence (forward-peaked). Likewise, an under-cosine distribution denotes the opposite condition where the angular distribution is more widely spread.

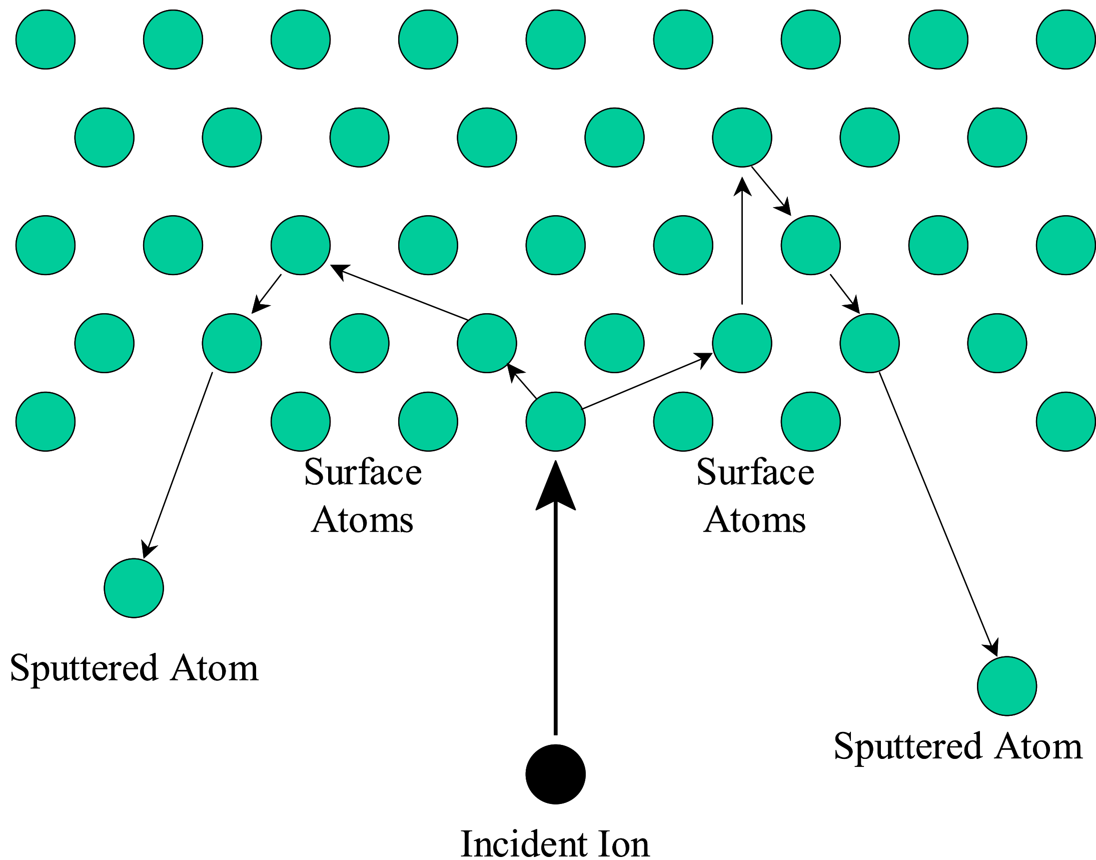

Figure 2-9. Physical Sputtering Process Diagram [25]

Sputtering using relatively low knock-on energies typically produces under-cosine distributions. Similarly, sputtering using relatively high knock-on energies produces over-cosine distributions [25].

Sputtering deposition consists of sputter etching where a substrate is located near the sputtering target so that the sputtered atoms are deposited on the substrate surface. The various types of sputtering deposition are defined by the incident ion generation sources, such as DC sputtering, magnetron sputtering, RF sputtering, etc. The simplest type of sputtering, DC sputtering, consists of a cathode (the target), an anode (the substrate or substrate holder), a vacuum chamber, a background gas, and a DC power supply, as shown in Figure 2-11.

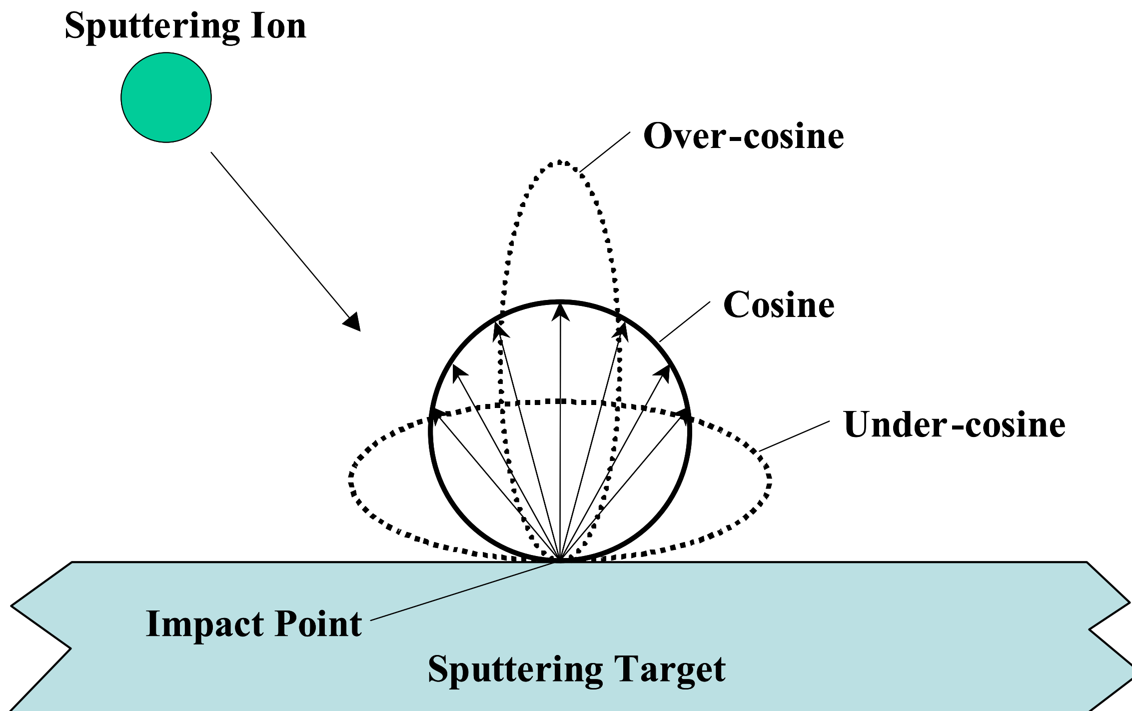

Figure 2-10. Angular Sputtering Emission Distribution Diagram [25]

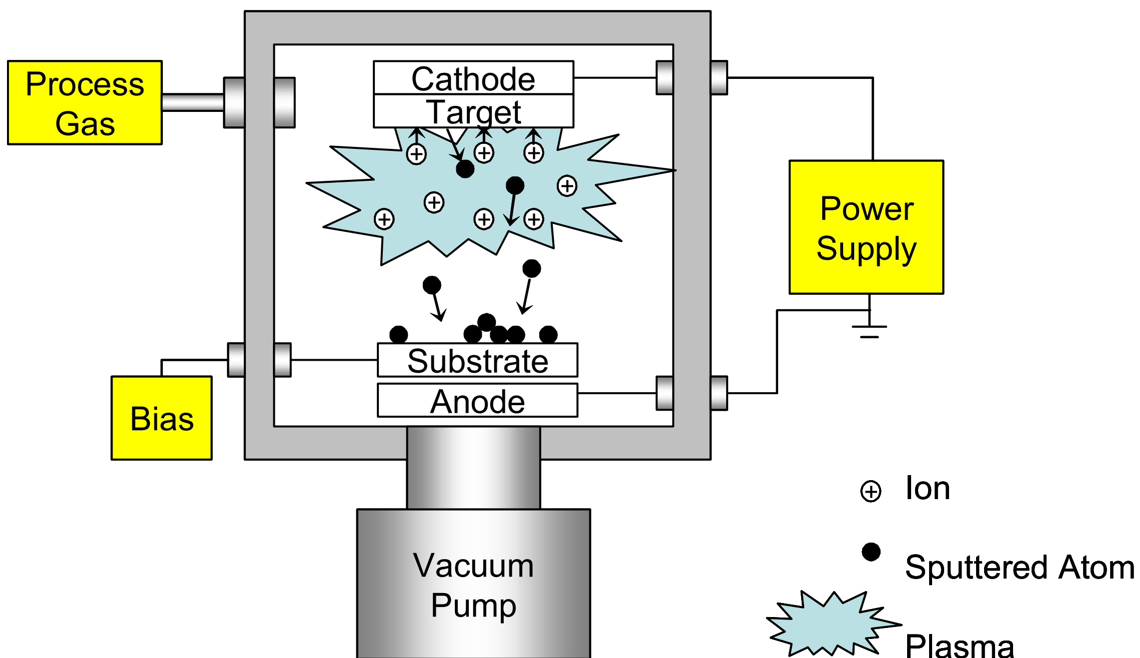

Figure 2-11. DC Sputtering Deposition System Schematic [26]

The chamber is initially evacuated to a relatively low pressure and then filled with a background gas. When an adequate voltage is applied between the anode and the cathode, the background gas breaks down into a plasma discharge. Ions from the plasma are rapidly accelerated toward the cathode and strike the target surface. As described previously, the impact of the accelerated ions cause target atoms to be sputtered from the surface of the target. These sputtered atoms traverse through the plasma and are deposited on the substrate [10; 24; 25]. Substantial amounts of the background gas can be incorporated into the sputtered film due to the relatively high background gas pressure and/or outgassing from the sputtering fixtures. To eliminate or dramatically reduce the incorporation of the background gas in the sputtered film, a slight bias or low negative charge is applied to the substrate. This bias creates a light ion "scrubbing" effect at the substrate surface that can remove the loosely attached gas atoms without disturbing the sputtered film [24]. DC sputtering cannot be used to deposit thin films if the target is insulating or if the background gas reacts with the target surface to create an insulating layer. For example, a metal target in an oxygen background gas may form an insulating oxide layer on the target surface that prohibits DC sputtering [10; 24].

RF sputtering overcomes the insulator sputtering issue associated with DC sputtering by replacing the DC power supply with an RF power supply [10; 24; 25]. RF sputtering utilizes the fact that electrons are much more mobile than ions. Thus, a negative voltage is developed on the cathode due to the difference in mobilities between the electrons and ions [10]. A secondary effect of RF sputtering is that the field oscillations in the plasma produce more electron motion within the plasma [10; 25].

These effects allow RF sputtering to be performed at lower background gas pressures and at higher yields than DC sputtering [10; 24; 25].

As compared to DC and RF sputtering, magnetron sputtering is currently the most commonly used type of sputtering and accounts for approximately 95% of all sputtering applications [25]. Magnetron sputtering enhances either the DC or RF sputtering by applying a magnetic field parallel to the cathode (and the target surface, typically). Secondary electrons, which are emitted from the cathode due to the ion bombardment, can only propagate along the E×B drift path, which is normal to both the applied electric field and the magnetic field. Since the E×B drift path is parallel to target surface, the secondary electrons are confined to a small spatial region around the cathode. This secondary electron confinement produces a dense plasma near the surface of the target. The plasma spatial confinement decreases the probability that the ions generated by the plasma will be lost to the vacuum chamber walls or the anode, which increases the ionization efficiency. The increased ionization efficiency allows magnetron sputtering systems to operate at low background gas pressures (around 1 mTorr) with relatively low power supply voltages, which in turn results in higher sputtering rates. Although there are many different magnetron sputtering system designs, most can be categorized as cylindrical post cathode, hollow cylindrical cathode, or planar cathode magnetron sputtering systems. As the names imply, the cathode shaped defines the differences among these systems. The schematic of a cathode post magnetron sputtering deposition system, which is capable of depositing thin films on multiple small-area substrates, is shown in Figure 2-12. Also, a schematic of the cylindrical post cathode is illustrated in Figure 2-14 b). For deposit thin films on single planar large-area surface, planar

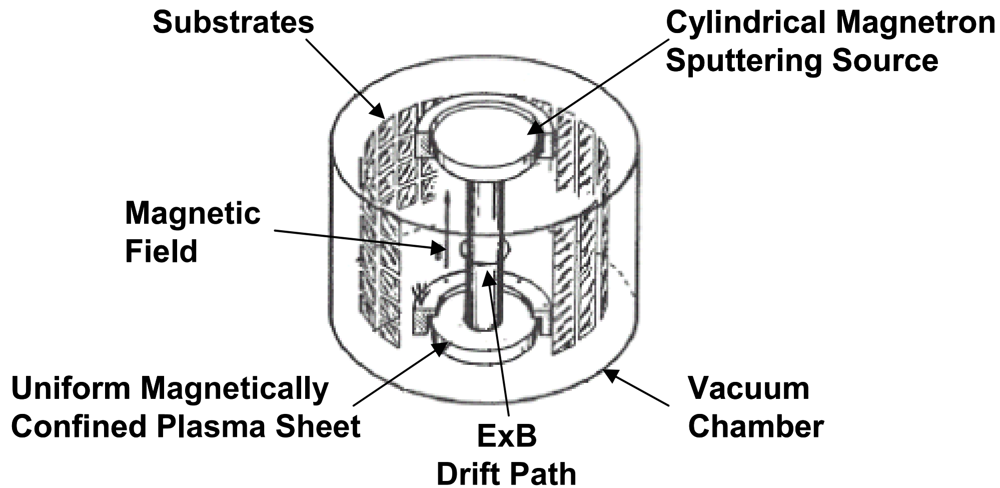

Figure 2-12. Cylindrical Magnetron (Post Cathode) Sputter Deposition System Schematic [10]

magnetron sputtering deposition systems are used more often than the cylindrical cathode post systems. Figure 2-13 shows the schematic of a planar magnetron sputtering cathode. Finally, a hollow cathode magnetron sputtering deposition system is most commonly used to deposit thin films on complex or irregularly shaped substrates. Figure 2-14 a)

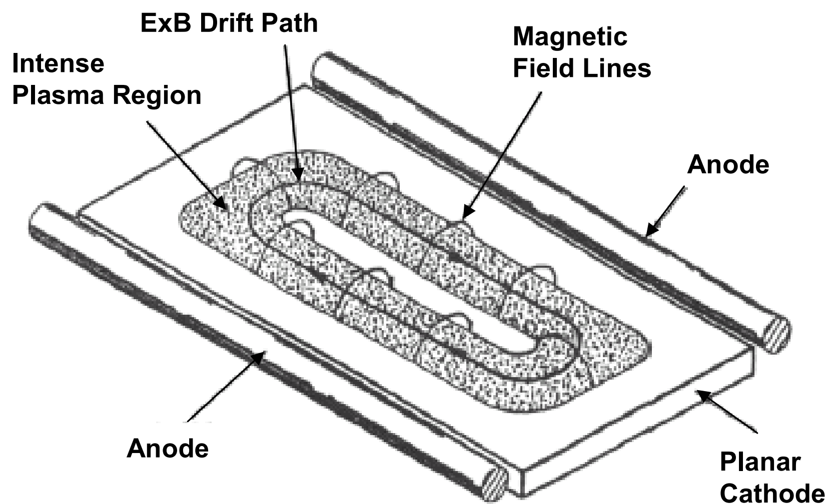

Figure 2-13. Planar Magnetron Sputter Deposition System Schematic [10]

displays the schematics of hollow cylindrical cathode [10; 25]. Table 2-2 lists several of the sputtering deposition parameters reported for the growth of YSZ. The range of several deposition parameters, particularly the substrate temperature and the sputtering power, vary considerable among the depositions. However, most of the other deposition parameters are relatively consistent, such as the target-to-substrate distance, sputtering pressure, background gas composition, and sputtering target composition.

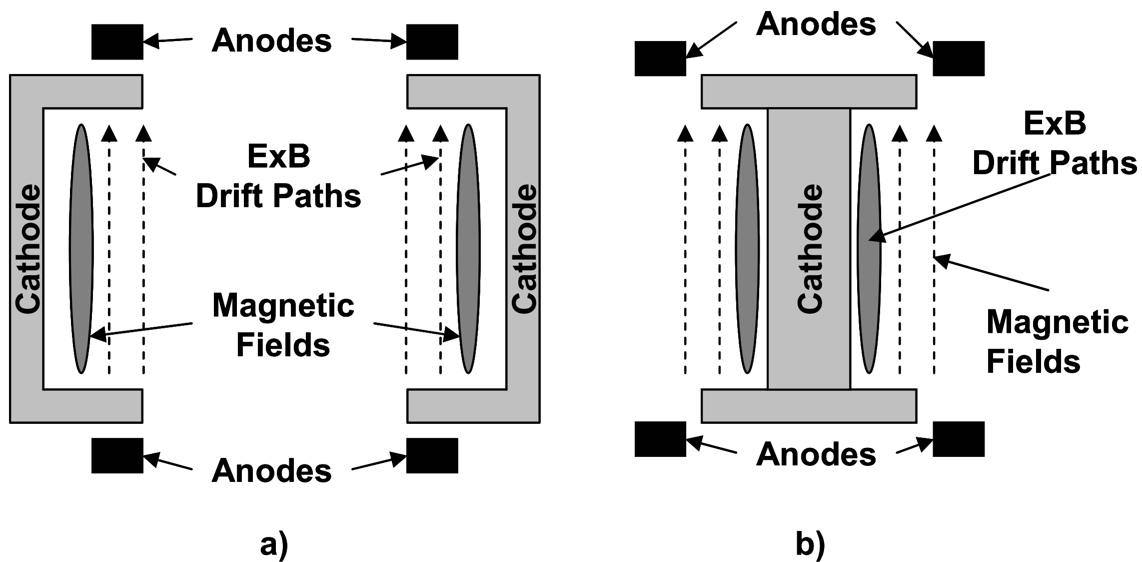

Figure 2-14. Schematic of a) Hollow Cathode Cylindrical Magnetron and b) Cylindrical Post Magnetron [25]

Table 2-2. Sputtering Deposition Parameters for YSZ Deposition

Parameter	**Values**
Sputtering type	Planar magnetron [27; 28; 29; 30; 31; 32; 33]
Target composition	YSZ [27; 28; 29; 30; 31; 32; 33]
Evacuation pressure (Torr)	10^{-6} [27; 29; 30; 31; 32]
Sputtering gas	Argon/Oxygen mix [27; 28; 29; 30; 31; 32; 33] Argon [28; 29]
Sputtering pressure (mTorr)	0.75-30 [31; 32] 1.5 [27] 4 [30] 10-37 [28; 29]

Table 2-2. Sputtering Deposition Parameters for YSZ Deposition (cont.)

Parameter	Values
Power supply	R.F. [27; 30; 31; 32; 33] Pulsed DC [28; 29]
Sputtering power (W)	75 [27] 30-100 [32] 100 [28; 29] 1000 [30; 31]
Target-to-substrate distance (cm)	3.5 [27] 5 [31; 32] 6 [28; 29; 30] 7 [33]
Substrate temperature (°C)	0-530 [31; 32] 27 [30] 200-400 [33] 600 [27] 800-830 [28; 29]

2.3.3 Ion Beam Deposition

Ion beam deposition, like sputtering deposition, bombards a target surface with ions so that atoms are ejected from the target surface due to the transfer of the kinetic energy from the bombarding ions to the target atoms. Unlike sputtering deposition in which the bombarding ions are generate from a plasma between the target and the substrate, ion beam deposition systems generate bombarding ions from a separate ion source, as shown in Figure 2-15. Thus, the substrate is physically separated from the ion generation plasma source, which allows the substrate temperature, ambient gas pressure, and type of bombardment particle to be controlled independent of the ion generation process parameters. In addition, the energy of the bombarding ions can be controlled more precisely than that of conventional plasma sputtering. However, ion beam deposition typically has a lower deposition rate than conventional plasma sputtering [10; 25].

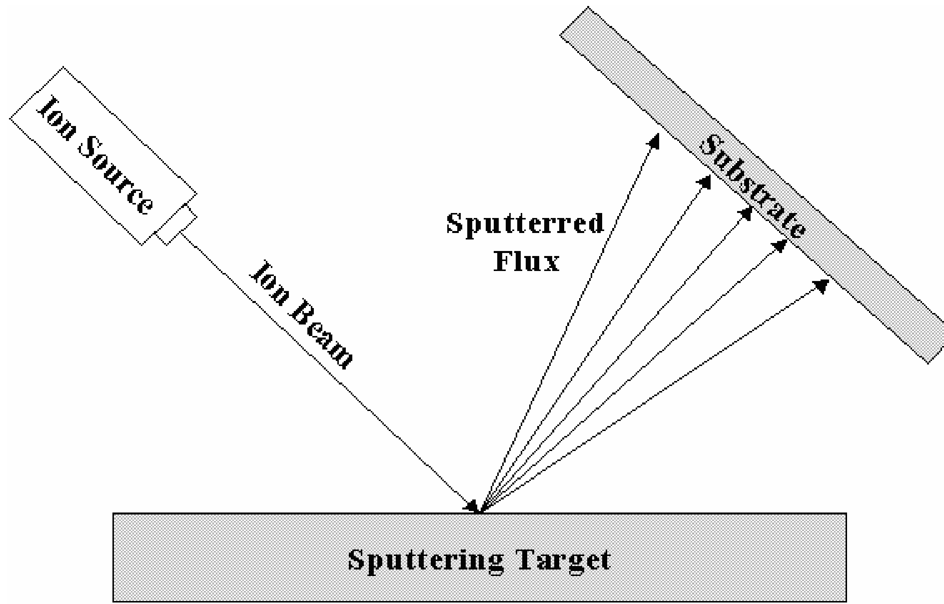

Figure 2-15. Ion Beam Sputtering Diagram [10]

In addition to ion beam deposition, ion beam assisted deposition (IBAD) systems use ion bombardment of the substrate to enhance another separate deposition process, such as dual ion beam sputtering or pulsed laser deposition [17; 25]. Figure 2-16 shows a dual ion IBAD system schematic. The ion gun for deposition, target, and substrate are identical to the ion beam deposition system described previously and shown in Figure 2-15. However, a second ion beam source (labeled “Ion Gun for Bombardment”) directly bombards the surface of the substrate without sputtering from the target. Thus, IBAD systems can independently control the ion flux and the molecular flux incident upon the substrate [17; 25]. The ion flux at the substrate is analogous to a “weak” plasma [17; 25]. The addition of this “weak” plasma significantly affects many of the thin film parameters, such as density, residual stress, index of refraction, electrical resistivity, adhesion, degree of crystallinity, crystalline phase, and surface roughness [17; 25]. Table 2-3 lists several

typical deposition parameters for depositing YSZ using a dual beam IBAD process.

IBAD pulsed laser deposition examples are described in Section 2.4.

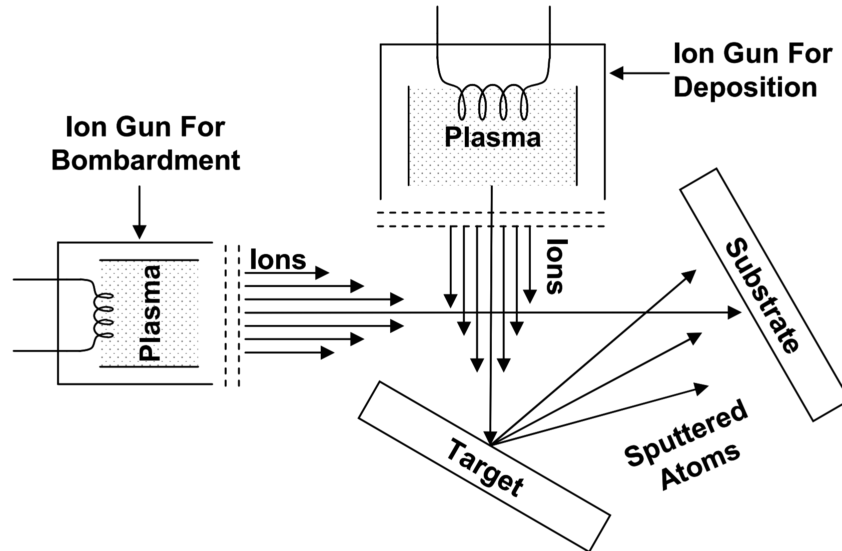

Figure 2-16. Dual Ion Beam IBAD System Schematic [17]

Table 2-3. Dual Ion Beam IBAD Parameters for YSZ Deposition

Parameter	Values
Bombardment source type	Kaufman [34; 37]
Bombardment beam size	2.5 cm diameter [35] 11 cm diameter [34; 35]
Bombardment ions	Argon [34; 35] Oxygen and argon [36; 37]
Bombardment energy	250 eV [37; 38] 300 eV [34; 35; 36]
Bombardment angle	10°-70° [37] 55° from substrate normal [34]
Sputtering source type	Kaufman [34; 37]
Sputtering beam size	2.5 cm diameter [35] 11 cm diameter [34; 35]
Sputtering ions	Xenon [34; 35] Argon [35; 36; 37]
Sputtering energy	1200 eV [37] 1500 eV [34; 35]
Sputtering target	YSZ [34; 35; 36; 37; 38]

Table 2-3. Dual Ion Beam IBAD Parameters for YSZ Deposition (cont.)

Parameter	Values
Sputtering pressure (μTorr)	75 [34] 225 [35] 250 [37]
Sputtering ambient	Oxygen [34] Oxygen, argon, and xenon[35]
Deposition rate (nm/sec)	0.01-0.1 [37] 0.05 [36] 0.3 [35] 0.4 [38]
Film thickness (nm)	250-700 [36] 600-800 [38] 8000 [35]

2.3.4 Vapor Phase Epitaxy

Vapor phase epitaxy (VPE), also referred to as chemical vapor deposition (CVD), is an epitaxial growth technique in which thin films are grown from vaporous compounds. These vaporous precursor compounds contain the constituents of the thin film along with a carrier gas. Figure 2-17 shows the growth of a thin film of arsenic-doped silicon using arsine (AsH_3) and silicon dichloride ($SiCl_2$) [15]. The AsH_3 and $SiCl_2$ molecules are "cracked," or separated into their elemental forms by heat and then may undergo a chemical reaction with the carrier gas hydrogen (H) above the heated substrate. The $SiCl_2$ and the H combine to form solid silicon (Si) and hydrogen chloride (HCl). The AsH_3 is "cracked" into the individual elements H and As. The solid Si and As land on the substrate and move to the appropriate crystallographic locations (diamond crystal structure atom sites) to form bonds with the existing exposed substrate or epitaxial layer.

Figure 2-18 shows an illustration of both horizontal and vertical VPE chambers. The stagnant layer provides a location for the constituent gases and the carrier gas to "crack." Figure 2-19 shows another horizontal VPE schematic, as well as the sources of the precusor gases that were not shown in Figure 2-18 [15; 39].

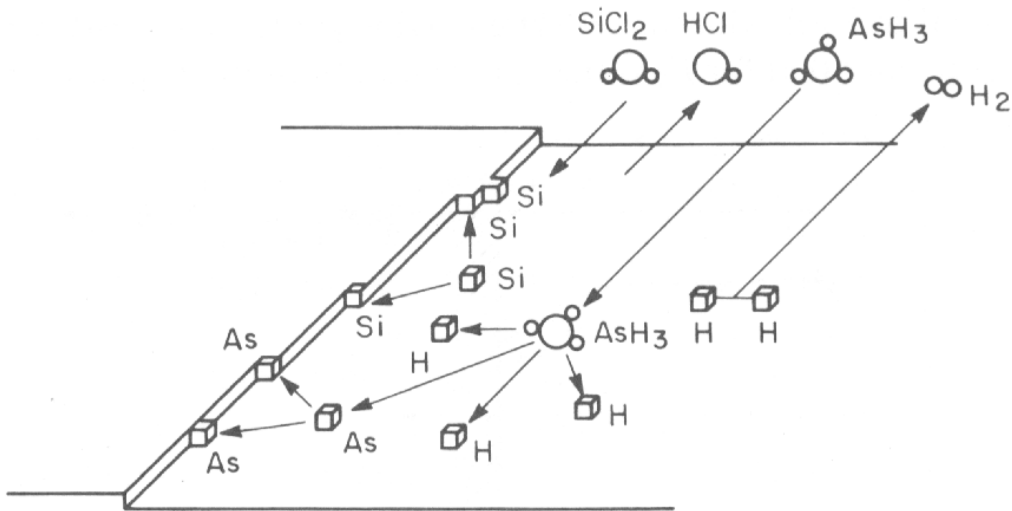

Figure 2-17. Vapor Phase Epitaxial Growth Process of Arsenic-doped Silicon [15]

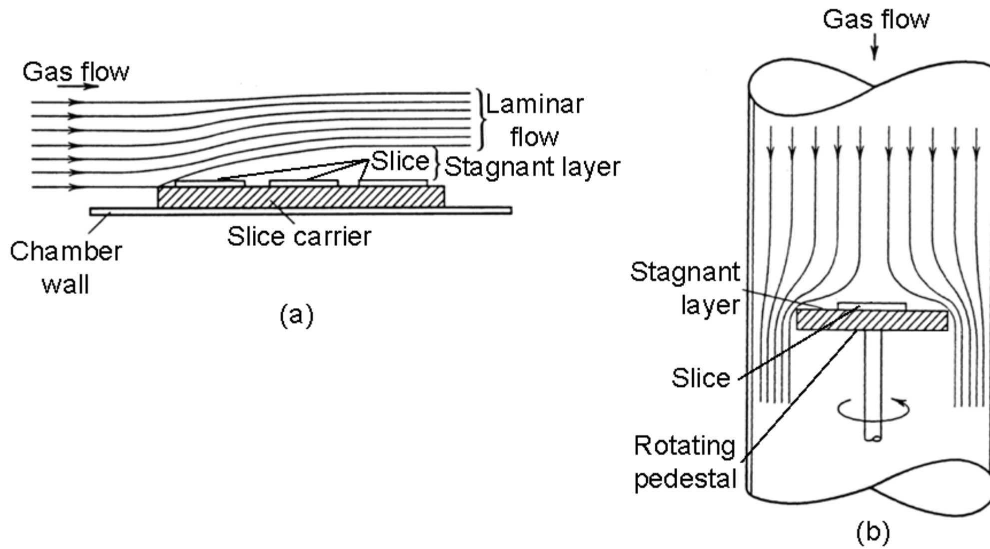

Figure 2-18. Horizontal (a) and Vertical (b) Vapor Phase Epitaxy Process [39]

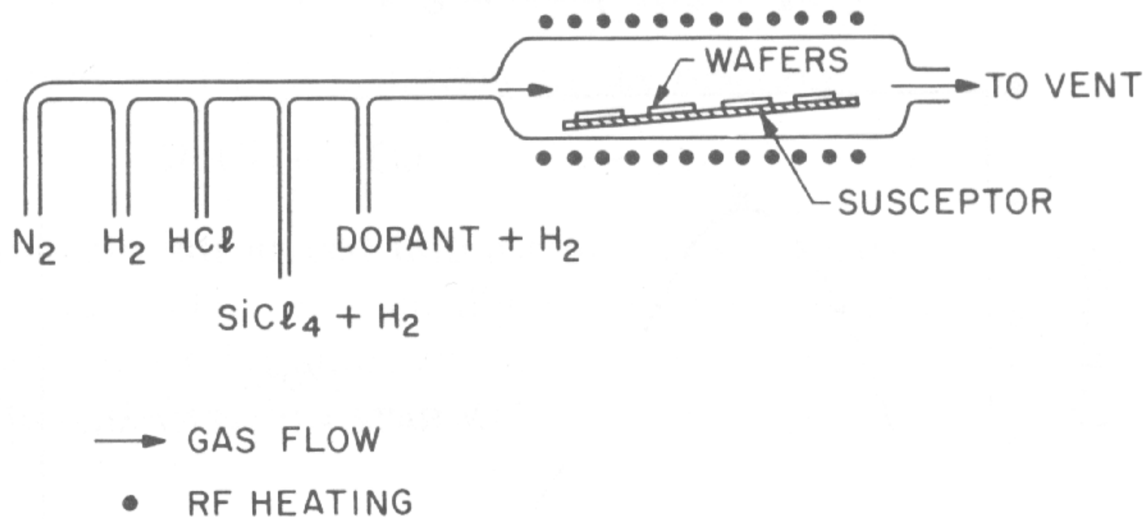

Figure 2-19. Horizontal Vapor Phase Epitaxy Schematic [15]

The VPE growth technique has several advantages, which make the use of VPE very common. VPE is generally a low temperature deposition process where the temperature is typically 30-50% of the melting point of the epitaxial material. Also, the use of high-purity gas sources enables the resultant thin film to have fewer impurities than the similar thin film grown using other deposition techniques that deposit material from solid sources, such as sputtering deposition. In addition to the higher purity of the thin film, the composition and thickness of the thin film can be made more uniform using VPE. Finally, the VPE process is well suited for mass production due to the high degree of automation possible, as well as relatively high growth rates (approximately 1 μm/minute) [15; 39].

However, these advantages also incur severe costs. Many of the gases used in a VPE system are toxic and require special handling. In addition, some of the gases are very expensive and may require preprocessing before use. Thus, the overall cost of the

VPE system is relatively expensive compared to other epitaxial growth techniques [15; 39].

Metal-organic chemical vapor deposition (MOCVD) is the most common VPE deposition method for growing YSZ thin films [12], although several other VPE techniques such as combustion CVD [40] and aerosol-assisted CVD exist [41]. MOCVD is a subset of the VPE deposition technique described previously in which the precusor are organometallic compounds and hydrides, such as dimethyl cadmium (DMCd), trimethyl gallium (TMGa), AsH_3, phosphine (PH_3), hydrogen selenide (H_2Se), hydrogen sulfide (H_2S), and trimethyl antimony (TMSb) [17; 25]. The use of organometallic compounds and hydrides in MOCVD allows the deposition temperature (typically 200°-800° C) to be lower than that of conventional CVD (typically 350°-1600° C) [10]. In addition, MOCVD is typically performed under lower pressures (10^{-3} Torr to 1 atm) than conventional CVD (100 Torr to 1 atm). Table 2-4 lists several of the MOCVD parameters for the deposition of YSZ thin films.

Table 2-4. MOCVD Parameters for the Deposition of YSZ

Parameter	**Values**
Zirconium precursor	$Zr(OBut^n)_4$ [43] $Zr(O{\cdot}t\text{–}C_4H_9)$ [44] $Zr(thd)_4$ [42; 45; 46; 47]
Zirconium precursor temperature (° C)	70 [44] 125-155 [42; 43; 46; 47]
Yttrium precursor	$Y\ (C_{11}H_{19}O_2)_3$ $Y(thd)_3$ [42; 43; 46; 47]
Yttrium precursor temperature (° C)	120-180 [42; 43; 45; 46; 47] 200 [44]

Table 2-4. MOCVD Parameters for the Deposition of YSZ (cont.)

Parameter	Values
Carrier gas	Argon at 150-600 sccm[45; 46; 47] Oxygen [43] Nitrogen at 80 sccm [44] Nitrogen at 150 sccm [42]
Oxygen flow rate (sccm)	40-50 [47] 300 [42; 45; 46] 600 [p2; p6]
Substrate temperature (° C)	600-850 [42; 43; 44; 45; 46; 47]
Total pressure (Torr)	4.0 [42] 5.0 [p4; 46] 11.3 [43]
Film thickness (nm)	150-200 [42] 4000 [46] 5000 [43]
Growth rate (nm/h)	300-400 [42] 1000 [46] 1250 [43]

2.4 Pulsed Laser Deposition

Pulsed Laser Deposition (PLD) is a conceptually and experimentally simple technique used to grow high quality thin films [48; 49]. A laser, generally external to the vacuum chamber, is focused onto and rastered across the surface of the source material or "target," similar to the sputtering target described in Section 2.3.2. As the target absorbs energy from the laser pulse, material is ejected from the target surface. For PLD, the term ablation is usually applied to this ejection of target material. The ablated material can be comprised of a variety of energetic species, which include atoms, molecules, electrons, ions, clusters, micro-sized particulates, and molten globules. The mean free path of the ablated material is relatively short compared to the target-to-substrate distance. As such, the ablated material expands rapidly in the vacuum to form a nozzle jet with hydrodynamic flow characteristics. The term "plume" refers to this nozzle jet of

ablated material [49]. After target ablations, the plume constituents are transferred from the target to the substrate, analogous to one of the molecular beams of molecular beam epitaxy (MBE). The plume constituents impinge upon the substrate and are deposited to form a thin film.

Figure 2-20 illustrates the primary components of a PLD system: a laser beam, substrate heater, substrate, and target. Also shown in Figure 2-20, the emission spectroscope enables time-of-flight (TOF) emissions spectroscopy. This is accomplished by monitoring the emission from a cross-section of the plume at a given distance from the substrate. TOF emission spectroscopy is discussed later in this chapter and in more detail in Chapter 5. In addition, Chapter 3 describes the experimental setup for two types of TOF emission spectroscopes, the TOF emission sensor system and the fast-imaging camera system.

Despite the conceptual simplicity of PLD, the interaction of the laser pulse with the target is extremely complex and difficult to model [49]. In addition, the dynamics of the plume as it travels from the target to the substrate are not well understood [48; 49]. To further complicate the subject, the plume dynamics are affected by the optical, topological, and thermodynamic properties of the target, some or all of which may vary during a thin film growth [48]. Current research indicates that the collision dynamics of the plume can be sensed for process control. A plume emits light at specific wavelengths as the plume constituents travel toward the substrate. These emissions are monitored as they pass a given distance away from the target surface [13; 14; 48]. The time-of-flight of the plume is defined as the time between the laser-target interaction and the peak of an emission wavelength (“Most Probable Time”) for a given distance from the target

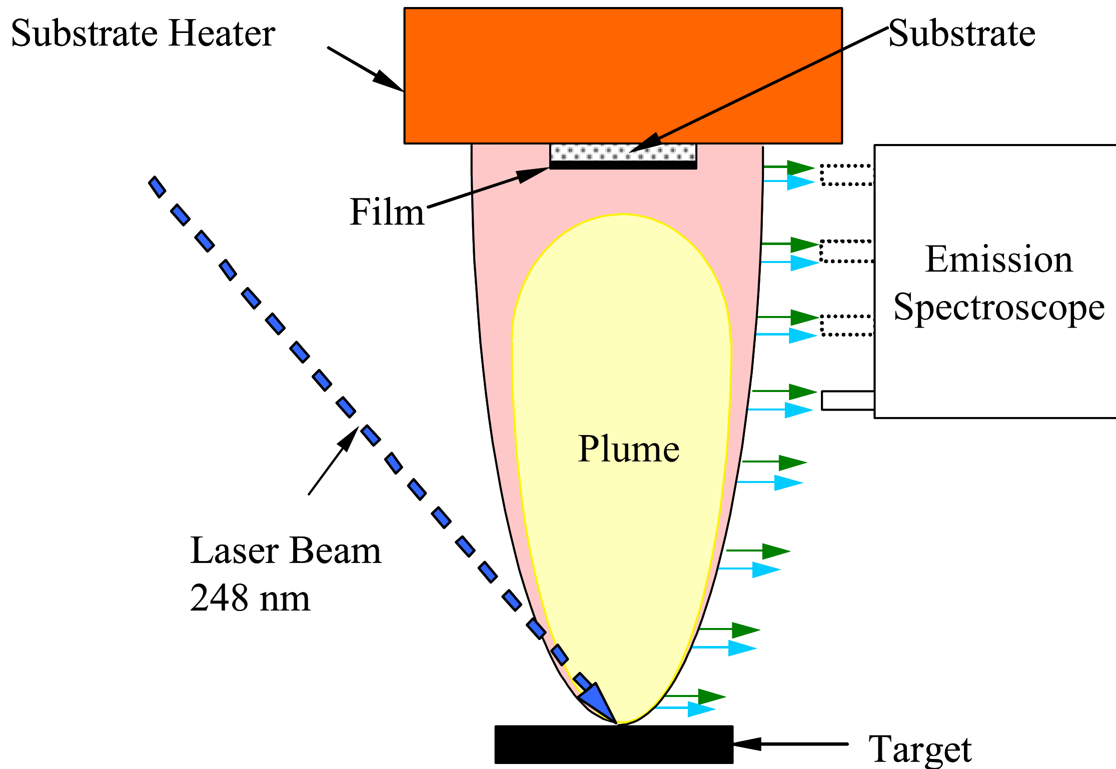

Figure 2-20. Pulsed Laser Deposition Schematic

surface. A typical TOF waveform is shown in Figure 2-21. As the laser ablates the target, very intense and relatively short-lived optical emissions are produced [49]. The fast-rising onset of these optical emissions, labeled "Fireball" in Figure 2-21, can be used as a reference to establish the time that the laser beam was incident upon the target (t=0) [13; 14; 48]. The term "main plume" in Figure 2-21 refers to the portion of the TOF waveform corresponding to the optical emissions of the plume as it passes through the cross-sectional area monitored by the TOF emission sensor system.

While the TOF emission sensor system monitors a fixed distance from the target surface over a range of time, the fast-imaging camera system, as described in Section 3.9, monitors a spatial range during a relatively short time interval. Comparing several images of the same spatial region taken at various time intervals after the laser ablates the

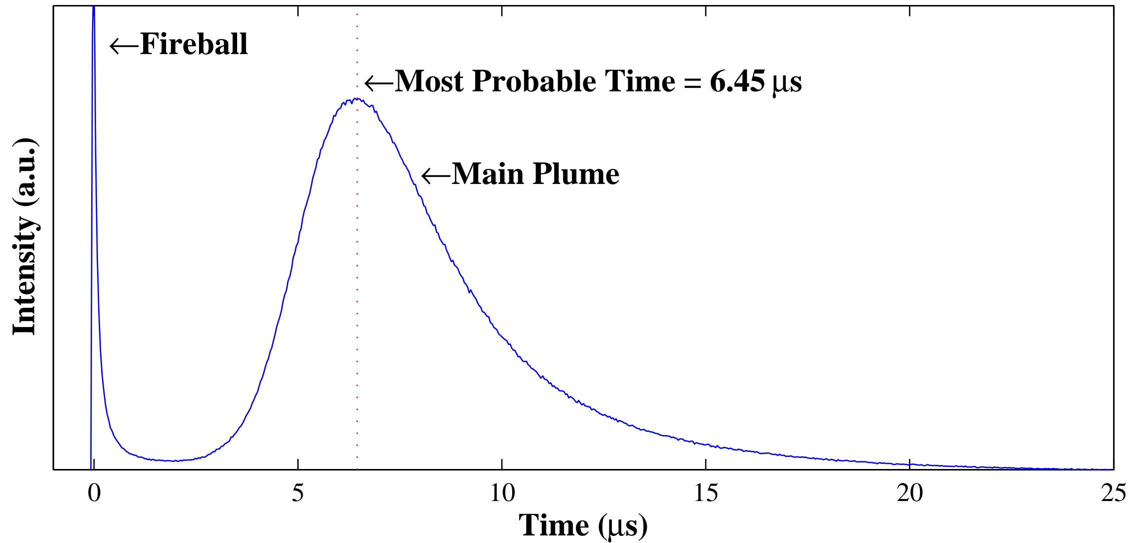

Figure 2-21. Slot 1 (64.7 mm From the Target Surface) Time-of-Flight 470±5 nm Emissions from YSZ Plume Ablated in 75 mTorr Oxygen using 1.57 J/cm^2 Laser Pulses

target reveals the propagation of the emitting portion of the plume (plume dynamics), as shown in Figure 2-22. All the images shown in Figure 2-22 monitor the same spatial range. However, each column presents the optical emissions captured at five different times after laser ablation. The arrows shown in the first column of each row (t=1 μs) indicate the direction of the laser beam and the horizontal location of the laser beam on the target. Although the target surface is not shown in any of the images, the distance from the target surface is referenced by the distance scale shown on the right side of Figure 2-22. An YSZ target was ablated using 10 J/cm^2 248-nm excimer laser pulses. The optical emissions were recorded in a 150 mTorr oxygen ambient environment or in a 150 mTorr argon ambient environment. In each ambient environment, the optical emissions were limited to 480±5 nm spectral range, which corresponds to excited zirconium oxide (ZrO*), or a 610±5 nm spectral range, which corresponds to excited yttrium oxide (YO*). The spectral filtering was performed by inserting optical bandpass

filters between the plume and the camera. Thus, the dynamics of the emitting portion of the plume as it travels from the target to the substrate for each ambient environment and monitoring spectral range are illustrated in each row of images taken of the plume at times 1 μs through 5 μs after the laser ablated the target, as shown in Figure 2-22 [13]. The colors for each image represent the optical intensity. Black corresponds to little or no emissions, while red corresponds to maximum relative intensity. Thus, the "slideshow" of images along each row reveal that the emitting portion of the plume is propagating away from the target as time progresses. In addition, comparing the YO* and ZrO* emissions show that each of these plume constituents propagate differently. Section 5.2 describes several TOF plume propagation theories in more detail and presents an analysis of similar fast-image camera system investigation results.

Films with specific material characteristics are much easier to reproduce by controlling one or more deposition parameters, so that the most probable time for a distribution of one or more particular plume components remains constant as it passes a given distance from the substrate surface. Figure 2-23 illustrates some of the deposition parameters and their corresponding effects. The parameters labeled as colored knobs are normally varied to control the deposition process. The laser excitation voltage, the laser pulse repetition rate, the laser pulse footprint (energy density), chamber ambient pressure, and chamber/substrate temperature are the primary variables adjusted in real-time to control the PLD process. In addition to *in-situ* emission spectroscopy, Raman spectroscopy has the potential to be used as a process control sensor [48], and is discussed in more detail in Appendix A.

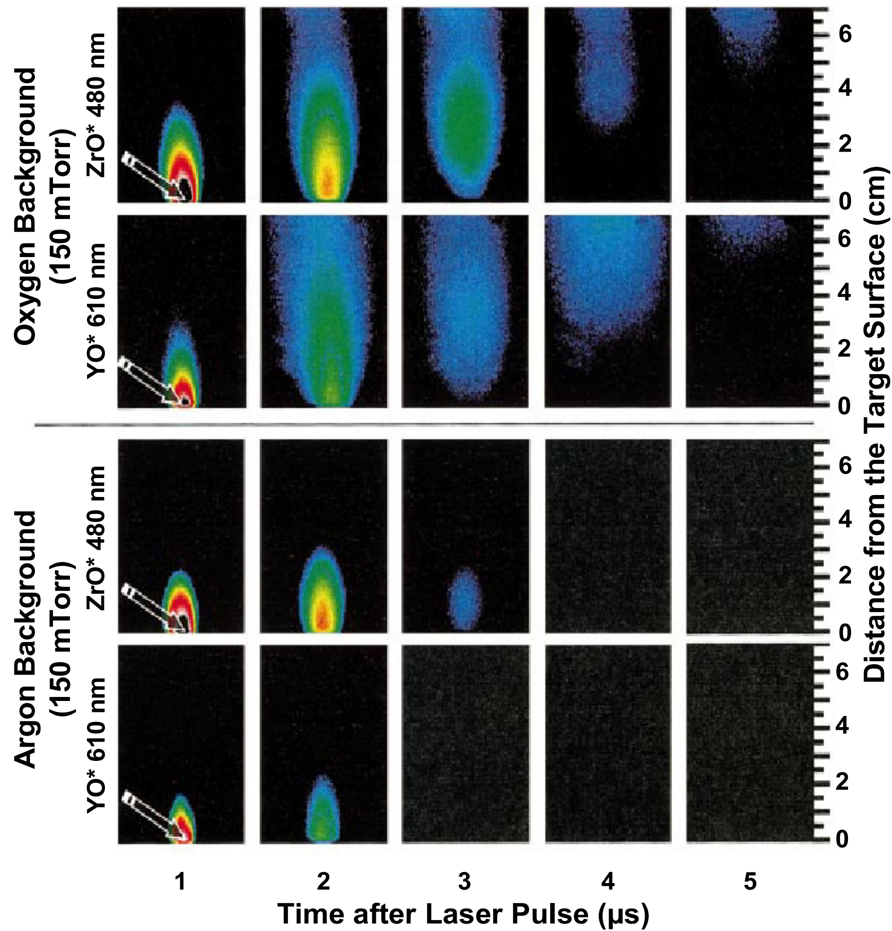

Figure 2-22. Time-resolved Images of Plumes Produced by Ablating an YSZ Target in 150 mTorr Oxygen or Argon Ambient Environments using 10 J/cm^2 248-nm Laser Pulses as Recorded by a Princeton Instruments 576-RBE Fast-imaging Camera System Through 480±5 nm and 610±5 nm Optical Bandpass Filters [13]

The versatility of PLD is derived from the range on bombardment energies that the plume is capable of delivering. The typical energies for generic PLD are approximately 100 eV. Ion beam assisted PLD can bombard the substrate with energies up to 300 eV. In addition to ion beam assisted PLD, PLD can be self-ion assisted through an appropriate substrate bias voltage. Applying a negative bias to the substrate accelerates the positively charged particles within the plume toward the substrate. Thus, no ion beam source is necessary. This self-ion assisted PLD can bombard the substrate

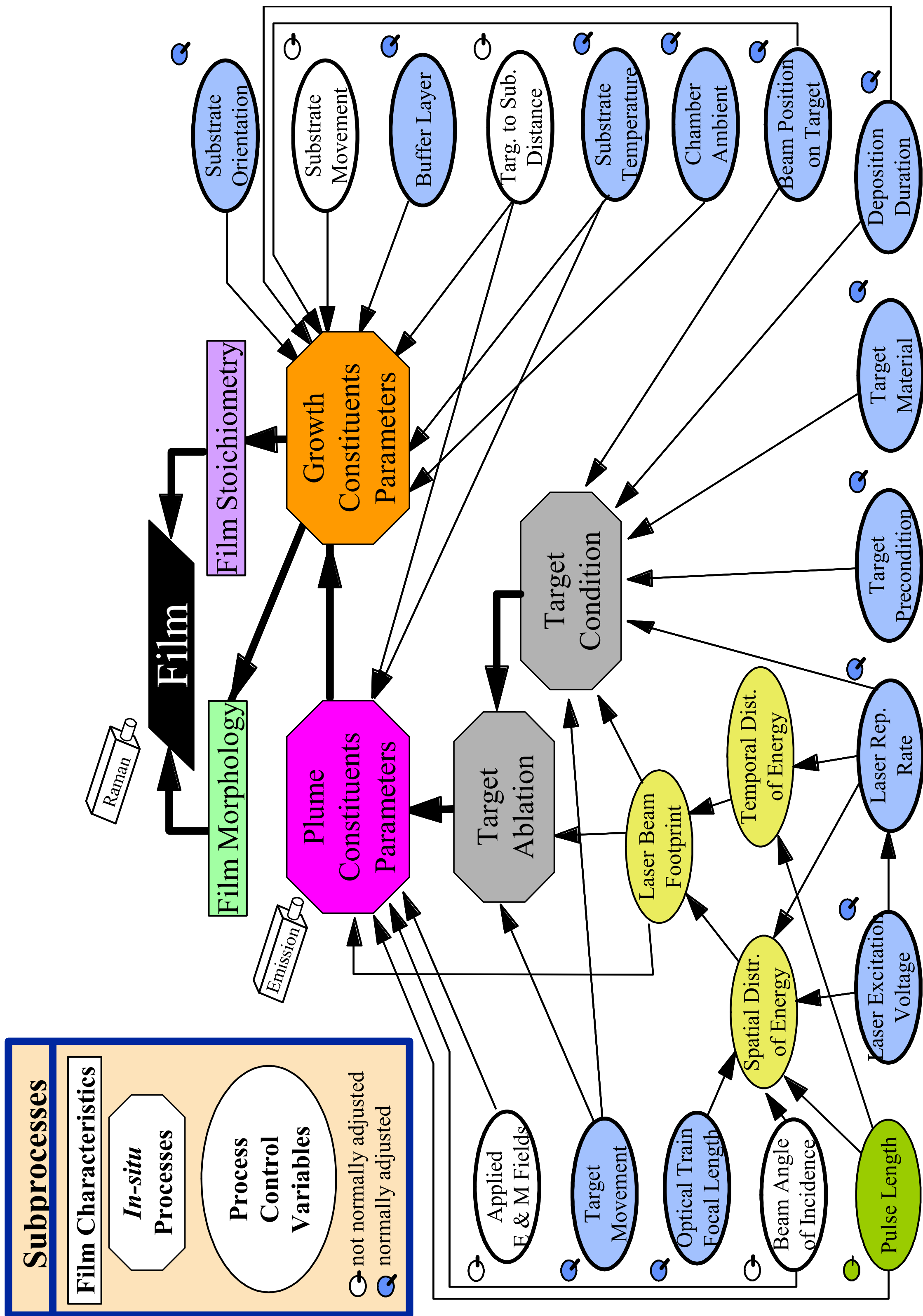

Figure 2-23. Pulsed Laser Deposition Variables [48]

with energies between 250-300 eV [50]. These energies are almost an order of magnitude greater than those of sputtering, which are typically up to 20 eV. Likewise, PLD bombardment energies are almost two orders of magnitude greater than thermal evaporation energies, which are typically less than 1 eV [10; 25]. Thus, PLD can grow a variety of thin films which cannot be grown using other methods. Typical PLD growth conditions for YSZ are divided into three distinct PLD categories: generic PLD, ion beam assisted PLD, and self-ion assisted PLD, as listed in Table 2-5.

Table 2-5. PLD Parameters for the Deposition of YSZ

Parameter	**Generic PLD**	**Ion Beam Assisted PLD**	**Self-Ion Beam Assisted PLD**
Target	YSZ [13; 51; 52; 53]	YSZ [54]	YSZ [13; 50; 55; 56]
Ambient gas	Oxygen [13; 51; 52; 53]	Argon or oxygen [54]	Argon and Oxygen [13; 50; 55; 56]
Ambient pressure (mTorr)	0.0075-7.5 [13] 0.4 [51; 53] 650 [52]	1 [54]	1.5 and 150 [13; 50; 55; 56]
Target-to-substrate distance (cm)	5.5 [53] 7 [13; 51]	4 [54]	7 [13; 50; 55; 56]
Substrate temperature (° C)	650 [52] 790 [51] 800 [13; 53]	70-130 [54]	100-300 [13; 50; 55; 56]
Laser wavelength (nm)	248 [53] 266 [51]	248 [54]	248 [13; 50; 55; 56]
Laser energy (mJ)	60 [51]	Not listed	300 [13; 50; 55; 56]
Laser fluence (J/cm^2)	1-3 [51] 3 [53]	2 [54]	10 [13; 50; 55; 56]
Laser repetition rate (Hz)	10 [51; 53]	40 [54]	40 [13; 50; 55; 56]
YSZ film thickness (nm)	40-50 [51] 80 [53] 330, 370, 2000 [52]	Not listed	1000-1200 [13; 50; 55; 56]

Table 2-5. PLD Parameters for the Deposition of YSZ (cont.)

Parameter	**Generic PLD**	**Ion Beam Assisted PLD**	**Self-Ion Beam Assisted PLD**
Ion source	N/A	Argon or oxygen [54]	N/A
Ion source-to-substrate distance (cm)	N/A	3 [54]	N/A
Ion source angle from substrate normal (°)	N/A	30-60 [54]	N/A
Ion beam diameter (cm)	N/A	3 [54; 56]	N/A
Substrate voltage	N/A	N/A	100-300 [13; 50; 55; 56]

2.5 Thin Film Analysis Techniques

Numerous techniques exist to characterize the material properties of thin films. The techniques available to analyze thin films grown as part of this research are discussed in this section. Many other techniques, such as atomic force microscopy and scanning tunneling microscopy, are also available [57]. However, these other techniques were not used in this research and as such, are not discussed in this section.

2.5.1 Light Microscopy

Dating back to the 17th century, the light microscope or "standard optical microscope" is one of the oldest thin film analysis instruments. Using a light microscope, it is possible to visually identify morphology, size, color, refractive indices, crystal systems, and opacity. The spatial resolution with white-light is sufficient to distinguish features as small as 0.2 μm. In typical use the light microscope is non-destructive. However, some light microscopy techniques may require the thinning of a material, which is a destructive process [57].

2.5.2 Scanning Electron Microscope

The scanning electron microscope (SEM) provides greater spatial resolution and depth of focus than the light microscope. The SEM can provide nanometer-level resolution and up to 300,000 times magnification. The primary use of the SEM is high magnification imaging. However, with optional accessories, elemental composition analysis is also possible. The typical use of the SEM is non-destructive [57].

2.5.3 Transmission Electron Microscopy

Transmission electron microscopes (TEM) are used to analyze the atomic structure and microstructure of solid materials. TEM systems analyze the diffraction of highly focused, monoenergetic electrons that bombard a thin specimen of material. This diffraction information is equivalent to an X-ray diffraction pattern, which is discussed in Section 2.5.5. In addition, TEM systems can image the thin sample. This image can show variations in mass, non-uniformity in sample thickness, structural defects in crystalline material, and phase contrasts. The typical lateral resolution is less than 0.2 μm. TEM analysis, which requires a thin sample that is typically less than 200 nm-thick, is destructive due to the sample preparation [57].

2.5.4 Energy-Dispersive X-Ray Spectroscopy

The collection and energy detection of X-ray spectra from a sample is defined as energy-dispersive X-ray spectroscopy (EDS). Atoms emit characteristic X-rays when ionized with high-energy radiation. EDS systems radiate samples and collect the X-ray spectra from the sample. Analysis of the collected X-ray spectra is used to determine

elemental composition of the sample. EDS systems are generally attached to an SEM or other electron column instruments. EDS is a non-destructive analysis technique. However, as with other electron beam tools, electron beam damage may occur. The typical lateral resolution of EDS is 0.5 μm to 1 μm. The depth of penetration is dependent upon the density of the sample and the intensity of the radiation source. EDS can detect a range of elements from boron to uranium [57].

2.5.5 X-Ray Diffraction

X-ray diffraction (XRD) can be used to identify the crystalline phase, orientation, and size of a thin film. XRD systems radiate a specimen with a collimated beam of X-rays. Crystalline materials will defract the X-ray radiation according to Bragg's law, as shown in Equation (2-2):

$$\lambda = 2 \cdot d \cdot \sin(\theta) \tag{2-2}$$

where d is *spacing between crystal planes*, λ is the *wavelength of the X-ray radiation*, and θ is the *diffraction angle*. XRD systems measure the intensity of the diffracted X-ray radiation as a function of twice the off normal incidence diffraction angle θ. In addition, the crystalline phase and orientation can also be calculated by an analysis of the refracted intensities as a function of the angle θ. Since the X-ray radiation is collimated, there is typically no lateral resolution. The penetration depth of the X-ray radiation is material and X-ray radiation source dependence. However, the penetration depth is typically limited to a few micrometers. XRD analysis is non-destructive for most materials [57].

2.5.6 Auger Electron Spectroscopy

Auger electron spectroscopy (AES) is used to identify the elemental composition at the surface of a thin film. Secondary electrons are created near the surface of the thin film by a focused electron beam. Auger electrons are secondary electrons that have the same energy characteristics of the elements. In many cases, Auger electrons can be used to identify the chemical bonds of the surface atoms in the material being measured. Thus, AES is defined as the detection and analysis of these Auger electrons. The shallow penetration depth of AES, typically 5 Å to 100 Å, provides information about the surface of the thin film only. In addition, the lateral resolution of AES is sufficient to distinguish features as small as 300 Å. AES is non-destructive. However, AES is often combined with ion sputtering to perform depth profiling, which provides chemical composition information as a function of the depth from the original thin film surface. In this process, the surface of the thin film is continually etched away by ion sputtering to expose a new surface, which is then analyzed by AES. Thus, depth profiling AES is destructive [57].

2.5.7 Mechanical and Optical Profiling

Mechanical profiling uses the movement of a diamond stylus over the test surface to determine surface roughness. Mechanical profiling can also be used to measure relative changes in thin film thickness. Mechanical profiling can map an entire area of a sample or a path along the sample. Typical depth resolution is 0.5 nm, with approximately 5 nm and 150 μm minimum and maximum step size, respectively. Lateral resolution is between 0.1 μm and 25 μm. Mechanical profiling is typically non-destructive for most materials [57].

Optical profiling uses optical interferometry to provide the same information as mechanical profiling. However, optical profiling has difficulty measuring multiple thin films, optically transparent, or extremely rough surfaces. Multiple thin films and optically transparent thin films cause phase errors in the reflected interference pattern, which prohibits topology measurements. Coating the sample with a thin optically opaque layer may solve this problem. Also, if the surface is too rough, the interference pattern will become so scattered that no topology can be measured. Optical profiling has a depth resolution of 0.1 nm, with 0.3 nm and 15 μm minimum and maximum step size, respectively [57].

2.6 Chapter Summary

An overview of thermal and intrinsic stresses in thin films was given in this chapter. In addition, the relationship between thin film microstructure and intrinsic stress was also described. Several typical methods for the growth of yttria stabilized zirconia were presented in this chapter. This chapter also described the PLD concept in general. Chapter 3 builds upon the general description of PLD presented here by giving details about the individual components that comprise the PLD system used in this research. In addition to the deposition systems discussed in this chapter, an overview of several thin film analysis techniques was given. These techniques were used throughout this research effort.

Bibliography

1. "Tutorial 22, Controlling Stress in Thin Films," Excerpt from unpublished article. n. pag. http://wwwflipchips.com/tutorial22.html. 17 April 2003.

2. Srikar, V. T., "Stresses in Microscale Structures: Origin, Implications & Measurements," Excerpt from unpublished article. n. pag. http://ultra.bu.edu/lab/journalclub/presentations/srikar.pdf. 17 April 2003.

3. Windischmann, H., "Intrinsic Stress in Sputtered Thin Films," *Journal of Vacuum Science and Technology A*, 9(4): 2431-2436, July/August 1991.

4. Thornton, J. A., and D. W. Hoffman. "Stress-related Effects in Thin Films," *Thin Solid Films*, 171: 5-31, 1989.

5. Kucuk, A., C. C. Berndt, U. Senturk, R. S. Lima, C. R. C. Lima. "Influence of Plasma Spray Parameters on Mechancial Properties of Yttria Stabilized Zirconia Coatings. I: Four Point Bend Test," *Material Science and Engineering*, A284: 29-40, 2000.

6. Matejicek, J., S. Sampath, P. C. Brand, and H. J. Prask, "Quenching, Thermal and Residual Stress in Plasma Sprayed Deposits: NiCrAlY and YSZ Coatings," *Acta mater*, 47(2): 607-617, 1999.

7. Wang, R. P., S. H. Pan, and Y. L. Zhou. "Stress Reduction by Ion Bombardment in CeO2 Films," *Solid State Communications*, 114: 613-616, 2000.

8. Clyne, T. W., "Residual Stresses in Thick and Thin Surface Coatings," Excerpt from unpublished article. n. pag. www.msm.cam.ac.uk/mmc/publications/twc010.pdf. 17 April 2003.

9. Johnson, C. A., J. A. Ruud, R. Bruce, and D. Wortman. "Relationships between Residual Stress, Microstructure and Mechanical Properties of Electron Beam-physical Vapor Deposition Thermal Barrier Coatings," *Surface and Coatings Technology*, 108-019: 80-85, 1998.

10. Bunshah, R. F., *Handbook of Hard Coatings*. New York: Noyes Publications, 2001.

11. Movchan, B. A., and A. V. Demchishin. "Study of the Structure and Properties of Thick Vacuum Condensates of Nickel, Titanium, Tungsten, Aluminium Oxide and Zirconium Oxide," *Metallov i Metallovedenie*, 28(4): 653-660, 1969.

12. Sheth, A., H. Schmidt, andV. Lasrado, "Review and Evaluation of Methods for Application of Epitaxial Buffer and Superconductor Layers," *Applied Superconductivity*, 6(10-12): 855-873, 1998.

13. Voevodin, A. A., J. G. Jones, and J. S. Zabinski. "Characterization of Zro_2/Y_2O_3 Laser Ablation Plasma in Vacuum, Oxygen, and Argon Environments," *Journal of Applied Physics*, 88(2): 1088-1096, 15 July 2000.

14. -----. “Structural Modification of Single-Axis-Oriented Yttria-Stabilized-Zirconia Films under Zirconium Ion Bombardment,” *Applied Physics Letters*, 78(6): 730-732, 5 February 2001.

15. Sze, S. M., *Semiconductor Devices: Physics and Technology*. New York: John Wiley & Sons, 1985.

16. Kovacs, G. T. A., *Micromachined Transducers Sourcebook*, Boston: MCB McGraw-Hill, 1998.

17. Mattox, D. M., *Handbook of Physical Vapor Deposition (PVD) Processing*. New Jersey: Noyes Publications, 1998.

18. “RF-sputtering and E-beam Evaporation Laboratory,” Excerpt from unpublished article. n. pag. http://www2.polito.it/research/thin-film/Strumenti/Sputtering/Sputtering.html. 19 May 2002.

19. Hartmanová, M., I. Thurzo, M. Jergel, J. Bartoš, F. Kadelc, V. Zelezný, D. Tunega, F. Kundracik, S. Chromik, and M. Brunel. “Characterization of Yttria-stabilized Zirconia Thin Films Deposited by Electron Beam Evaporation on Silicon Substrates,” *Journal of Materials Science*, 33: 969-975, 1998.

20. Matthews, A., S. J. Young, M. Joseph, C. Rebholz, J. M. Schneider, and S. J. Dowey. “Partially Ytrria-stabilized Zirconia Coatings Porduced Under Plasma-assisted EBPVD with Bipolar Pulsed Bias and Under Electron bombarment-assisted Positive Bias Conditions,” *Surface and Coatings Technology*, 94-95: 123-130, 1997.

21. Paranthaman, M., A. Goyal, F. A. List, E. D. Specht, D. F. Lee, P. M. Martin, Q. He, D. K. Christen, D. P. Norton, J. D. Budai, and D. M. Kroeger. “Growth of Biaxially Textured Buiffer Layers on Rolled-ni Substrates by Electron Beam Evaporation,” *Physica C*, 275: 266- 272, 1997.

22. Yang, C. Y., S. E. Babcock, A. Goyal, M. Paranthaman, F. A. List, D. P. Norton, D. M. Kroeger, and A. Ichinose. “Microstructure of Electron-beam-evaporated Epitaxial Yttria-stabilized Zirconia/CeO_2 Bilayers on Biaxially Textured Ni Tape,” *Physical C*, 307: 87-98, 1998.

23. Yang, J., S. K. Gog, H. Z. Liu, and H. W. Gu. “ Texture and Surface Morphololgy of Yttria-stabilized Zirconia Buffer Layer on Ni-based Tapes by Electron Beam Evaportation,” *Physcial C*, 386: 337-341, 2003.

24. *The Basics of Sputtering*. New York: Materials Research Corporation, 1970.

25. Seshan, K., *Handbook of Thin-Film Deposition Processes and Techniques - Principles, Methods, Equipment and Applications (2nd Edition)*. Noyes Publications/William Andrew Publishing, 2002.

26. “Media & Materials – Technical Resources.” Excerpt from unpublished article. n. pag. http://www.dsi.a-star.edu.sg/tracks/media/tech_resources/sputtering.html. 19 May 2002.

27. Boulouz, M., A. Boulouz, A. Giani, and A. Boyer. “Influence of Substrate Temperature and Target Composition on the Properties of Yttria-stabilized Zirconia Thin Films Grown by R.F. Reactive Magnetron Sputtering,” *Thin Solid Films*, 323: 85-92, 1998.

28. Brown, P., T. Khan, P. Stampe, R. Kennedy, S. Sayed, Yu. A. Vlasov, and G. L. Larkins. “Pulsed DC Magnetron Sputtering of YSZ Buffer Layers on Si (100),” Excerpt from unpublished article. n. pag. http://www.fiu.edu/~vlassovy/1MJ07.pdf. 19 May 2002.

29. -----. “Sputtering of YSZ Buffer Layers on (100) Si for Use in $YBa_2Cu_3O_7$ Based Microwave Circuits,” *Physica C*, 366: 102-108, 2002.

30. Gao, P., L. J. Meng, M. P. dos Santos, V. Teixeira, and M. Andritschky. “Study of ZrO_2-Y_2O_3 Films prepared by R.F. Magnetron Reactive Sputtering,” *Thin Solid Films*, 377-378: 32-36, 2000.

31. Tomaszewski, H. J. Haemers, J. Denul, N. De Roo, and R. De Gryse, “Yttria-stabilized Zirconia Thin Films Grown by Reactive R.F. Magnetron Sputtering,” *Thin Solid Films*, 287: 104-109, 1996.

32. -----. “Yttria-stabilized Zirconia Thin Films Grown by R.F. Magnetron Sputtering from an Oxide Target,” *Thin Solid Films*, 293: 67-74, 1997.

33. Yang, J., D. Shi, X. Wang, A. Liu, and G. Yuan. “Epitaxial YSZ/CeO_2 and YBCO on Cube Textured Nickel,” *Physica C*, 337: 67-70, 2000.

34. Dzick, J., J. Hoffmann, S. Sievers, L. O. Kautschor, and H. C. Freyhardt. “Ion-beam-assisted Texturing of YSZ Layers,” *Physica C*, 372-376: 723-728, 2002.

35. Freyhardt, H. C., J. Hoffmann, J. Wiesmann, J. Dzick, K. Heinemann, A. Isaev, F. Garcia-Moreno, S. Sievers, and A. Usoskin. “YBaCuO Thick Films on Planar and Curved Technical Substrates,” *IEEE Transactions on Applied Superconductivity*, 7(2): 1426-1431, 2 June 1997.

36. Iijima, Y., N. Tanabe, O. Kohno, and Y. Ikeno. “In-plane Aligned $YBa_2Cu_3O_{7-x}$ Thin Films Deposited on Polycrystalline Metallic Substrates,” *Applied Physics Letters*, 60(6): 769-771, 10 February 1992.

37. Mao, Y. J., C. X. Ren, J. Yuan, F. Zhang, X. H. Liu, and S. C. Zou. “Study on the Growth of Biaxially Aligned Yttria-stabilized Zirconia Films During Ion Beam Assisted Deposition,” *Journal of Vacuum Science and Technology A*, 15(5): 2687-2692.

38. Wu, X. D., S. R. Foltyn, P. Arendt, J. Townsend, C. Adams, I. H. Campbell, P. Tiwari, Y. Coulter, and D. E. Peterson. "High Current $YBa_2Cu_3O_{7-x}$ Thick Films on Flexible Nickel Substrates with Textured Buffer Layers," *Applied Physics Letters*, 65(15): 1961-1963, 10 October 1994.

39. Lott, Lt Col J. A. Class handout, EENG 596, Integrated Circuit Technology. Graduate School of Engineering and Management, Air Force Institute of Technology, Wright-Patterson AFB OH, January 1998.

40. Shoup, S. S., S. Shanmugham, D. Cousins, A. T. Hunt, M. Paranthaman, A. Goyal, P. Martin, and D. M. Kroeger. "Low-Cost Combustion Chemical Vapor Deposition of Epitaxial Buffer Layers and Superconductors," *IEEE Transactions on Applied Superconductivity*, 9(2): 188-195, 2 June 1999.

41. Wang, H. B., C. R. Xia, G. Y. Meng, and D. K. Peng. "Deposition and Characterization of YSZ Thing Films by Aerosol-assisted CVD," *Materials Letter*, 44: 23-28, May 2000.

42. Chevalier, S., M. Kilo, G. Borchardt, and J. P. Larpin. "MOCVD Deposition of YSZ on Stainless Steels," *Applied Surface Science*, 205: 188-195, 2003.

43. Chour, K. W., J. Chen, and R. Xu, "Metal-organic Vapor Deposition of YSZ Electrolyte Layers for Solid Oxide Fuel Cell Applications," *Thin Solid Films*, 304: 106-112, 1997.

44. Chun, S. Y., and N. Mizutani. "The Transport Mechanism of YSZ Thin Films Prepared ny MOCVD," *Applied Surface Science*, 171: 82-88, 2001.

45. Garcia, G., J. Casado, J. Llibre, and A. Figueras. "Preparation of YSZ Layers by MOCVD: Influence of Experimental Parameters on the Morphology of the Films," *Journal fo Crystal Growth*, 156: 426-432, 1995.

46. Garcia, G., A. Figueras, J. Casado, J. Llibre, M. Mokchah, G. Petot-Ervas, and J. Calderer. "Yttria-stabilized Zirconia Obtained by MOCVD: Applications," *Thin Solid Films*, 317: 241-244, 1998.

47. Martinez, E., J. Esteve, G. Garcia, A. Figueras, and J. Llibre. "YSZ Protective Coatings Elaborated by MOCVD on Nickle-based Alloys," *Surface and Coatings Technology*, 100-101: 164-168, 1998.

48. Biggers, R. R., G. Kozlowski, J. G. Jones, D. V. Dempsey, R. Kleismit, I. Maartense, J. D. Busbee, T. Peterson, and R. Perrin. "Process Control and Pulsed Laser Deposition of Materials," *Integrated Ferroelectrics*, 28(1-4): 201-211, 2000.

49. Chrisey, D. B. and G. K. Hubler, *Pulsed Laser Deposition of Thin Films*. New York: John Wiley & Sons, 1994.

50. Voevodin, A. A., J. G. Jones, and J. S. Zabinski. “Structural Modification of Single-axis-oriented Yttria-stabilized-zirconia Films under Zirconium Ion Bombardment,” *Applied Physics Letters*, 78(6): 730-732, 5 February 2001.

51. Göres, J., P. J. Jung, D. B. Fenner, and J. I. Budnick. “*In Situ* Plume-emissions Monitoring During Pulsed-laser Deposition of $YBa_2Cu_3O_{7-\delta}$ and Yttria-stabilized Zirconia thin Films,” *Review of Scientific Instruments*, 68(1): 170-177, January 1997.

52. Lei, C. H., G. Van Tendeloo, M. Siegert, J. Schubert, and Ch. Buchal. “Structural Investigation of the Epitaxial Yttria-stabilized Zirconia Films Deposited on (001) Silicon by Laser Ablation,” *Journal of Crystal Growth*, 222: 558-564, 2001.

53. Trtík, V., R. Aguiar, F. Sánchez, C. Ferrater, and M. Varela. “Study of the Epitaxial Growth of CeO_2 (001) on Yttria-stabilized Zirconia/Si (001),” *Journal of Crystal Growth*, 192: 175-184, 1998.

54. Reade, R. P., P. Berdahl, and R. E. Russo. “Laser Deposition of Biaxially Textured Yttria-stabilized Zirconia Buffer Layers on Polycrystalline Metallic Alloys for High Critical Current Y-Ba-Cu-O Thin Films,” *Applied Physics Letters*, 61(18): 2231-2233, 2 November 1992.

55. Jones, J. G., A. A. Voevodin, J. S. Zabinski. “Characterization of Plume Fluence for Laser Ablation of Yttria Stabilized Zirconia in Mixed Oxygen and Argon Environments,” *Surface and Coatings Technology*, 146-157: 258-262, 2001.

56. Voevodin, A. A., J. G. Jones, and J. S. Zabinski. “Structure Control of Pulsed Laser Deposited ZrO_2/Y_2O_3 Films,” *Journal of Vacuum Science and Technology A*, 19(4):1320-1324, Jul/Aug 2001.

57. Brundle, C. R., C. A. Evans, Jr., and S. Wilson, *Encyclopedia of Materials Characterization: Surfaces, Interfaces, Thin Films*, Boston: Butterworth-Heinemann, 1992.

3 Experimental Setup

3.1 Overview

All the pulsed laser depositions and experiments conducted in this research were performed in the large area chamber located at the Air Force Research Laboratory Materials and Manufacturing Directorate (AFRL/ML), Wright-Patterson Air Force Base, Ohio, Area B, Building 651 Room 193. An excimer laser, optics, scanning mirror, in-chamber energy meter, target carousel, substrate manipulator system, and quartz lamp heater system comprise the majority of the pulsed laser deposition (PLD) system, as shown in Figure 3-1. In addition, the pressure control system, time-of-flight emission sensor system, fast-imaging camera system, retractable Raman probe, and software

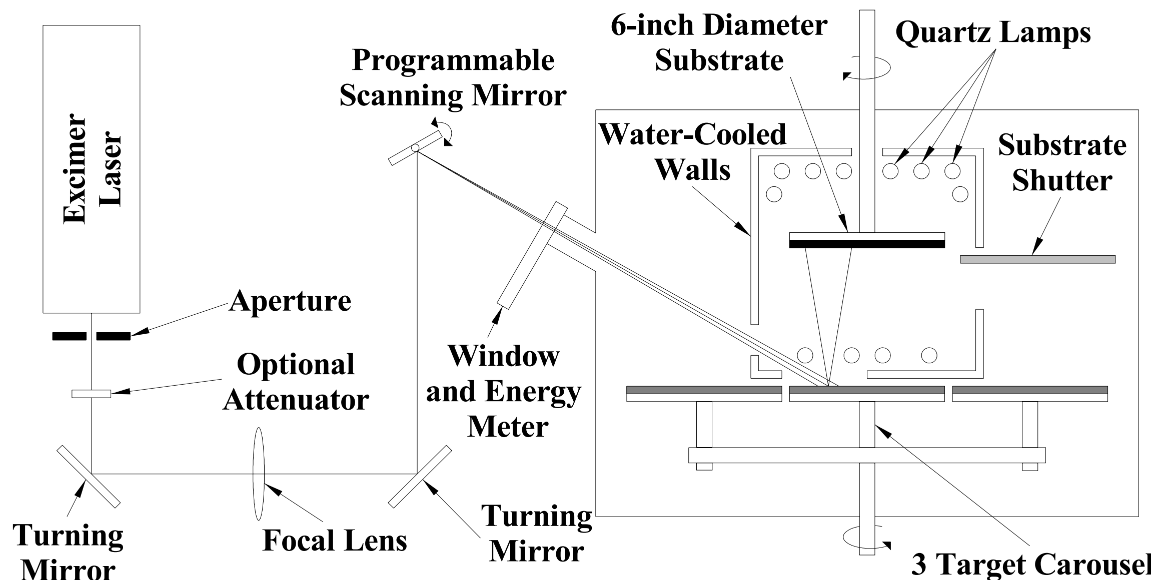

Figure 3-1. Pulsed Laser Deposition System Diagram

control are part of the PLD system but are omitted from Figure 3-1 for clarity. The remainder of this chapter describes each of these components in detail.

3.2 Excimer Laser

The PLD system utilizes a Lambda Physik LPX® 305i excimer laser to produce the laser ablation pulses. Table 3-1 summarizes the capabilities of the Lambda Physik LPX® 305i.

Table 3-1. Lambda Physik LPX® 305i Specifications [1]

	ArF	KrF	XeF
Wavelength	193 nm	248 nm	351 nm
Maximum Energy	650 mJ	1200 mJ	400 mJ
Average Power	25 W	50 W	15 W
Maximum Repetition Rate	50 Hz	50 Hz	50 Hz
Pulse Duration	20 ns	25 ns	30 ns
Pulse-to-Pulse Stability	±5%	±3%	±3%

The LPX® 305i emits rectangular pulses at rates up to 50 Hz with full-width half-maximum (FWHM) pulse widths of 10 to 15 mm in the vertical direction and 30 mm in the horizontal direction [1]. The laser beam diverges 1 mrad in the vertical direction and 3 mrad in the horizontal direction [1]. This divergence constrains the optical system, which is more thoroughly discussed in Section 3.3. The LPX® 305i was configured for 248 nm using a KrF gas fill for all of the research reported in this dissertation.

The LPX® 305i operates in one of two modes, constant voltage or constant energy. In constant voltage mode, the LPX® 305i maintains the excitation voltage at a constant user-defined level between 14.5 kV and 21.0 kV [1]. The number of pulses since a gas refill, the age of the current gas fill, and the repetition rate commanded

determine the laser pulse energy for a commanded constant excitation voltage [1]. In constant energy mode, the LPX® 305i monitors the laser pulse energy with a built-in energy detector and adjusts the excitation voltage to maintain the commanded laser energy. The LPX® 305i will stop firing if the excitation voltage required to maintain the commanded laser energy falls outside the excitation voltage operating range [1]. Both the constant voltage and the constant energy modes were used for the research presented in this dissertation.

3.3 Laser Optic System

A rectangular aperture, optional optical attenuator, horizontal and vertical turning mirrors, focal lens, programmable beam steering mirror, entrance window, and in-chamber energy meter comprise the laser optic system, as shown in Figure 3-2. A 25 mm horizontal by 20 mm vertical rectangular aperture placed 130 mm in front of the LPX® 305i clips the laser pulse to ensure that the laser pulse remains on the optics and to limit the laser pulse to the central portion of the beam. As discussed in Section 3.2, the laser excitation voltage must lie between 14.5 and 21.0 kV. Growth conditions may require a laser pulse with energy less than that produced using a 14.5 kV excitation voltage. An optional barium fluoride window placed after the aperture can be inserted to attenuate the laser pulse, which lowers the laser pulse energy in the chamber while maintain an exciting voltage greater than 14.5 kV. Following the optional attenuator, a 3.5-inch diameter mirror, labeled “horizontal turning mirror” in Figure 3-2, reflects the laser pulse toward the focal lens. A magnesium fluoride 1000-mm lens focuses the laser pulse onto the target. After the lens, another first-surface reflecting mirror, labeled “vertical turning mirror,” in Figure 3-2, directs the laser pulse toward the programmable scanning mirror.

The horizontal and vertical turning mirrors are first-surface reflecting mirrors comprised of optically flat glass substrates coated with aluminum and magnesium fluoride films.

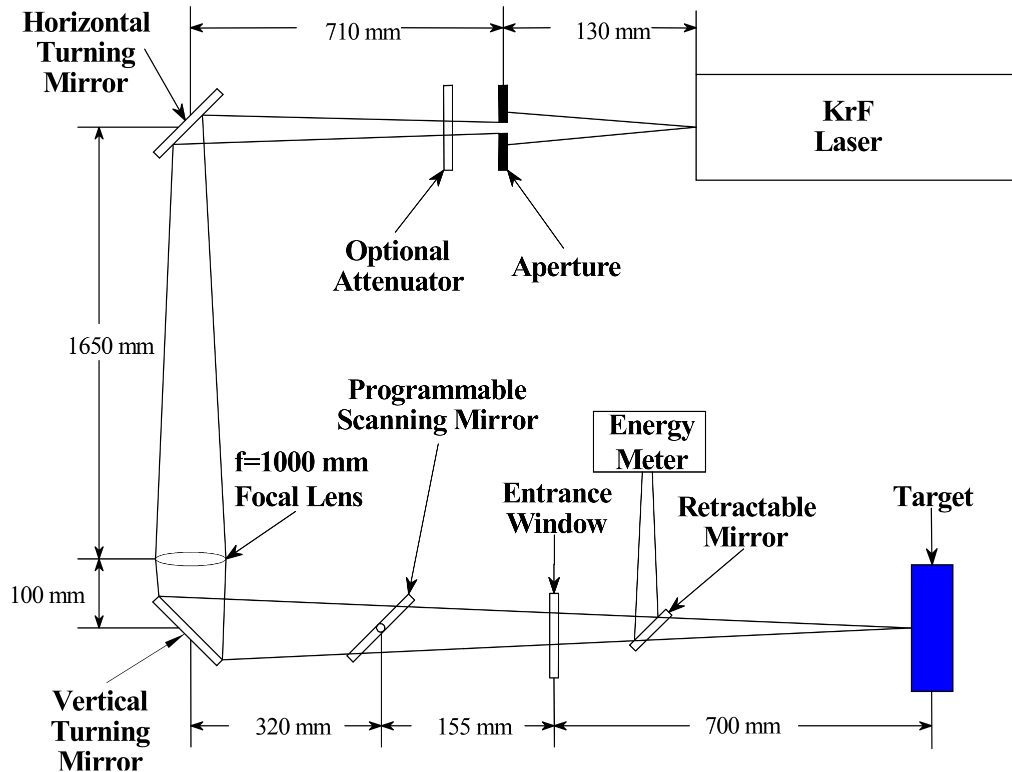

Figure 3-2. Optical Path Diagram

The aluminum films reflect approximately 90 percent of the 248-nm laser pulse. The magnesium fluoride films prevent the aluminum films from oxidizing. The programmable scanning mirror controls the radial location of the laser pulse on the target. The laser pulse enters the chamber through the magnesium fluoride entrance window. A retractable mirror placed between the entrance window and the target directs the laser pulse to either the target or an energy meter sensor. A Moletron Energy Max 500 energy meter monitors the laser pulse energy inside the chamber when the retractable mirror is inserted. Typical laser pulse energies inside the chamber range from 100 to 400 mJ per

laser pulse at 10-40 Hz repetition rates. The laser pulse is focused to produce a footprint of approximately 2 mm by 7 mm.

3.4 Target Carousel

The target carousel, capable of handling three six inch targets, moves to one of six default positions: three are load positions and three are ablate positions. Each of the three load positions allows access to one of the three targets from the front of the chamber. Each of the three ablate positions coaxially align one of the three targets directly under the substrate. In addition to selecting which target to load or ablate, the target carousel also rotates in place all three targets at a constant user-commanded rate. A magnetic coupler weakly connects the carousel to stepper motors on the outside of the chamber. When the targets are rotating, the carousel rocks slightly from one of the six target positions. This slight rocking motion imparts some randomness to the position of the laser pulse footprint on the target but does not change the location of the laser pulse footprint with respect to the substrate. Thus, the rocking motion is beneficial for large diameter targets (targets greater than three inches in diameter). However, with smaller diameter targets, the rocking motion creates the possibility for the laser pulse footprint to drift off the edge of the target and strike the target carousel. An optional manual carousel lock prevents the target carousel from rocking during growths using small diameter targets, but also limits the deposition to a single target since the carousel is not allowed to move to another target selection.

3.5 Substrate Manipulation System

The substrate shutter, variable substrate height control, substrate holder/rotation system, and substrate biasing system comprise the substrate manipulation system. The substrate shutter, when inserted between the target and the substrate, shields the substrate from the plume, which prevents any deposition on the substrate. Ablating the target with the substrate shutter inserted removes contamination from the surface of the target and allows deposition conditions to be initialized without affecting the subsequent film growth. For example, the time-of-flight sensor system, which is discussed in Section 3.8, can be used to control the LPX305i laser excitation voltage so that the time-of-flight for a specific plume constituent remains constant throughout the deposition process. However, the constant time-of-flight control algorithm requires initialization (typically a few hundred laser pulses) during which the excitation voltage is varied to produce the desired time-of-flight. During this initialization, the plume is depositing material under conditions that may not be the desired deposition conditions. Until the initialization is completed, the substrate shutter is inserted and the plume deposits material on the substrate shutter rather than on the substrate. Once the control algorithm stabilizes the plume, the substrate shutter is retracted, and the uncoated substrate is exposed to the plume.

The variable substrate height control allows the target-to-substrate distance to be varied from 55 mm to 145 mm. Activation of the substrate shutter and *in-situ* Raman spectroscopy for substrates less than four inches in diameter both require the substrate to be raised to the near maximum position, which is an atypical growth position for both silicon carbide and yttria stabilized zirconia (YSZ). A Hastelloy substrate holder holds

the substrate inverted above the target, so that the substrate surface faces down toward the target surface. For six-inch diameter substrates, C-shaped clamps hold the substrate to the substrate holder. For smaller substrates, Hastelloy substrate masks clamp the substrate to the substrate holder. The substrate rotation shaft connects the substrate holder to the substrate rotation system. Since the laser pulse scanning is limited to motion along the radius of the target and substrate, uniform thickness films require rotation of the substrate. A stepper motor rotates the substrate at a constant commanded rate. A Stanford Research PS310 power supply and a brush assembly, which allows the substrate to be biased while rotating, comprise the substrate biasing system. The PS310 is capable of delivering up to either 1250 V or 20 mA [2]. The substrate is negatively biased with respected to the chamber so that positively charged ions within the plume are accelerated toward the substrate.

3.6 Pressure Control System

A roughing pump, turbomolecular pump, valve control panel, pressure gauges, multi-gas controller, gas sources, and various valves comprise the pressure control system. Figure 3-3 illustrates the general configuration of the pressure system. A Varian Turbo-V 550 eight-inch turbomolecular pump and controller produce a vacuum of less than 10^{-6} Torr when exposed to the chamber through the main valve. A Leybold Trivac D16BCS mechanical pump, labeled “Roughing Pump” in Figure 3-3, either evacuates the chamber down to vacuum levels suitable for turbomolecular pumping or removes the back pressure from the turbomolecular pump (“backs”), as determined by the mutually-exclusive operation of the two rougher valves. An Epion valve control panel manages all vacuum valves in the system by allowing only three modes of operation: back turbo only,

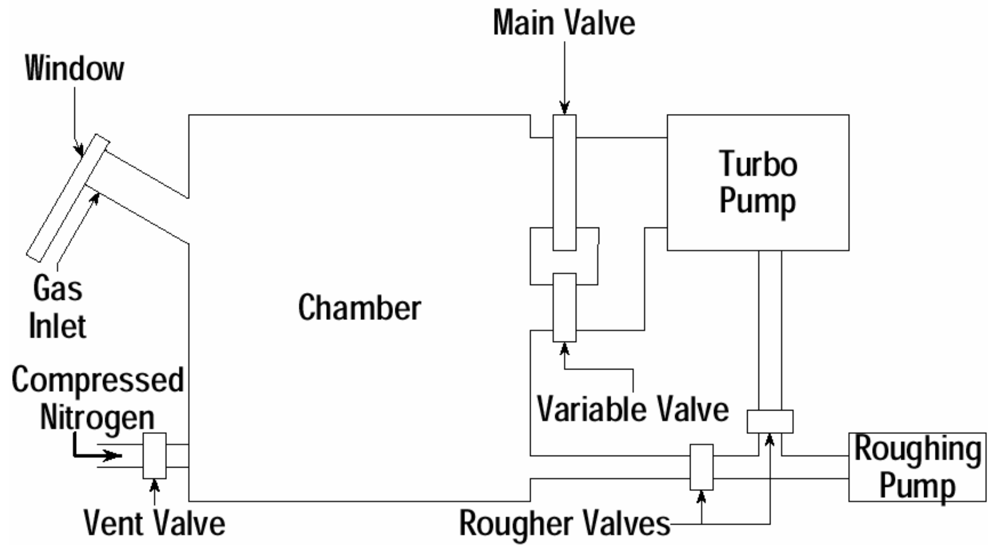

Figure 3-3. Pressure Control Vacuum Diagram

pump down, and up to air. The back turbo only mode closes all valves, except the rougher valve to the turbomolecular pump. The up to air mode operates as back turbo only mode, but also opens the vent valve to purge the chamber with compressed nitrogen. In pump down mode, the valve control panel closes all valves except the rougher valve so that the roughing pump evacuates the chamber down below one Torr. Once the chamber reaches less than one Torr in pump down mode, the valve control panel switches the roughing pump to back the turbomolecular pump and opens the main valve. A Granville-Phillips 307 Vacuum Gauge Controller monitors the vacuum using a Granville-Phillips model 274006 ionization vacuum gauge for the chamber and two Granville-Phillips model 275 Convectron® vacuum gauges, one for the roughing line and one for the chamber. In addition to monitoring these gauges, the vacuum gauge controller also commands the valve control panel, when in pump down mode, to switch from roughing the chamber to pumping with the turbomolecular pump. This vacuum set point is programmable and is currently set at one Torr.

In addition to the pumping portion of the pressure control system, a multi-gas controller, gas sources, variable turbo valve, and adaptive pressure controller enable the chamber to maintain a constant pressure and gaseous composition. The MKS 647B multi-gas controller provides a constant flow of any combination of up to four gas sources [3]. Currently only three of the four channels are utilized to provide oxygen, nitrogen, and argon ambient environments for the deposition environments. The MKS 647B controls three MKS Type 1179A Mass-Flo® Controllers, one for each gas source, to provide flow rates of up to 10 standard cubic centimeters per minute (sccm) each [4]. As shown in Figure 3-3, the gases enter the chamber near the laser window, which helps prevent plume particles from depositing on the laser window. The variable turbo valve, which bypasses the main turbo valve, controls the flow of gas into the turbo when the valve control panel operates in back turbo only mode. Using an MKS type 120A Baratron® Vacuum Gauge to monitor pressure in the chamber, a VAT PM5 Adaptive Pressure Controller commands the position of the variable turbo valve to maintain a given pressure. The MKS type 120A Baratron® Vacuum Gauge and VAT adaptive pressure control both have dynamic pressure ranges that are currently configured for up to one Torr [5; 6], which limits the pressure levels to the mTorr range.

3.7 Temperature Control

Quartz lamps, a lamp power supply, a water-cooled heater chamber, a thermocouple, and a temperature controller comprise the temperature control system. Twelve General Electric QH1200T3/Cl/HT quartz lamps wired in parallel provide heat to the substrate. The lamps are arranged six above the substrate, two above and beside the

substrate, and four below the substrate. A Power Ten, Inc. P63C-8083 power supply generates a constant voltage to all twelve lamps. A Eurotherm EPC900 temperature controller senses the heater chamber temperature using a Chromel-Alumel K-type thermocouple and adjusts the output voltage of the lamp power supply to produce the commanded temperature. The water-cooled heater chamber limits the area to be heated to a small volume surrounding the substrate. The valve control panel, described in Section 3.6, enables the lamp power supply only when there is sufficient water flow and a vacuum exists in the chamber. Loss of either water flow or vacuum will immediately disable the lamp power supply as a safety precaution. The Hastelloy substrate holder and stainless steel substrate rotation shaft, as described in Section 3.5, limit the chamber's operating temperature range to 900°C and below.

3.8 Time-of-Flight Emission Sensor System

An optical bandpass filter, a photo multiplier tube (PMT), a PMT power supply, spatial filters, a signal amplifier, and a Tektronics TDS 540D digital oscilloscope comprise the time-of-flight (TOF) emission sensor system. An optical bandpass filter limits the wavelengths of light exposed to the PMT. For example, excited zirconium (Zr^*) emits at several wavelengths, including 468.8 nm, 471.0 nm, and 473.9 nm [7]. Thus, for YSZ, an optical bandpass filter centered at 470 nm with a 10-nm spectral width allows the Zr^* emissions to be monitored independently of the other species in the YSZ plume [7]. A Hamamatsu R7400U-04 PMT, which is sensitive to emissions in a UV to near IR spectral range of 185 nm to 850 nm [8], detects the optical emissions that are transmitted through the optical bandpass filter. A DC bias voltage applied to the PMT determines the gain of the PMT [8]. Typical bias voltages range from 500 to 750 V for

the YSZ plume detection. A Fluke 415B high voltage power supply produces the bias voltage for the PMT. Inside the chamber, twelve horizontal stainless steel plates spaced approximately 1.83 mm apart and aligned parallel to the target and substrate spatially filter the plume into eleven distinct horizontal cross sections or “slots.” The PMT detects emission through only one of the eleven slots at any given time, as determined by the manual positioning of the PMT, which is external to the chamber, as shown in Figure 3-4. Table 3-2 lists the distances between the spatial filters and the target surface. A change in either capacitance or load on the PMT output can alter the TOF signal. A Kota Microcircuits, Inc. E104 low-noise signal amplifier buffers the PMT output from transmission-line effects and adds 14 dB of gain [9]. A Tektronics TDS 540D four channel digital oscilloscope digitizes the PMT output and allows the software to record the signal, as described in Section 3.11. Time jitter between the trigger output signal from the LPX® 305i excimer laser and the actual time of the laser pulse has been observed to vary up to one microsecond, which can create significant TOF signal error especially when averaging multiple TOF signals to reduce systematic noise. The laser pulse detection and trigger conditioning circuit, as shown in Figure 3-5, reduces the time jitter errors. The circuit is placed behind the horizontal turning mirror, shown in Figure 3-2, and detects the small fraction of the laser pulse that is transmitted through the mirror. When diode D1 is exposed to the laser pulse, current flows into the base of transistor Q1, which allows Q1 to conduct. This current produces a voltage across resistor R2. Diode D2 and resistor R3 apply this voltage pulse to the input of the Schmitt triggered inverter U1A. The Schmitt triggered inverter reduces signal bounce and conditions the signal into a clean inverted pulse. Schmitt triggered inverter U1B inverts the pulse to produce a

positive-logic TTL compatible trigger output. The delay through the circuit is less than40 ns, which is equal to temporal data resolution of the digital oscilloscope. In addition, the 40-ns delay is similar to the laser pulse width, which varies between 20 to 30 ns [1].

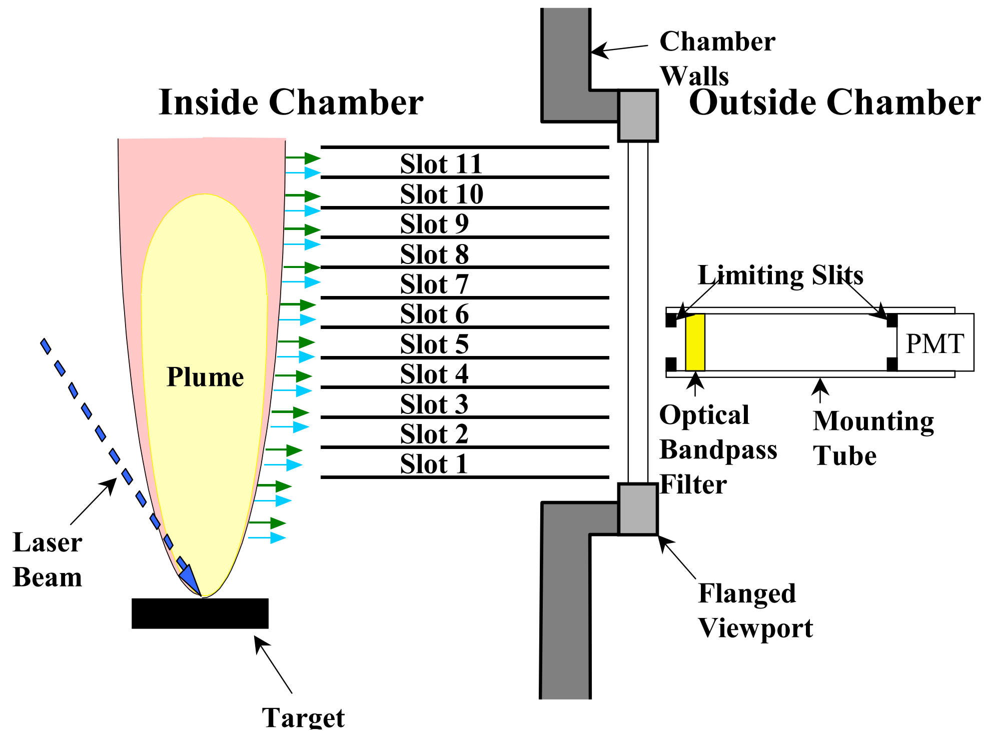

Figure 3-4. Time-of-Flight Emission Sensor System Diagram

Table 3-2. Distance of Photo Multiplier Tube Spatial Filters from Target

Slot	Minimum (mm)	Mean (mm)	Maximum (mm)
1	63.8	64.7	65.6
2	68.3	69.2	70.1
3	70.3	71.2	72.1
4	74.3	75.2	76.1
5	77.3	78.2	79.1
6	80.8	81.7	82.6
7	83.3	84.2	85.1
8	87.3	88.2	89.1
9	90.3	91.2	92.1
10	93.8	94.7	95.6
11	97.3	98.2	99.1

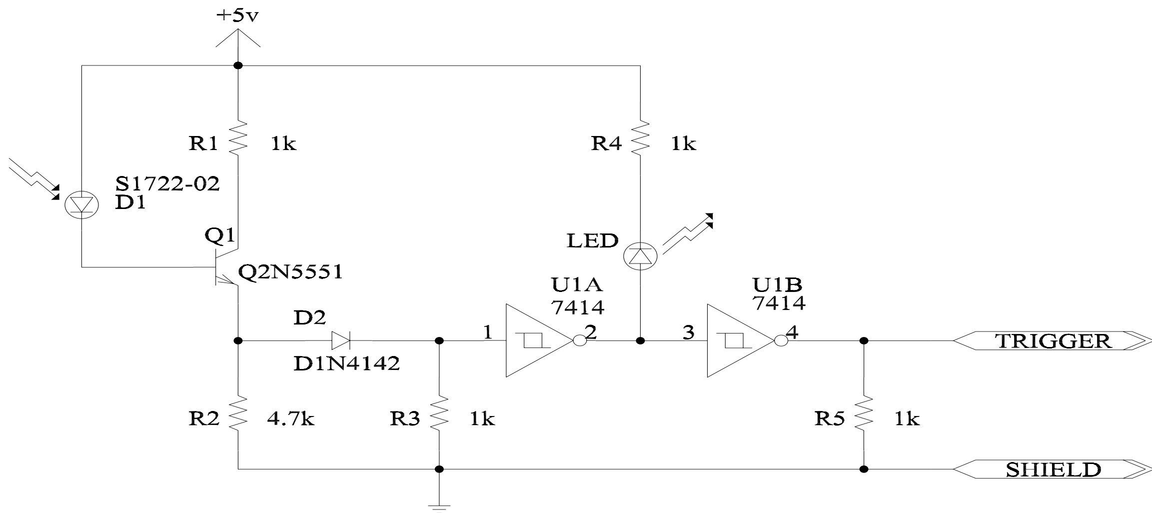

Figure 3-5. Laser Pulse Detector and Trigger Conditioning Circuit Schematic

3.9 Fast-imaging Camera System

A Princeton Instruments® PI-MAX™ 512 fast-imaging camera and optical bandpass filters provide images of the plume emissions for optical diagnostics. The camera utilizes an intensified charge-coupled device (ICCD) with nanosecond-level gate timing to acquire multiple images of the plume at discrete time intervals [10]. The PI-MAX™ 512 captures time-resolved images whose spectra range from 450 nm to 900 nm [10]. Stacking these time-resolved images together produces a "slide-show" of the plume emissions as the plume propagates from the target to the substrate. The images are typically acquired at 200 ns intervals with 100 ns integration times. The circuit shown in Figure 3-5 synchronizes the Princeton Instruments® ST133A Camera Controller with a Pulse Timing Generator (PTG) card to the laser pulse so that the camera's time origin coincides with the start of the laser pulse with less than a 40 ns delay. A square two-inch optical bandpass filter limits the plume emissions to a small spectral region of interest,

currently centered at 470 nanometer with a spectral width of 10 nm for YSZ plumes. This optical region contains only excited zirconium (Zr*) emissions when ablating from an YSZ target in an oxygen ambient environment [7]. Thus, the fast-imaging camera and optical filter provide insight into the spatial and temporal distribution of the Zr* emissions in the plume. This is similar to multiple TOF sensors monitoring the emissions at numerous discrete distances from the target surface.

3.10 Raman Spectroscopy System

A Raman probe [11], an Echelle spectrometer [12], excitation laser, fiber optic cabling, and acquisition computer comprise the Raman spectroscopy system. PLD has been described as “an interrupted deposition process with multiple repetitions” [13]. An EIC Laboratories Raman probe [11] enables Raman spectra to be taken during such interruptions in the PLD growth process. The principle components of the Raman probe are shown in Figure 3-6. A Coherent DPSS 532-200 Nd:YAG excitation laser [14] produces a 200-mW, 532.0-nm excitation signal that is transmitted to the Raman probe via a fiber optic cable. A coupling lens focuses the excitation signal through a dichroic filter and onto the focusing lens. The 1 cm focusing lens tightly focuses the excitation signal onto the substrate at an approximately 35-degree angle of incidence from the substrate normal. The focusing lens also collects the Raman signal but not the reflected excitation signal since the excitation signal is not at normal incidence to the substrate. The bandpass dichroic filter transmits the excitation wavelength, 532 nm, and reflects all other wavelengths near 532 nm. This allows the Stokes and anti-Stokes Raman signal to be reflected while the dominant portion of the Rayleigh scattering signal passes through the dichroic filter. Thus, the return signal that is monitored by the spectrometer has a

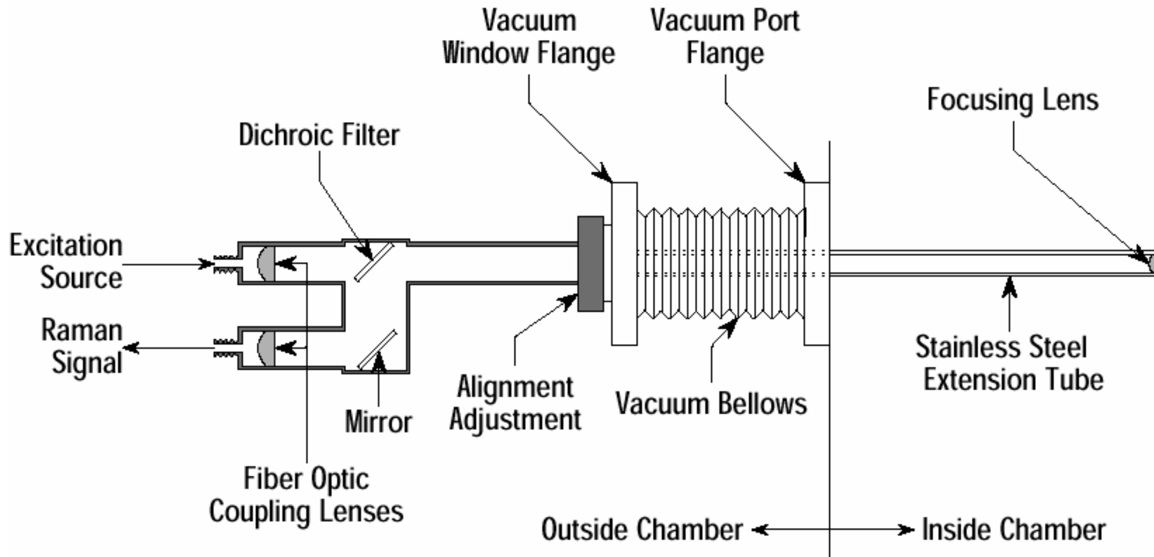

Figure 3-6. Raman Probe Schematic

greatly attenuated Rayleigh scattering component. Another coupling lens directs the Raman signal into a fiber optic that transmits the Raman return signal to the spectrometer. An EIC Laboratories VIS500 Echelle [15] spectrometer acquires the Raman spectra and an Andor DU-420BV CCD camera [16] digitizes the Raman spectra. The entire Raman probe is retractable, as shown by the vacuum bellows and vacuum flange in Figure 3-6. This allows the Raman probe to be inserted to a position where the focusing lens is near the substrate for acquisition, and then retracted when not in use to avoid depositing on the focusing lens. A Raman acquisition computer oversees the Raman spectra acquisition and responds to remote requests from the system control computer through a Microsoft ActiveX® software interface [17].

3.11 Software Control and Logging

Software routines written using LabVIEW® from National Instruments [18] provide a user interface and data logging capability for the deposition system when

executed on the system control computer. A separate LabVIEW® [18] routine controls each of the systems described in the Sections 3.2 through 3.10 using a National Instruments PCI-GPIB IEEE 488.2 interface card, a National Instruments PCI-232/8 multiport RS-232 interface card, or a TCP/IP interface to a remote computer. Each of the system routines operates in parallel with and independent of the other system routines. This distributed system control allows the removal of unneeded systems or the addition of new systems without the need to recode the entire software. Each system routine can be controlled locally from the front panel of the associated system routine (local mode) or globally from a single top-level routine (global mode). When in global mode, the top-level routine manages each system routine by scheduling operations based upon times specified in a deposition "recipe." The global mode allows minimal user interaction and improved run-to-run control consistency, while local mode provides the ease of operation and flexibility preferred for simple depositions and recipe development. In addition to the control and system routines, a separate logging routine polls each of the system routines at a user-defined rate and records the variables of interest to a single log file per deposition cycle.

3.12 Chapter Summary

The pulsed laser deposition (PLD) system and the associated diagnostic sensor systems were presented in this chapter. This chapter also described the PLD system's software logging and control. All depositions performed for this dissertation were grown using the PLD system described in this chapter. In addition, this chapter described the *in-situ* Raman spectroscopy system used for the research presented in Appendix A.

Bibliography

1. *User Manual: LPX® Series Handheld Keypad*, Ft. Lauderdale, FL: Lambda Physik, April 2000.

2. *Series PS300 High Voltage Power Supplies*, rev 2.6, Sunnyvale CA: Stanford Research Systems, November 2000.

3. *Multi Channel Flow Ratio/Pressure Controller Type 647B Instruction Manual*, rev 11.96, Andover MA: MKS Instruments, November 1999.

4. *MKS Type 1179A Mass-Flo® Controller Instruction Manual*, rev B, Andover MA: MKS Instruments, October 1996.

5. *MKS Type 120A High Accuracy Pressure Transducer*, rev E, Andover MA: MKS Instruments, July 1996.

6. *Installation, Operating, and Maintenance Instructions*, Haag, Switzerland: VAT Vakuumventile AG, 1 January 1994.

7. Voevodin, A. A., J. G. Jones, and J. S. Zabinski. "Characterization of Zro_2/Y_2O_3 Laser Ablation Plasma in Vacuum, Oxygen, and Argon Environments," *Journal of Applied Physics*, 88(2): 1088-1096, 15 July 2000.

8. *Hamamatsu Metal Package Photomultiplier Tube R7400U Series*, Bridgewater NJ: Hamamatsu Photonics K.K. Electron Tube Center, April 2000.

9. *KE Series Encased Amplifiers*, Rev 1A, South Portland, ME: Fairchild Semiconductor, 2001.

10. *Princeton Instruments® PI-MAX™ Camera Users Manual*, Rev 3.B, Trenton NJ: Roper Scientific, Inc., 12 June 2002

11. *Technical Note #12: High Resolution Raman Spectroscopy Using an Echelle Spectrograph*. Norwood, MA: InPhotonics Inc., 1998.

12. *Process RamanProbe™*. Product Brochure. Norwood, MA: InPhotonics Inc., 2002.

13. Jones, J. G., A. A. Voevodin, and J. S. Zabinski. "Characterization of Plume Fluence for Laser Ablation of Yttria Stabilized Zirconia in Mixed Oxygen and Argon Environments," *Surface and Coatings Technology*, 16: 258-262, 2001.

14. *Operator's Manual Diode-Pumped, Solid-State (DPSS) Model 532 Laser*. Santa Clara CA: Coherent Laser Group, 1991.

15. High Resolution Raman Spec*trometer*. Product Brochure. Norwood, MA: InPhotonics Inc., no date.

16. *Spectroscopy CCD DU420*. Product Brochure: Belfast, Northern Ireland, no date.

17. Brown, N., and C. Kindel. *Distributed Component Object Model Protocol -- DCOM/1.0*. Microsoft Corporation, Internet-Draft submitted to IETF, 1998.

18. *LabVIEW*®. Version 6.0, IBM, CD-ROM. Computer Software. National Instruments, Austin, TX, 2000.

4 Controlled-Stress Deposition of Yttria Stabilized Zirconia

4.1 Overview

An initial and essential step, in developing large area controlled stress growths using pulsed laser deposition (PLD), is to determine which of the many potential deposition parameters significantly contribute to the stress of the deposited film. Figure 2-23 shows the typical deposition parameters and the associated effects of these deposition parameters on the deposition process. This chapter describes the investigation into the typical deposition parameters that significantly affect film stress.

In addition to determining which typical deposition parameters affect film stress, a physical theory relating the film stress to the influence of the relevant deposition parameters is necessary to develop a process control method. Without a physical theory, the entire parameter space for the relevant deposition parameters must be explored. Although much of this parameter space must be investigated in order to validate the theory, a few PLD growths using well-chosen points within the entire parameter space can characterize the process, once the theory has been validated. Thus, the two goals of this chapter are to determine which deposition parameters significantly affect film stress and to derive/apply a relevant physical theory to the film stress control process. This chapter focuses on yttria stabilized zirconia (YSZ) depositions. YSZ was chosen as the material to be deposited due its excellent mechanical and optical properties, as described in Chapter 2. In addition, other research within the Air Force Research Laboratory

Materials and Manufacturing Directorate (AFRL/ML) investigated PLD-grown YSZ for superconducting film buffer layers [1; 2]. Thus, the YSZ stress characterization presented in this chapter was chosen to be compatible with these ongoing efforts.

The two goals of this chapter (determine which deposition parameters significantly affect film stress and to derive/apply a relevant physical theory to the film stress control process) were achieved. Laser fluence, ambient pressure, target-to-substrate distance, and target surface condition were found to be the PLD variables that most significantly affect yttria stabilized zirconia (YSZ) film stress. A model was developed to correlate film stress with laser fluence, ambient pressure, and target-to-substrate distance. The target surface condition was held constant by sanding the target surface before each deposition. In addition to the previously listed deposition parameters, the impact of laser repetition rates between 10 and 40 Hz on film stress was investigated and found to have no significant effect. The influence of initial substrate heating on film stress was also investigated. The effect of initial substrate heating was not determined since initial substrate heating, when combined with substrate heating from the plume, was found to damage the polymer substrates.

4.2 Theory

The PLD model described in Section 2.4 relates the 17 deposition parameters to film parameters through characteristics of the plume constituents [3]. Often there exists a direct correlation between film properties and plume parameters [3; 4]. Plume velocity, more specifically the change in plume velocity with distance from the target surface and time (plume dynamics), is one such plume parameter [3]. Thus, an understanding of plume dynamics is essential to correlate plume velocity with film properties.

One proposed theory of plume dynamics, the "blast wave model," models the relationship between distance and ambient pressure as a function of time [5; 6; 7; 8], as shown in Equation (4-1):

$$D(t) = \xi_0 \cdot (E/P)^{0.2} \cdot t^n \quad (\text{mm}) \tag{4-1}$$

where *D* is *distance* (mm), ξ_0 is a *scaling constant* (mm·μs^{-n}·mTorr$^{0.2}$· J$^{-0.2}$), *E* is *explosion energy* (J), *P* is *pressure* (mTorr), *t* is *time* (μs), and *n* is an *exponential constant.* The blast wave model was initially derived to describe the propagation of shock waves resulting from the detonation of an explosive charge. There are at least two noteworthy differences between a shock wave propagating through air and a plume propagating in a vacuum or low-pressure environment: relative particle velocity distribution difference and variations in the shape/direction of the propagation between the shock wave and the PLD plume. The shock wave is characterized by a sharp change in pressure that is defined as the shock front [8]. In context of explosive detonations, the distance *D* in Equation (4-1) represents the distance of the shock front from the detonation origin. When Equation (4-1) is used to describe plume velocities, the distance *D* in Equation (4-1) represents distance of the plume from the target surface. However, the distance *D* is not as clearly defined for plume dynamics as it is for explosive detonations. As shown in Figure 2-21, optical emissions, which are indicative of plume presence, are present during a range of times for a given distance from the target surface. Figure 2-22 also illustrates that at a given time optical emissions exist over a range of distances from the target surface. Thus, there is not a sharply defined time at which the plume arrives at a given distance. Secondly, the shock front propagates away from the

detonation location as a spherically-symmetric wave when a spherical charge is detonated at the center of the charge [8]. For non-spherical charges, the shock wave can be closely approximately by a spherical wave for distances that are an order of magnitude longer than the largest dimension of the non-spherical charge [8]. However, as shown in Figure 2-22, the plume propagates normal to the target surface in a non-spherical wave.

Despite the difference between the shock front and plume propagation, the blast wave model is currently the best available model to describe plume dynamics for the range of PLD parameters explored in this chapter. The conceptual similarities between the detonation of an explosive charge and laser ablation are readily apparent. Both are highly energetic processes that are triggered by a relatively short explosion or ablation. Thus, the use of the blast wave model to describe plume dynamics is not unreasonable. In addition to the blast wave model, Geohegan shows the applicability of a linear model to describe plume dynamics for high vacuum deposition in the μTorr pressure range [7]. For PLD environments in the mTorr pressure range, Geohegan also applies a drag model to the plume for distances from the target surface less than or equal to 2cm [7]. However, the deposition parameters explored in this chapter consist of ambient pressures in the mTorr range and target-to-substrate distances greater than 4.5 cm. For these PLD conditions, Geohegan states that blast wave model is the best available model to describe plume dynamics [7]. Thus, the remainder of this chapter assumes that the blast wave model adequately represents the plume dynamics for the range of deposition parameters explored in this dissertation. Chapter 5 shows the validity of this assumption and describes the other plume dynamics models in more detail.

As defined previously, plume dynamics denote the change in plume velocity with distance from the target surface and time. As such, Equation (4-1), which relates distance and time, is not the most intuitive expression and should be transformed to relate velocity to distance from the target surface. Plume velocity, v, is defined as the derivative of distance with respect to time, as shown in Equation (4-2) [5]:

$$v(t) \equiv \frac{dD(t)}{dt} = \xi_0 \cdot (E/P)^{0.2} \cdot n \cdot t^{n-1} \quad (\mathrm{km/s}) \tag{4-2}$$

Solving Equation (4-1) for time and substituting the result into Equation (4-2) produces velocity as a function of distance and independent of time, as shown in Equation (4-3) [5]:

$$v(D) = \xi_0^{1/n} \cdot n \cdot (E/P)^{0.2/n} \cdot D^{(n-1)/n} \quad (\mathrm{km/s}) \tag{4-3}$$

Equation (4-3) states that for a given explosion energy and ambient pressure, the velocity decreases as a function of distance when the exponential constant n is less than unity. Previous research fit experimental data to Equation (4-3) and calculated values of 0.4 and 0.6 for the exponent n [5; 6]. Equation (4-3) also asserts that an increase in explosion energy and/or a decrease in pressure will produce an initially greater velocity that decays at the same rate with respect to distance.

Given that the plume dynamics are described by Equation (4-3), the remainder of this chapter assumes that plume velocity at the substrate determines the film stress. Qualitatively, this assumption appears valid. If the velocities of the plume constituents are too fast, the substrates and any previous film growth can be damaged. For example, the kinetic energy of zirconia at 20 km/s is 187 eV. Such high kinetic energy is sufficient

to cause substrate damage similar to sputtering the substrate. Conversely, if the kinetic energy of the plume constituents is low, the deposition rate will be slow and the surface activation energy will not be sufficient to grow high-quality films. Thus, the kinetic energy of the plume is similar to ion-assisted deposition [5]. The assumption that the plume velocity determines the film stress is shown in Chapter 8.

Using the constant velocity assumption, there is some plume velocity at the substrate that produces growths exhibiting no curvature. The actual value of this constant velocity, defined as v_{flat}, need not be known for further analysis. When combined with Equation (4-3), this velocity, v_{flat}, can be used to interpolate among the pressure-distance combinations at a given explosion energy E that produce growths exhibiting a desire stress, such as the stress that produces films exhibiting no curvature. The explosion energy E is an unknown function of laser fluence, which is a combination of both laser energy and laser footprint size. However, for a given laser energy and laser footprint size, the explosion energy E remains constant. Equation (4-4) defines a new constant C that groups all the constant terms: explosion energy E, velocity v_{flat}, exponential constant n, and scaling constant ξ_0. This simplifies Equation (4-3) to include only pressure, distance, n, and the new constant C, as shown in Equation (4-5):

$$C = \frac{\xi_0^{\,5} \cdot n^{5n} \cdot E}{\left(v_{flat}\right)^{5n}} \quad \left(\text{mTorr} \cdot \text{mm}^{5\cdot(1\text{-n})}\right) \tag{4-4}$$

$$P = C \cdot D^{5\cdot(n-1)} \quad \left(\text{mTorr}\right) \tag{4-5}$$

where C is a *constant* (mTorr·mm$^{5(1\text{-n})}$), v_{flat} is *velocity that produces film exhibiting no substrate curvature* (km/s), ξ_0 is a *scaling constant* (mm·μs^{-n}·mTorr$^{0.2}$·J$^{-0.2}$), E is

explosion energy (J), *P* is *pressure* (mTorr), *D* is *target-to-substrate distance* (mm), and *n* is an *exponential constant.*

Previous research has highlighted the relationship between plume dynamics and various film properties. For example, the electrical properties of PLD-grown $YBa_2Cu_3O_{7-x}$ (YBCO) films were theorized to be proportional to the velocity of the film constituents in the plume [5; 6; 9; 10; 11; 12; 13]. In fact, a P-D scaling law, similar to that presented in Equation (4-5), was employed to determine the optimal pressure for a range of target-to-substrate distances [5; 6]. Other research reported on the use of plume constituents' velocities as a feedback sensor to control the laser energy per pulse and ambient pressure [9; 10; 11; 12; 13]. In addition, previous research has related the plume dynamics to crystalline quality of several II-VI compound semiconductors, namely ZnS, ZnSe, CdS, CdSe, and CdTe [14]. However, the current literature does not contain any references to possible relationships between the mechanical properties of PLD-grown films and plume dynamics, which is the focus of this chapter. Section 4.3 describes an experiment designed to correlate the mechanical properties, specifically film stress, of PLD-grown YSZ films with plume dynamics.

4.3 Experiment

To determine the effect of the pressure and the target-to-substrate distance on film stress, many YSZ thin films were grown on nine-micrometer thick polymer substrates, specifically a colorless, low dielectric, radiation-resistant polyimide, denoted CP1, that was developed by NASA Langley Research Center [15; 16; 17]. Previous experience has shown that the film curvature was most sensitive to changes in the oxygen pressure and target-to-substrate distance combinations near the no curvature condition. Thus, the no

curvature condition was chosen as the desired stress to be characterized. The growths were performed using various oxygen pressures and target-to-substrate distances at a given laser fluence. The CP1 polymer substrates were initially flat when clamped between the substrate holder and the substrate holder mask. The clamping of the CP1 polymer substrate did not alter the curvature of the CP1 polymer substrates.

YSZ thin films were deposited on the CP1 polymer substrates using the PLD system described in Chapter 3. The LPX-305i was operated in constant energy mode at 700 mJ at 40 Hz for 30 minutes to produce laser pulses of 220 mJ inside the chamber. The laser pulse footprint size was approximately 2 mm by 7 mm, which corresponded to a laser fluence of 1.57 J/cm^2. The oxygen pressure and target-to-substrate distance were varied to produce films with no curvature. The conditions that produced YSZ films on CP1 polymer substrate with no curvature were fitted to Equation (4-5) to determine the experimental values of C and n. The LPX-305i was then operated in constant energy mode at 500 mJ at 40 Hz for 30 minutes to produce laser pulses of 165 mJ inside the chamber, which corresponded to a laser fluence of 1.17 J/cm^2. Again, the oxygen pressure and target-to-substrate distance were varied to produce films with no curvature, and the conditions that produced films with no curvature were also fitted using Equation (4-5). Additionally, YSZ thin films on CP1 polymer substrates were grown at 40 Hz for 30 minutes at a fixed target-to-substrate distance while varying the LPX-305i laser energy and oxygen pressure to determine the effect of laser fluence on the explosion energy E from Equation (4-3).

4.4 Data

YSZ thin films grown by PLD on CP1 polymers exhibit stress from compressive to tensile as evident by the direction and magnitude of the substrate curvature. The direction of the substrate curvature indicates either compressive or tensile stress. The film stress is compressive if the substrate curls away from the YSZ film or tensile if the substrate curls toward the YSZ film. The magnitude of the stress is visually quantitized into one of four categories: tightly curled, loosely curled, bowed, and flat. Substrates exhibiting tightly curled and loosely curled stress are ignored due to the difficulty in describing the amount of curl. The bowed category is defined as a substrate that is curved but without the ends overlapping. A substrate with little or no curvature is categorized as flat. Figure 4-1 shows an example of each stress category.

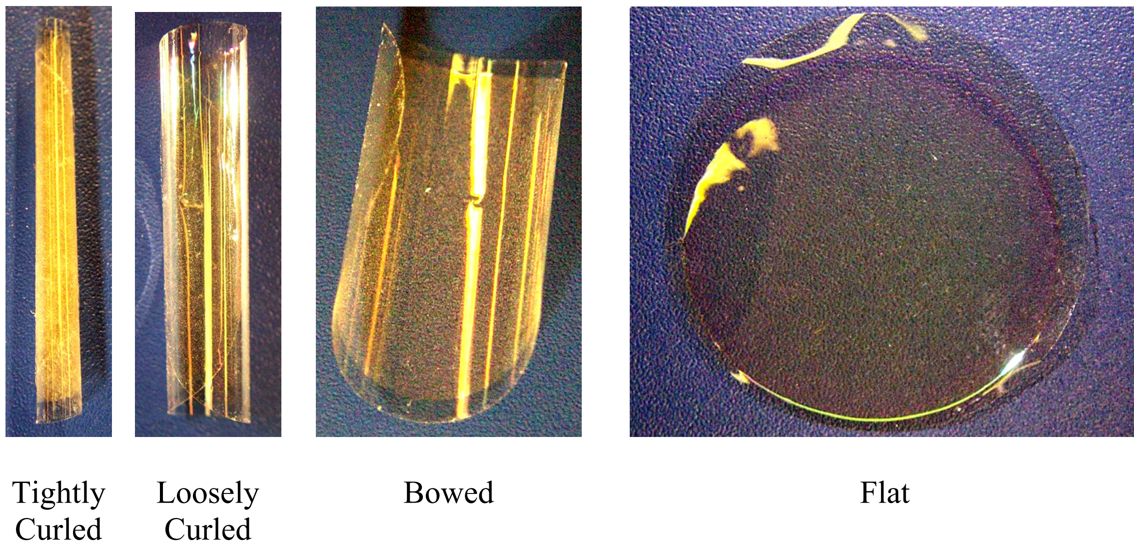

Figure 4-1. Examples of Stress Quantitization Categories

At any given target-to-substrate distance and laser fluence, there exists some pressure, designated the no curvature pressure, that produces substrates exhibiting no

curvature. Table 4-1 summarizes some pressure-distance combinations (no curvature PD combinations) for several laser fluences that produce substrates with no curvature for YSZ thin films on CP1 polymer substrates. Figure 4-2 also displays these no curvature PD combinations.

Table 4-1. YSZ on CP1 Polymer Substrates Growth Parameters Yielding Films Categorized as Flat

Fluence (J/cm^2)	Distance (mm)	Oxygen Pressure (mTorr)
1.57	56.7	195
1.57	64.7	165
1.57	71.7	145
1.57	81.7	126
1.57	91.7	110
1.57	111.7	85
1.48	56.7	190
1.38	56.7	180
1.29	56.7	173
1.17	56.7	165
1.17	111.7	73

For any given target-to-substrate distance, increasing or decreasing the oxygen pressure from the no curvature pressure produces growths with tensile stress or compressive stress, respectively. For a given target-to-substrate distance, a ±2 mTorr oxygen pressure variation from the no curvature pressure results in substrates that exhibited slight curvature, but are still categorized as flat. A ±5 mTorr oxygen pressure variation from the no curvature pressure produces substrates with sufficient curvature to be quantitized as bowed. Substrates that are quantitized as either tightly or loosely curled require at least a ±15 mTorr oxygen pressure variation from the no curvature pressure.

As stated in Section 4.3, the no curvature PD combinations were found by investigating the effect of varying the oxygen pressure at each target-to-substrate

distances listed in Table 4-1. During this investigation, many YSZ on CP1 polymer growths produced substrates that were categorized as bowed or curled. Table 4-2 lists the oxygen pressure, target-to-substrate distance, and laser fluence combinations that produced films categorized as bowed.

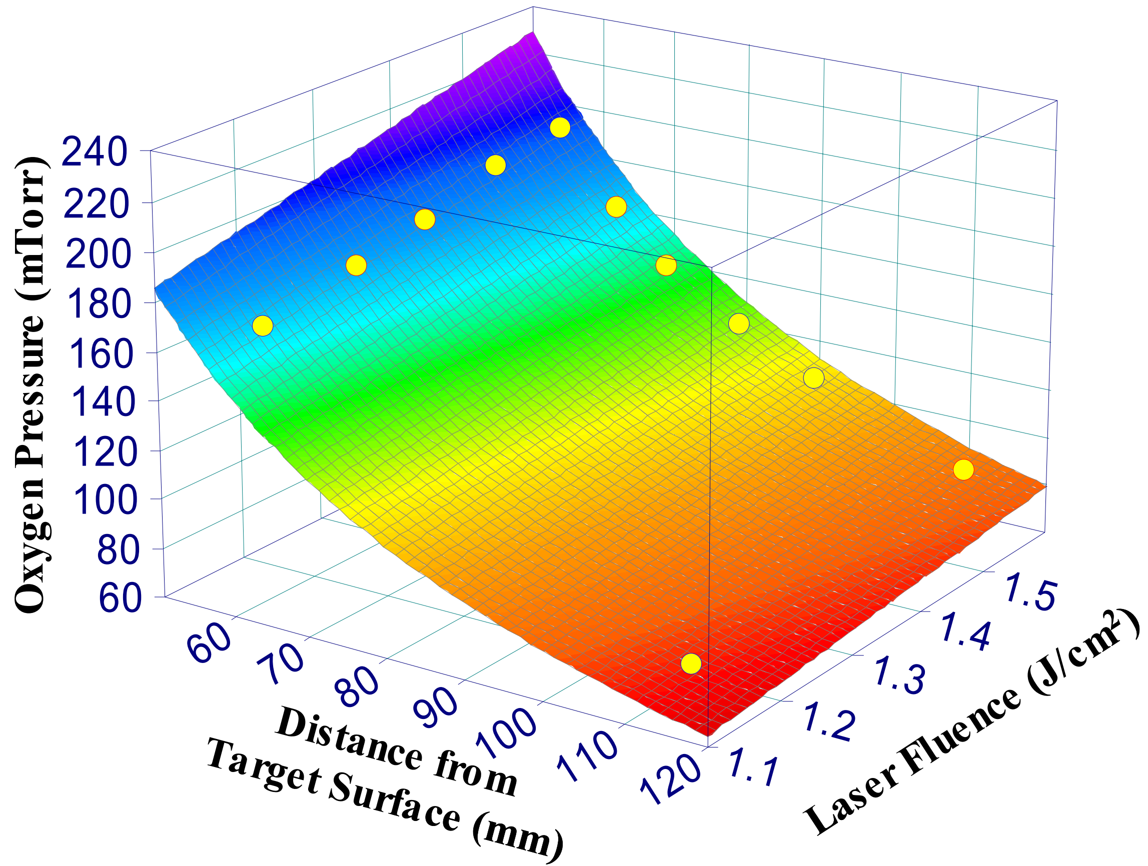

Figure 4-2. Oxygen Pressure, Laser Fluence, and Target-to-Substrate Distance Combinations Plot of YSZ on CP1 Polymer Substrates Yielding Films Categorized as Flat

Table 4-2. YSZ on CP1 Polymer Substrates Growth Parameters Yielding Films with Bowed Curvature

Fluence (J/cm^2)	Distance (mm)	Bowed Away from Film Oxygen Pressure (mTorr)	Bowed Toward Film Oxygen Pressure (mTorr)
1.57	56.7	190	NA
1.57	71.7	135	155
1.57	91.7	NA	120
1.57	111.7	80	90
1.17	56.7	160	170
1.17	111.7	70	75
1.48	56.7	185	NA
1.38	56.7	175	185
1.29	56.7	165	NA

4.5 Analysis

Section 4.2 presents a theory stating that ambient pressure and target-to-substrate distance PLD parameters predominantly determine the plume velocity for a given laser fluence. In addition, Section 4.2 describes the blast wave model, as shown in Equation (4-3), which relates the velocity to a function of distance from the target surface. If the plume velocity theory and plume dynamics model are correct, then the pressure-distance relationship for YSZ thin films on CP1 polymer substrates with no curvature, as listed in Table 4-1, should fit Equation (4-5). Equation (4-5) describes the relationship between pressure and target-to-substrate distance for a given laser fluence. Table 4-3 lists the fitted value and the 95% confidence intervals for C and n, which were calculated using TableCurve 2D [18] and the 1.57 J/cm^2 data listed in Table 4-1. Figure 4-3 displays the computed fit as the solid line and the pressure-distance combinations that produce growths with no curvature as the data points. The 1.57 J/cm^2 laser fluence bowed curvature PD combinations, as listed in Table 4-2, are also shown in Figure 4-3. As previously stated, a ±5 to 15 mTorr pressure variation from the no curvature pressure for

a given target-to-substrate distance results in substrates with sufficient curvature to be quantified as bowed. For a given target-to-substrate distance, the no curvature pressure is bounded between the bowed toward the film and the bowed away from the film pressures. As such, the bowed pressures estimate the worst-case no curvature quantitization error for each target-to-substrate distance. As shown in Figure 4-3, the largest pressure variation is ±10 mTorr. The actual no curvature quantitization error for each target-to-substrate distance is less than this ±10 mTorr worst case variation. As stated previously, a ±2 mTorr pressure variation from the no curvature pressure produces substrates that start to bow, but are still quantitized as flat. Thus, a ±2 mTorr pressure variation is a better estimate of the typical no curvature quantitization error than the worst case ±10 mTorr pressure variations derived from the bowed curvature bounding pressures. In addition, a ±2 mTorr typical quantitization error agrees well with the 95% confidence intervals shown in Figure 4-3. As shown in Figure 4-3 and listed in Table 4-1 and Table 4-2, the pressures that produce growths categorized as bowed deviate less than 8% from the no curvature pressures for any given distance. The actual tolerance of the no curvature point must be less than this deviation. Replacing the qualitative curvature categorization method with some quantitative stress measurement technique will reduce the worst case ±10 mTorr no curvature range. However, one of the goals of this research is to produce growths with a given curvature. The 8% worst case quantitization error range is more than sufficient to accomplish this goal.

Table 4-3. Fitting Statistics for No Curvature Pressure Distance Relationship When Ablating with a 1.57 J/cm^2 Laser Fluence

Parameter	Lower 95% Confidence Interval	Fitted Value	Upper 95% Confidence Interval
C (mTorr·mm$^{5(1-n)}$)	20036	25276	30516
n (unitless)	0.74907	0.75883	0.76859

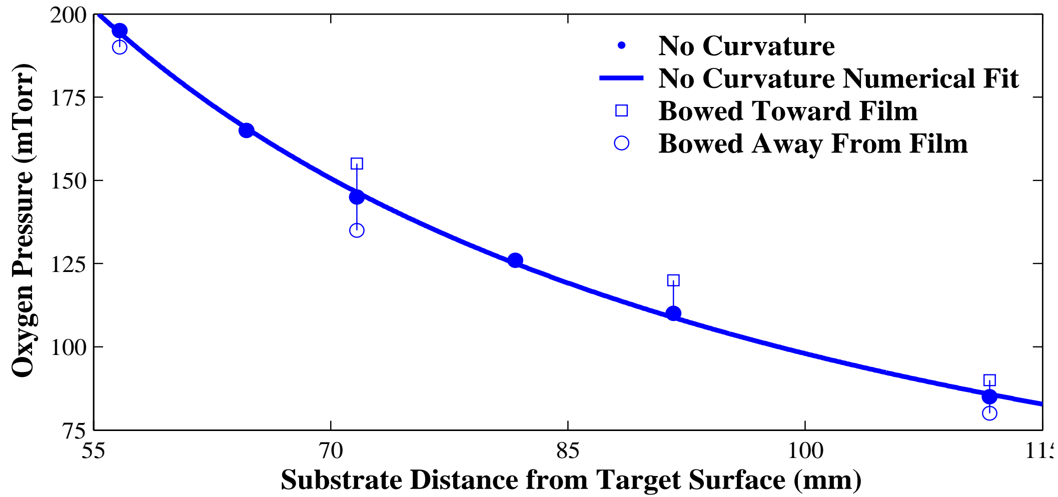

Figure 4-3. YSZ on CP1 Polymer Pressure-Distance Combinations That Produce No Curvature, Theoretical Fit, and Bowed Curvature Pressure-Distance Combinations using a 1.57 J/cm^2 Laser Fluence

The pressure-distance relationship described by Equation (4-5) utilizes the correlation between constant laser fluence and constant explosion energy. This correlation allows the explosion energy to be combined into the constant *C*. However, including the laser fluence into the model enables the PLD user more flexibility and an additional degree of freedom in the PLD parameter space. Equation (4-5) does not describer how the explosion energy *E* relates to laser fluence. Intuitively, explosion energy *E* should be proportional to laser fluence. Five pressure and laser fluence combinations at a fixed substrate to target distance of 56.7 mm produced substrates exhibiting no curvature, as listed in Table 4-1. Equation (4-3) shows that the explosion

energy E to pressure P quotient must be constant to produce the same velocity v_{flat} at a fixed target-to-substrate distance D, such as 56.7 mm. If laser fluence is linearly related to the explosion energy E for the range of laser fluences listed in Table 4-1, then the pressure which produces substrates exhibiting no curvature at a fixed target-to-substrate distance must be linearly related to laser fluence. Figure 4-4 displays the pressure and laser fluence combinations listed in Table 4-1 at a fixed target-to-substrate distance of 56.7 mm, as well as a linear fit to the data shown by the dashed line. As stated previously, the laser fluence is a combination of the laser footprint size on the target and the average energy per laser pulse. The laser fluence was varied by adjusting in the commanded laser energy between 500 and 700 mJ, which corresponded to an average energy per laser pulse of 165 and 220 mJ inside the chamber. The laser footprint size on the target remained constant at 14 mm^2. Table 4-4 lists the fitting statistics for the data shown in Figure 4-4 and listed in Table 4-1.

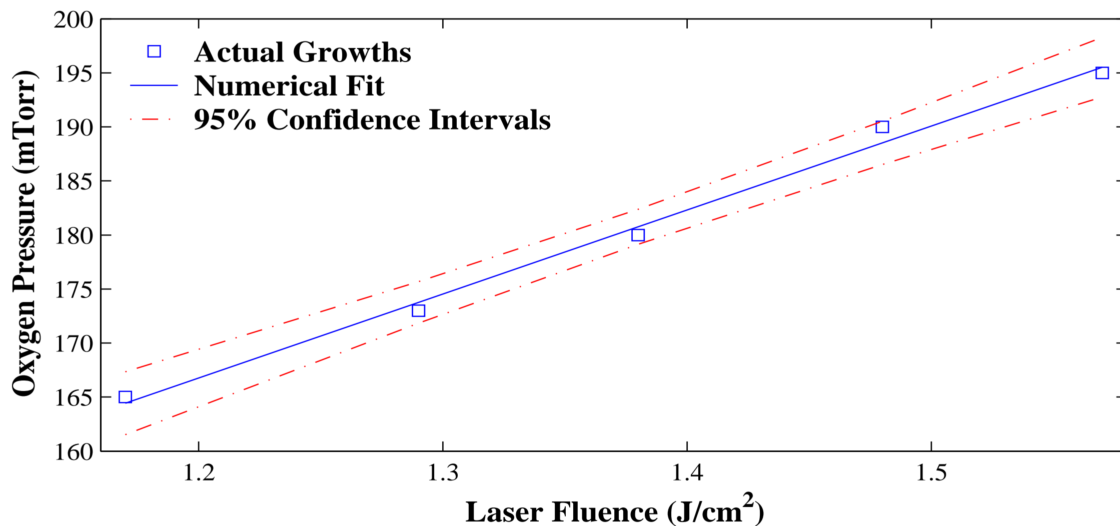

Figure 4-4. Pressure and Laser Fluence Combinations (Varied by Adjusting Average Energy per Laser Pulse at a Fixed Footprint Size of 0.14 mm^2) that Produce Substrates Exhibiting no Curvature at a Target-to-Substrate Distance of 56.7 mm

Table 4-4. Fitting Statistics for No Curvature Pressure Fluence Relationship When Ablating with a Target-to-Substrate Distance of 56.7 mm and a Laser Footprint Size of 14 mm^2

Parameter	Lower 95% Confidence Interval	Fitted Value	Upper 95% Confidence Interval
Slope (J/J)	66.106	77.696	89.286
Offset (J)	57.481	73.534	89.588

Figure 4-4 shows that approximating the explosion energy E with a linear function of laser fluence fits the data adequately. The scaling constant ξ_0 in Equations (4-1) through (4-4) is still unknown since no velocities at the substrate have been measured. However, the goal of this experiment is not to find the velocity v_{flat} but to find a relationship among pressure, laser fluence, and target-to-substrate distance that produces substrates exhibiting no curvature. Thus, the actual magnitude of the velocity v_{flat} is not important, and the scaling constant ξ_0 can remain arbitrary. Equation (4-6) linearly relates laser fluence to explosion energy, as described previously:

$$E = \alpha \cdot F + \beta \quad (\mathrm{J}) \tag{4-6}$$

where E is *explosion energy* (J), α is *slope* (J/J), β is *offset* (J), and F is laser fluence. Substituting this definition of explosion energy E into Equation (4-4) produces Equation (4-7).

$$C = \frac{\xi_0^{\,5} \cdot n^{5n}}{\left(v_{flat}\right)^{5n}} (\alpha \cdot F + \beta) \quad \left(\mathrm{mTorr} \cdot \mathrm{mm}^{5 \cdot (1-n)}\right) \tag{4-7}$$

Equation (4-7) contains the constants ξ_0, α, β, and v_{flat} that can be regrouped into new slope and offset coefficients. Equations (4-8) and (4-9) define the new slope and offset coefficients that relate the variable C to laser fluence F:

$$m = \frac{\xi_0^{\ 5} \cdot n^{5n} \cdot \alpha}{\left(v_{flat}\right)^{5n}} \quad \left(\mathrm{mTorr} \cdot \mathrm{mm}^{5\cdot(1\text{-n})} \cdot \mathrm{mJ}^{-1}\right) \tag{4-8}$$

$$b = \frac{\xi_0^{\ 5} \cdot n^{5n} \cdot \beta}{\left(v_{flat}\right)^{5n}} \quad \left(\mathrm{mTorr} \cdot \mathrm{mm}^{5\cdot(1\text{-n})}\right) \tag{4-9}$$

where m is *slope* ($\mathrm{mTorr{\cdot}mm^{5\cdot(1\text{-n})}{\cdot}mJ^{-1}}$) and b is *offset* ($\mathrm{mTorr{\cdot}mm^{5\cdot(1\text{-n})}}$). Substituting Equations (4-8) and (4-9) into Equation (4-7) reduces the variable C to a function of two variables, as shown in Equation (4-10).

$$C = m \cdot F + b \quad \left(\mathrm{mTorr} \cdot \mathrm{mm}^{5\cdot(1\text{-n})}\right) \tag{4-10}$$

Combining Equation (4-10) with Equation (4-5) produces Equation (4-11), which the relationship upon the relevant PLD parameters that produce substrate exhibiting no curvature.

$$P = \left(m \cdot F + b\right) \cdot D^{(n-1)/0.2} \quad \left(\mathrm{mTorr}\right) \tag{4-11}$$

Using TableCurve 3D [19] to fit every pressure, laser fluence, and target-to-substrate distance combination listed in Table 4-1; *m*, *b*, and *n* are computed to be 9890.9, 10196, and 0.75807, respectively. Table 4-5 contains the relevant fitting statistics. The exponential constant *n* agrees very closely, a deviation of approximately 0.1%, with the previously computed values from the 1.57 $\mathrm{J/cm^2}$. In addition, the worst case fitting residual is 2 mTorr and the worst case 95% confidence intervals vary less than –3.25 and +2.00 mTorr from the no curvature PDF combination. These statistics agree well with the quantitization error of ±2 mTorr described previously. Figure 4-2 illustrates the

surface described by Equation (4-11) and the fitted parameters listed in Table 4-5. Using the values for *m*, *b*, and *n* listed above, Equation (4-11) can be used to interpolate among pressure, laser fluence, and target-to-substrate distance combinations that will produce films exhibiting no curvature for combinations of parameters near the ranges listed in Table 4-1.

Table 4-5. Fitting Statistics for No Curvature Pressure Distance Fluence Relationship When Ablating with a 14 mm^2 Constant Laser Footprint Size

Parameter	Lower 95% Confidence Interval	Fitted Value	Upper 95% Confidence Interval
m ($mTorr \cdot mm^{5(1-n)} \cdot mJ^{-1}$)	8161.7	9890.4	11619.1
b ($mTorr \cdot mm^{5(1-n)}$)	8646.2	10196.5	11746.7
n (unitless)	0.75208	0.75807	0.76406

While the "blast wave model" can be used to interpolate among the pressure, laser fluence, and target-to-substrate distance combinations that produce substrates exhibiting no curvature, the actual plume dynamics as a function of time and distance were not measured. Thus Equations (4-1) through (4-3), which describe the theoretical velocity of the plume, have not been proven. Further discussion of the theoretical velocity and the assumption that velocity determines the stress in the film will be postponed until Chapter 5, which reports on the investigation into the plume dynamics monitored by the TOF emission sensor system and the fast imaging camera system.

As shown in Figure 2-23 and discussed in Section 2.4, there are many deposition parameters that can be varied in order to obtain a desire film quality. Of the deposition parameters typically varied, only target-to-substrate distance, laser fluence, and ambient pressure have been discussed as the dominant factors that control stress in YSZ films

grown on CP1 polymer substrates. Other parameters, such as repetition rate and substrate biasing, were investigated and determined to contribute very little to the stress in the deposited films.

The first additional PLD parameter investigated, repetition rate, has a drastic impact on the quality of the films if the substrates are not attached to a sufficient thermal heatsink. Initial investigations of YSZ growths on six-inch diameter CP1 polymer substrates were performed with the CP1 polymer suspended on a mounting ring, similar to the head of a drum. These growths were limited to repetition rates below 20 Hz. At repetition rates greater than or equal to 20 Hz, the CP1 polymer appears "burned," as apparent by a slightly brownish color and severe deformation of the normally taught polymer. The assumption that the cause was thermal was verified using an optical pyrometer. Although the pyrometer was not calibrated for the emissivity of the CP1 polymer, a relative temperature threshold for the damage was found. Initial testing on one-inch and two-inch diameter CP1 polymer substrates revealed no change in the pressure-distance combination for repetition rates between 10 and 40 Hz. These one-inch and two-inch diameter substrates were grown while clamped to an aluminum substrate holder, which acted as a heatsink. Similarly, final testing on six-inch diameter CP1 polymers still mounted to a Pyrex mold, as discussed in Chapter 7, also showed no damage or substantial change in stress due to laser repetition rate. Due to the limited temperature range of the CP1 polymer substrates and the heating of these substrates by the plume, all depositions were performed initially at room temperature. The inner heater chamber, as described in Section 3.7, was cooled with chilled water at approximately 12° C.

In addition to any repetition rate effects, the effect of substrate biasing of film stress was also investigated. A substrate bias range of 150 to 225 volts was chosen to be compatible with growth conditions described in the current literature. Previous research found that negative substrate biasing, with a threshold of 100 to 150 volts, was necessary to initiate crystal growth of YSZ on randomly oriented polycrystalline substrates [2]. In addition, above this threshold and up to 300 volts, a slight increase in the crystalline size was observed with the increase in the substrate bias [2]. The substrate biasing accelerates the positively-charged plume constituents toward the substrate. Substrate biasing in this manner is analogous to ion-beam assisted deposition [2; 20]. There was negligible change in the curvature of the YSZ thin films on CP1 polymer substrates for negatively biased substrates from 150 to 225 volts over the range of laser fluences, pressures, and target-to-substrate distances listed in Table 4-1.

4.6 Conclusion

The combination of laser fluence, ambient pressure, and target-to-substrate distance can be used to control the stress in YSZ films grown on CP1 polymer substrates. The effects caused by varying these parameters should apply to materials other than YSZ and to substrates other than CP1. The effect of substrate bias and laser repetition rate on the stress in the YSZ films was investigated and found not to have any significant effect. However, without adequate heat dissipation for the CP1 polymer substrate, repetition rates greater than or equal to 20 Hz were found to be destructive. While other PLD parameters that were held constant may also affect the stress of the YSZ films on CP1 polymer substrates, the combination of laser fluence, ambient pressure, and target-to-substrate distance are sufficient to control the stress of the deposited films.

The "blast wave model" proposed in [5; 6; 7] for controlling the electrical properties of superconducting films can be used to interpolate among the pressure, laser fluence, and target-to-substrate distance combinations that produce thin film growth with equivalent stresses. The calculated shape variable n from Equation (4-5) is computed to be 0.75883. This value is comparable to the values of 0.4 and 0.6 used in previous literature for uniform electrical properties of superconductors [5; 6; 7]. Furthermore, the shape variable n is shown to be independent of laser fluence, which allows the "blast wave model" to also account for any variation in the laser fluence.

Although the equations derived from the "blast wave model" can be used to interpolate among parameters necessary to produce films with equal stresses at various pressure, target-to-substrate distance, and laser fluence combinations, the assumptions that the plume distance from the target as a function of time varies as specified by the "blast wave model" and the assumption that plume velocity at the substrate determines the film stress have not been proven. Further investigation into the plume dynamics using the TOF system is necessary and is presented in Chapter 5.

Bibliography

1. Voevodin, Andrey A., J. G. Jones, and Jeffery S. Zabinski. "Characterization of Zro_2/Y_2O_3 Laser Ablation Plasma in Vacuum, Oxygen, and Argon Environments," *Journal of Applied Physics*, 88(2): 1088-1096, 15 July 2000.

2. Voevodin, A. A., J. G. Jones, and J. S. Zabinski. "Structural Modification of Single-Axis-Oriented Yttria-Stabilized-Zirconia Films under Zirconium Ion Bombardment," *Applied Physics Letters*, 78(6): 730-732, 5 February 2001.

3. Biggers, R. R., G. Kozlowski, J. G. Jones, D. V. Dempsey, R. Kleismit, I. Maartense, J. D. Busbee, T. Peterson, and R. Perrin. "Process Control and Pulsed Laser Deposition of Materials," *Integrated Ferroelectrics*, 28(1-4): 201-211, 2000.

4. Chrisey, Douglas B. and Graham K. Hubler, *Pulsed Laser Deposition of Thin Films*, New York: John Wiley & Sons, 1994.

5. Kim, H. S. and H. S. Kwok. "Correlation Between Target-Substrate Distance and Oxygen Pressure in Pulsed Laser Deposition of $YBA_2CU_3O_7$," *Applied Physics Letters*, 61(18): 2234-2236, 2 November 1992.

6. Kwok, H. S., H. S. Kim, D. H. Kim, W. P. Shen, X. W. Sun, and R. F. Xiao. "Correlation Between Plasma Dynamics and Thin Film Properties in Pulsed Laser Deposition," *Applied Surface Science*, 109-110: 595-600, 1997.

7. Geohegan, D. B. "Fast ICCD-Photography of YBCO Laser Ablation Plume Propagation in Vacuum and Ambient Oxygen," *Applied Physics Letters*, 60: 2732-2734, 1992.

8. Brinkley S. R., Jr. and W. E. Gordon. *Engineering Design Handbook - Principles of Explosives Behavior*. AMC Pamphlet AMCP 706-180, U.S. ARMY, 1972.

9. Biggers, R. R., G. Kozlowski, J. G. Jones, D. V. Dempsey, R. Kleismit, I. Maartense, J. D. Busbee, T. L. Peterson, and R. E. Perrin. "Process Control and Pulsed Laser Deposition of Materials," *Integrated Ferroelectrics*, 28(1-4): 201-211, 2000.

10. Biggers, R. R., J. G. Jones, I. Maartense, J. D. Busbee, D. V. Dempsey, D. C. Liptak, D. P. Lubbers, C. V. Varansi, and D. B. Mast. "Emission Spectral-Component Monitoring and Fuzzy-Logic Control of Pulsed-Laser-Deposition Process," *Engineering Applications of Artificial Intelligence*, 11(5): 627-635, October 1998.

11. Biggers, R. R., P. T. Murray, D. B. Mast, I. Maartense, T. L. Peterson, D. V. Dempsey, C. V. Varanasi, S. P. Murray, D. P. Lubbers, S. Laube, B. C. Lovett, E. K. Moser, J. L. Brown, D. C. Liptak, and J. D. Busbee. "Spectral-Component Monitoring and Control of Pulsed Laser Deposition of YBCO Films," *SPIE*, 2999: 371-382, 1997.

12. Biggers, R. R., C. V. Varansi, I. Maartense, D. V. Dempsey, D. B. Mast, D. C. Liptak, J. G. Jones, T. L. Peterson, P. T. Murray, and J. D. Busbee. "Spectral-Component Monitoring of the Plumes Generated During the Deposition of RE(Y,Nd) $Ba_2Cu_3O_{7-x}$ Films by Pulsed Laser Ablation," *In Situ Process Diagnostics and Intelligent Material Processing, Symposium Materials Research Society*, Warrendale, PA, 215-219, 1998.

13. Biggers, R. R., J. G. Jones, N. C. Boss, J. D. Busbee, G. Kozlowski, D. V. Dempsey, R. Kleismit, T. L. Peterson, R. M. Nekkanti, and P. N. Barnes. "Plume Emission Spectra, Plume imaging, and YBCO Raman Backscattering for Improved Real-Time Process Control of PLD YBCO on Nickel Tapes," *Applied Superconductivity Conference*, Virginia Beach, VA, September 2000.

14. Shen W. P. and H. S. Kwok. "Crystalline Phases of II-VI Compound Semiconductors Grown By Pulsed Laser Deposition," *Applied Physics Letters*, 65(17): 2162-2164, 24 October 1994

15. St. Clair, A. K. and St. Clair, T. L., U.S. Patent 4,595,548 to NASA June 17, 1986.

16. St. Clair, A. K. and St. Clair, T. L., U.S. Patent 4,603,061 to NASA July 29, 1986.

17. "Thin Film…Large Payoff," *Spinoff*, no vol.: 98, 1998.

18. *TableCurve 2D*. Version 5.1, IBM, CD-ROM. Computer Software, SYSTAT Software Inc., Richmond CA, 2001.

19. *TableCurve 3D*. Version 4.0, IBM, CD-ROM. Computer Software, SYSTAT Software Inc., Richmond CA, 2001.

20. Voevodin, A. A., J. G. Jones, and J. S. Zabinski. "Structure Control of Pulsed Laser Deposited ZrO_2/Y_2O_3 Films," *Journal of Vacuum Science and Technology A*, 19(4):1320-1324, Jul/Aug 2001.

5 Optical Diagnostics of the Yttria Stabilized Zirconia (YSZ) Plume

5.1 Overview

Chapter 4 showed that the YSZ film stress could be controlled using a combination of ambient pressure, target-to-substrate distance, and laser fluence. In addition, a theory was derived that predicts the relationship among these three pulsed laser deposition (PLD) parameters that produces YSZ films on CP1 polymer substrates with no stress. However, these deposition parameters were derived by varying only one deposition parameter while holding the other deposition parameters as constant as possible. Thus, the plume was controlled using an open-loop control scheme.

This chapter presents the investigation on the applicability of plume emission sensors to the film stress control problem. In addition, previously developed plume dynamics theories are applied to the film stress control problem. Finally, any correlations between the relevant variables from these plume dynamics theories and the resulting YSZ film stress is investigated. Thus, the goals of the research presented in this chapter are 1) to discover and characterize YSZ plume parameters that significantly affect stress and 2) to develop/apply a measurement method so that the relevant YSZ plume parameters can be used as a feedback input to close the loop between deposition parameter and YSZ plume behavior.

The two goals of this chapter were achieved. The time-of-flight (TOF) emission sensor system, as described in Section 3.8, monitored the plume velocity during both diagnostic depositions and during the YSZ growths discussed in Chapter 4. Both the TOF emission sensor system and the fast imaging camera system monitored the spectrally filtered plume emissions (TOF waveforms). Two velocity parameters were extracted from the TOF waveforms: the most probable velocity and the streaming velocity from the shifted center-of-mass Maxwell-Boltzmann (SCMMB) distribution. Although the most probable velocity was faster for the vacuum condition ($<10^{-6}$ Torr) than for the typical YSZ growth pressures (50-250 mTorr), the most probable velocity did not vary significantly among the non-vacuum pressures. Thus any correlations between the most probable velocity and film characteristics were not found. However, the streaming velocity did vary significantly with two of the investigated PLD parameters, namely ambient pressure and target-to-substrate distance. In addition, the diagnostic depositions showed that the streaming velocity was approximately 6250 m/s for the PDF combinations that produced YSZ films on CP1 polymer substrate that exhibited no curvature, as described in Chapter 4. Finally, real-time monitoring of the streaming velocity was incorporated into the PLD system described in Chapter 3. The laser excitation voltage was adjusted so that the streaming velocity tracked the commanded plume velocity. Thus, the real-time monitoring and feedback of the streaming velocity was used to compensate for gradual PLD parameters variations, such as target surface condition.

5.2 Theory

Chapter 4 describes a theory (constant velocity blast wave theory) that relates ambient pressure, target-to-substrate distance, and laser fluence combinations to film stress. The correlation between the PDF combinations and film stress is based upon two assumptions: 1) the PDF combinations produce a plume that propagates according to the "blast wave" model and 2) the plume velocity at the substrate determines the film stress. Other research also utilizes the constant velocity blast wave theory, which implicitly depends upon these two assumptions, to correlate PLD parameters to various film properties [1; 2; 3]. For example, consider $YBa_2Cu_3O_{7-x}$ (YBCO) thin films. Previous research indicates that a correlation exists between the pressure and target-to-substrate distance combinations (PD combinations) and the electrical properties of superconducting $YBa_2Cu_3O_{7-x}$ (YBCO) thin films deposited using PLD [1; 2]. Also, a similar correlation exists between the PD combinations and the crystalline quality of several II-VI compound semiconductors, namely ZnS, ZnSe, CdS, CdSe, and CdTe [3]. In addition, preliminary experimental data supports the assumption that plume velocity at the substrate predominately determines the stress in constant velocity blast wave theory by showing that the plume velocities at the substrate are the same for all PD combinations that produce YBCO films with the desired electrical properties. However, neither the plume velocities nor the methods used to measure these velocities are reported [1].

In other research, the plume velocity at the substrate is investigated using both optical time-of-flight (TOF) spectroscopy and ion TOF spectroscopy [2]. The data from

both types of spectroscopy is modeled by a shifted center-of-mass Maxwell-Boltzmann (SCMMB) distribution, as described in Equation (5-1) [2; 4; 5; 6; 7]:

$$f(v) = A \cdot (v)^3 \cdot \exp\left(-\frac{m \cdot (v-u)^2}{2 \cdot k \cdot T}\right) \quad \text{(unitless)} \qquad (5\text{-}1)$$

where A is *scaling amplitude* (s^3/m^3), m is *atomic mass of plume constituent* (kg), v is velocity (m/s), u is *streaming velocity* (m/s), k is *Boltzmann's constant* (J/K), and T is *effective plume temperature* (K). The optical TOF data (TOF waveform) is fitted to a SCMMB distribution, which determines the plume velocities to be approximately 8000 m/s for the PD combinations that produced YBCO films with the desired electrical properties. The corresponding ion TOF data is also fitted to a SCMMB distribution, which calculates the velocities to be approximately 12,000 m/s [2]. Although both experiments measure the plume velocities at the substrate, neither attempts to investigate the plume velocity as a function of pressure and distance from the target surface (plume dynamics) [1; 2; 3]. The plume velocity must be measured at multiple distances from the target surface under various ambient pressures in order to gain an understanding of the plume dynamics and any correlations between plume dynamics and PLD-grown film properties.

Fast photography has also been used to investigate the plume dynamics for PLD-grown YBCO. Geohegan initially applied fast photography to plume dynamics in 1992. However, Geohegan's investigation did not spectrally filter the optical emissions, and as such, did not separately observe the emissions from each of the plume constituents [8]. Each constituent of the YBCO plume has been shown to propagate at different velocities

as determined by the various deposition parameters [9; 10; 11]. In addition, Geohegan's investigation only monitored emissions that were less than 3.5 cm from the target surface and ignored the plume dynamics beyond this distance [8]. Other studies have extended Geohegan's work. For example, Voevodin et al. recorded the time-integrated YSZ plume spectra in an oxygen ambient environment and attributed the spectral emissions near 470 nm and 780 nm to zirconia and oxygen collisions, respectively [12]. Then, Voevodin et al. limited the optical emissions fast photography investigation to the 470 and 780 nm spectral regions with the use of optical bandpass filters [12]. However, even this study monitored only the spatial region from target surface to approximately 70 mm from the target surface [12]. As described in Sections 5.3 and 5.4, fast photography is not limited to this spatial region and can be used to investigate the plume dynamics at further distances from the target surface.

Three theories describing plume dynamics have been proposed: the constant velocity model [8], the "blast wave model" [1; 2; 8], and the "drag force model" [8]. The constant velocity model predicts that the distance of the plume from the target surface is linearly proportional to time. This model applies to YBCO plumes propagating in a vacuum [8]. The blast wave model, also described as the "shock model," describes a spherical wave that propagates symmetrically outward from the location of a detonation [1; 13]. Even though the plume does not propagate as a spherical wave, the blast wave model is used to describe the YBCO plume dynamics for low ambient pressure conditions using Equation (5-2) [1; 2; 8]:

$$D = \xi_0 \cdot \left(E / P\right)^{0.2} \cdot t^n \quad (\text{mm}) \tag{5-2}$$

where D is *distance from the target surface* (mm), ξ_0 is a *scaling constant* (mm·μs^{-n}·mTorr$^{0.2}$·J$^{-0.2}$), E is *explosion energy* (J), P is *pressure* (mTorr), t is *time* (μs), and n is an *exponential constant.* The blast wave model is the same model used in Chapter 4 to determine the PDF combinations that produce YSZ films on CP1 polymer substrates that do not exhibit any curvature. The "drag force model" assumes that the plume has some initial velocity and experiences a retarding viscous force with a magnitude that is proportional to the velocity. Thus, solving for the distance from the target surface as a function of time yields Equation (5-3) [8]:

$$D(t) = x_{final}\left(1 - \exp\left(-\beta \cdot t\right)\right) \quad \left(\text{mm}\right) \tag{5-3}$$

where D is *distance from the target surface* (mm), t is *time* (μs), x_{final} is *final plume "stopping distance" from target surface* (mm), and β is a *viscous force time constant* (μs^{-1}). Unfortunately, each of these three models describes the plume dynamics only under a limited set of deposition conditions. Figure 5-1 illustrates the applicability of each of the three models. As stated previously, the constant velocity model fits well for plumes propagating in a vacuum. The drag model corresponds to the plume dynamics for a short time after ablation and under low pressures, but deviates as time increases. Again under low pressures, the blast wave model (shock model) does not describe the initial plume dynamics, but does predict the plume dynamics after the plume has propagated a few centimeters.

In addition to fast photography, TOF emission sensor systems, like the one described in Section 3.8, can monitor optical emissions as a function of time at one or more fixed distances from the target surface. In order to investigate the dynamics of a

particular constituent of the plume, spectroscopic analysis identifies the various sources of optical emission within the YSZ plume when ablating in an oxygen ambient

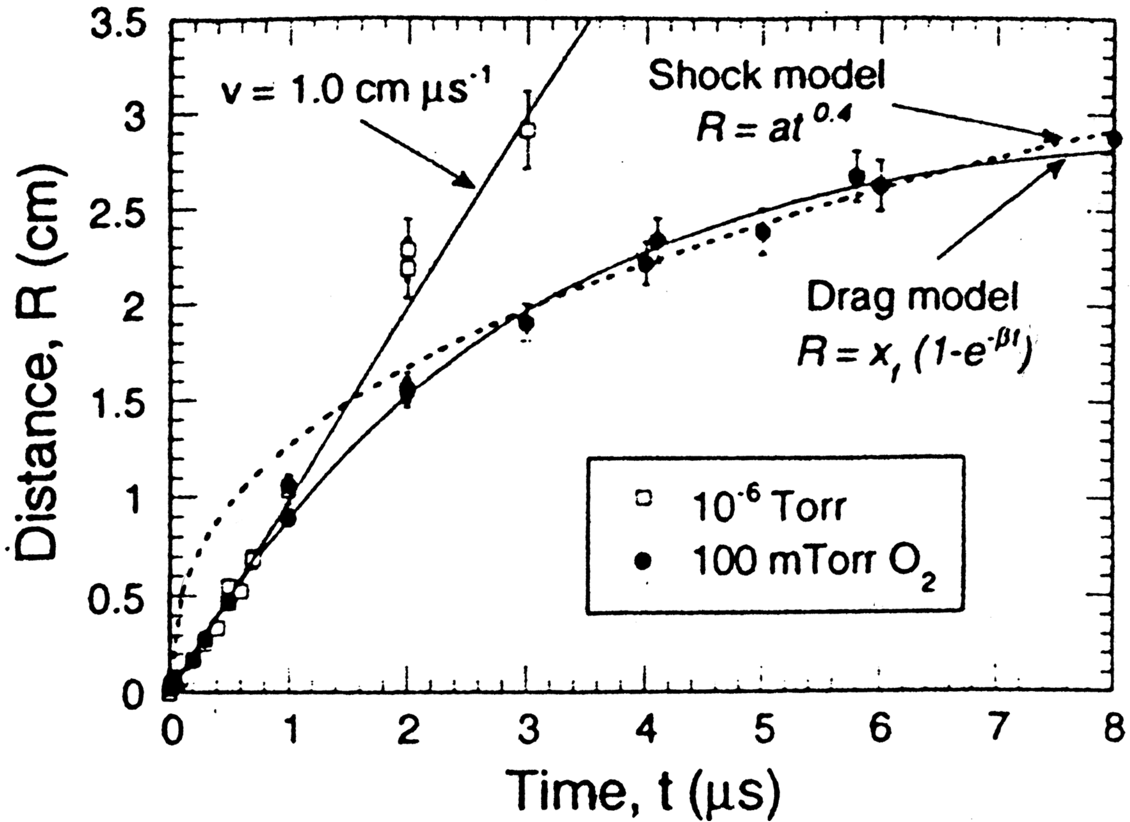

Figure 5-1. Results from an YBCO Plume Dynamics Investigation using Fast Photography [8]

environment [12]. Monitoring the YSZ emissions near either 470 nm or 480 nm is recommended in order to exploit both the strengths of these emissions and the spectral separations from other emissions [12]. Figure 5-2 compares the optical transmission characteristics of the two optical bandpass filter to the recorded YSZ spectra (one for the TOF emission sensor system described in Section 3.8 and one for the fast imaging camera system described in Section 3.9). Within the spectral region of 460 to 490 nm, only the five spectral emission peaks labeled "(A)" through "(E)" in are significant.

Furthermore, both optical bandpass filters limit the significant spectral emissions to peaks "(B)" though "(D)." Figure 5-3 illustrates a portion of the atomic energy level diagram for excited zirconium (Zr*). Transitions (B), (C), and (D) in Figure 5-3 correspond to the emission peaks labeled (B), (C), and (D) in Figure 5-2. Payling and Larkins [14] list many other optical emissions in the 460 to 490 nm spectral region. However, for the 465 nm to 475 nm spectral region transmitted by the optical bandpass filters, intensity of the emissions corresponding to Transitions (B), (C), and (D) are at least an order of magnitude greater all other Zr* emissions. The spectra emission peaks labeled "(A)" and "(E)" in Figure 5-2 have been attributed to excited zirconium oxide (ZrO*) transitions

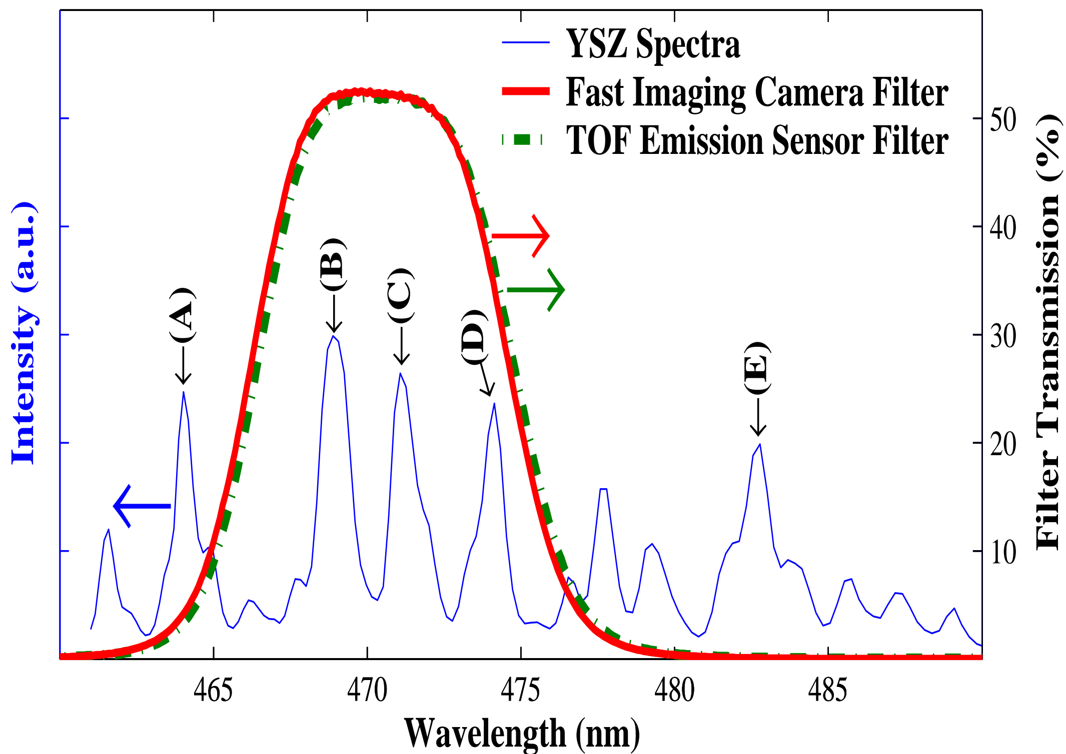

Figure 5-2. Percent Transmission of Optical Bandpass Filters Compared to the YSZ Spectra Acquired During Pulsed Laser Ablation in a 150 mTorr Oxygen Ambient Environment using a 1.57 J/cm^2 Laser Fluence. Spectral Emission Peaks are Labeled (A) through (E) for Reference

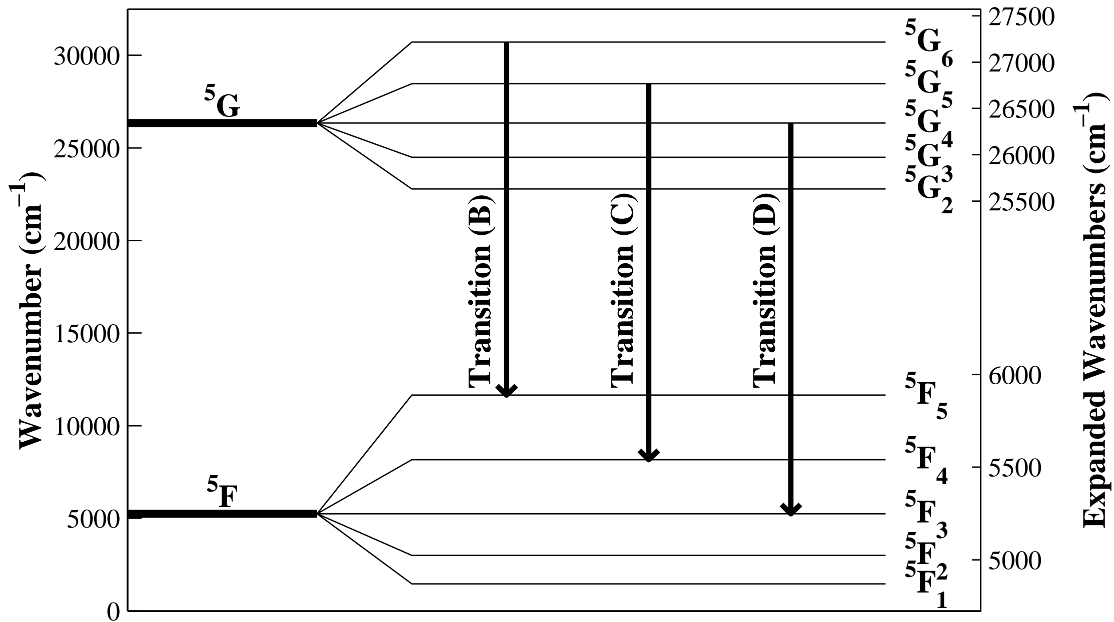

Figure 5-3. Zr* ^{5}G and ^{5}F Atomic Energy Level Diagram [14]

from the α, $C^3\Delta$ to the $X'^3\Delta$ atomic energy levels [12; 15]. Table 5-1 lists all relevant optical emissions near the 470-480 nm spectral region and the corresponding source of the emissions for the YSZ plume in an oxygen ambient. As shown in Figure 5-2, commercially available 10-nm bandpass filters, centered at either 470 nm or 480 nm, sufficiently isolate the respective Zr* or ZrO* optical emissions from other optical emissions [12] over the entire collection range of the detector; a Hamamatsu R7400U-04

Table 5-1. Spectra Content of Plume Emissions from YSZ Ablation in an Oxygen Ambient Near 470 nm [12; 14; 15]

Specie	Transition/Peak	Reference Wavelength (nm)	Experimental Wavelength (nm)
ZrO*	(A)	464.1	464.0
Zr*	(B)	468.8	468.9
Zr*	(C)	471.0	471.2
Zr*	(D)	473.9	474.0
ZrO*	(E)	482.8	482.8

photomultiplier tube (PMT) [16] as described in Section 3.8. Figure 5-4 shows an example of optical emissions that are spectrally limited to 470±5 nm by a 470-nm centered bandpass filter and collected from a spatial cross-section of the plume through Slot 1, which is located 64.7 mm from the target surface. The TOF waveform shown in Figure 5-4 contains a distinct emission feature, labeled "fireball", that occurs approximately when the laser pulse impacts the target surface. Very intense Bremsstrahlung emissions produce a sharp, almost instantaneous, response from the TOF emission sensor system [7]. Since the Bremsstrahlung emissions are spread in a continuum throughout the visible spectrum [7], it is not possible to spectrally filter out the fireball signal. Fortunately, the intensities due to the fireball emissions decay quickly relative to the entire signal lifetime [7], and the intensities (labeled "main plume" in Figure 5-4) generated by optical emissions after the 2 μs time mark can be attributed almost exclusively to plume collisions.

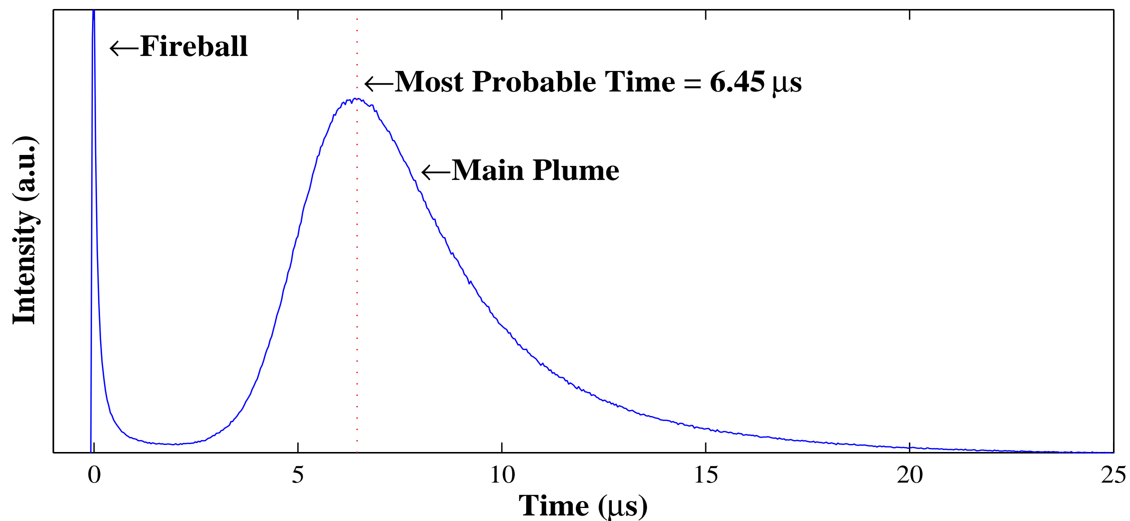

Figure 5-4. Slot 1 (64.7 mm From the Target Surface) Time-of-Flight 470±5 nm Emissions from YSZ Plume Ablated in 75 mTorr Oxygen using 1.57 J/cm^2 Laser Pulses

Analysis of the plume dynamics using the TOF emission sensor system requires extracting either the time after ablation that the plume reaches a fixed distance or the plume velocity in a given spatial region. Thus, the TOF sensor system inputs the intensity as a function of time data (TOF waveform) to one of two algorithms to extract velocity estimates. A common and simple algorithm extracts the most probable time, which is defined as the time of maximum intensity after the fireball [9; 10; 11; 17], as shown in Figure 5-4. The most probable velocity is simply determined by dividing the mean distance of the slot from the target surface by the most probable time, as shown in Equation (5-4). Another known algorithm fits the TOF waveform, excluding the intensities due to the fireball, to an SCMMB distribution [2; 4; 5; 6; 7], as described in Equation (5-1). Again, defining velocity as the mean distance of the slot from the target surface divided by time, as shown in Equation (5-4), transforms Equation (5-1) from a function of velocity into a function of time as shown in Equation (5-5):

$$v = \frac{d_i}{t} \quad (\text{m/s}) \tag{5-4}$$

$$f(t) = A \cdot \left(\frac{d_i}{t}\right)^3 \cdot \exp\left(\frac{-m \cdot \left(\frac{d_i}{t} - u\right)^2}{2 \cdot k \cdot T}\right) \quad (\text{unitless}) \tag{5-5}$$

where t is *time after laser pulse* (s), A is *scaling amplitude* (s^3/m^3), m is *atomic mass* (kg), k is *Boltzmann's constant* (J/K), T is *effective plume temperature* (Kelvin), d_i is *mean distance from target surface to slot i* (m), and u is *streaming velocity* (m/s). Figure 5-5 shows an example of the emission intensity as a function of time. This waveform is fit to

Equation (5-5) using a least square error method. The associated residuals are also shown in Figure 5-5.

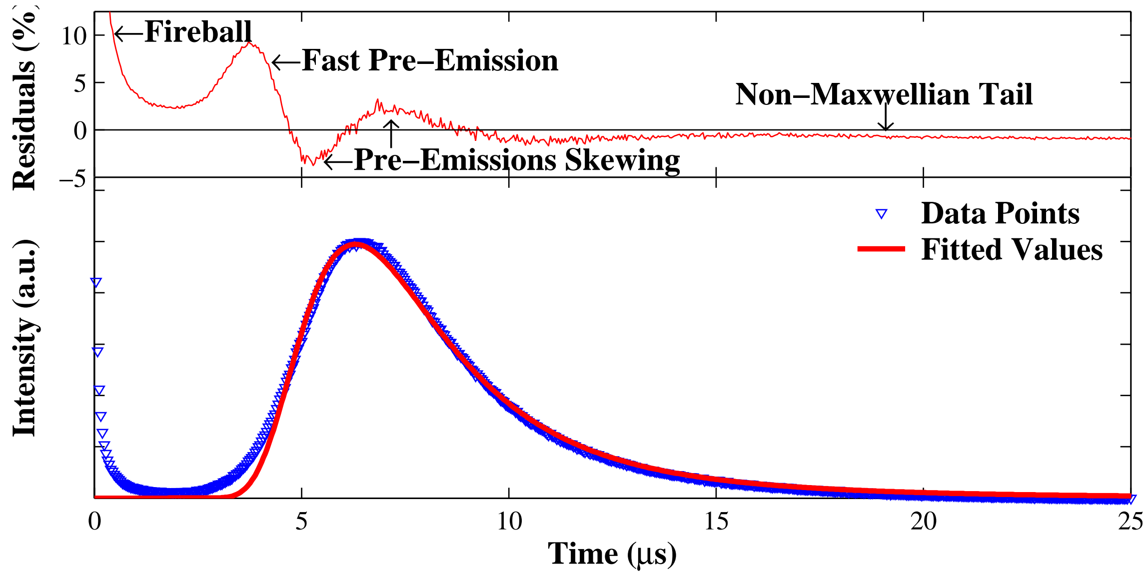

Figure 5-5. Slot 1 (64.7 mm From the Target Surface) Time-of-Flight 470±5 nm Emissions from an YSZ Plume Ablated in 75 mTorr Oxygen using 1.57 J/cm^2 Laser Pulses Fitted to a Shifted Center-of-Mass Maxwell-Boltzmann Velocity Distribution

An examination of Figure 5-5 reveals three regions in which the SCMMB distribution deviates from the TOF data. The first region is due to the fireball emissions, as described previously. The large residuals that exist previous to the 2 μs time mark can be attributed to the fireball, which is present in the TOF data but is not included in the SCMMB model, as defined in Equation (5-5). The fireball shape at a given slot distance from the target surface does not change with deposition parameters, such as laser fluence and ambient pressure. As such, the fireball intensities vary only in amplitude for a given slot. The second region of deviations, labeled "fast pre-emission," spans from times 2.5 to 4.75 μs in Figure 5-5. The theoretical velocity distribution rises rapidly from zero

starting at approximately 3 μs. However, the TOF waveform has a more gradual rise from a non-zero intensity. The source of this deviation is not known, but has been reported in other research [18]. The fast pre-emissions cause the least square error fitting algorithm to skew the theoretical velocity distribution to sooner times, which results in a slightly faster streaming velocity. The actual time of the fast pre-emission and the resulting skewing vary with the deposition parameters. The final region of deviation is the long-lived "non-Maxwellian tail" that occurs after 12 μs in Figure 5-5, as evidenced by the non-zero residuals. Again, the actual time of the non-Maxwellian tail varies with the deposition parameters. To remove the residuals caused by the fireball, previous research has added the sum of two single-sided exponential distributions to the SCMMB distribution. However, modeling of the fireball does not eliminate the pre-emission skewing or the non-Maxwellian tail [18]. Since the fireball most significantly affects the TOF waveform during or before the fast pre-emissions, sectioning the data to exclude early times, such as all times before 4.75 μs, can reduce both the effects. This sectioning has little effect on the SCMMB distribution since these early times correspond to velocities much greater than the expected velocities of the plume. Likewise, the non-Maxwellian tail can be sectioned out of the fitted data as well. Sectioning the data in this manner does not significantly change the fitted values of either the streaming velocity u or the effective temperature T. However, the 95% confidence intervals for these fitted parameters are reduced, and the goodness-of-fit measures are improved.

Three goodness-of-fit measures are used to measure the correctness of the least square error fit: r^2 coefficient of determination, fit standard error, and F-statistic [19]. Equations (5-6) through (5-8) define three statistics used to calculate these goodness-of-

fit measures: the sum of squares due to error (SSE), the sum of squares about the mean (SSM), and the degree of freedom (DOF) [19]:

$$SSE = \sum_{i=1}^{n} w_i (y_i - \hat{y}_i)^2 \tag{5-6}$$

$$SSM = \sum_{i=1}^{n} w_i (y_i - \bar{y}_i)^2 \tag{5-7}$$

$$DOF = n - m \tag{5-8}$$

where *i* denotes i^{th} *data point*, *w* is *weighting coefficient*, *y* is *data value*, $\bar{y}$ is *mean data value*, $\hat{y}$ is *predicted data value*, *n* is *number of data points*, and *m* is *number of coefficients to fit*. All sectioned data points are equally weighted with a weighting coefficient of one. The r^2 coefficient of determination is defined as shown in Equation (5-9) [19]:

$$r^2 = 1 - \frac{SSE}{SSM} \tag{5-9}$$

where *SSE* and *SSM* are as previously defined. The r^2 coefficient of determination relates the explained variation to the total variation. As the fit improves, r^2 approaches unity, while an r^2 equal to zero denotes a complete lack of fit. The second goodness-of-fit measure is fit standard error, as defined in Equation (5-10) [19]:

$$\text{Fit Standard Error} = \sqrt{\frac{SSE}{DOF}} \tag{5-10}$$

where *SSE* and *DOF* are as previously defined. The fit standard error approaches zero as the fit improves. The final goodness-of-fit measure is the F-statistic, which is defined in Equation (5-11) [19]:

$$F - statistic = \frac{\frac{SSM - SSE}{m-1}}{\frac{SSE}{DOF}} \qquad (5\text{-}11)$$

where *SSE*, *SSM*, *DOF*, and *m* are as previously defined. The F-statistic approaches infinity when the fitted data approaches the measured data. Since neither the fireball nor the pre-emissions shown in Figure 5-5 are accounted for in Equation (5-4), the measured data contained in Figure 5-5 is sectioned to remove all data before time 4.5 **μs** and after time 12 **μs**. Since the pre-emissions and non-Maxwellian tail times vary with the deposition parameters, the actual beginning and end times of the data sectioning vary. Thus, the start and stop times for the data sectioning are chosen to maintain at least the upper seventy percent of the main plume's intensity. Sectioning the data in this manner reduces the pre-emissions skewing of the velocity, eliminates the need to model the fireball, and produces fitting parameters with smaller confidence intervals. Table 5-2 lists some of the relevant fitting statistics for the data fit shown in Figure 5-5. The 95% confidence intervals for both the streaming velocity *u* and the effective temperature *T* are reasonably close to the fitted value, which indicate a good fit. As described previously for the desired goodness-of-fit measures, the r^2 coefficient of determination is near unity, the fit standard error is near zero, and the F-statistic is large. Thus, all three goodness-of-fit measures indicate a close fit. In addition, a graphical interpretation of Figure 5-5 reveals a close fit in the non-sectioned range.

Table 5-2. Time-of-Flight Emissions from YSZ Plume Shifted Center-of-Mass Maxwell-Boltzmann Velocity Distribution Fitting Statistics

Parameter	Lower 95% Confidence Interval	Fitted Value	Upper 95% Confidence Interval
Streaming Velocity (m/s)	7171	7228	7285
Plume Temperature (K)	110900	113000	115200
r^2 Coefficient of Determination	NA	0.99451	NA
Fit Standard Error	NA	8.8976×10^{-3}	NA
F-statistic	NA	13403	NA

5.3 Experiment

Two sets of experiments were performed to investigate the plume dynamics and any relationships between the observed plume dynamics and film properties. The first set of experiments ablated an YSZ target using 1.57 mJ/cm^2 fluence laser pulses at 40 Hz in an oxygen ambient environment and monitored the 465 nm to 475 nm optical emissions, which corresponded to collision of Zr* within the plume. There was no substrate holder inserted into the chamber so that the plume would propagate unimpeded from the target surface to the top of the deposition chamber. The TOF emission sensor system, as described in Section 3.8, monitored the optical emission at 11 discrete distance ranges from the target surface, as defined in Table 3-2, while the oxygen pressure was varied from high vacuum (less than 1 μTorr) to 200 mTorr in 25 mTorr steps. The TOF waveforms were analyzed to determine if the plume dynamics behave as predicted by the "blast wave model" described previously in this chapter and Chapter 4. In addition to the TOF emission sensor system, a fast imaging camera system, as described in Section 3.9, also acquired time resolved images of the 465 nm to 475 nm optical emissions of the plume. Both the fast imaging camera system data and the TOF emission sensor system

acquisitions were taken simultaneously so that the both sensor systems were monitoring the same plume. Data sets from the fast imaging camera system were analyzed and compared to the TOF waveforms from the TOF emission sensor system.

The controlled stress investigation described in Chapter 4 was also monitored using the TOF emission sensor system through the slot closest to the target (Slot 1), which was located 64.7 mm above the target surface. The TOF waveforms were recorded at the mid-point of the YSZ depositions, except for depositions in which the target-to-substrate distance was less than or equal to 64.7 mm. For the YSZ growth using these close target-to-substrate distances, the substrates were retracted and the substrate shutter was engaged after the YSZ film was deposited. The TOF waveform was then recorded. Thus, the TOF waveforms were recorded immediately subsequent to the actual film depositions but before the substrates were removed from the chamber. This "after deposition acquisition" was necessary since the substrate optically shielded the closest TOF sensor slot for all target-to-substrate distances less than approximately 65 mm, as described in Section 3.8. For target-to-substrate distances within approximately 2 mm of the Slot 1 height, fluorescing of the plume near the substrate interfered with the optical measurements. Finally, the TOF waveforms were analyzed to determine if any correlation between the plume dynamics and film stress existed.

5.4 Data and Analysis

The first set of experiments investigated the optical TOF emissions in terms of distance from the target surface and oxygen pressure, for a fixed laser fluence of 1.57 J/cm^2. The most probable time increases as the target-surface-to-monitored-slot distance is increased, as expected. Thus, for a constant pressure and laser fluence, the acquired

waveforms shift to the right with an increase in monitored distance from the target surface, as shown in Figure 5-6. Since the actual magnitude of the TOF waveform is irrelevant to either the most probable velocity or the SCMMB velocity extract algorithms, the TOF waveforms shown in Figure 5-6 have been normalized to emphasize the shape of the waveforms and to allow for easier visual comparison between waveforms. In addition to shifting to longer times with an increase in distance from the target surface, the TOF waveforms' full-width-at-half-maximum values also increase as the distance is increased, as expected. The pre-emission regions appear to be increasing with distance the target surface, while the fireball emissions do not. As such, the apparent amplitude increase in the pre-emission region is caused by the normalization, not by a change in the shape of the waveform.

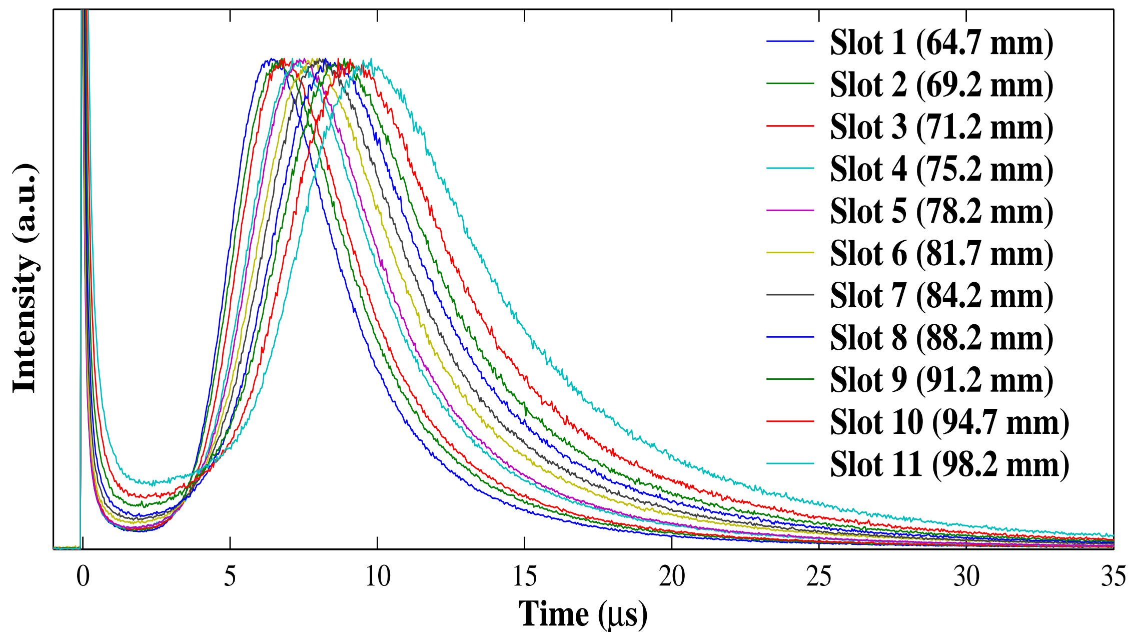

Figure 5-6. Example Normalized TOF Waveforms of YSZ Emissions near 470 nm When Ablating using 1.57 J/cm^2 Laser Pulses in a 75 mTorr Oxygen Ambient Environment

Although the TOF waveforms exemplified in Figure 5-6 behave as expected, the TOF waveforms deviate from the theoretical SCMMB plus fireball distribution model as the distance from the target surface and/or oxygen pressure increase. The deviations are most apparent at Slot 11, which is located at the maximum distance from the target surface (monitoring further distances would require extensive modifications to the deposition chamber). When ablating YSZ with an oxygen pressure of 75 mTorr or less, the TOF emissions at Slot 11 produce the expected waveform. However, another peak appears at approximately 3 μs between the main plume and the fireball when the pressure is increased above 75 mTorr, as shown by the peak labeled "secondary peak" in Figure 5-7.

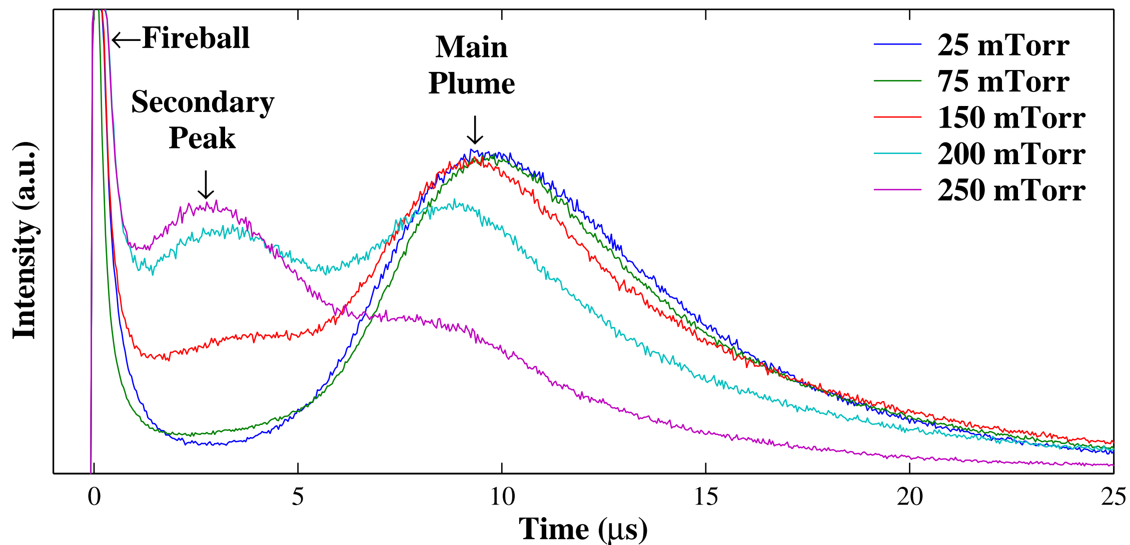

Figure 5-7. Slot 11 (98.2 mm From the Target Surface) 470±5 nm Time-of-Flight Emissions from YSZ Plume Ablated in Oxygen using 1.57 J/cm^2 Laser Pulses

Since the bimodal velocity distribution shown in Figure 5-7 does not match the expected velocity distribution and since the TOF emission sensor system is a custom-

manufactured apparatus, another sensor system is needed to verify the integrity of the TOF emission sensor system. YSZ films are grown at room temperature on the CP1 polymer substrates. Therefore, the inner chamber's heater shield is not necessary and is removed to allow the fast imaging camera system to monitor the optical emissions through a viewport on the front of the chamber, as described in Section 3.9. Figure 5-8 shows several "snapshots" of an YSZ plume as it propagates from the target to the substrate. The opening in the heater chamber limits these images to a region 47.8 mm (bottom of image) to 123.5 mm (top of image) from the target surface. A square two-inch optical bandpass filter limits the optical emissions to 470±5 nm, as shown in Figure 5-2. Each image depicted in Figure 5-8 is normalized to emphasize the contrast between the optical emissions from the plume and the background. To minimize the motion distortion caused by the moving plume, the fast imaging camera system captures the image with a gating time of 100 ns. The starting time of each frame is varied from 200 ns to 20 μs in 200 ns increments, which results in 100 frames. Each frame captures the ICCD-integrated intensities of 20 plumes. The multiple-plume integration is required to compensate for the low signal to noise ratio, which is a result of both the weak optical emission and the short gating time.

As the plume propagates toward the substrate, the plume shifts horizontally from the right side of the image, as shown at time 5 μs, to the middle of the image, as shown at time 20 μs. This shift is not caused by a misalignment of the camera relative to the target surface. The Y-axis of each image is normal to the target surface. Thus, the plume does not propagate normal to the target, but inclines back toward the path of the laser pulse (left side of each image). This effect, denoted as "plume tilt," has been observed in other

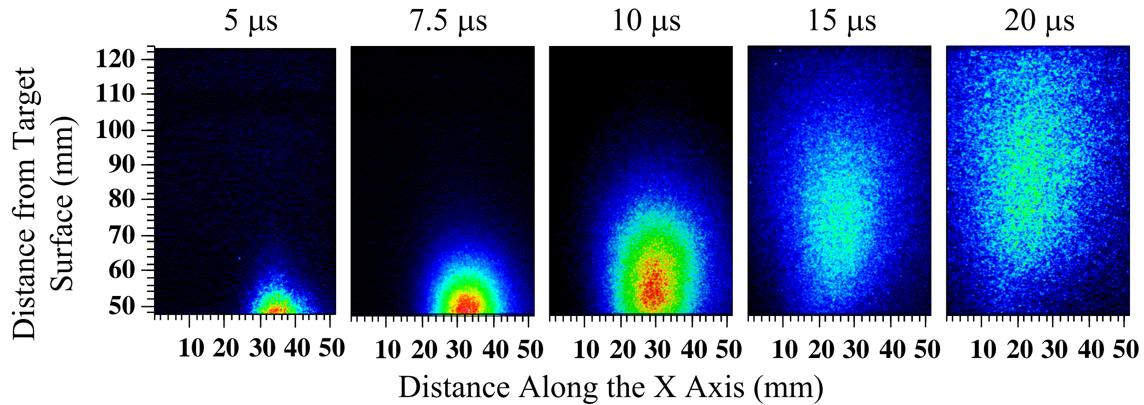

Figure 5-8. Time-Resolved Normalized Images of YSZ Plume in 75 mTorr Oxygen Ablated Using 1.57 J/cm^2 and a 470±5 nm Optical Bandpass Filter

research [7; 20; 21; 22; 23]. The magnitude of the plume tilt is slight and, as such, the distance above the target surface approximates the distance that the plume travels.

In order to use the fast imaging camera system to verify the TOF emission sensor system, the fast imaging camera system data must be processed to produce an output that resembles the TOF waveform. The TOF emission sensor system integrates the spectrally-filtered optical emissions within a spatial cross-sectional area parallel to the target surface. As shown in Figure 5-4 through Figure 5-6, the TOF waveforms report optical intensity as a function of time for a slot at a given distance from the target surface. Thus, each frame of the fast imaging camera system data is sectioned by row to limit the image to a spatial region corresponding to a given TOF slot. The data within this sectioned spatial range is then summed in both the X and the Y direction to produce a scalar value that represents the total intensity within the given spatial range at the frame time. Plotting the integrated scalar values against the corresponding frame times produces an extracted waveform comparable to the output of the TOF emission sensor system. Figure 5-9 compares the waveform from the TOF emission sensor system to the

extracted TOF waveform from the fast imaging camera system. The two waveforms are nearly identical, except for the fireball region that is recorded by the TOF emission sensor system but is excluded from the fast imaging camera system data. The fast imaging camera system records the spectrally-filtered plume intensities starting at 200 ns after the laser pulse. Before recording, the fast imaging camera system is effectively shuttered (ICCD gain set to zero) so that the Bremsstrahlung emissions are not recorded. However, the TOF emission sensor system monitors the plume emissions at all times. Thus, the Bremsstrahlung emissions saturate the TOF emission sensor system's detector (PMT), which is described in Section 3.8. The PMT output decays quickly with time, as discussed previously. For non-bimodal waveforms, the PMT output has decayed sufficiently so that the output due to the Bremsstrahlung emissions is negligible

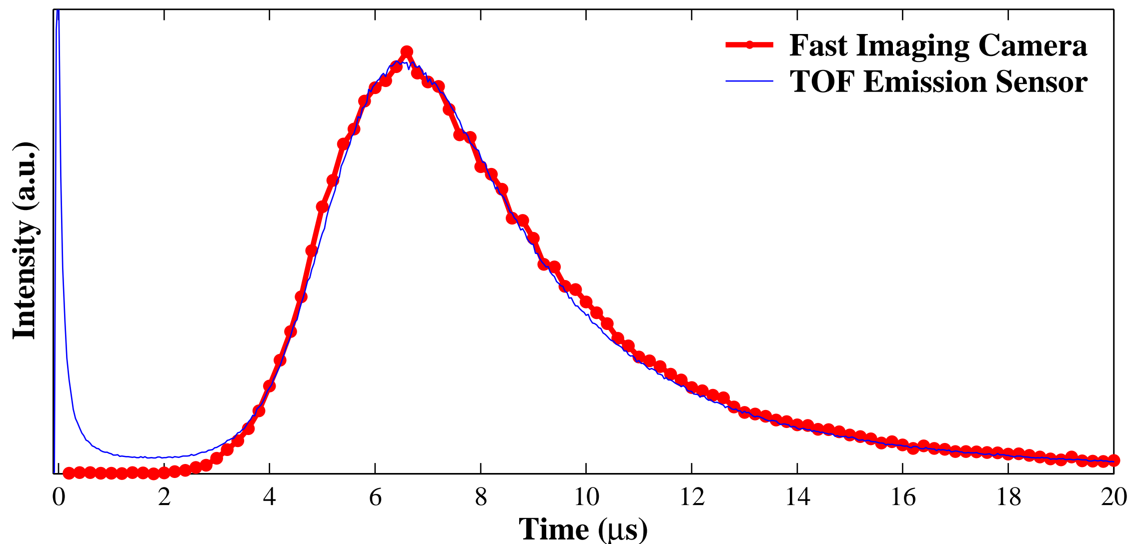

Figure 5-9. Comparison of Time-of-Flight 470±10 nm Emissions from YSZ Plume Ablated in 100 mTorr Oxygen using 1.57 J/cm^2 Laser Pulse at Slot 1 (64.7 mm From the Target Surface) as Monitored Using the TOF Emission Sensor System and as Extracted from the Fast Imaging Camera System Data

compared to the output corresponding to the main plume, as shown in Figure 5-4 though Figure 5-6 and Figure 5-9. However, for the bimodal waveforms, the PMT output due to the Bremsstrahlung emissions has not had sufficient time to decay before the emissions caused by the secondary peak are detected, as shown in Figure 5-7. Figure 5-10 shows a TOF waveform extracted from the fast imaging camera system that corresponds to Slot 11 and the waveform from the TOF emission sensor system at Slot 11. The TOF waveform extracted from the fast imaging camera system and the TOF waveform recorded by the TOF emission sensor system are both bimodal with modes centered at approximately 3 and 9 μs. However, the main plume maximum intensity is approximately three times greater than the secondary peak maximum intensity for the fast imaging camera system extracted waveform, while the corresponding peak intensities are

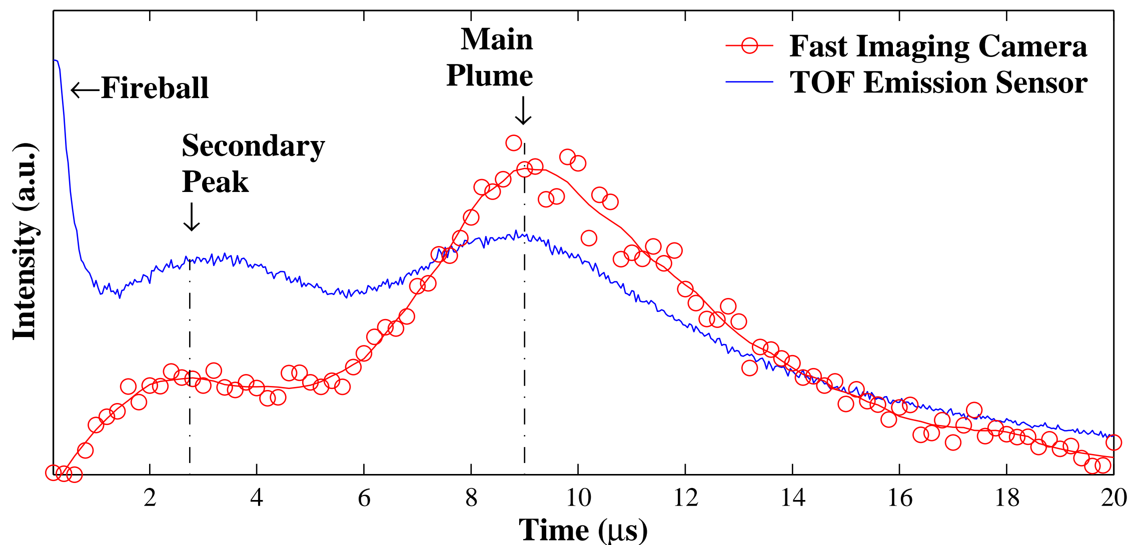

Figure 5-10. Comparison of Time-of-Flight 470±10 nm Emissions from YSZ Plume Ablated in 200 mTorr Oxygen using 1.57 J/cm2 Laser Pulse at Slot 11 (98.2 mm From the Target Surface) as Monitored Using the TOF Emission Sensor System and as Extracted from the Fast Imaging Camera System Data

approximately equal for the TOF emission sensor system waveform. The inclusion of the fireball in the TOF emission sensor system waveform accounts for the majority of the relative intensity deviations between the two waveforms shown in Figure 5-10. Despite the differences in the relative intensities between the two waveforms, the fast imaging system sensor extracted TOF waveform agrees well with the TOF emission sensor system waveform. This correlation validates that the bimodal emission distribution is real and not a product of the TOF emission sensor system. In addition, similar bimodal distributions are reported in other research [7; 24; 25; 26; 27; 28; 29; 30; 31; 32; 33]. The cause of the bimodal distribution is not currently known. Further recommended investigations into the cause of the bimodal emission distributions are discussed in Chapter 8.

Besides validating the TOF emission sensor system, the fast imaging camera system readily allows the spectrally-filter emission intensities versus distance-from-the-target-surface relationship to be analyzed. This is similar to the analysis performed by Geohegan, as shown in Figure 5-1. The geometry of the inner heater chamber limits the fast imaging camera systems data to a spatial region between 47.8 to 123.5 mm from the target surface. Thus, the maximum intensity occurs at the minimum observable distance of 47.8 mm for all times up to approximately 5 μs, since the maximum emission intensities occur below the minimum observable distance. After approximately 5 μs the maximum plume emission intensities are within the viewable spatial region, as shown in Figure 5-11. The linear fit shown in Figure 5-11 is not applicable since the y-intercept of the line is 41 mm, which implies that the plume exists at 41 mm immediately after the laser pulse arrives at the target. The shock model and the drag model fit the data equally

well. Most of the information capable of distinguishing between the shock model and the drag model is contained within the data corresponding to the first 40 mm from the target surface, which is not visible to the fast imaging camera system, as revealed by the drastic waveform shape difference between the shock model and the drag model during the initial 5 μs of Figure 5-11. Therefore, the analysis does not conclusively differentiate between the applicability of shock model and the drag model. Additionally, the drag model implies that the plume emissions never travel beyond a fixed “stopping” distance, denoted “x_{final}” in Equation (5-3). The drag model fit shown in Figure 5-11 has a stopping distance equal to 89.7 mm. Initially, this stopping distance limitation appears to invalidate the model since the plume must travel beyond the fitted stopping distance to reach the substrate. However, the spectrally-filtered plume emission intensity dramatically decreases as the distance from the target surface increases. Thus, the drag model is applicable to the problem since the spectrally-filtered plume emissions are nearly extinguished at the stopping distance and beyond. The shock model also fits the data and has no stopping distance limitation. Therefore, all subsequent analysis will utilize the shock model, which is in agreement with the results reported by Geohegan [8].

Although the fast imaging camera system validates the TOF emission sensor system, the additional processing required to extract either the most probable time or the streaming velocity limits the use of the fast imaging camera system for “real-time” control processing. Since the fast imaging camera system is analogous to multiple (approximately 100) TOF emission sensor systems that simultaneously monitor the plume emissions, the fast imaging camera system requires approximately 18 megabytes of storage per capture, as compared to approximately 20 kilobytes for a single waveform

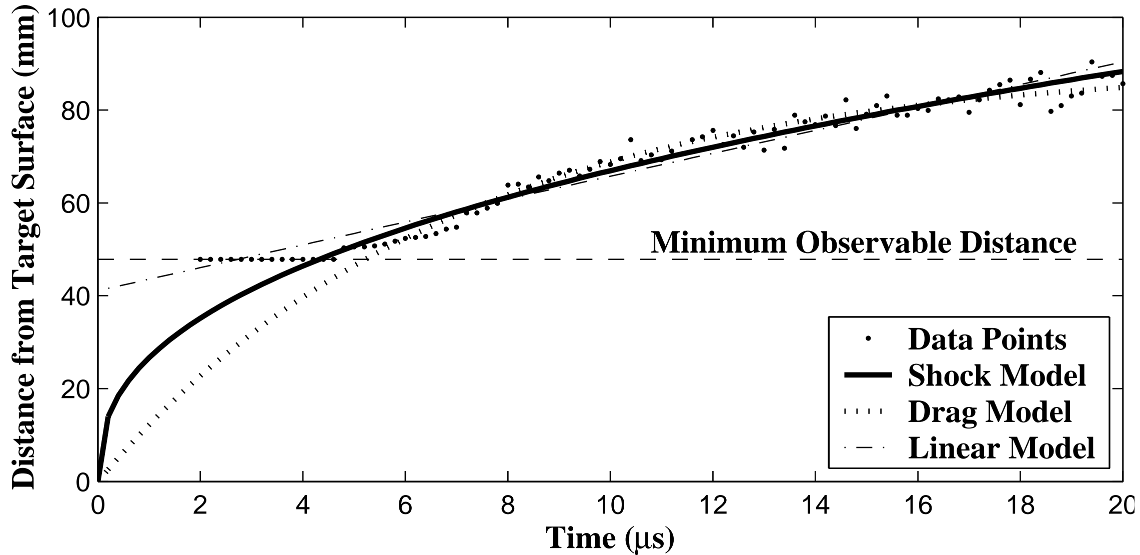

Figure 5-11. Distance from the Target Surface Corresponding to Maximum Emission Intensity as Recorded by the Fast Imaging Camera System Through a 470±10 nm Optical Bandpass Filter When Ablating an YSZ Target in 200 mTorr Oxygen using 1.57 J/cm^2 Laser Pulse

acquired using the TOF emission sensor system. More importantly, the signal to noise ratio (SNR) of the fast imaging camera system, as currently configured, is much less than that of the TOF emission sensor system. The fast imaging camera system's SNR can be improved by increasing the frame integration times (currently 100 ns) and/or integrating more plumes per frame (currently 20). However, the fast imaging camera system's added costs of increased file size, additional post-processing requirements, and decreased SNR outweigh the increased spatial resolution benefit, as compared to the TOF emission sensors system. Therefore, the fast imaging camera system is precluded from further use in this investigation.

Even though the TOF waveforms are bimodal, further investigation of the plume dynamics as reported by the TOF emission sensor system is possible over a large subset of the initial range of distances from the target surface and oxygen pressures since the

bimodal distributions are apparent only at relatively large distances from the target surface and under relatively high pressures. For example, at the slot closest to the target surface (Slot 1 at 64.7 mm from the target surface) the secondary peak is not visible in any of the TOF waveforms for oxygen pressures up to 250 mTorr. In addition, the most probable velocity extract algorithm is relatively insensitive to the secondary peak for most PD combinations. Thus for PD combinations that produce bimodal TOF emission distributions, the secondary peak is ignored when extracting the most probable times/velocities. Figure 5-12 reports the most probable time for several PD combinations. The most probable time appears to be a linear function of distance for all pressures. Also, the most probable time is less for the vacuum condition than all other pressures, as expected. However for each slot, the most probable times for all non-vacuum pressures are approximately the same, which is contrary to the expected result. The most probable times were expected to increase significantly with pressure for each slot. Linear fits for both the vacuum and non-vacuum most probable times are also shown in Figure 5-12.

If the most probable time is linear with distance, then the velocity must be constant. In addition, if the velocity is constant, then the magnitude of the velocity is the slope of the linear fit of distance to the most probable time, as shown in Figure 5-12. The two linear fits corresponding to the vacuum and non-vacuum condition have a time intercept of zero, which signifies that at time zero the plume is at the target. The most probable velocity is calculated as the distance from the target surface divided by the most probable time, as described by Equation (5-4). Figure 5-13 shows that the most probable velocity for each pressure is approximately constant for all distances. In addition, the

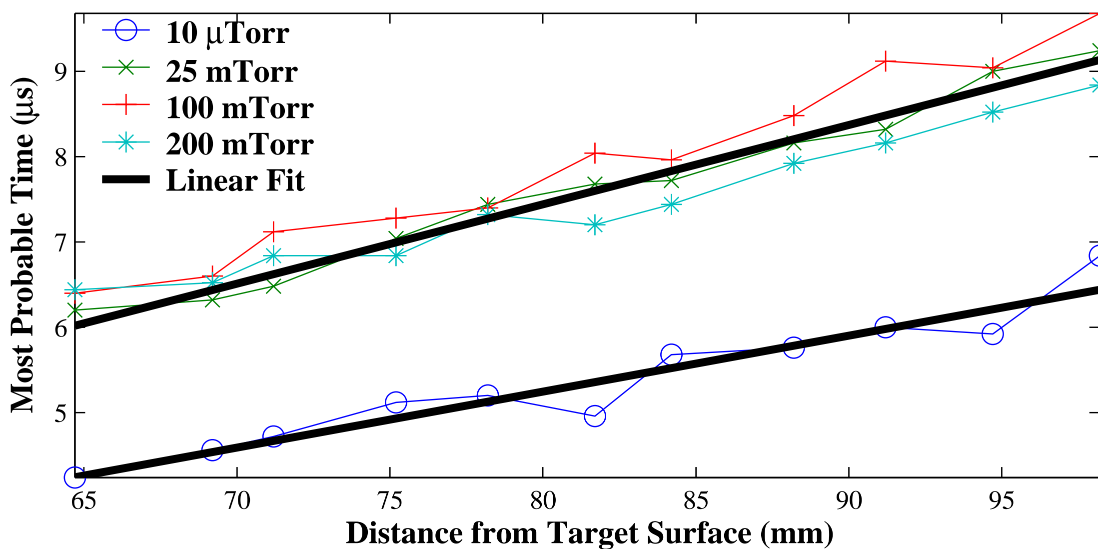

Figure 5-12. Most Probable Time as Monitored via the 470±5 nm Time-of-Flight Emissions from the YSZ Plume Ablated in Oxygen using 1.57 J/cm^2 Laser Pulses

most probable velocity in a vacuum, approximately 15.25 km/s, is greater than the velocity for all other pressures, as expected. However, the non-vacuum most probable velocities appear to be approximately constant for all distance and pressures, at 10.75 km/s. The most probable velocities for the non-vacuum pressure were expected to decrease with distance and to decrease more rapidly with an increase in oxygen pressure. This result, as shown in Figure 5-13, is other than as expected.

Although the investigation of the plume dynamics as reported by the TOF emission sensor system using the most probable velocities produces unexpected results, the investigation was repeated, and the TOF waveforms were fitted to the sum of a SCMMB distribution and a fireball model. The sum of two single-sided exponential distributions was used to model the fireball [18]. The most probable velocity extraction method described previously ignores the secondary peak, when present. However, when the secondary peak is significant as compared to the main plume, the least squares fitting

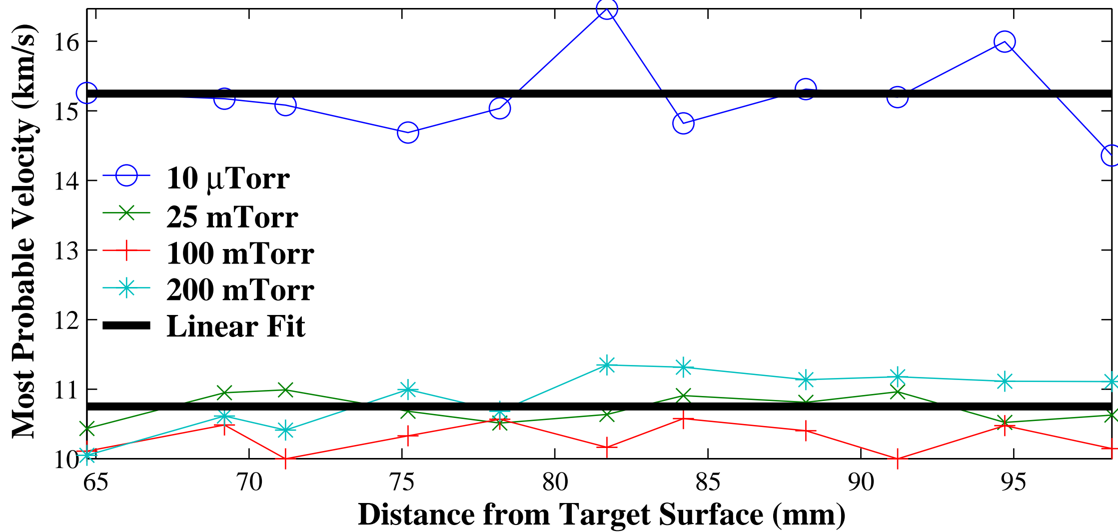

Figure 5-13. Most Probable Velocity as Monitored via the 470±5 nm Time-of-Flight Emissions from the YSZ Plume Ablated in Oxygen using 1.57 J/cm^2 Laser Pulses

algorithm shifts the fitted parameters to faster streaming velocities and higher effective temperatures if the secondary peak is not modeled. In addition, the 95% confidence intervals for both the streaming velocity and the effective temperature significantly broaden, and the goodness-of-fit measures become worse when the secondary peak is ignored. Thus, for TOF waveforms exhibiting a significant secondary peak, a second SCMMB distribution is included in the data fitting. When the second SCMMB distribution is included, the goodness-of-fit measures improve, but the 95% confidence intervals for both SCMMB distributions indicate a relatively large range for each fitting parameter. For example, the streaming velocity u for the SCMMB distribution that models the secondary peak is approximately zero with a 95% confidence interval from –7000 m/s to 7000 m/s, which implies almost no integrity in the fitted value. The 95% confidence interval for the streaming velocity u of the SCMMB distribution that models the main plume is not as broad, but still too broad to be of use. In addition, although the

peaks from both the main plume and the secondary peak are far enough apart in time to distinguish visually, the peaks are not always separable enough to allow the fit to converge. When the secondary peak is significant but of lower amplitude than the main plume, the fitting software [19] most often cannot find a solution. Thus, the TOF waveforms that exhibit a significant secondary peak are excluded from the SCMMB fitting investigation. Further investigation is needed to characterize the plume dynamics, especially those exhibiting bimodal optical emissions, and is discussed in Chapter 8. Figure 5-14 presents the streaming velocity u contour plot, which interpolates between data points to estimate the path of equivalent streaming velocities. The actual data points are marked as "x" for reference. In addition, PD combinations that produce YSZ films on CP1 polymer substrates that exhibit no curvature, as reported in Chapter 4, are marked as "▼."At 50 mTorr and below the streaming velocity u does not significantly vary with distance from the target surface and can be approximated as constant. Above 50 mTorr, the streaming velocity u decreases with distance and/or oxygen pressure. The shapes of the equal-velocity contour lines resemble the velocity predicted by the blast wave model. In addition, the PD combinations for YSZ films on CP1 polymer substrates that exhibit no curvature lie along a constant velocity of approximately 6250 m/s. Thus, for the PD combinations that produce films exhibiting no curvature and that are within the target-surface-to-slot distances that can be monitored, the streaming velocity at the substrate is indicative of the film stress. Further investigation is needed to expand the ranges of distances and pressures for which the velocity at the substrate-stress correlation is valid and is discussed in Chapter 8. Figure 5-15 displays the effective temperature T in terms of distance from the target surface and oxygen pressure. Again, the measured points are

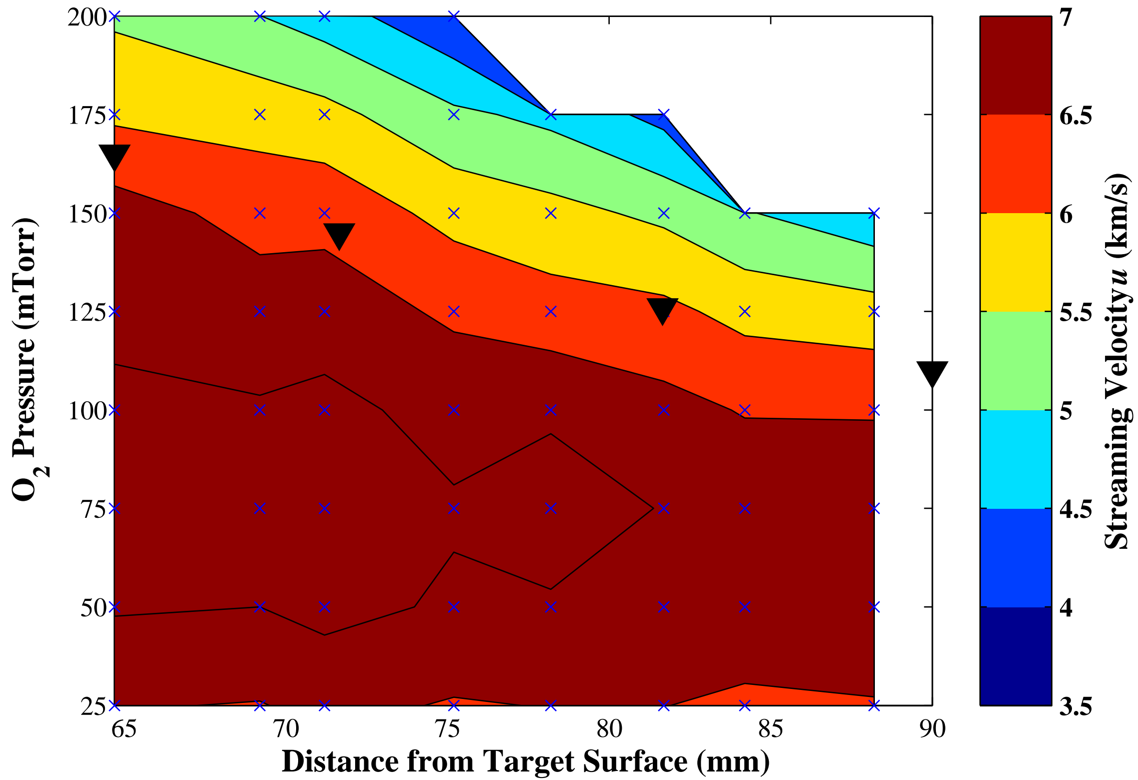

Figure 5-14. Streaming Velocity as Monitored via the 470±10 nm Time-of-Flight Emissions from YSZ Plume Ablated in Oxygen using 1.57 J/cm^2 Laser Pulses

marked as "x" and the PD combinations that produce YSZ films on CP1 polymer substrates that exhibit no curvature are marked as "▼." For each non-vacuum pressure that is monitored, the effective temperature *T* increases with distance from the target surface. For each distance from the target surface that is monitored, the effective temperature *T* initially decreases with an increase in pressure until a local minimum is reached at pressures between 75 and 100 mTorr. At 100 mTorr and above, the effective temperature *T* continually increases with an increase in pressure for each distance monitored. The local minimum is evident when examining Figure 5-15 for each distance and along the Y-axis direction. Although the streaming velocity *u* does correspond well with the constant-velocities theory predicted by the blast wave model, the blast wave

model does not make any predictions about the effective temperature *T*. In addition, there does not appear to be a direct correlation between effective temperature and the no curvature PD combinations.

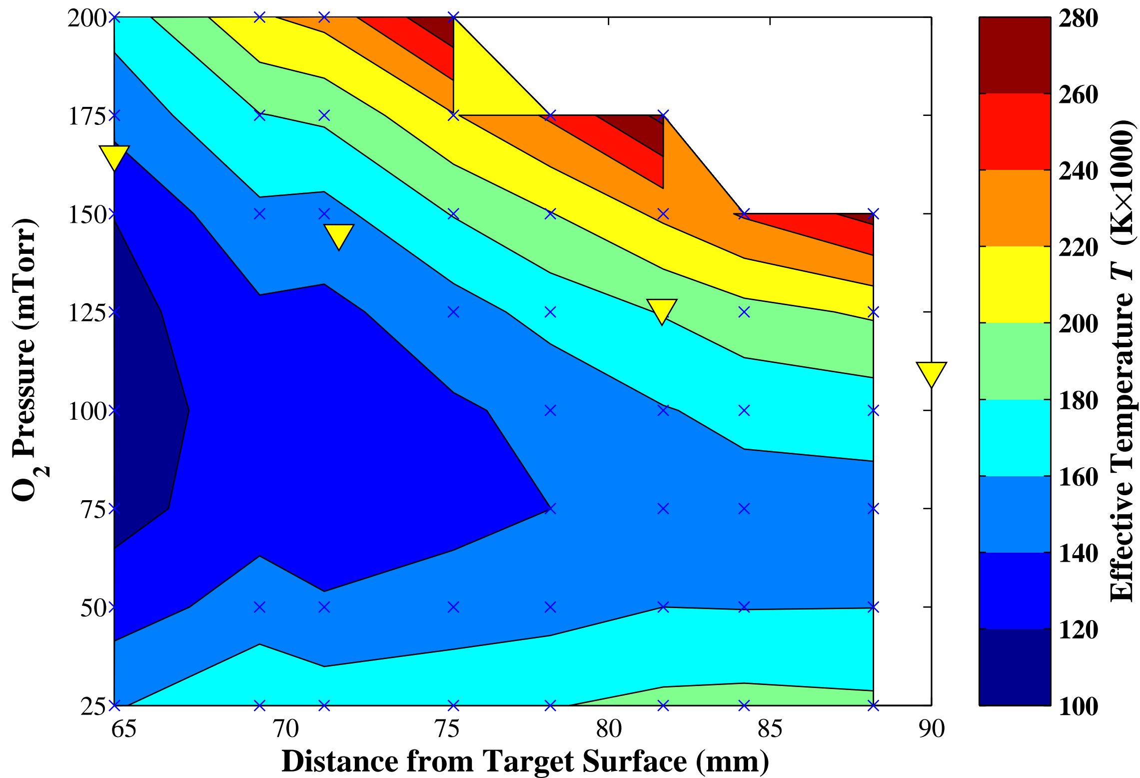

Figure 5-15. Effective Temperature as Monitored via the 470±5 nm Time-of-Flight Emissions from YSZ Plume Ablated in Oxygen using 1.57 J/cm^2 Laser Pulses

The second set of experiments monitored the streaming velocity and the effective temperature at a fixed target-surface-to-monitored-slot distance. The deposition conditions are set to produce YSZ films on CP1 polymer substrates with no curvature. In addition, the plume parameters are monitored during or immediately after the actual depositions that produces the YSZ films described in Chapter 4. Figure 5-16 plots the streaming velocity *u* and effective temperature *T* versus oxygen pressure. The streaming

velocity decreases as the oxygen pressure increases, as expected. In addition, the effective temperatures increase with increased oxygen pressure, as expected. The Zr* constituents within the plume (as defined by the spectrally-filtered emissions) do not all travel at the same velocity. This range of velocities is exemplified by the corresponding range of times during which the plume produces emissions, as shown in Figure 5-5. For the TOF waveform displayed in Figure 5-5, the plume emits significantly during the 3 to 15 μs time range, which corresponds a 4.3 to 21.5 km/s plume velocity range. The streaming velocity expresses an aggregate plume velocity, similar to the mean or median statistics for a distribution. Likewise, the effective temperature describes the velocity range's "spread," similar to a full-width-at-half-maximum (FWHM) value or standard deviation statistic for a distribution. Thus, the decrease in streaming velocity with an

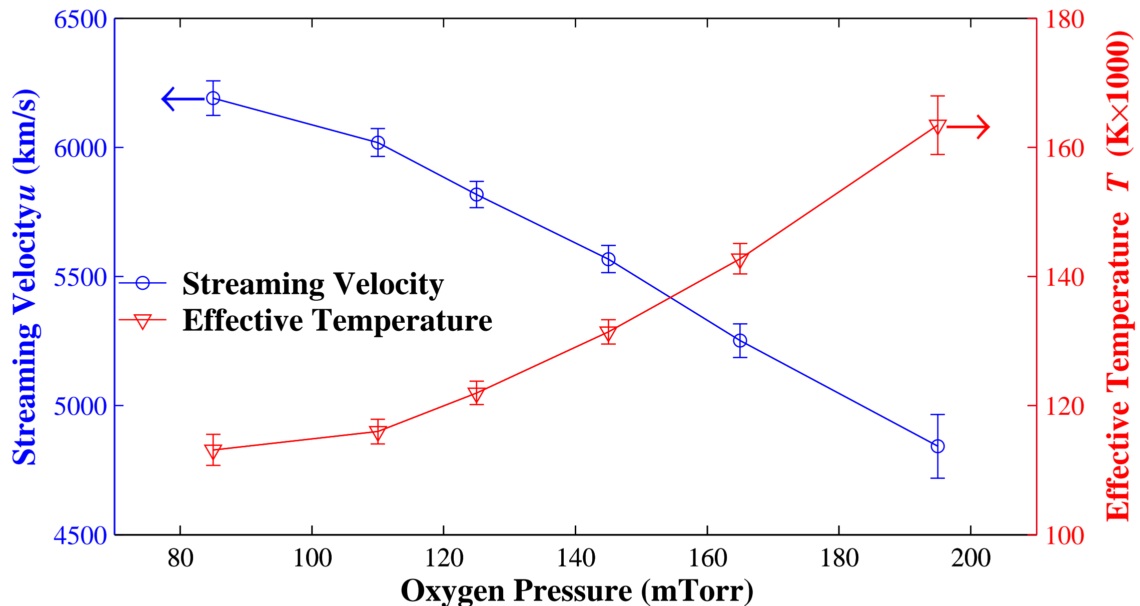

Figure 5-16. Streaming Velocity *u* and Effective Temperature *T* Monitored Through Slot 1 (64.7 mm From the Target Surface) as a Function of Oxygen Pressure

increase in oxygen pressure implies that the Zr* constituents within the plume (as defined by the spectrally-filtered emissions) are subjected to more collisions at the increased oxygen pressures. Therefore, the Zr* plume constituents at the monitored slot are traveling at a reduced velocity due to the additional loss of kinetic energy from the increased number of collisions. The effective temperature increase with oxygen pressure reveals that the additional collisions broaden the range of plume velocities. Visual comparison of the normalized TOF waveforms shown in Figure 5-17 shows very little change in the time corresponding to the peak emission intensity, previously defined as the most probable time. This result is in good agreement with the results from the first set of experiments that found that the most probable time and most probable velocity did not vary with oxygen pressure. However, the FWHM value increases with oxygen pressure, as described by the increase in effective temperature with oxygen pressure. Neither the

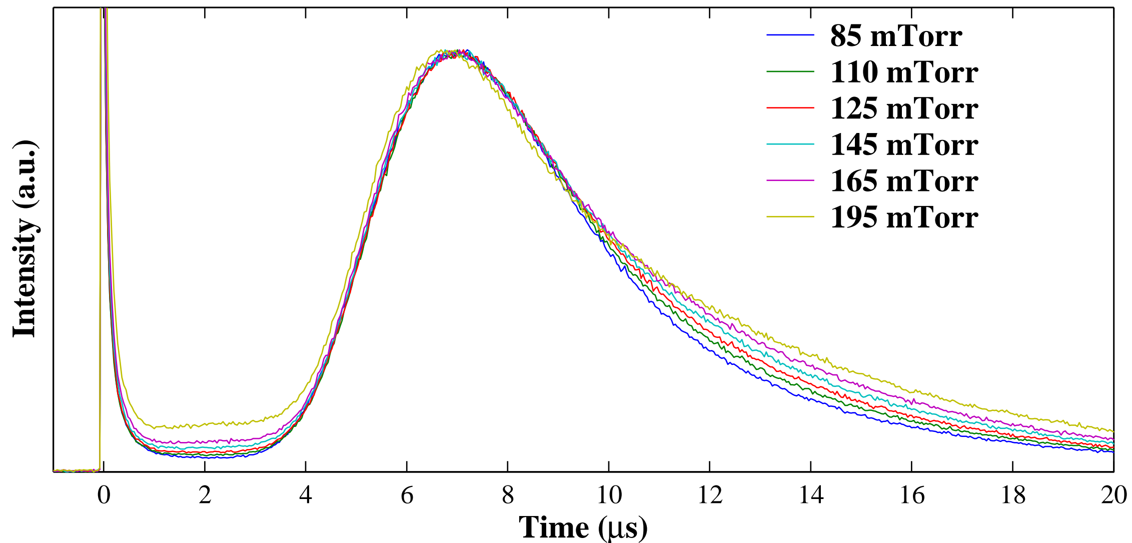

Figure 5-17. Normalized TOF Waveforms of YSZ Emissions near 470 nm When Ablating using 1.57 J/cm^2 Laser Pulses and No Curvature Pressure/Target-to-substrate Distance Combinations

most probable time nor the most probable velocity describes the spread of velocities. Therefore, the streaming velocity and effective temperature combination provide more information about the plume velocity than the most probable velocity parameter. Thus, the streaming velocity and effective temperature combination greatly enhance the ability to reproduce the plume, either to minimize run-to-run variations or to compare plumes among different PLD systems.

For a constant distance and explosion energy (laser fluence), the velocity decreases with an increase in pressure, as predicted by the blast wave model. In addition, the blast wave model describes the relationship between pressure and plume velocity, as shown in Equations (4-3) and (5-12):

$$v(E,P,D) = \xi_0^{1/n} \cdot n \cdot (E/P)^{0.2/n} \cdot D^{(n-1)/n} \quad (\mathrm{km/s}) \tag{5-12}$$

where *D* is *distance* (mm), ξ_0 is a *scaling constant* (mm·μs^{-n}·mTorr$^{0.2}$· J$^{-0.2}$), *E* is *explosion energy* (J), *P* is *pressure* (mTorr), and *n* is an *exponential constant.* For a given laser fluence (which corresponds to a fixed explosion energy E) and fixed distance from

the target surface, the variables *E*, *D*, ξ_0, and *n* can be combined into a constant C′, as shown in Equation (5-13). Substituting Equation (5-13) into Equation (5-12) reduces the plume velocity to a function of pressure only, as shown in Equation (5-14).

$$C' = \xi_0^{1/n} \cdot n \cdot (E)^{0.2/n} \cdot D^{(n-1)/n} \quad (\mathrm{km/s \cdot mTorr^{-0.2/n}}) \tag{5-13}$$

$$v = C' \cdot (P)^{-0.2/n} \quad (\mathrm{km/s}) \tag{5-14}$$

According to Equation (5-14), the velocity should decrease as the pressure increases. Figure 5-16 shows that the velocity does decrease as the pressure increases. However, Equation (5-14) states that the shape of the pressure/velocity curve should be concave up and to the right, while the pressure/velocity curve shown in Figure 5-16 is almost flat and curves concave down and to the left. Thus, the blast wave model is too simplistic to describe the relationship between the plume velocity and ambient pressure for the range of pressures investigated. Although the relationship predicted by the blast wave model may hold true for pressure on a much larger scale, no conclusions can be drawn from pressure range investigated.

Finally, the results from both sets of experiments are compared to determine how blocking the plume propagation with a substrate hold affects the streaming velocity and the effective temperature, as compared to allowing the plume to propagate unimpeded up to the top of the chamber. Figure 5-14 and Figure 5-15 relate the fitting parameters without the substrate holder present to oxygen pressure and distance from the target surface, which includes the Slot 1 (64.7 mm from the target surface) data. Figure 5-16 relates the streaming velocity and effective temperature with the substrate holder inserted to oxygen pressure for the no curvature PD combinations. Although the streaming velocity slows approximately 18% when the substrate holder is present, the shapes of the pressure/streaming velocity curves are nearly identical, as shown in Figure 5-18. The effective temperature also agrees well between the “with” and “without” substrate holder conditions, as shown in Figure 5-19. The first set of experiments, in which the substrate holder was not present, concludes that the streaming velocity at the no curvature PD combinations was constant at approximately 6250 m/s. This conclusion can now be

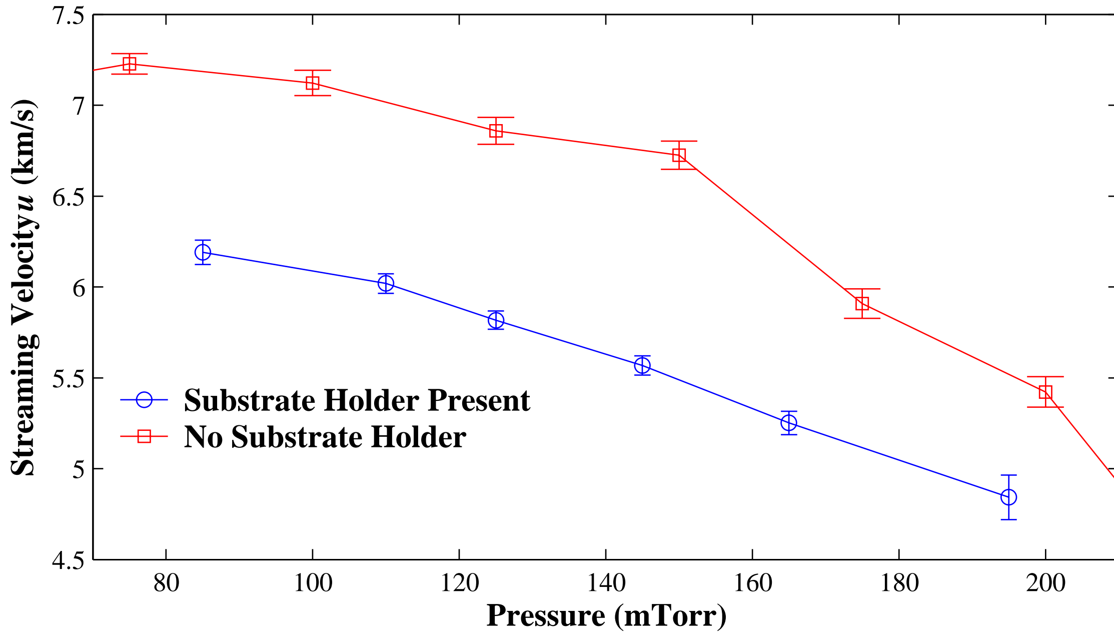

Figure 5-18. Comparison between the Streaming Velocities at Slot 1 (64.7 mm From the Target Surface) Measured During Diagnostic Depositions and During the Growth of YSZ of CP1 Polymer Substrates that Exhibit no Curvature using 1.57 J/cm^2 Laser Pulses

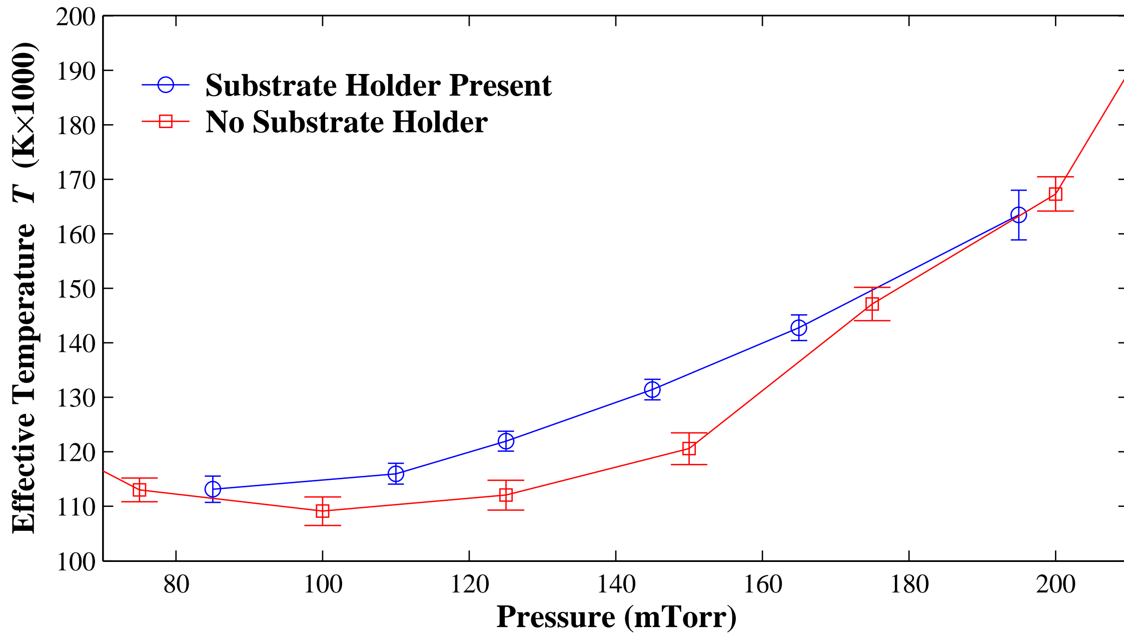

Figure 5-19. Comparison between the Effective Temperature at Slot 1 (64.7 mm From the Target Surface) Measured During Diagnostic Depositions and During the Growth of YSZ of CP1 Polymer Substrates that Exhibit no Curvature using 1.57 J/cm^2 Laser Pulses

extended to include conditions in which the substrate holder is present. However, the streaming velocity of 6250 m/s at the substrate should be approximately 18% less (~5300 m/s).

The purpose of the experiments presented in this chapter is to determine if the streaming velocity and/or effective temperature at a given distance from the target surface are indicative of film stress. As shown in Figure 5-16, both the streaming velocity and the effective temperature at Slot 1 vary with oxygen pressure. A LabVIEW® [34] software routine combined with MatLAB® [35] least square error fitting algorithms provides "real-time" streaming velocities and effective temperatures by fitting the TOF data to Equation (5-5). These fitted parameters are used for closed-loop control of the excitation voltage to produce a constant streaming velocity at Slot 1, which greatly improves the run-to-run repeatability as measured by the substrate curvature. Furthermore, the target topology changes with ablation, which affects the film stress. For the depositions reported here and in Chapter 4, sanding of the target surface between depositions is required to ensure an equivalent laser fluence between runs. Using the streaming velocity to control the excitation voltage of the laser compensates for the changing target topology and greatly increases the interval between sanding, while maintaining the same run-to-run repeatability.

5.5 Conclusion

The optical emissions monitored by the TOF emission sensor system provide insight into the plume dynamics by extracting plume stream velocity and plume effective temperature for the TOF waveform. In addition, the shifted center-of-mass Maxwell-Boltzmann velocity distribution adequately models the TOF signal under most deposition

conditions. However, as the target to substrate distance and oxygen pressure are increased, the TOF signal becomes bimodal, which invalidates the SCMMB distribution's applicability. The cause of the bimodal distribution is still not known. For the TOF signals where the SCMMB distribution applies, the streaming velocity agrees well with the velocity predicted by the blast wave model described previously. The data supports the blast wave model under most conditions and validates the blast wave model for the range of pressures and distances measured. However, further investigations into the plume dynamics are needed for a complete understanding of any correlation between plume dynamics and film properties. These further investigations should not be based upon optical emission, but rather other techniques, such as absorption and ion TOF spectroscopy. Again, the source of the bimodal distribution is not known and should be investigated further, as described in Chapter 8.

In addition to modeling the TOF waveforms using an SCCMB distribution, the most probable velocity was extracted from the TOF waveforms. Unfortunately, the most probable velocity did not significantly vary with oxygen pressure and distance from the target surface. Thus, the most probable velocity was not used as a control input for the PLD system.

Although the most probable velocity does not significantly vary with pressure or distance, the streaming velocity does vary with distance and pressure. The current version of the PLD software now includes a "real-time" streaming velocity and effective temperature extraction capability. The streaming velocity is very sensitive to pressure and distance from the target surface. As such, the streaming velocity can be used to

control laser excitation voltage to compensate for changing target topology. In addition, such control is extremely useful for comparison among dissimilar deposition systems.

Bibliography

1. Kim, H. S. and H. S. Kwok. "Correlation Between Target-Substrate Distance and Oxygen Pressure in Pulsed Laser Deposition of $YBA_2CU_3O_7$," *Applied Physics Letters*, 61(18): 2234-2236, 2 November 1992.

2. Kwok, H. S., H. S. Kim, D. H. Kim, W. P. Shen, X. W. Sun, and R. F. Xiao. "Correlation Between Plasma Dynamics and Thin Film Properties in Pulsed Laser Deposition," *Applied Surface Science*, 109-110: 595-600, 1997.

3. Shen W. P. and H. S. Kwok. "Crystalline Phases of II-VI Compound Semiconductors Grown By Pulsed Laser Deposition," *Applied Physics Letters*, 65(17): 2162-2164, 24 October 1994.

4. Anderson, J. B. and J. B. Fenn, "Velocity Distributions in Molecular Beams from Nozzle Sources," *The Physics of Fluids*, 8(5): 780-787, May 1965.

5. Anderson, J. B., R. P. Andres, and J. B. Fenn. "Supersonic Nozzle Beams," *Advances in Chemical Physics*, 10: 275-315, 1966

6. Zheng, J. P., Z. Q. Huang, D. T. Shaw, and H. S. Kwok. "Generation of High-energy Atomic Beams in Laser-superconducting Target Interaction," *Applied Physics Letters*, 54(3): 280-282, 16 January 1989.

7. Chrisey, D. B. and G. K. Hubler, *Pulsed Laser Deposition of Thin Films*, New York: John Wiley & Sons, 1994.

8. Geohegan, D. B. "Fast ICCD-Photography of YBCO Laser Ablation Plume Propagation in Vacuum and Ambient Oxygen," *Applied Physics Letters*, 60: 2732-2734, 1992.

9. Biggers, R. R., G. Kozlowski, J. G. Jones, D. V. Dempsey, R. Kleismit, I. Maartense, J. D. Busbee, T. L. Peterson, and R. E. Perrin. "Process Control and Pulsed Laser Deposition of Materials," *Integrated Ferroelectrics*, 28(1-4): 201-211, 2000.

10. Biggers, R. R., P. T. Murray, D. B. Mast, I. Maartense, T. L. Peterson, D. V. Dempsey, C. V. Varanasi, S. Murray, D. P. Lubbers, S. Laube, B. Lovett, E. K. Moser, J. L. Brown, D. C. Liptak, and J. D. Busbee. "Spectral-Component Monitoring and Control of Pulsed Laser Deposition of YBCO Films," *SPIE*, 2999: 371-382, 1997.

11. Biggers, R. R., J. G. Jones, N. C. Boss, J. D. Busbee, G. Kozlowski, D. V. Dempsey, R. Kleismit, T. L. Peterson, R. Nekkanti, and P. N. Barnes. “Plume Emission Spectra, Plume imaging, and YBCO Raman Backscattering for Improved Real-Time Process Control of PLD YBCO on Nickel Tapes,” *Applied Superconductivity Conference*, Virginia Beach, VA, September 2000.

12. Voevodin, A. A., J. G. Jones, and J. S. Zabinski. “Characterization of Zro_2/Y_2O_3 Laser Ablation Plasma in Vacuum, Oxygen, and Argon Environments,” *Journal of Applied Physics*, 88(2): 1088-1096, 15 July 2000.

13. Brinkley S. R., Jr. and W. E. Gordon. *Engineering Design Handbook - Principles of Explosives Behavior*. AMC Pamphlet AMCP 706-180, U.S. ARMY, 1972.

14. Payling, R. and P. L. Larkins. *Optical Emission Lines of the Elements*. New York: John Wiley & Sons, 1999.

15. Pearse, R. W. B. and A. G. Gaydon. *The Identification of Mocular Spectra (4th Edition)*. London: Chapman and Hall, 1976.

16. *Hamamatsu Metal Package Photomultiplier Tube R7400U Series*, Bridgewater NJ: Hamamatsu Photonics K.K. Electron Tube Center, April 2000.

17. Biggers, R. R., J. G. Jones, I. Maartense, J. D. Busbee, D. V. Dempsey, D. C. Liptak, D. P. Lubbers, C. V. Varansi, and D. B. Mast. “Emission Spectral-Component Monitoring and Fuzzy-Logic Control of Pulsed-Laser-Deposition Process,” *Engineering Applications of Artificial Intelligence*, 11(5): 627-635, October 1998

18. Perram, G. P. “HTS PLD Plume Dynamics.” Presentation at AFOSR Meeting, University of California, San Diego CA, January 2001.

19. TableCurve 2D. Version 5.1, IBM, CD-ROM. Computer Software, SYSTAT Software Inc., Richmond CA, 2001.

20. Davanloo, F., E. M. Juengerman, D. R. Jander, T. J. Lee, C. B. Collins, and E. Matthias. “Mass Flow in Laser-Plasma Deposition of Carbon under Oblique Angles of Incidence,” *Applied Physics A*, 54(4): 369-372, 1992.

21. Greer, J. A., and H. J. Van Hook. “Uniformity Considerations for “In-Situ” Laser-ablated $Y_1Ba_2Cu_3O_{7-x}$ Films Over Three Inch Substrates,” *Materials Research Society Symposia Proceedings*, 169: 463-468, 1990.

22. Lowndes, D. H., D. P. Norton, J. W. McCamy, R. Feenstra, J. D. Budai, D. K. Christen, and D. B. Poker. “In Situ Growth of High Quality Epitaxial $YBa_2Cu_3O_{7-x}$ Thin Films at Moderate Temperatures by Pulsed Laser Ablation,” *Materials Research Society Symposia Proceedings*, 169: 431-434, 1990.

23. Foote, M. C., B. B. Jones, D. B. Hunt, J. B. Barner, R. P. Vasquez, and L. J. Bajuk. "Composition Variations in Pulsed-laser-deposited Y-Ba-Cu-O Thin Films as a Function of Deposition Parameters," *Physica C*, 201(1-2): 176-182, 1992.

24. Chen, K. R., J. N. Leboeuf, R. F. Wood, D. B. Geohegan, J. M. Donato, C. L. Liu, A. A. Puretzky. "Laser-solid Interaction and Dynamics of Laser-ablated Materials," *Applied Surface Science*, 96-96: 45-49, April 1996.

25. Geohegan, D. B. and A. A. Puretzky. "Dynamics of Laser Ablation Plume Penetration Through Low Pressure Background Gases," *Applied Physics Letters*, 67(2): 197-199, 10 July 1995.

26. -----. "Laser Ablation Plume Thermalization Dynamics in Background Gases: Combined Imaging, Optical Absorption and Emission Spectroscopy, and Ion Probe Measurements," *Applied Surface Science*, 96-98: 131-138, April 1996.

27. -----. "Dynamics of Pulsed Laser Ablation for Thin Film Growth," *Advanced Applications of Lasers in Materials Processing/Broadband Optical Networks/Smart Pixels/Optical MEMS and Their Applications. IEEE/LEO 1996 Summer Topical Meeting*: 13-14, 5 August 1996.

28. Hansen, T. N., J. Schoue, J. G. Lunney. "Ion Time-of-flight Study of Laser Ablation of Silver in Low Pressure Gases," *Applied Surface Science*, 138-139: 184-187, January 1999.

29. Leboeuf, J. N., K. R. Chen, J. M. Donato, D. B. Geohegan, C. L. Lie, A. A. Puretzky, R. F. Wood. "Modeling of Dynamical Processes in Laser Ablation," *Applied Surface Science*, 96-98: 14-23, April 1996.

30. Tam, A. C. "Laser Ablation and Deposition," *Summaries of Papers Presented at the Conference on Laser and Electro-optics CLEO*, 252, 2 June 1996.

31. Park, S, M., and J. Y. Moon. "Laser Ablation of a $Pb(Zr_xTi_{1-x})O_3$ Target in a Pulsed Oxygen Jet," *Applied Surface Science*, 174(2): 87-92, 16 April 2001.

32. Wood, R. F. "Dynamics of Plasma Propagation and Splitting During Pulsed Laser Ablation," *IEEE International Conference on Plasma Science*, 96, 20 June 1999.

33. Wood, R. F., J. N. Leboeuf, K. R. Chen, D. B. Geohegan, A. A. Puretzky. "Dynamics of Plume Propagation, Splitting, and Nanoparticle Formation during Pulse-Laser Ablation," *Applied Surface Science*, 127-129: 151-158, May 1998.

34. *LabVIEW*®. Version 6.0, IBM, CD-ROM. Computer Software. National Instruments, Austin, TX, 2000.

35. *MatLAB*®. Version 6.1, IBM, CD-ROM. Computer Software. The MathWorks, Natick, MA, 2001.

6 Large Area Pulsed Laser Deposition of Yttria Stabilized Zirconia

6.1 Overview

Chapters 4 and 5 describe the ability to control yttria stabilized zirconia (YSZ) film stress using pulsed laser deposition (PLD) and to control the plume streaming velocity using the TOF emission sensor system. These efforts were conducted using small area substrates (two inches in diameter or less). While these efforts are necessary for large-area controlled-stress depositions, the large-area aspect was ignored, until now. Thus, a method to grow uniform-thickness films on large-area substrates (greater than four inches in diameter) remains to be developed. However, the relevant deposition parameters that control stress (laser fluence, target-to-substrate distance, and ambient pressure) should be considered constant. Therefore, the goal of the research presented in this chapter is to develop a method for depositing uniform-thickness YSZ films on six-inch diameter silicon substrates without damage to the CP1 polymer and without varying the deposition parameters that significantly affect the film stress.

6.2 Theory

The plume generated during the PLD process deposits material on the substrate with some spatial distribution of film thickness. The angular distribution of the plume (ADP), which determines the spatial distribution of film thickness, is a topic currently undergoing extensive research. Many models that attempt to describe the film thickness

as a function of the ADP have been proposed. Two methods are commonly used to measure the ADP. The first and most common method, referred to as the "film-based" method, uses a substrate as a flux detector. The film thickness is measured, generally *ex-situ*, to determine the spatial distribution of film thickness, which is proportional the flux distribution under most conditions. The second method, referred to as the "probe-based" method, uses one or more movable probes to resolve the flux at some location and angle from the plume [1].

Many factors, such as plume orientation, target topography, target-to-substrate distance, laser footprint size, laser pulse parameters, and ambient gas effects, can influence the ADP, which determines the spatial distribution of the film thickness (SDFT) [1]. The plume orientation is always normal to the target when the laser pulse is at normal incidence [1; 2; 3; and 4]. Even if the laser pulse is incident at a non-normal angle to the target, the plume is usually oriented normal to the target [1; 5; 6; 7; 8]. However in some deposition systems, an effect in which the plume is angled back toward the direction of the laser pulse, denoted "plume tilting," has been observed [1; 2; 9; 10; 11]. Plume tilting can affect both the location and the shape of the SDFT. Another factor that can affect the ADP is target topography. Since the plume is generally oriented normal to the target, any target surface topography, such as target craters created by previous laser ablation, can alter the plume's orientation [1:207-208, 3]. In addition, the target-to-substrate distance may affect the ADP. Previous research has reported changes in the ADP as a function of target-to-substrate distance when measured using a film-based method [1:208-209; 12; 13]. Also, the laser footprint size can affect the ADP independent of the laser fluence. For example, increasing the laser footprint size and the

laser pulse energy, so that the laser fluence remains constant, has been reported to decrease the broadness of the angular distribution. This effect has been attributed to intraplume collisions. Thus, the SDFT resulting from a deposition using a single large laser footprint is not equivalent to the SDFT resulting from scanning multiple smaller laser footprints over an equivalent area on the target [1; 6]. In addition to the size of the laser footprint, the characteristics of the laser pulse itself, such as laser fluence, wavelength, and pulse length, affect the ADP [1; 5]. Finally, an increase in ambient pressure due to the inclusion of an ambient gas will broaden the ADP, as compared to depositions in a vacuum [1; 6].

Three methods for producing uniform thickness depositions are commonly used to compensate for the SDFT produced by the ADP. The first method, denoted as the "off-axis" method, utilizes a static laser footprint on a rotating target. The center of the target is located at some fixed offset distance "d" from the center of the rotating substrate, as shown in Figure 6-1. The target-to-substrate distance and the plume's angular distribution determine the fixed offset distance "d". The second common method, labeled "rotational/translational" method, combines the "off axis" method with a variable offset distance "d" to scan the plume across the rotating substrate, as shown in Figure 6-1 [1].

The PLD system described in Chapter 3 exemplifies the third common large area PLD method, referred to as the "raster" method. The raster method scans the laser footprint across a rotating target so that the plume is rastered across a rotating substrate [1]. The position of the laser footprint on the target is controlled by a radius and angle scanning scheme. The target is rotated at a constant commanded rotation rate so that the

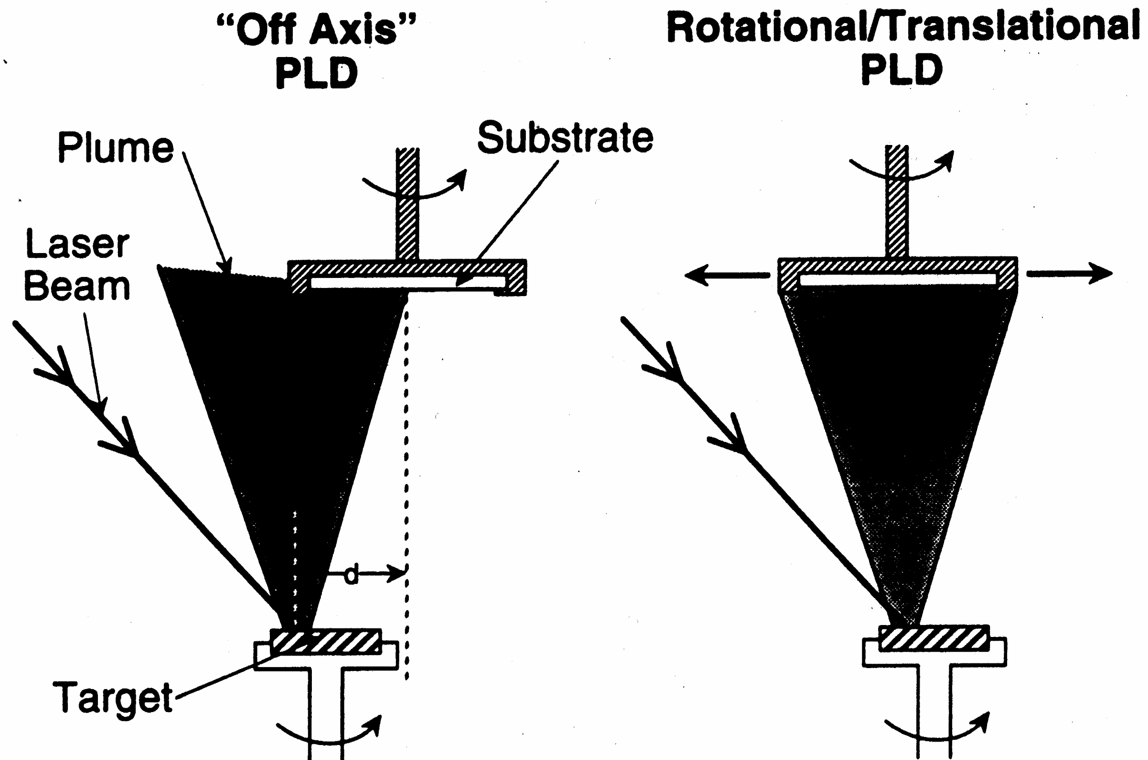

Figure 6-1. "Off-Axis" and "Rotational/Translational" Large Area PLD Method Configuration [1]

angle is a uniform function of time. The laser footprint radial location on the target is varied with time. Thus, the laser footprint location spirals in from the edge to the center of the target, in a manner similar to the tracks on a vinyl record, and then back to the edge of the target. The spacing between these laser footprint location "tracks" is determined by the rotation rate of the target and the rate of change in the radial position.

As described in Chapter 3, the substrate is located coaxially with the target at a variable distance above the target. The substrate is also rotated at a constant commanded rate. Thus, the location of the plume on the substrate is determined in a polar coordinate scheme, similar to the location of the laser footprint on the target. However, the radial position of the laser footprint on the target (RPLFT) may or may not produce a film with

maximum thickness at the same radial position on the substrate. A mapping from the RPLFT to the radial position of maximum film thickness (RPMFT) on the substrate needs to be constructed. An experiment designed to determine this mapping is described in Section 6.3. In addition, numerical simulations of thin film thickness require either knowledge of the average SDFT per pulse or information about the SDFT when depositing while rotating both the substrate and target with the laser footprint at a given fixed RPLFT. Section 6.3 describes experiments designed to evaluate these spatial film thickness distributions. Given these spatial distributions, numerical simulations should predict the theoretical radial position as a function of time (radial profile) that will produce growths with a desired SDFT, such as uniform film thickness. Actual growths will be conducted to verify that the theoretical radial profile is valid. Section 6.3 details such an experiment.

6.3 Experiment

Initially, uniform coatings of YSZ on six-inch silicon wafers were grown by iteratively correcting deviations in film thickness. The corrections were generated assuming that a given RPLFT would produce a SDFT, such that the RPMFT should equal the given RPLFT. These corrections, defined as the "equal radial assumption", provided a linear mapping from the RPLFT to the RPMFT. Thus, the equal radial assumption provided the necessary corrections to the radial profile to account for variations in film thickness. The first step in the iterative process was to mask areas of the substrate before PLD growth. After PLD growth, the mask and film growth on top of the mask were removed in a "lift-off" process, which exposed an uncoated area of the substrate. Then, a Tencor P-10 Surface Profilometer was used to measure the step-height between the

exposed substrate and the surface of the YSZ film at a given substrate radial location. The step height measurement was used to estimate the film thickness at the corresponding substrate radial position. Figure 6-2 displays an example of the step-height measurement.

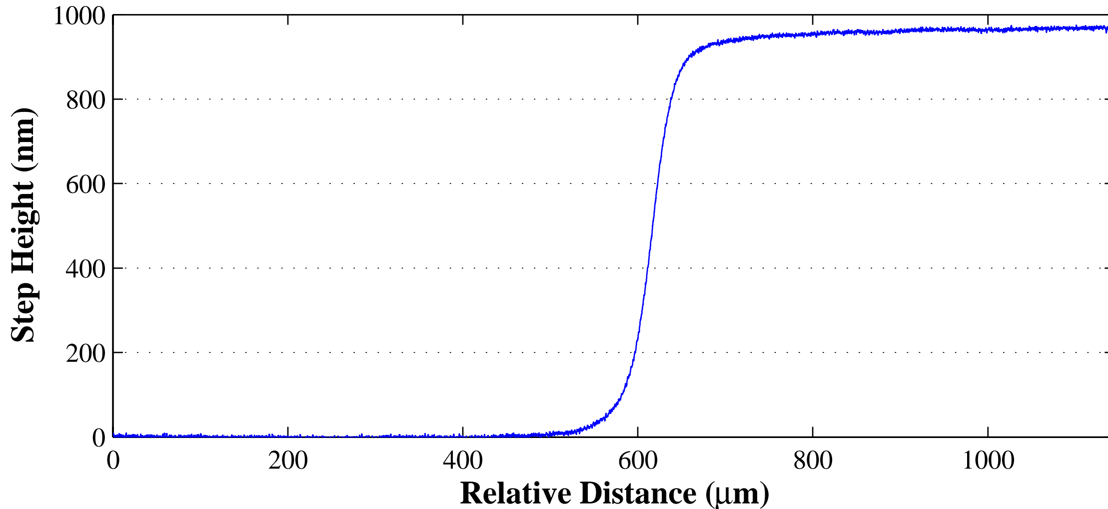

Figure 6-2. Tencor P-10 Surface Profilometer Step Height Measurement

The step-height data was used to estimate the film thickness for a single substrate radial position. A manual selection of the substrate and thin film regions in terms of relative distance was required to extract the film thickness from the step-height data. Step-height measurements were made at multiple substrate radial positions to determine the variation in thin film thickness as a function of substrate radial position. Given these estimates of film thickness, corrections to the radial profile were generated. For film thickness estimates below the average film thickness, the equal radial assumption indicated that the amount of time the laser footprint dwelled near the corresponding target radial position needed to be increased. Therefore, the amount of time spent at a given

target radial position was proportional to the film thickness at a corresponding substrate radial position. Using the corrections generated from the step-height measurements, the iterative cycle was repeated. As with any iterative process, the correctness of the initial guess for the first iteration determines if the iterative process will converge and, if so, how many iterations are required for convergence. The radial profile that produced uniform target wear was chosen as the initial guess. All the iterative growths were performed under the deposition conditions listed in Table 6-1.

Table 6-1. Deposition Conditions for Uniform Film Thickness on Large Area Substrates Testing

Deposition Parameter	Value
Laser Fluence	1.38 J/cm^2
Laser Repetition Rate	40 Hz
Ambient Gas	oxygen
Ambient Pressure	125 mTorr
Ambient Flow	7.0 sccm
Target-to-substrate Distance	86.7 mm
Substrate Bias	-225 V
Target Rotation Rate	15 rpm
Substrate Temperature	~23° C

In addition to the iterative method, a numerical simulation-based method was employed. Due to the required user interaction and the actual thickness measuring process, the Tencor P-10 was slow and tedious to use for extracting the film thickness as a function of substrate radius. Also, the masking process produced slight variations near the exposed substrate-YSZ film transition area, which limited the accuracy of film thickness measurements made near the center of the substrate. A Filmetrics F50 Thickness Mapping System was purchased to replace the Tencor P-10. The Filmetrics F50 was capable of scanning semi-transparent thin films from 300 Å to 50 μm with ± 10

Å accuracy on substrates up to eight inches in diameter with greater than 250 μm positional accuracy [14]. The Filmetrics F50 analyzed the optical reflectance from the substrate and thin film over a range of visible wavelengths to determine the film thickness at a given position on the substrate [14]. In addition, unlike the Tencor P-10 surface profilometer, the Filmetrics F50 did not require masking of the substrate and, as such, was nondestructive. Also, the Filmetrics F50 was designed to do mapping of an entire surface without user intervention rather than requiring user interaction to scan along a single given path, like the Tencor P-10.

Given the increased capability of the Filmetrics F50 over the Tencor P-10, approximately 1000 equally spaced measurements were made from the center of the substrate to the outer edge (radial scan), as opposed to approximately 15 equally spaced measurements. In addition to radial scans, the Filmetrics F50 mapped up to 4000 points to determine the film thickness variation over the entire surface of the substrate. This increased ability to map many points across a surface, rather than along a masked line, provided a mechanism to investigate the SDFT on the substrates with a much greater spatial resolution than the Tencor P-10.

The first spatial thickness distribution investigation was performed without the substrate rotating, with the target rotating, and with no radial scanning of the laser footprint on the target. Using the deposition system in this manner, referred to as the "static plume configuration," the plume did not move relative to the substrate, which allowed measurement of the average SDFT per pulse to be performed. Using the deposition parameters listed in Table 6-1, four different target radial positions were investigated to determine the effects of RPLFT on the SDFT.

The second investigation was performed with both the target and substrate rotating, but without any radial scanning of the target. Using this mode of operation, referred to as the "rotating plume configuration," the plume was scanned across the substrate along a circular path at a constant radius. The rotating plume configuration produced film thickness distributions in terms of substrate radial location rather than Cartesian coordinates, which were used in the static plume configuration. Growths at eight different target radial positions were performed using the rotating plume configuration and the deposition parameters listed in Table 6-1.

Finally, numerical simulations using data acquired from the static plume configuration were conducted and compared to the data taken using the rotating plume configuration. Another numerical simulation was performed to calculate the theoretical radial profile required to produce uniform large area thin films using the data from the rotating plume configuration. YSZ film was deposited on a six-inch diameter silicon substrate using the deposition parameters listed in Table 6-1 to validate the theoretical radial profiles. The results of these simulations are presented in Section 6.4. All YSZ films in this chapter were grown on silicon substrates rather than on the CP1 polymer substrates described in Chapter 4 due primarily to the low cost and availability of the silicon substrates compared to that of the CP1 polymers. Also, the Filmetrics 50 thickness mapping system and the Tencor P-10 surface profilometer required the substrate to be nearly flat [14; 15]. For best thickness measurement accuracy, the Filmetrics F-50 required the substrate to be reflective [14]. Thus, the possible curvature and visible transparency of the large area CP1 polymer substrates prohibit their use as substrates for the film thickness diagnostic depositions described in this chapter.

6.4 Data and Analysis

The iterative method, described in Section 6.3, was implemented to produce uniform thickness YSZ thin films on six-inch silicon substrates. The results are shown in Figure 6-3 and described in Table 6-2.

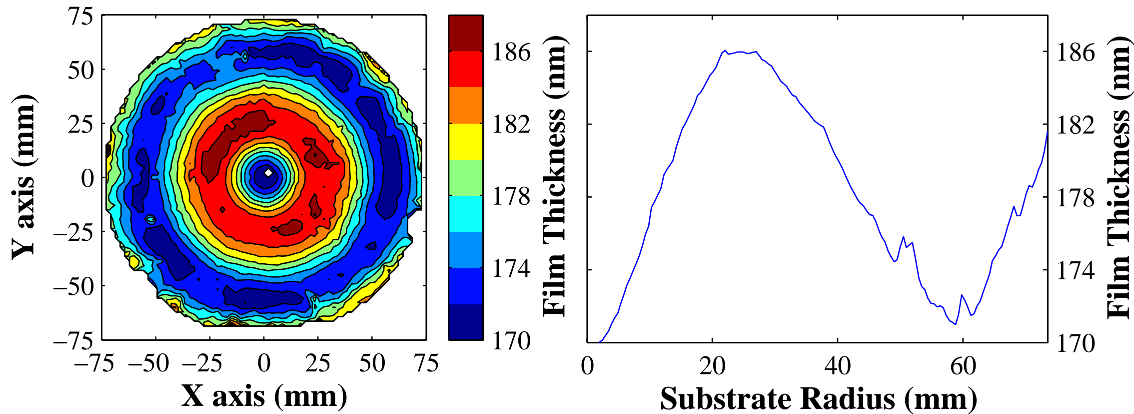

Figure 6-3. Contour Mapping and Radial Cross-Section of YSZ Film on Six-Inch Diameter Silicon Substrate Grown Using the Iteratively Derived Radial Profile that Produced the Most Uniform Thickness to Date

Table 6-2. Uniform Thickness Statistics of YSZ Film on Six-Inch Diameter Silicon Substrate Grown Using the Iteratively Derived Radial Profile that Produced the Most Uniform Thickness to Date

Maximum Thickness	186.1 nm
Minimum Thickness	169.5 nm
Mean Thickness	178.2 nm
Standard Deviation of Thickness	5.27 nm 3.0 % of mean thickness
Absolute Variation of Thickness	+7.9 nm, -8.7 nm +4.4%, -4.9% of mean thickness

The initial radial profile was designed to produce uniform wear of the target when depositing with a constant laser repetition rate and constant angular target rotation rate. Under these conditions, the amount of time spent at any given target radius is

proportional to the circumference at the given target radial position. Both the initial profile, which is inversely proportional to the target radial position, and the final iterative profile can be equivalently expressed in terms of velocity as a function of radial location or in terms of radius location as a function of time, as shown in Figure 6-4.

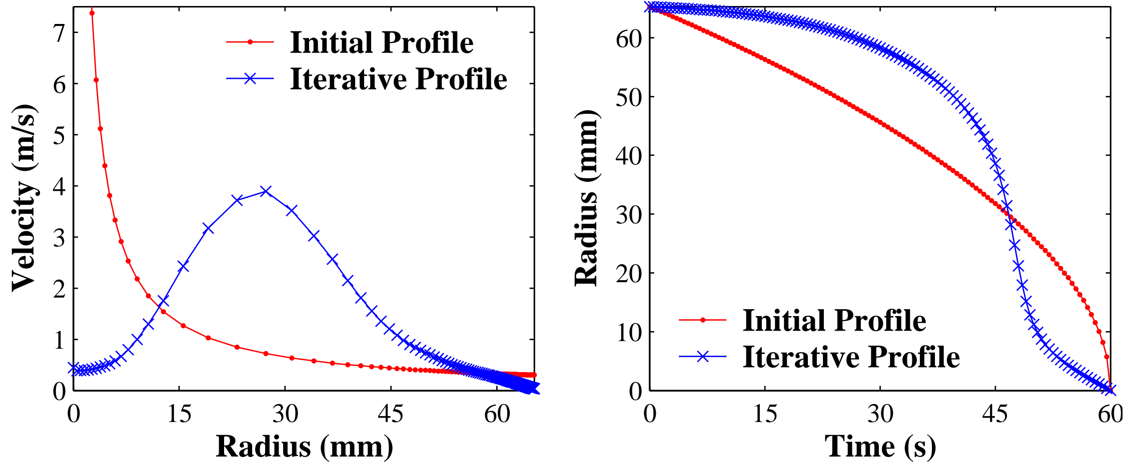

Figure 6-4. Initial Radial Profile and Final Radial Profile for YSZ Film on Six-Inch Diameter Silicon Substrate Grown Using the Iteratively Derived Radial Profile that Produced the Most Uniform Thickness to Date

The iterative corrections were generated using the equal radius assumption. If this assumption is valid, then the initial radial profile and the final iterative radial profile should be very similar. However the iterative profile deviated significantly from the initial profile derived for uniform wear of the target, as evident in Figure 6-4. In addition, further iterative corrections from the iterative profile shown in Figure 6-4 produced films with greater variations in film thickness. This deviation between the initial and iterative radial profiles, combined with the inability to continue the iterative correction procedure beyond the iterative radial profile shown in Figure 6-4, indicated

that the equal radial assumption is invalid. Therefore, a new mapping of target radial location to the radial location of peak film thickness on the substrate was required.

In order to determine the relationship between the target radial location and the radial location of peak film thickness on the substrate, and to investigate the ability to perform numerical simulations of film thickness in terms of radial profiles, four YSZ films on six-inch silicon substrate were grown using four different target radial positions. Each growth was performed using the static plume configuration and measured with a Filmetrics F50. The Filmetrics F50 acquired measurements along a user-specified grid over the entire six-inch diameter substrate. A 3860-point equally spaced square grid produces measurements with a spatial resolution of 2.14 mm, which was chosen to remain within the 4000-point software limitation of the Filmetrics F50. Figure 6-5 shows the film thickness measurements for each growth performed using the static plume configuration at the four different target radial positions.

A visual inspection of the four contour mappings shown in Figure 6-5 reveals an offset between the target radial position and the substrate location of peak film thickness. In addition, there exist slight variations in the amplitude and shape of the SPDT among the four different contour maps. The laser pulse was incident on the target from the 3 o'clock position on the contour maps shown in Figure 6-5. Thus, the RPMFT is back toward the laser pulse, as evident by the position offset. A visual inspection of the plume, as viewed through the observation port at the front of the chamber, and images taken using the fast imaging camera system, described in 3.9, verified that slight "plume tilting," as described in Section 6.2, occurred. "Peak static substrate radial location" defines the substrate radial location of maximum film thickness for YSZ films grown

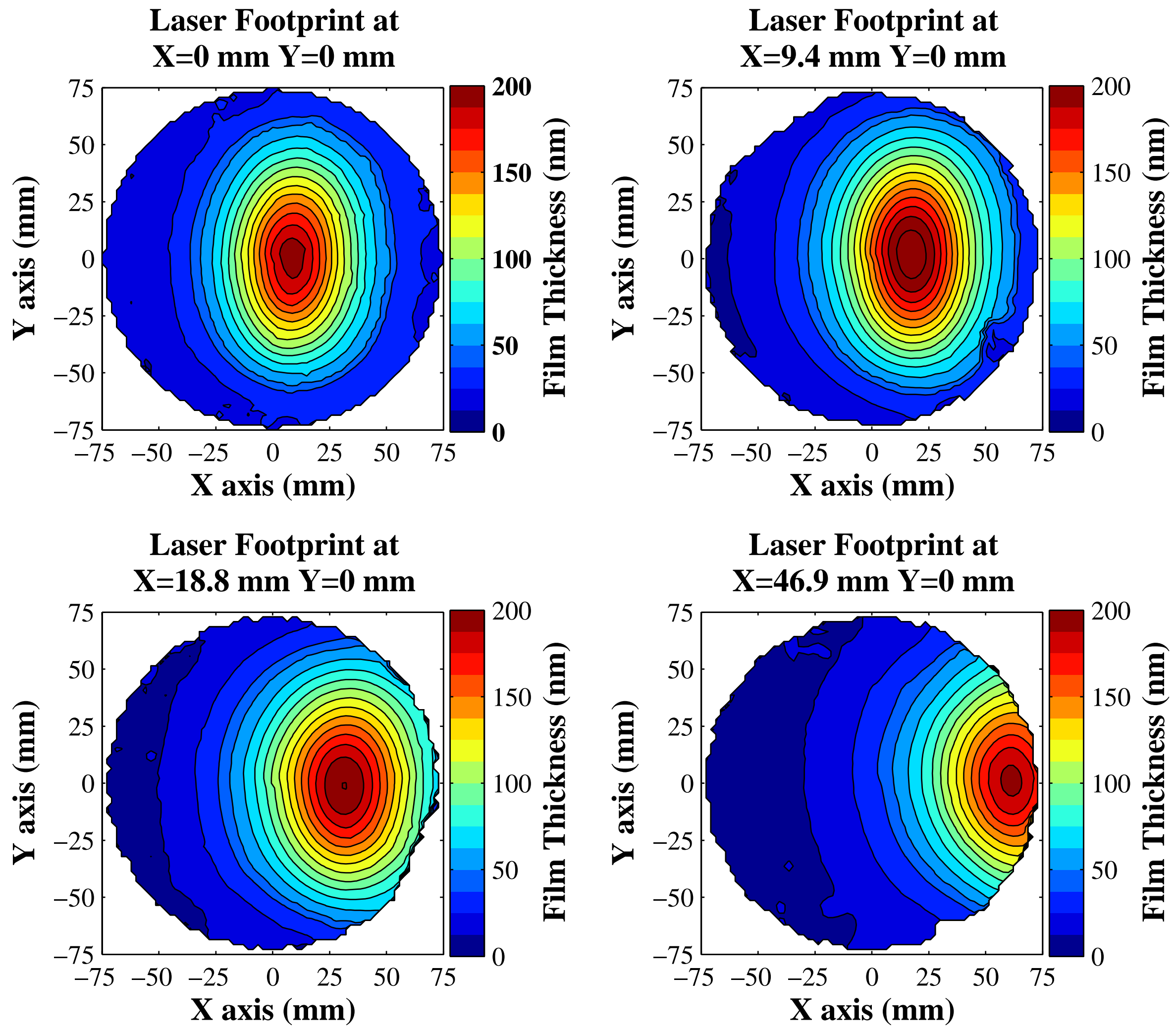

Figure 6-5. Contour Mapping of Film Thickness of YSZ Film on Six-Inch Diameter Silicon Substrates Grown Using the Static Plume Configuration at Four Different Target Radial Positions

using the static plume configuration. A linear mapping approximates the relationship between target radial position and the peak static substrate radial location, as shown by the data points and linear fit in Figure 6-6.

Most of the slight variation in the peak film thickness can be attributed to the variable distance between the focal lens and the target caused by scanning the laser footprint radially across the target. The focal lens is positioned to focus the laser pulse

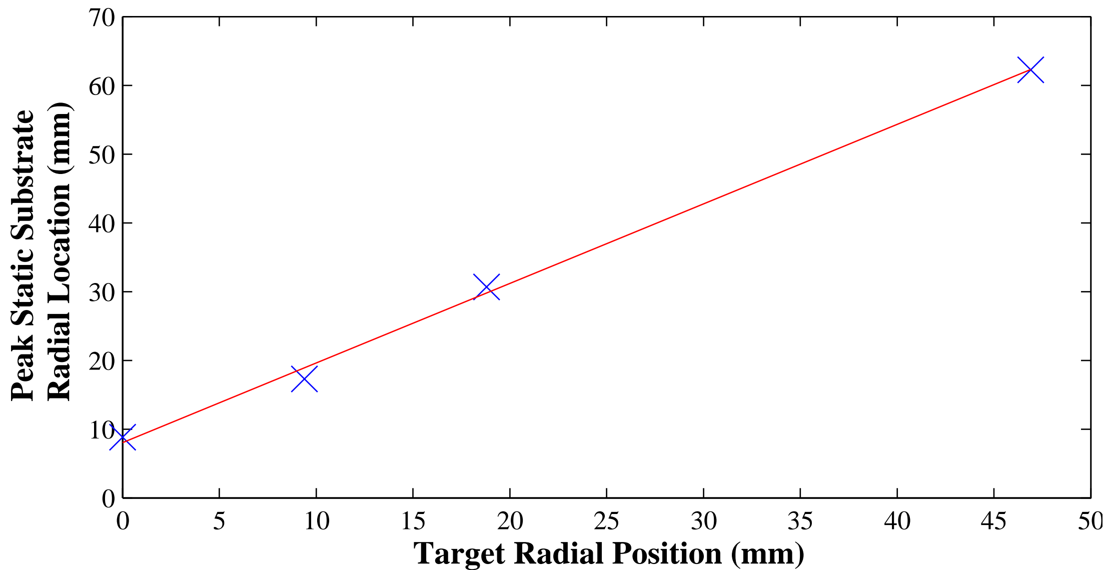

Figure 6-6. Relationship Between Laser Footprint Target Radial Position and Radial Location of Peak Film Thickness on the Substrate

near the center radial location of the target, approximately 35 mm. As the laser footprint is scanned toward the edge or the center of the target away from the 35 mm target radial location, the footprint is slightly defocused. The total change in pathlength from the focal position is less than ±34 mm or less than 3% of the effective focal length of the focusing lens, which produces an almost negligible change in laser fluence. However using the static plume configuration and an equal number of laser pulses, YSZ films grown with target radial positions near the 35 mm target radial location measured slightly thicker than the films grown with the target radial positions near either the target edge or the target center. In addition, other factors, such as target wear, may also contribute to variations in film thickness. Table 6-3 lists the peak film thickness, which varies less than 4.5%, for each of the four growths.

Table 6-3. Peak Film Thickness of YSZ on Six-Inch Diameter Silicon Substrates Grown Using the Static Plume Configuration

Target Radial Position (mm)	0	9.4	18.8	46.9
Peak Film Thickness (nm)	195	210	200	193

Although there is very little change in the amplitude of the four YSZ films grown using the static plume configuration, the spatial distribution of film thickness, or shape, does vary with the target radial position, most noticeably along the X direction at Y=0, as shown in cross-sectional comparison of Figure 6-7.

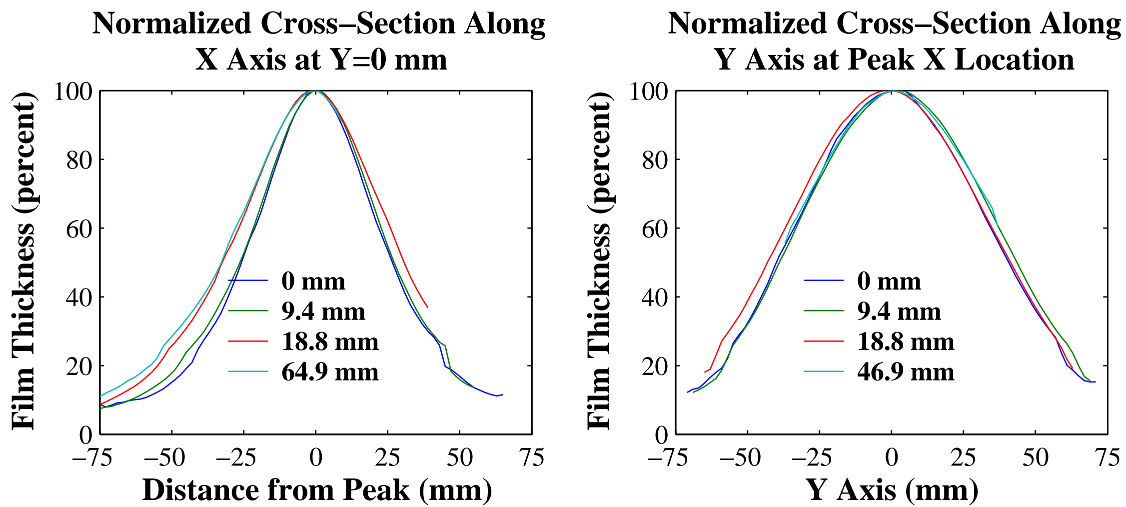

Figure 6-7. Cross-Sectional Comparison of YSZ on Six-Inch Silicon Substrates Grown Using the Static Plume Configuration at Four Target Radial Positions

A common distribution used to model the spatial distribution of film thickness is the cosine N distribution, as shown in Equation (6-1):

$$Thickness = \cos^{n}\theta \quad (\text{percent}) \tag{6-1}$$

where *thickness* is the *percentage of the maximum film thickness* (percent), n is a *power constant* (unitless), and θ is the *angle between the laser footprint location and the*

measurement location on the target (radians). Figure 6-7 displays the normalized film thickness cross-sections along the X and Y axes, which is fitted to Equation (6-1) using TableCurve 2D [16]. Table 6-4 lists statistics from the cosine N fittings. Typical values of *n* cover a broad range from 1.5 to 70 [1]. Therefore the *n* value range of 6 to 15.5 listed in Table 6-4 is consistent with values reported in the current literature. The fitted *n* values along both the X and Y axes decrease as the laser footprint radial position increases. The increase in the *n* value indicates a more narrowly distributed film thickness. These results are visually apparent in Figure 6-7, predominantly along the X axis. The results of the graphical and fitted cross-sectional film thickness comparisons indicate that the film thickness spatial distribution changes with laser footprint target radial positions. Therefore, any simulations that require these diagnostics deposition results cannot be based upon a single diagnostic deposition as initially intended.

Table 6-4. Statistics for the Normalized Cross-Sectional Film Thickness Along the X and Y Axis When Fitted to a Cosine N Distribution

		Target Radial Position			
		0 mm	9.4 mm	18.8 mm	64.9 mm
Along X Axis	Lower 95% Confidence Interval	14.81	13.66	10.73	9.56
	Fitted Value	15.36	14.15	11.02	9.89
	Lower 95% Confidence Interval	15.92	14.65	11.31	10.22
Along Y Axis	Lower 95% Confidence Interval	7.13	6.64	6.52	6.12
	Fitted Value	7.22	6.85	6.62	6.34
	Lower 95% Confidence Interval	7.30	7.07	6.74	6.57

A numerical simulation, denoted “static numerical simulation,” was performed using the film thickness distribution from the YSZ films shown in Figure 6-5, which were grown using the static plume configuration. The static numerical simulation begins by rotating copies of the four film thickness distributions about the center of the substrate by

multiples of 2.25 degrees between 0 and 360 degrees. The 2.25-degree angular spacing corresponds to the angular displacement of the substrate per pulse when using a 40 Hz laser repetition rate and 15-rpm substrate rotation rate. The rotated copies of the film distribution were then summed to simulate the film thickness distribution of a rotating target (ablated at a constant RPLFT) and rotating substrate. Accordingly, the static numerical simulation should approximate the thickness distribution of the films grown using the rotating plume configuration. This comparison is discussed later in this section. Figure 6-8 displays the results of the static numerical simulation.

The two contour mappings shown in the top row of Figure 6-8 reveal that the target radial position of 0.0 and 9.4 mm produced simulation results with a maximum film thickness at the center of the substrate. The simulation using the 18.8 mm target radial position data produced a similar result, but the maximum was at a substrate radius of 6 mm with a slight dip in the center. Exploiting the rotational symmetry about the center of the substrate, Figure 6-9 presents a more enlightening cross-sectional view of the static numerical simulation results.

The static numerical simulation is repeated using simulated target radial positions between 0 and 65 mm by interpolating among the four YSZ growths shown in Figure 6-5. The interpolation translates the maximum film thickness location on the substrate to a new substrate location. The new substrate location corresponded to the desired target radial location as specified by the linear fit shown in Figure 6-6. The interpolated film thickness distribution was then rotated and summed as previously described. Figure 6-10 displays the simulated mapping of the target radial location to the radial location of peak simulated film thickness on the substrate, with the solid line and "+" markers. The linear

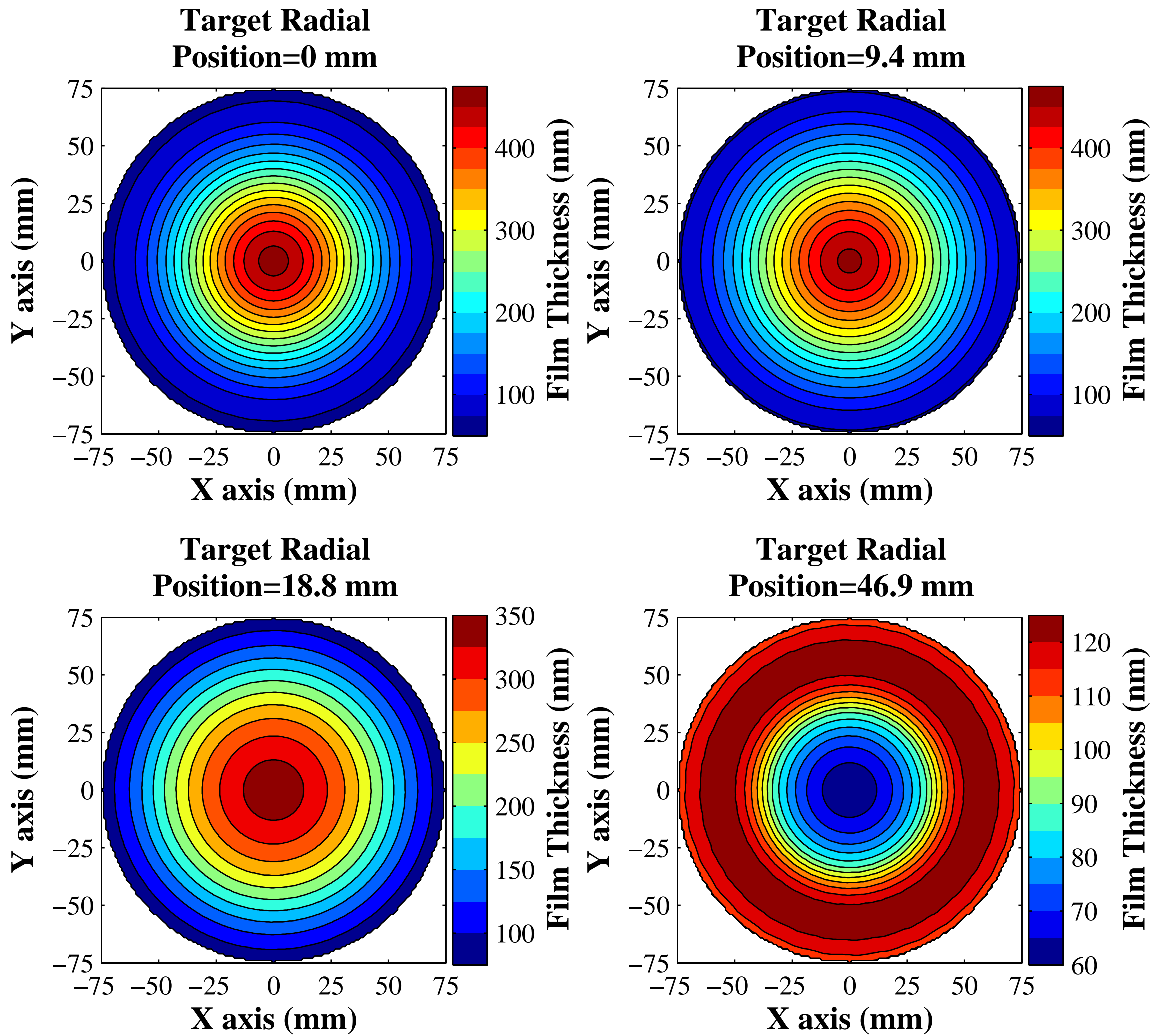

Figure 6-8. Results of Static Numerical Simulations Using the Static Plume Configuration for YSZ on Six-Inch Silicon Substrates

approximation of peak static substrate radial location to target radial location as shown in Figure 6-6 is included in Figure 6-10 as the dashed line.

The results of the simulated mapping predicted that ablating at any target radial location less than 27 mm results in a maximum simulated film thickness at the center of the substrate. The RPLFT was varied exclusively from the center to the edge across a rotating substrate and did not cross the center of the target. However, the width of the

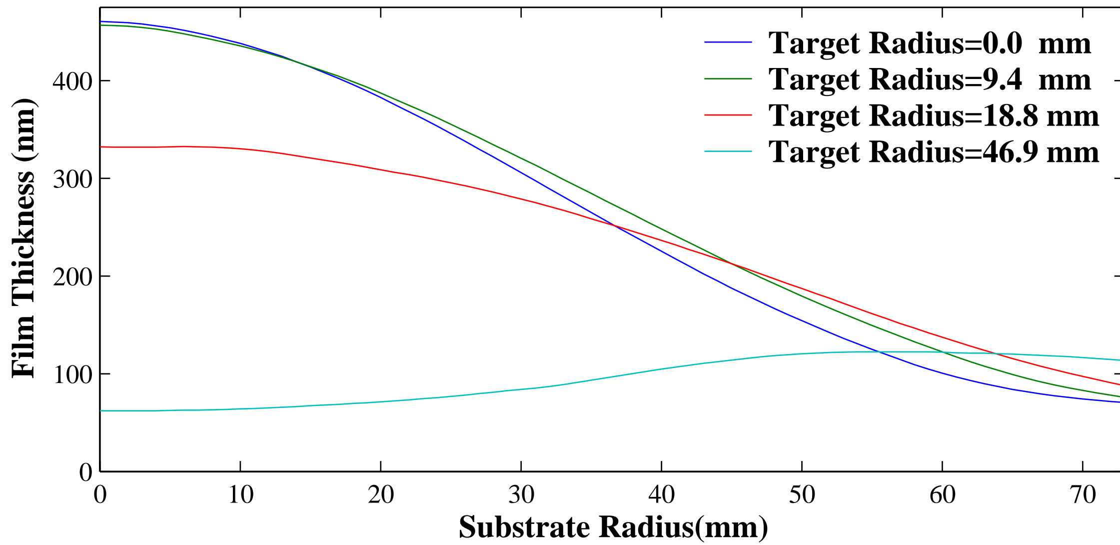

Figure 6-9. Cross-sectional View of Static Numerical Simulation Results

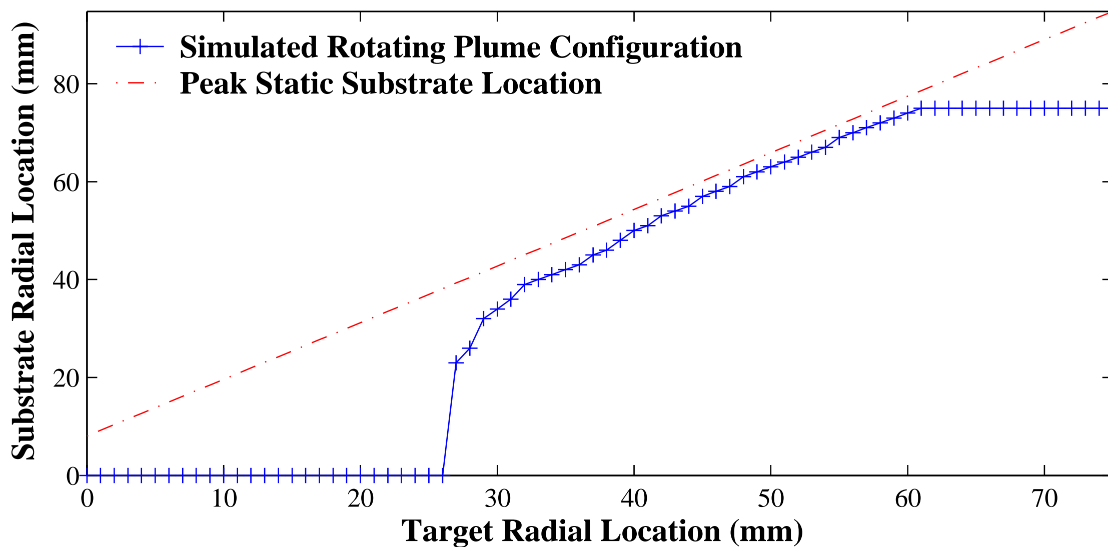

Figure 6-10. Mapping of Target Radial Location to Radial Location of Peak Simulated Film Thickness on Substrate

SDFT produced contributions to the film thickness on both sides of the substrate center when the RPLFT was less than 27 mm. Thus, the simulated RPMFT was found at the center of the substrate. In addition, ablating at any PRLFT greater than 60 mm produced a simulated RPMFT at the edge of the substrate. The actual RPMFT continued to

increase as the target radial location increased. However, the simulation truncated the film thickness calculations at the maximum radius of the substrate. If a larger simulated substrate were used, the substrate radial location of peak simulated film thickness would continue to asymptotically approach the peak static substrate location, up to the maximum radius of the larger simulated substrate.

The static numerical simulation results needed to be verified by actual growths using the rotation plume configuration, as described in Section 6.3. YSZ films were grown on six-inch silicon substrates at eight uniformly spaced RPLFT between the center of the target and a location near the edge of the target using the deposition parameters listed in Table 6-1 with the substrate rotating at 15 rpm. Figure 6-11 presents the film thickness distribution for the four depositions at different RPLFTs, which were grown using the rotating plume configuration. Again taking advantage of the rotational symmetry about the center of the substrate, Figure 6-12 displays the cross-section of each of the YSZ films grown using the "rotating plume configuration" at eight different target radial locations.

The amplitude and shape of the cross-sectional data appears to be similar to the predictions from the static numerical simulation. However upon more detailed analysis, the actual shape does vary significantly from the static numerical simulation predictions. For RPLFTs near the center and the edge of the target, the static numerical simulation predictions approximate the cross-sectional data. However, for RPLFTs not near the center or the edge of the target, the results deviate in both amplitude and shape. These deviations are most likely caused by the inability of the Filmetrics F50 to measure film thickness less than 30 nm. The errors in the film thickness measurements below 30 nm

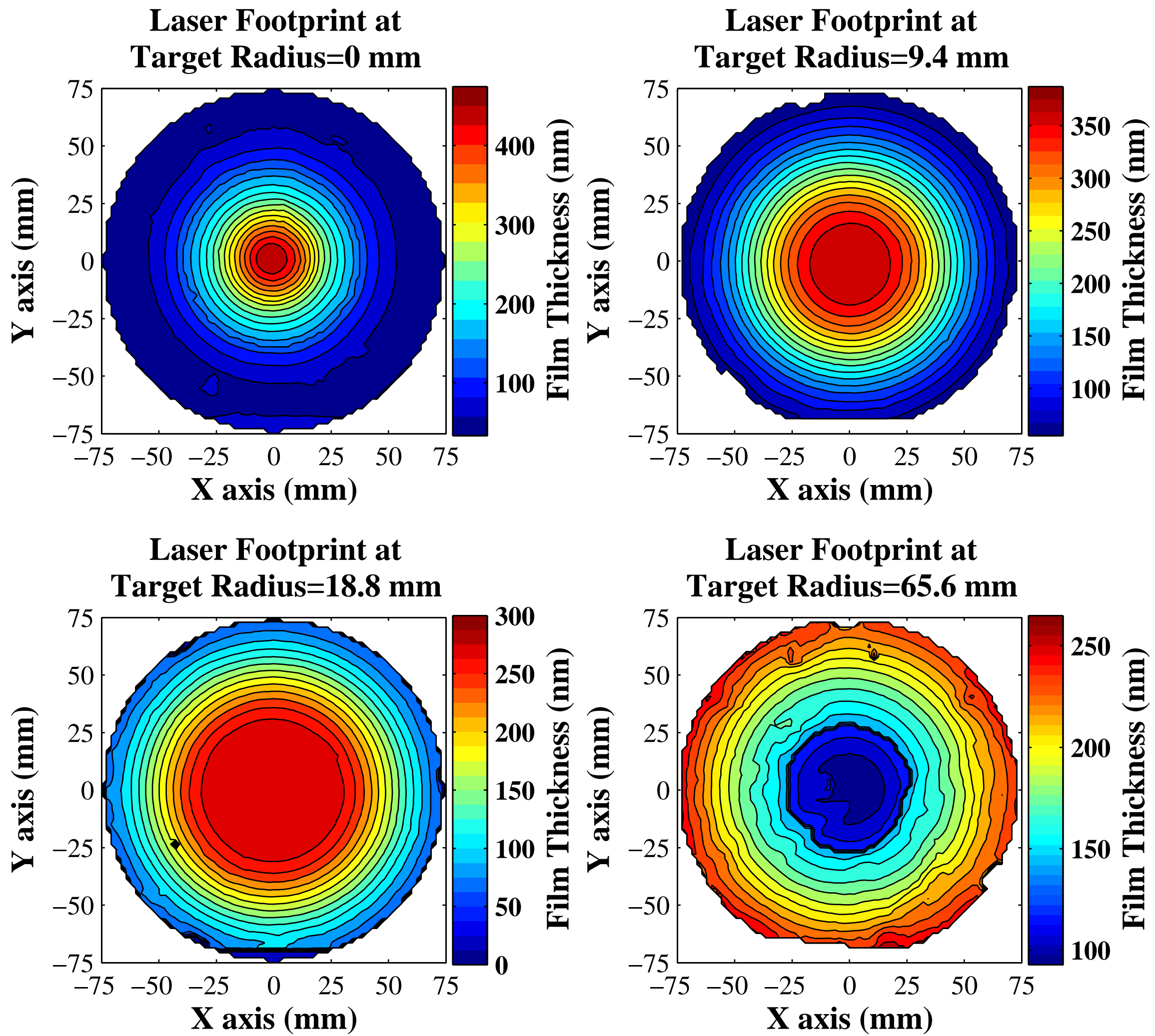

Figure 6-11. Contour Mapping of Film Thickness of YSZ Film on Six-Inch Diameter Silicon Substrates Grown Using the Rotation Plume Configuration

are amplified 160 times due to the summing of the static simulation. However, the minimum thickness for each of the YSZ films grown using the rotating plume configuration is greater than 30 nm. Figure 6-13 shows the comparisons between the measured film thickness and the static numerical simulation results.

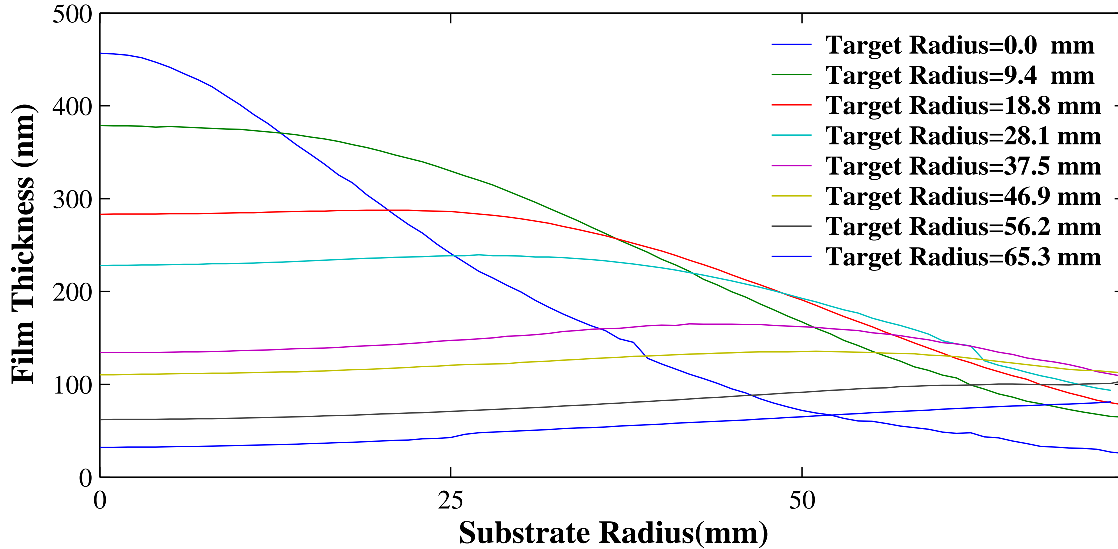

Figure 6-12. Cross-section of Film Thickness of YSZ Film on Six-Inch Diameter Silicon Substrates Grown Using the Rotation Plume Configuration

The term “static mapping” defines the relationship between the RPLFT and the RPMFT produced from the static numerical simulation results. Similarly, “rotated mapping” denotes the mapping of the RPLFT to RPMFT measured from growths using the rotating plume configuration. As evident from the variations in shape and amplitude of the film thickness shown in Figure 6-13, the static mapping and the rotating mapping were not equivalent. Figure 6-14 displays the static mapping and the rotated mapping, as well as the linear approximation of the peak static substrate radial location to the target radial location, as shown in Figure 6-6.

The maximum substrate size for the rotated mapping growths was reduced to approximately 73 mm due to slight misalignments between the geographic center of the substrate and the center of rotation of the substrate. The center of rotation of the substrate was found using the rotational symmetry of the radial cross-section of film thickness. The RPMFT will continue to asymptotically approach the peak static substrate

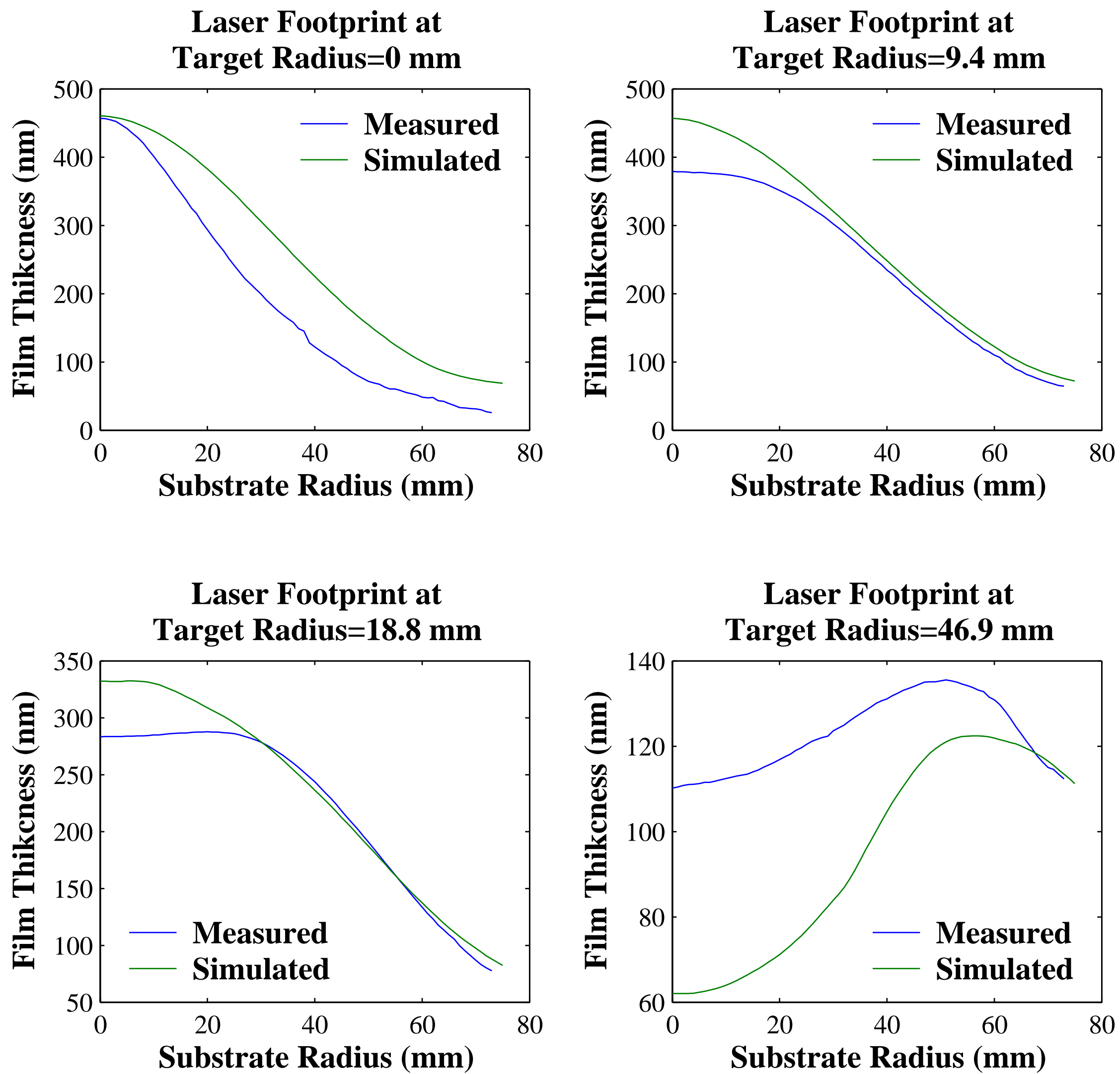

Figure 6-13. Comparison of the Static Numerical Simulation Results and Actual Growths Using the Rotation Plume Configuration for YSZ on Six-Inch Silicon Substrates

location, as described previously for the static mapping in this section. As evident in Figure 6-14, the static mapping is equivalent to the rotating mapping for RPLFTs that are not in the 10 mm to 26 mm range. Given this range of RPLFTs for the static numerical simulation, the RPMFT occurs at or near the center of the substrate. The actual RPMFTs that correspond to RPLFTs between 10 mm and 26 mm are very sensitive to errors in

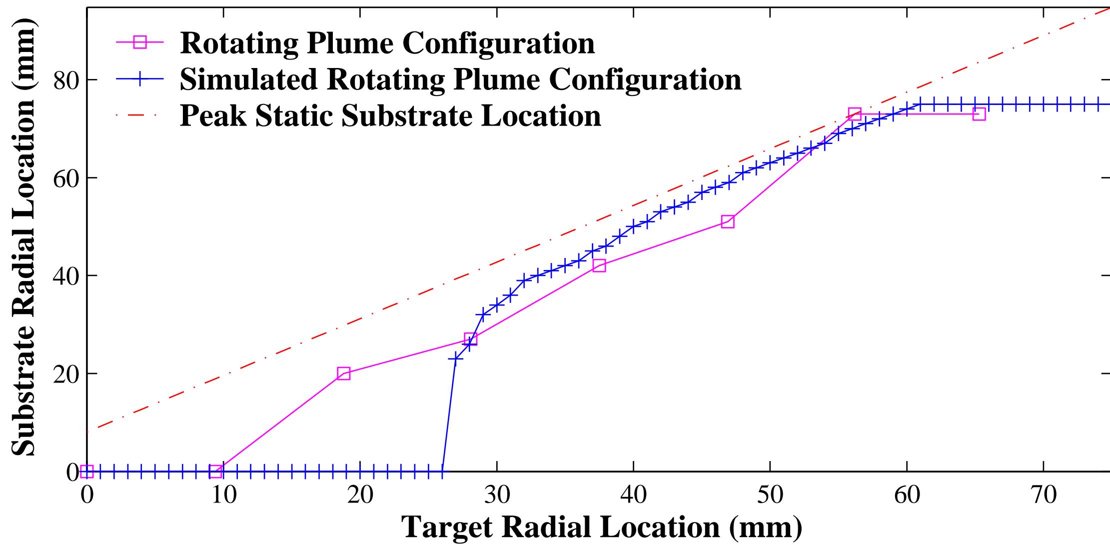

Figure 6-14. Mapping of Target Radial Location to Radial Location of the Peak Film Thickness on Substrate

thickness. This sensitivity, combined with the errors produced by the minimum film thickness measuring capability of the Filmetrics F50, produced the contradictions in the static and rotating mappings for target radial locations between 10 mm and 26 mm shown in Figure 6-14.

The cross-sections from the YSZ films grown using the rotating plume configuration, as shown in Figure 6-12, represent the contributions to the total film thickness made by ablating each distinct RPLFT using the deposition parameters listed in Table 6-1 (with a 15 rpm substrate rotation rate and approximately 72,000 laser pulses). Allowing each cross-section of film thickness to be used as a pseudo-basis function, there exists some linear combination of these pseudo-basis functions that produce a uniform film thickness. By definition, a basis function must have an additive inverse. In the physical sense (relative to this research), an additive inverse means ablating at the corresponding RPLFT for a negative number of pulses so the film thickness is decreased.

This is not possible for a deposition system, so the term pseudo-basis is applied. Given that the cross-sectional data are pseudo-basis functions, linear algebra cannot be applied to determine the coefficients of the linear combination of pseudo-basis functions. Another limitation is that the RPLFT scanning has a maximum velocity, which translates into a minimum amount of time to traverse between adjacent pseudo-basis functions. Therefore the coefficients of the linear combination must have a minimum. Given these constraints, a least squares error algorithm was applied to determine the coefficients that would result in a uniform film thickness. These coefficients determine the relative amount of time the radial profile will dwell about the corresponding target radial position. This calculated radial profile produces YSZ film on a six-inch diameter substrate with the film thickness distribution and cross-section as shown in Figure 6-15 and described in Table 6-5.

As listed in Table 6-5, the YSZ film thickness varies by 9.9 percent of the mean film thickness. This variation approximately equals the iteratively corrected film thickness variations listed in Table 6-2, which varies by 9.3 percent of the mean film

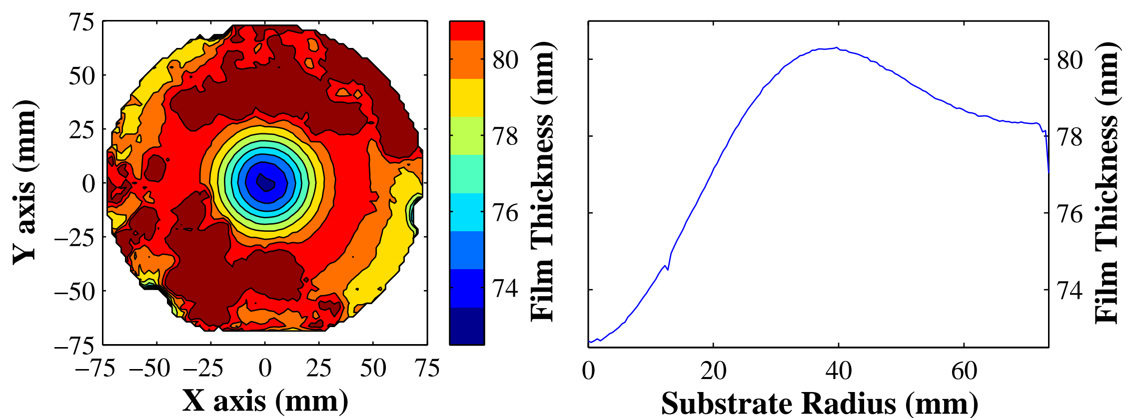

Figure 6-15. Contour Mapping and Cross-Section of YSZ Film on Six-Inch Diameter Silicon Substrate Grown Using the Calculated Theoretical Profile Method

Table 6-5. Uniform Thickness Statistics of YSZ Film on Six-Inch Diameter Silicon Substrate Grown Using the Calculated Radial Profile

Maximum Thickness	80.3 nanometer
Minimum Thickness	72.6 nanometer
Mean Thickness	77.81 nanometer
Standard Deviation of Thickness	2.38 nanometer 3.1 % of mean thickness
Absolute Variation of Thickness	+2.48 nanometer, -5.19 nanometer +3.2%, -6.7% of mean thickness

thickness. Likewise, the standard deviation expressed as a percentage of the mean is approximately equal between YSZ films grown using the iterative correction method and the numerical simulation method. These similarities are expected as both methods are designed to produce uniform thickness films. Although the radial profile appears radically different when inspected using radial velocity as a function of the target radial position, the calculated radial position as a function of time agrees closely with the calculated radial position as a function of time. The comparison of the equivalent expressions of radial profiles for both the iterative correction method and the numerical simulation method are shown in Figure 6-16.

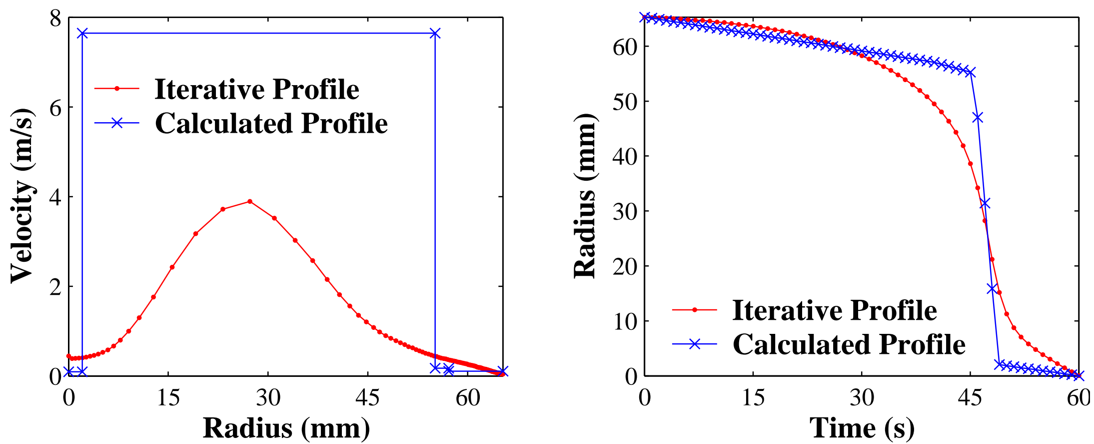

Figure 6-16. Comparison of the Calculated Radial Profile Designed to Produce Uniform Thickness Films and the Iterative Radial Profile

6.5 Conclusion

Radial profiles derived from both an iterative correction method and a numerical simulation method produced YSZ films on six-inch diameter silicon substrates with less than ten percent total variation in thickness over the entire six-inch diameter area. However, the iterative correction method requires a mapping between the target radial location and radial location on the substrate of maximum film thickness in order to generate corrections. The initial assumption that the target radial location equaled the radial location on the substrate of maximum film thickness was not correct. Given a correct mapping, the iterative correction method becomes a powerful technique capable of producing uniform thickness films on silicon substrates with less than ten percent total variation in thickness over the entire six-inch diameter area. In addition, the numerical simulation method generates this mapping and provides a theoretical radial profile that should produce films that are more uniform in thickness. Since the numerical simulation is necessary to produce the mapping between the target radial position and the substrate radial position of peak thickness required by the iterative correction method, both methods should be combined by applying the theoretical radial profile as the initial guess for the iterative correction method. Combining both techniques yields an efficient mechanism for generating uniform thickness films by greatly reducing the number of PLD growths required when using the iterative method alone.

The static numerical simulation manipulated the average film thickness distribution per pulse to produce the pseudo-basis functions necessary to generate the theoretical radial profile. However, the average film thickness distribution varied as a function of the target radial location. One of the primary advantages for using the

average film thickness distribution to calculate the theoretical radial profile is to limit the number of diagnostic growths necessary to produce both the pseudo-basis functions and the mapping between the target radial position and the substrate radial position of peak thickness. If the average film thickness distribution can be accurately measured and does not vary with target radial position, then only a single diagnostic growth is required to generate the theoretical radial profile. However, the average film thickness distribution varies slightly with target radial position. Most of this variation may be removed if the focal lens is moved continuously during a deposition so that the laser footprint remains tightly focused for all target radial positions. This focal length compensation is not necessary for the six-inch diameter substrates used in this research, but will become necessary as the substrate diameters are increased. In addition to the variation in the average film thickness distribution with respect to the target radial position, the minimum thickness measurement errors must be reduced. Either a more compatible measurement system should be utilized or the number of pulses per diagnostic deposition must be increased so that the minimum film thickness is greater than the minimum thickness measurable by the Filmetrics F50.

In addition, since the average film thickness distribution did vary with the target radial position, multiple diagnostic depositions are required to fully characterize the pseudo-basis functions. Therefore, given the need for multiple diagnostic depositions, it is not advantageous to use the average film thickness distribution. Rather, if depositions are performed under normal deposition conditions, except using a fixed laser footprint at one of several target radial locations, the pseudo-basis function can be extracted from the film thickness radial cross-section. A least square error algorithm can then produce the

necessary coefficients for a linear combination of the pseudo-basis functions. These coefficients represent the relative time that the laser footprint must dwell at the corresponding target radial position.

The methods used to produce radial profiles capable of yielding uniform film thickness, as described previously, can be applied directly to the deposition of materials other than YSZ. In addition, these methods are directly applicable to PLD depositions on substrates other than silicon, as discussed in Chapter 8. Also, the desired film thickness need not be a uniform thickness. Any desired film thickness distribution that is rotationally symmetric about the center of the substrate can be produced. Finally, these methods are not limited to six-inch diameter substrates and can be scaled to larger substrate diameters. The only limiting factor for scalability is the capacity of a PLD system.

Bibliography

1. Chrisey, D. B. and G. K. Hubler, *Pulsed Laser Deposition of Thin Films*, New York: John Wiley & Sons, 1994.

2. Davanloo, F., E. M. Juengerman, D. R. Jander, T. J. Lee, C. B. Collins, and E. Matthias. "Mass Flow in Laser-Plasma Deposition of Carbon under Oblique Angles of Incidence," *Applied Physics A*, 54(4): 369-372, 1992.

3. Fogarassy, E. C., J. P. Stoquert, P. Siffert, J. Perriere, and F. Rochet. "High T_C YBaCuO and BiSrCaCuO Superconducting Thin Films Deposited by Pulsed Excimer Laser Evaporation," *Journal of Less Common Metals*, 151: 249-256, 1989.

4. Lubben, D., S. A. Barnett, K. Suzuki, S. Gorbatkin, and J. E. Greene. "Laser-induced Plasmas for Primary Ion Deposition of Epitaxial Ge and Si Films," *Journal of Vacuum Science and Technology B*, 3(4): 968-974, 1985.

5. Hansen, S. G., and T. E. Robitaille. "Characterization of the Pulsed Laser Evaporation Process: Selenium Thin-film Formation," *Applied Physics Letters*, 50(6): 359-361, 1987.

6. Muenchausen, R. E., K. M. Hubbard, S. Foltyn, R. C. Estler, N. S. Nogar, and C. Jenkins. “Effects of Beam Parameters on Excimer Laser Deposition of $YBa_2Cu_3O_{7-\delta}$,” *Applied Physics Letters*, 56(6): 578-580, 1990.

7. Neifeld, R. A., S. Gunapal, C. Liang, S. A. Shaheen, M. Croft, J. Price, D. Simons, and W. T. Hill. “Systematics of Thin Film Formed by Excimer Laser Ablation: Results on $SmBa_2Cu_3O_7$,” *Applied Physics Letters*, 53(8): 703-704, 1988.

8. Venkatesan, T., X. D. Wu, A. Inam, and J. B. Wachtman. “Observation of Two Distinct Components During Pulsed Laser Deposition of High T_c Superconducting Films,” *Applied Physics Letters*, 52(14): 1193-1195, 1988.

9. Greer, J. A., and H. J. Van Hook. “Uniformity Considerations for “*In-Situ*” Laser-ablated $Y_1Ba_2Cu_3O_{7-x}$ Films Over Three Inch Substrates,” *Materials Research Society Symposia Proceedings*, 169: 463-468, 1990.

10. Lowndes, D. H., D. P. Norton, J. W. McCamy, R. Feenstra, J. D. Budai, D. K. Christen, and D. B. Poker. “*In Situ* Growth of High Quality Epitaxial $YBa_2Cu_3O_{7-x}$ Thin Films at Moderate Temperatures by Pulsed Laser Ablation,” *Materials Research Society Symposia Proceedings*, 169: 431-434, 1990.

11. Foote, M. C., B. B. Jones, D. B. Hunt, J. B. Barner, R. P. Vasquez, and L. J. Bajuk. “Composition Variations in Pulsed-laser-deposited Y-Ba-Cu-O Thin Films as a Function of Deposition Parameters,” *Physica C*, 201(1-2): 176-182, 1992.

12. Gorbunov A. A., and V. I. Konov. “Spatial Characteristics of Laser Pulsed Plasma Deposition of Thin Films,” *SPIE*, 1352: 95-99, 1989.

13. Afonso, C. N., R, Serna, F. Catalina, and D. Bermejo. “Good-Quality Ge Films Grown by Excimer Laser Deposition,” *Applied Surface Science*, 46: 249-253, 1990.

14. *Operation Manual for the Filmetrics F50 Thin-Film Mapping System*, rev 2.3, San Diego, CA: Filmetrics Inc., 1999.

15. *KLA-Tencor® P-10 Reference Manual*, rev. A, Milpitas, CA: KLA-Tencor Corportation, 1998.

16. *TableCurve 2D*. Version 5.1, IBM, CD-ROM. Computer Software, SYSTAT Software Inc., Richmond CA, 2001.

7 Yttria Stabilized Zirconia Coatings for Stress-Shaped Polymer Mirrors

7.1 Overview

Chapters 4 through 6 developed the necessary research areas to deposit uniform-thickness controlled-stress large-area yttria stabilized zirconia (YSZ) films using pulsed laser deposition (PLD). However, these research areas need to be combined to demonstrate the ability to desirably modify the shape of large area (six-inch diameter) CP1 polymer mirrors using a stressed YSZ coating grown by pulsed laser deposition (PLD), which is the initial step toward a 25-meter diameter mirror for the space-based telescope described in Chapter 1. Hence, the goal of this chapter is to produce YSZ films on undamaged CP1 polymers that desirably affect the shape of the CP1 polymers.

The goal of this chapter was met. Compressively-stressed YSZ coatings were grown on initially-flat six-inch diameter suspended CP1 polymer substrates without damage to the substrate using a range of oxygen pressures from 50 to 100 mTorr. The curvature of the resulting CP1 polymer substrates was measured using a Zygo interferometer and was found to increase with a decrease in oxygen pressure and/or YSZ deposition duration (film thickness). However the maximum laser repetition rate was found to be 10 Hz. Laser repetition rates at frequencies greater than 10 Hz damaged the CP1 polymer substrates. The 10 Hz maximum laser repetition rate severely restricted the YSZ growth rate. YSZ films were deposited on six-inch diameter CP1 polymer

substrates that were still mounted to the casting mold at laser repetition rate of 40 Hz (maximum rate that the laser can produce at the desired output energy) without damage to the substrate. However, substrate release and mounting issues currently limit the substantial benefits of this technique.

7.2 Experiment

Two sets of experiments were performed to demonstrate the ability to produce stress-shaped YSZ coatings on CP1 polymer substrates. The first set of experiments deposited YSZ coatings on approximately nine-micrometer thick CP1 polymer substrates that were suspended on an aluminum ring in a manner similar to the head on a drum. The substrates were six inches in diameter and were initially flat. The curvatures of the aluminum-ring mounted CP1 polymer substrates were measured using a ZYGO interferometer and determined to be approximately flat with less than one 632.8 nm wavelength of curvature [1; 2]. Figure 7-1 shows a suspended CP1 polymer substrate mounted to an aluminum ring.

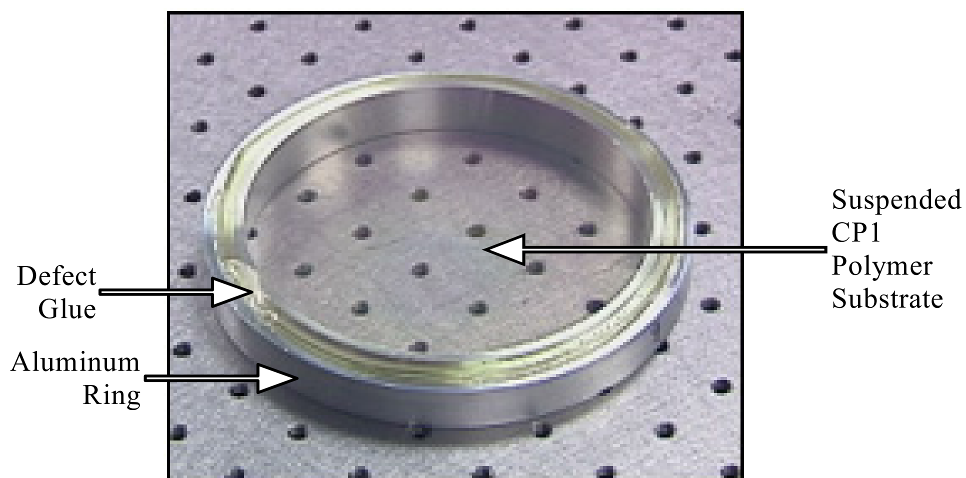

Figure 7-1. Initially Flat CP1 Polymer Substrate Suspended on an Aluminum Mounting Ring [2]

The aluminum ring was fabricated with four threaded holes to facilitate mounting the ring to an aluminum backing plate. The aluminum backing plate allowed the CP1 polymer substrates to be held and rotated inside the PLD chamber in a manner similar to the Hastelloy substrate holder described in Section 3.5. YSZ coatings were then deposited on the CP1 polymer substrates. Multiple depositions using a range of deposition parameters were used to grow YSZ coatings on the CP1 polymer substrates. Table 7-1 lists the deposition parameters that produced undamaged YSZ coatings.

Table 7-1. Deposition Parameters for Initially Flat CP1 Polymer Substrate Suspended on an Aluminum Mounting Ring

Parameter	Value
Laser Fluence	1.38 J/cm^2
Laser Repetition Rate	10 Hz
Ambient Gas	oxygen
Ambient Pressure	50-100 mTorr
Ambient Flow	2.5-3 sccm
Target-to-substrate Distance	76.2 mm
Substrate Bias	-225 V
Target Rotation Rate	15 rpm
Substrate Rotation Rate	15 rpm
Initial Substrate Temperature	~23° C

In addition to depositing YSZ on suspended CP1 polymer substrates, YSZ coatings were deposited by PLD on CP1 polymer substrates that were still attached to the casting mold. The CP1 polymer substrates were cast in a concave Pyrex mold coated with an aluminum silicon dioxide coating, which improved the CP1 casting and eased the release from the mold. The mold was six inches in diameter and parabolic in shape with a six-inch focal length [3]. Figure 7-2 shows the Pyrex mold with a cast CP1 polymer substrate before coating and subsequent mirror release.

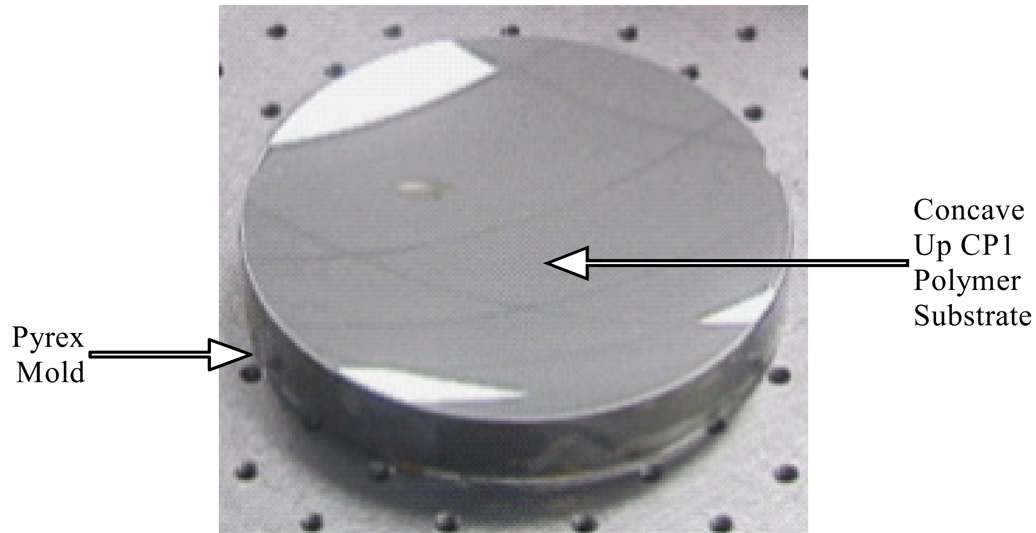

Figure 7-2. Concave Up Pyrex Mirror Mold with Cast CP1 Polymer Substrate [3]

The Pyrex mold was glued to the same aluminum backing plate used to mount the suspended CP1 polymer substrate using Cole-Parmer Extra Fast Setting Epoxy. YSZ coatings were then deposited on the CP1 polymer substrate. Table 7-2 lists the deposition parameters used in a successful YSZ film growth.

Table 7-2. Growth Parameters for Cast CP1 Polymer Substrate Cast in a Concave Pyrex Mirror Mold

Parameter	Value
Laser Fluence	1.38 J/cm^2
Laser Repetition Rate	10 Hz
Ambient Gas	oxygen
Ambient Pressure	150 mTorr
Ambient Flow	7.5 sccm
Target-to-substrate Distance	80.5 mm
Substrate Bias	-225 V
Target Rotation Rate	15 rpm
Substrate Rotation Rate	15 rpm
Initial Substrate Temperature	~23° C
Deposition Length	120 minutes/72000 pulses

After the YSZ coating was deposited, the CP1 polymer substrate was glued to an aluminum mounting ring, as shown in Figure 7-3. After mounting the CP1 polymer substrate was released from the mold.

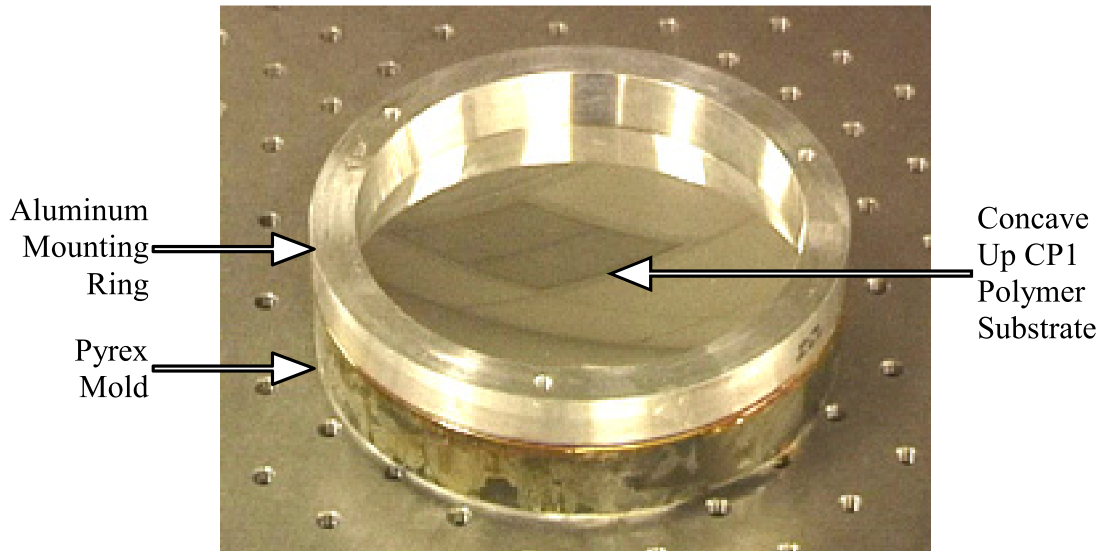

Figure 7-3. YSZ-Coated CP1 Polymer Substrate Still Mounted to a Concave Pyrex Mirror Mold and Aluminum Ring [3]

7.3 Data and Analysis

Coating the suspended CP1 polymer substrate with YSZ using the deposition parameters listed in Table 7-1 did not damage or weaken the CP1 polymer [2]. Other growths of YSZ on suspended CP1 polymer substrates at repetition rates greater than 10 Hz damaged the CP1 polymer substrates, as discussed in Section 4.5. Both a severe deformation in shape and a brownish color of the CP1 polymer substrates indicated the damage. On the undamaged suspended CP1 polymer substrate, a visual inspection of the YSZ coating revealed a taut semi-transparent surface with a yellow tint. The thickness of the YSZ coating grown on the suspended CP1 polymer substrate was thicker at the center

and decreased as the radius increased, as was evident by the variation in color of the YSZ coating. This thickness profile was not intentional but was the result of using the best available iteratively-derived radial profile available at the time, as described in Chapter 6. As described in Chapter 6, no measurement techniques were available to non-destructively measure the thickness of the YSZ coatings on the CP1 polymer substrates. However, diagnostic depositions of YSZ on silicon substrates showed that film thickness was uniform within 16.5% of the maximum film thickness, as shown in Figure 7-4. The radial profile used during this diagnostic deposition and for the suspended CP1 investigation is also shown in Figure 7-4. The magnitudes of the film thickness between the YSZ film on CP1 polymer substrate and the diagnostic depositions may vary due to differences in the substrates. However, the relative film thicknesses should remain constant. Thus, the thickness of the YSZ films deposited on the suspended CP1 polymer substrates vary less than 20% of the maximum film thickness.

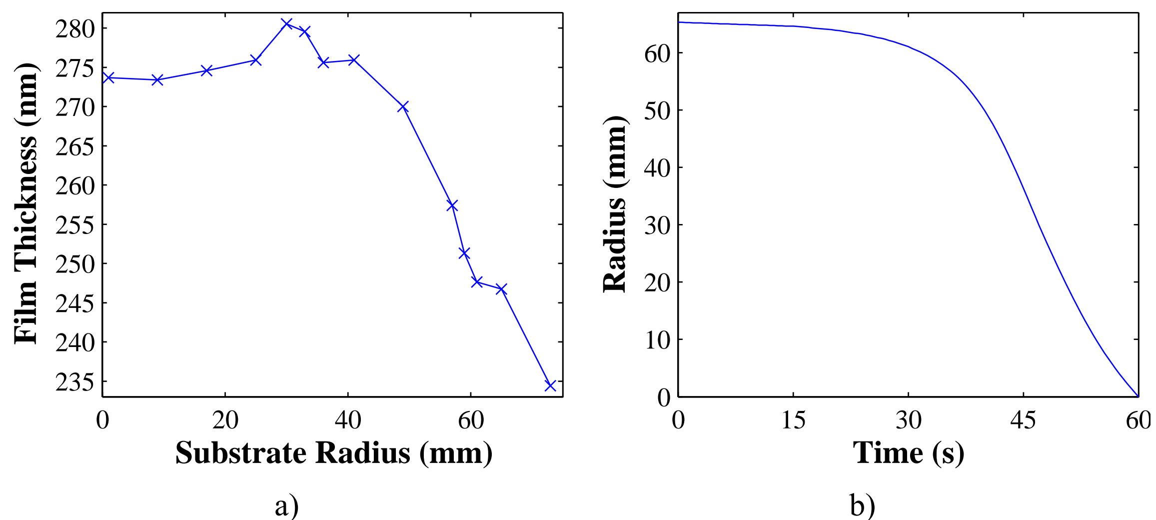

Figure 7-4. YSZ Film Thickness on a 6-inch Diameter Silicon Substrate a) Grown using the Radial Profile b) and the Deposition Conditions Listed in Table 7-1

Despite the variations in thickness, the desired result of a residual stress-shaped surface was present, predominantly in the more thickly coated area near the center. Due to the compressive stress in the YSZ coating, the substrate bows upward so that the resulting shape is convex away from the mounting ring, which was the desired result. Some shape errors caused by the boundary conditions from the mounting ring existed. However, these errors only affected a region within approximately one half inch from the edge of the mirror [2]. Figure 7-5 shows ZYGO interferometer measurements of both the entire mirror and the central 1.3 inch-diameter portion. The curvature apparent in the central area shown in Figure 7-5b) was measured using a ZYGO interferometer and is shown in Figure 7-6.

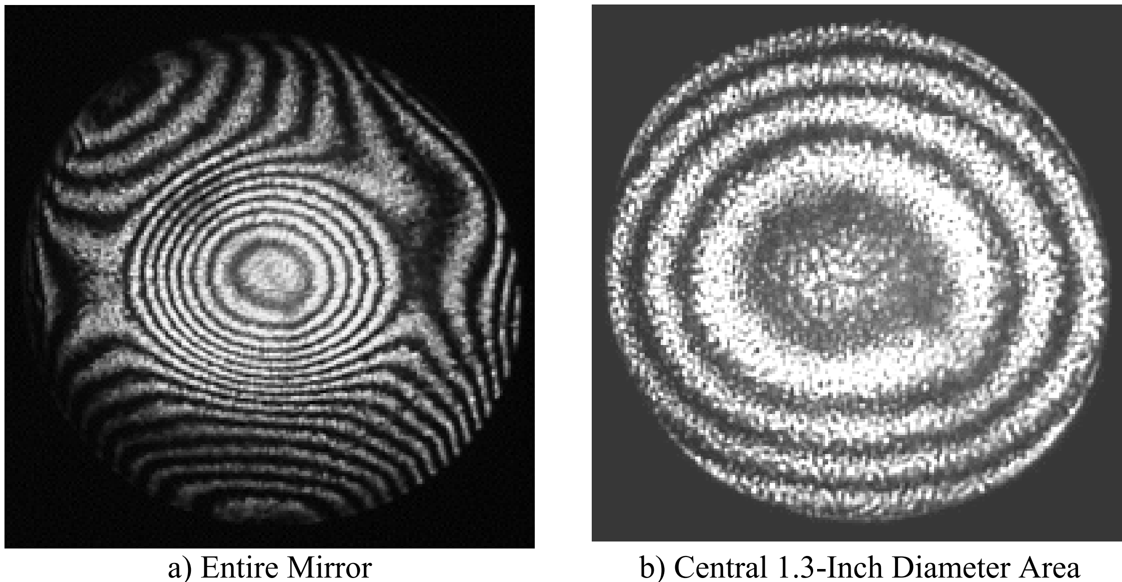

a) Entire Mirror b) Central 1.3-Inch Diameter Area

Figure 7-5. ZYGO Interferometer Images of Initially Flat CP1 Polymer Substrate Suspended on an Aluminum Mounting Ring [2]

Zernike polynomials are commonly used to characterize lens and mirrors [4]. The ZYGO interferometer was able to characterize the curvature of the center portion of the

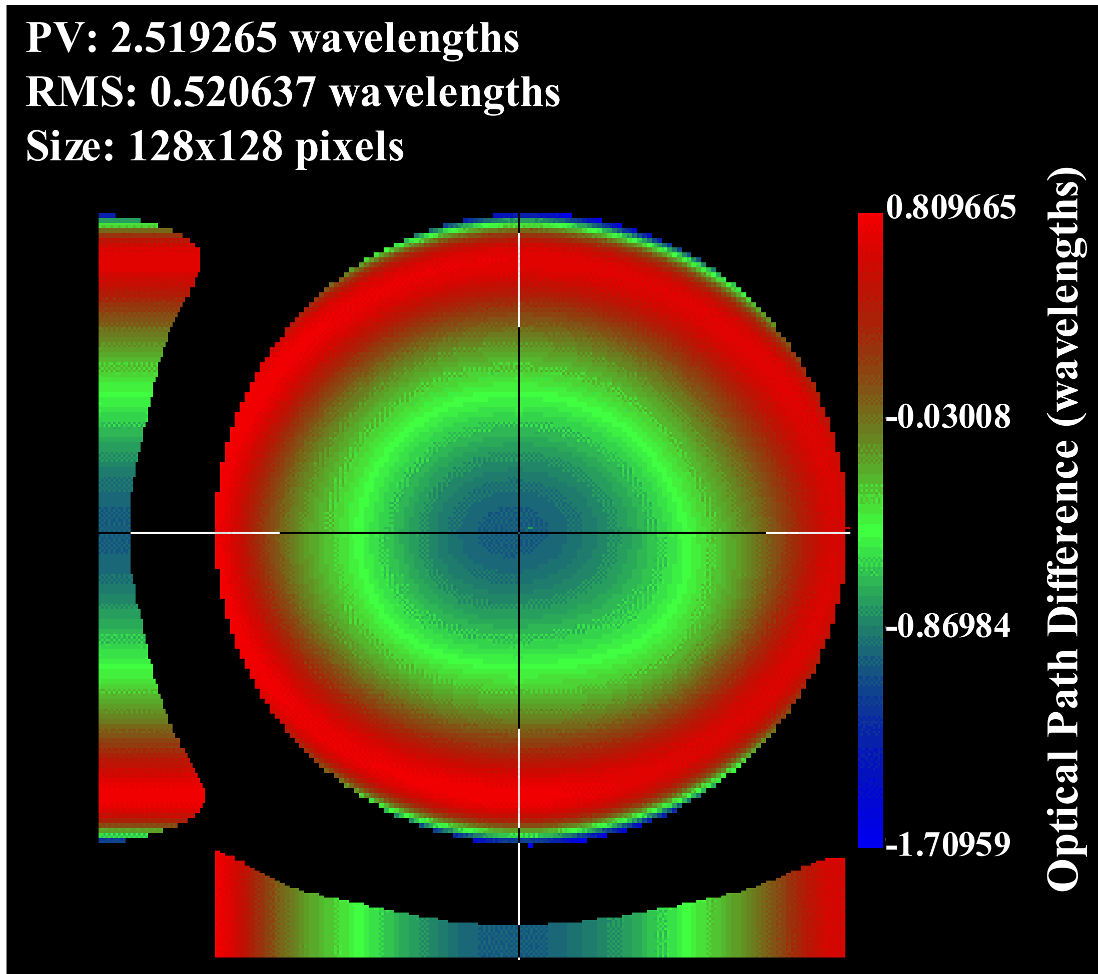

Figure 7-6. Central 1.3-Inch Diameter Optical Path Difference Plot of the Initially Flat CP1 Polymer Substrate Suspended on an Aluminum Mounting Ring Displaying 2.51 Wavelengths (1594.2 nm) Peak-to-Valley Deviation and 0.52 Wavelengths (329.5 nm) Root Mean Square Deviation [2]

mirror in terms of Zernike polynomials coefficients. The most significant coefficient was the focus term, which corresponded to a focal length of 61.3 meters [2]. Although such a long focal length is impractical for use in the intended application, it is sufficient to demonstrate that applying a stressed YSZ coating to an initially flat CP1 polymer substrate produces mirrors with parabolic curvature, as required for the space telescope application described in Chapter 1.

Other growths were performed under conditions similar to those listed in Table 7-1, except for greater oxygen pressure and more laser pulses. As shown in Chapters 4 and 0, decreases in oxygen pressure produces YSZ films on CP1 polymer substrate with more compressive or less tensile stresses. All of the growths performed on suspended CP1 polymer substrates were designed to possess compressive stress. The ability to control the curvature of the CP1 polymer substrate was investigated in parallel with the large area uniformity effort. As such, the YSZ coatings on the suspended CP1 polymer mirrors were non-uniform in thickness. However, for the YSZ coatings described in this chapter, all coatings were within 20% thickness uniformity with the increased thickness near the center of the mirror, as described previously and shown in Figure 7-4. Although the YSZ coatings were not uniform in thickness, the focus term of the Zernike polynomial increased with a decrease in oxygen pressure [1]. The increase in the focus term of the Zernike polynomial corresponds to more curvature in the mirror [4], which results in a mirror with a shorter focal length. In addition to decreasing the oxygen pressure, increasing the YSZ coating thickness increased the Zernike polynomial focal term, which indicated a decrease in the focal length of the mirror [1].

Finally, besides depositing YSZ coatings on suspended CP1 polymer substrates, depositing YSZ coatings using the deposition parameters listed in Table 7-2 did not damage the CP1 polymer substrates that were still attached to the mold. After the CP1 polymer substrate was glued to a mounting ring and removed from the mold, a visual inspection revealed a semi-transparent substrate with obvious curvature [3]. Figure 7-7 displays the YSZ-coated CP1 polymer substrate mounted to an aluminum mounting ring. The CP1 polymer substrate surface shown is the surface that was in contact with the

mirror mold and therefore is convex up in shape. There is a mounting error apparent near the 8 o'clock position. The glue used to mount the CP1 polymer substrate to the aluminum ring "ran" and caused the distortion shown [3].

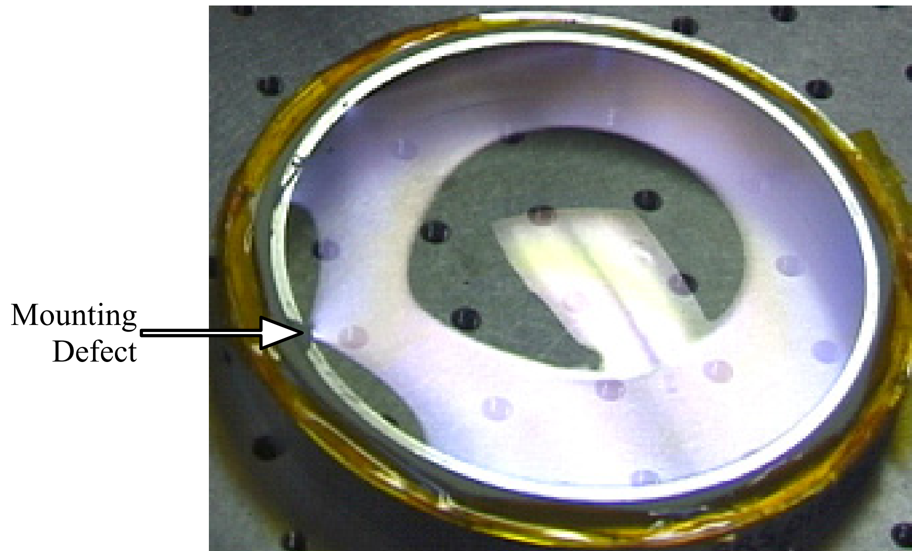

Figure 7-7. Image of Coated and Released CP1 Polymer Substrate Grown in Pyrex Mold and Mounted to an Aluminum Ring with Concave Surface Down [3]

Although the initial visual inspection revealed a substantial curvature, the mirror "pulled flat" within one day. The edges of the mirror were soaked in deionized water to aid in the release from the mold. Analysis has shown that the loss of curvature resulted from changes in humidity during the release/mounting process [3]. Although most of the curvature was lost, Zygo interferometric images were acquired to illustrate the remaining curvature after the mirror was pulled flat, as shown in Figure 7-8.

Five other YSZ films were grown on the CP1 polymer substrates still attached to the mold. These YSZ films were deposited using the default deposition parameters listed in Table 7-2. Two YSZ films exhibited high surface roughness when the laser fluence

was greater than 1.38 J/cm^2. Due to the high surface roughness, these mirrors were not processed further. Another mirror was grown using the identical deposition parameters as those used to grow the mirror shown in Figure 7-8. However, this mirror was destroyed in transit. Another mirror was grown using the deposition parameters listed in Table 7-3. These parameters are identical to those listed in Table 7-2, except for the oxygen pressure, oxygen flow rate, laser repetition rate, and deposition duration. A visual inspection of this mirror revealed similar results to those of the mirror shown in Figure 7-8. The surface roughness was sufficiently smooth, as evidenced by a lack of "haziness" on the YSZ film surface. Also, the CP1 polymer membrane appeared to be undamaged and still adhered to the mold. However, the mirror failed to release from the mold. The cause of the lack of release has been attributed to mounting errors near the edge of the mirror.

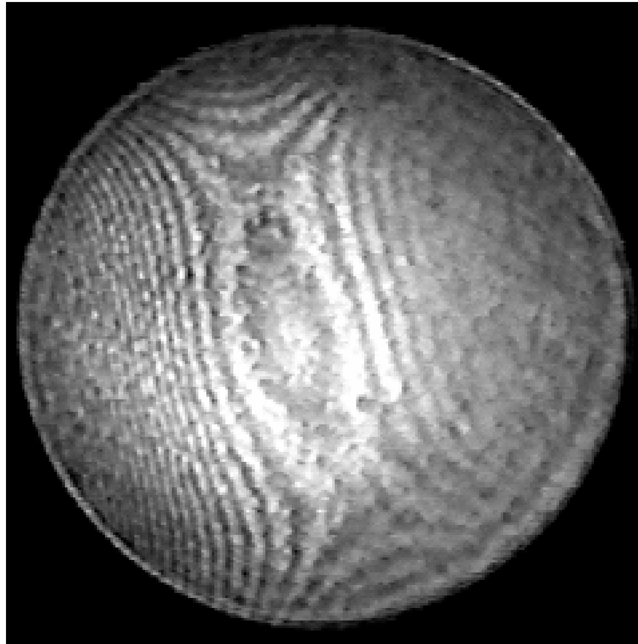

Figure 7-8. Zygo Interferometer Image of an YSZ-Coated and Released CP1 Polymer Substrate Grown in Pyrex Mold and Mounted to an Aluminum Ring [3]

Table 7-3. Growth Parameters for Cast CP1 Polymer Substrate Cast in a Concave Pyrex Mirror Mold

Parameter	Value
Laser Fluence	1.38 J/cm^2
Laser Repetition Rate	40 Hz
Ambient Gas	Oxygen
Ambient Pressure	75 mTorr
Ambient Flow	4.0 sccm
Target-to-substrate Distance	80.5 mm
Substrate Bias	-225 V
Target Rotation Rate	15 rpm
Substrate Rotation Rate	15 rpm
Initial Substrate Temperature	~23° C
Deposition Length	240 minutes/576000 pulses

7.4 Conclusion

As described in this chapter, YSZ films were deposited on six-inch diameter CP1 polymer substrates without damage to the substrate. In addition, the stress in the YSZ films was controllable by adjusting the oxygen pressure in relation to the YSZ film thickness. A decrease in oxygen pressure produced more compressively stressed YSZ films, which resulted in more substrate curvature. The YSZ films were deposited on CP1 polymer substrates that were suspended on an aluminum ring, as well as CP1 polymer substrates that were still attached to the casting mold.

The YSZ films that were deposited on the suspended CP1 polymer mirrors produced curvatures that corresponded to focal lengths as low as 61.3 meters. CP1 polymer mirrors with focal lengths less than 61.3 meters can be grown using the YSZ films that are thicker and/or more compressively stressed. The non-uniform thickness of the YSZ layer limited the area of the mirrors that exhibited curvature to the central 1.5-

inch diameter region. Further investigation should be performed by repeating the experiment with the suspended CP1 polymer substrates using the current state-of-the-art uniform thickness techniques, as described in Chapter 6. These further investigations are described in Chapter 8. The principal drawback to depositing YSZ films on the suspended CP1 polymer mirrors is the lack of heat dissipation that limits the maximum laser repetition rate to 10 Hz. The low laser repetition rate requires longer deposition time to grow the thick YSZ films necessary to sufficiently deform the mirrors. Further investigation into methods to overcome this heat dissipation problem is needed and is described in more detail in Chapter 8.

To overcome the heat dissipation problem, depositing YSZ films on CP1 polymer mirrors that are still attached to the casting mold was investigated. The laser repetition rate was increased to 40 Hz without any damage to the substrate. However, mounting problems currently limit the effectiveness of this solution. Several YSZ films were grown on CP1 polymer mirrors that were still attached to the casting mold. Two attempts were made to mount these YSZ-coated CP1 polymer mirrors. The first attempt suffered from both mounting defects and mounting-induced stress, which limited the effectiveness of the YSZ coating to shape the mirror. During the second attempt, the mirror did not release from the mold. Again, mounting error was cited as the problem. The mounting issues limit the potential of this deposition technique and are being addressed by SRS Technologies in an ongoing research effort.

As stated in Section 7.1, the goal of the research presented in this chapter was to desirably affect the shape of the CP1 polymer substrates using PLD-grown YSZ films. This goal was achieved. However, the modeling and further research necessary to apply

this shape-modifying technique to a final product that meets the specifications of the intended application was not part of this goal and is outside the scope of this research. Currently, SRS Technologies is pursuing finite-element modeling of the film stress and substrate curvature relationship, as well as investigating improvements in their mounting and release technology. Both the modeling and mounting improvement efforts are crucial to the maturation of the stress-shaped polymer mirror concept, as described in Chapter 8.

Bibliography

1. Patrick, Brian. Optical Engineer, SRS Technologies, Huntsville AL. Personal Correspondence. 27 November 2001.

2. Patrick, Brian. Optical Engineer, SRS Technologies, Huntsville AL. Personal Correspondence. 20 October 2002.

3. Patrick, Brian. Optical Engineer, SRS Technologies, Huntsville AL. Personal Correspondence. 22 October 2002.

4. Malacara, Daniel. *Optical Shop Testing*. New York: John Wiley & Sons, 1978.

8 Conclusion, Contributions, and Recommendations

8.1 Introduction

As stated in Chapter 1, the goals of this research were to produce controlled-stress, large-area, pulsed-laser-deposited yttria stabilized zirconia (YSZ) thin films on CP1 polymer substrates and to investigate relevant sensors for control of the PLD process with respect to thin film stress. This chapter describes the successful completion of these goals, as well as the associated accomplishments and contributions. In addition, areas that deserve further investigation are described in Section 8.3.

8.2 Conclusion and Contributions

The stress of yttria stabilized zirconia (YSZ) deposited by pulsed laser deposition (PLD) can be controllably varied between compressive and tensile stress. The combination of deposition parameters, namely target-to-substrate distance, ambient pressure, and laser fluence, determine the magnitude and direction of the film stress. Open-loop control is achieved by holding these relevant deposition parameters constant. The ability to control stress enables a multitude of unique devices to be fabricated. For example, the residual stress in the structural thin film layers for microelectromechanical systems (MEMS) devices were either tolerated or attempts were made to remove the stress through various techniques, such as post-deposition annealing. However, the research presented in this dissertation shows that the net YSZ thin film stress can be controlled. Therefore, the YSZ film stress is capable of becoming a desirable design

parameter. For example, the application described in Chapter 1 requires a uniform predetermined film stress over the substrate. Also, many MEMS devices can benefit from the use of controlled stress films for device operation and self-assembly. In addition, the stress control scheme and relevant deposition parameters are not specific to the PLD growth of YSZ. Thus, the controlled-stress deposition technique described in this dissertation can be extended to other materials.

In addition to the ability to deposit controlled stress YSZ films, an applicable theory has been developed to characterize the relationship among the relevant deposition parameters and their effect on the YSZ film stress. This theory provides the PLD researcher with a mechanism to optimize other design constraints while still maintaining the desired film stress. Since the relationship among the relevant deposition parameters has two degrees of freedom, deposition parameters can be adjusted to compensate for variations among the variety of PLD systems. Previous to this research, deposition conditions were reported as optimal for a given PLD system without any means to transition these parameters to other PLD systems. The physics-based theory described in Chapter 4 allows for researchers to characterize the film stress dependence of their unique PLD system and possibly different thin film material systems with a minimum of three well-chosen deposition parameter combinations.

A shifted center-of-mass Maxwell-Boltzmann (SCMMB) distribution adequately models the plume time-of-flight, as observed by optical emission sensors. The streaming velocity parameter from the SCMMB distribution predicts the stress in the YSZ film. In addition, real-time fitting software was developed to enable closed-loop control of the plume by varying the laser excitation energy. Previous to this research, most PLD

process control focused on the most probable velocity, which is the velocity associated with the maximum emission signal intensity. However, this research has shown that the most probable velocity is not well suited to PLD process control for YSZ film stress. Real-time fitting of a SCMMB distribution produces streaming velocities that are at least one order of magnitude more sensitive to YSZ film stress. With the exception of sensors that monitor the deposited film during growth, the plume is the final measurable PLD parameter. As such, closed-loop control using a plume diagnostic sensor provides much greater run-to-run stability than depositions performed while holding deposition parameters constant. The second overarching goal of this research was to investigate applicable sensors for the control of film stress. The optical emission time-of-flight sensor system sufficiently satisfies this goal.

The optical emission time-of-flight closed-loop control of the YSZ plume dramatically enhances the current state of PLD process control. The maturity of PLD as a common deposition technique requires such sensor systems that can be used to translate results among dissimilar PLD systems. Currently, most PLD systems rely on open-loop deposition parameter control, such as ambient pressure, laser fluence, etc. Application-independent process-monitoring sensor systems are required to translate the system-specific deposition parameters into process parameters, such as plume's streaming velocity and effective temperature. The streaming velocity represents a statistic average velocity, while the effective temperature indicates the spread of the velocities. As such, both the streaming velocity and the effective temperature provide a process control metric that can be used to reproduce the results from one PLD system to another. Without this ability to reproduce results among dissimilar PLD system, the "optimal" results quote in

the current literature cannot be universally applied to all PLD systems. If these "optimal" results were presented in terms of process parameters rather than deposition parameters, PLD would be a much more mature deposition technique. Thus, correlation between streaming velocity from the optical emission sensor system and the YSZ film stress has a much greater impact since these results can be easily reproduced on another PLD system equipped with a similar optical emission sensor system.

In addition to the controlled-stress deposition of YSZ, large-area depositions were performed, which yielded YSZ films on six-inch diameter substrates with total thickness variations of less than ten percent and a standard deviation of less than three percent of the total film thickness. Previous to this research, most large-area PLD plume rastering techniques used *ad hoc* methods to grow uniform thickness films. Chapter 6 presents both an empirical and analytical approach to large-area depositions by PLD. The radial location of the laser foot on the target as a function of time (radial profile) corresponding to the best effort from the empirical approach was shown to be equivalent to the radial profile derived from the analytical approach. The iterative correction method used in the empirical approach assumed that ablating the target at a given target radial location would produce a film thickness distribution centered about a substrate radial location equal to the given target radial location (equal radius assumption). Thus, the radial profile was modified so that the dwell time about a given target radial position was increased. This radial profile modification was assumed to increase the relative film thickness about the equivalent substrate radial location. This iterative correction method generated radial profiles that continued to improve the YSZ film thickness uniformity up to the "best effort" growth described in Chapter 6. Further iterative corrections beyond

this "best effort" growth produced films with more variation in the film thickness. Thus, the iterative method did not converge, which indicated that the equal radius assumption was invalid. Although the iterative corrections failed to converge, the best effort radial profile produced an YSZ film that varied less than ± 5% of the mean film thickness (172.8 nm), which was sufficient to satisfy the needs for the application described in Chapter 1. Also, the analytical approach highlighted the invalid assumption and provided a more accurate algorithm for generating the iterative corrections. The rastering methodology used in the deposition of large-area YSZ films on silicon can be directly applied to other materials. Furthermore, the rastering methodology has no limits as to the scale of the substrate. The only limiting factor for substrate diameter scalability is the physical constraints of the deposition system. The rastering methodology is also not limited to uniform thickness deposition. Almost any thickness profile that possesses radial symmetry can be grown using the rastering methodology described in this research. Part of the goal of this research was to control the shape of the large-area CP1 polymer mirrors. These uniform thickness depositions satisfy the large-area aspect of this goal.

Controlled-stress YSZ films can be deposited on CP1 polymer substrates without damage to the CP1 polymer. YSZ films were successfully deposited on both the released and unreleased CP1 polymer substrates. In addition, the controlled-stress YSZ films deposited on the released CP1 polymer substrates were shown to modify the shape of the initially flat substrates. The shaped changed from an optically flat surface to a parabolic shape over the center section of the CP1 polymer substrate. One of the two overarching goals of this research was to produce parabolic membrane mirrors using stress-shaped

film depositions. The ability to desirably modify the shape of the CP1 polymers satisfies this goal.

8.3 Future Research Recommendations

Although all of the goals of this research effort were accomplished, several areas of research that warrant further investigation were uncovered. These areas are listed below in chapter order.

The theory described in Chapter 4 correlates the affect of deposition parameters to YSZ film stress. This correlation should not be limited to the specific PLD system used in this research nor YSZ. Therefore, the research should be re repeated using other materials and other PLD systems.

Chapter 5 shows that the streaming velocity predicts film stress over a limited range of target-to-substrate distances and oxygen pressures. Only target-to-substrate distances between 55 and 120 could be investigated without extensive modifications to the current PLD system. The existing PLD system should be modified to include other target-to-substrate distance ranges, particularly the 0 to 55 mm range. Alternately, the investigations presented in Chapters 4 and 5 could be repeated using a PLD system that allows a larger target-to-substrate distance range to be investigated. For films that exhibit no curvature, the oxygen pressure is highly correlated with the target-to-substrate distance. Therefore, an increased target-to-substrate distance range investigation will include an increased oxygen pressure range.

The optical time-of-flight sensor system described in Chapters 3 and 4 measures the optical emissions of particles passing through a spatial region located at a fixed distance from the target. However, only a fraction of the particles that pass through the

monitored spatial region emit. Thus, the optical emissions are indicative of particles passing through some spatial region, but the lack of emissions does not imply a lack of particles, only a lack of emitting particles. In addition, not all deposition conditions are conducive to particle emissions. Therefore, further investigation should be conducted using a sensor that monitors all particles passing through some spatial region.

The bimodal plume emissions distributions were observed at various distances from the target surface and under several oxygen pressures, as described in Chapter 5. Such bimodal plume emission distributions have been reported in the current literature. However, the source of the bimodal plume emission distributions has not been sufficiently explained and warrants further investigation.

The rastering method derived in Chapter 6 should directly apply to other materials and substrates larger than six inches in diameter. Therefore, the experiments presented in Chapter 6 should be repeated with larger substrates and other target materials. Also, the empirical approach to plume rastering should be performed again using the valid mapping function, as described in Chapter 6. Applying the valid mapping function to the iterative correction process can reduce the film thickness variations reported previously.

For suspended CP1 polymer substrates, the dominant problem is currently heat dissipation, as described in Chapter 7. The intrinsic heat from the plume can damage the CP1 polymer substrates when the laser repetition rate is greater than 10 Hz. Although depositions are feasible at laser repetition rates less than or equal to 10 Hz, increases in the substrate diameter will require substantial increases in the deposition time. Thus, higher laser repetition rates are extremely desirable. More research into an appropriate heatsink for the released CP1 polymer substrates is needed.

For the unreleased CP1 polymer substrates described in Chapter 7, the limiting factor is the ability to mount the YSZ-coated substrate to a mounting ring without inducing damage and/or defects. Further polymer mounting and release research is needed.

Modeling and further growths of YSZ on CP1 polymer substrates are required to refine the shape of the stress-shaped CP1 polymer mirrors. YSZ films grown on initially flat suspended CP1 polymer substrates produced polymers mirrors with a 61.3-meter focal length. The compressive stress in the YSZ coating should be increased in order to decrease the focal length. Thus, more compressively-stressed YSZ thin films should be grown on suspended CP1 polymer substrates. In addition, other coating materials should be investigated.

Appendix A *In-situ* Raman Spectroscopy During the Pulsed Laser Deposition of Silicon Carbide

A.1 Overview

Chapters 4 through 7 focused on developing and producing stress-controlled yttria stabilized zirconia (YSZ) films deposited by pulsed laser deposition (PLD) on both silicon and CP1 polymer substrates. Initially, the stress in the films was controlled via maintaining constant pre-determined deposition parameters. The next step included YSZ plume monitoring to compensate for slight variations in deposition conditions. However, the closed-loop control was limited to the YSZ plume. Measurements of plume parameters were shown to be correlated with thin film parameters, such as stress. However, the thin film parameters were not directly measured until after the PLD growth was complete (*ex-situ*). Directly measuring the thin film parameters of interest as the thin film is deposited will provide better control over the deposition process. Thus, the closed-loop process control should incorporate non-intrusive thin film stress measurements during the PLD growth process. Materials that emit Raman scattered light are defined as Raman-active materials. Raman spectroscopy provides the ability to non-destructively measure the stress in Raman-active thin film materials, such as silicon carbide and YSZ. In addition, Raman spectroscopy offers the possibility to perform this stress measurement *in-situ*. Therefore, the goal of the research presented in this appendix is to investigate the applicability, benefits, and limitation of *in-situ* Raman spectroscopy

for stress measurement with respect to closed-loop feedback for controlled-stress film depositions.

All goals of this appendix were met. SiC was chosen as the thin film material to be grow using PLD and investigated using Raman spectroscopy. The ability to grown SiC thin films with controlled stress would enhance current SiC microelectromechanical systems (MEMS) projects within Air Force Research Laboratory Materials and Manufacturing Directorate (AFRL/ML) [1]. The acquisition of SiC Raman spectra was demonstrated under typical SiC PLD growth conditions using an approximately 500-μm thick SiC sample. In addition, the ability to acquire Raman spectra during the PLD growth process was demonstrated with the growth of silicon carbide (SiC) on silicon substrates. However, only the silicon substrate's Raman spectra were acquired using both *in-situ* and *ex-situ* Raman spectroscopy. The SiC thin films did not absorb the 532-nm Raman excitation laser sufficiently to produce significant Raman scattering. However, for the SiC thin films grown up to 3-μm thick by PLD on silicon substrates, the silicon Raman spectra was observable throughout the deposition process. The silicon Raman spectra acquired during the growth of SiC showed that the Raman mean wavenumber corresponding to silicon (nominally 520 cm^{-1}) shifted with temperature and also with the growth of the SiC thin film on the silicon substrate. However, the shift in the silicon Raman mean wavenumber due to stress could not be computed without an accurate silicon temperature measurement, which was not available. The experiments were repeated with yttria stabilized zirconia (YSZ). As with SiC, the YSZ Raman spectra were not acquired with either *in-situ* or *ex-situ* Raman investigations.

In order to get an accurate temperature measurement, an analysis of the Stokes to anti-Stokes intensity ratio for the silicon Raman spectra was performed. This analysis showed that the intensity ratio could be used to calculate the silicon temperature. These calculations were verified against a thermocouple-based temperature measurement system. Again, silicon Raman spectra were recorded during the PLD growth of a SiC thin film on a silicon substrate. Post-deposition analysis of the Stokes to anti-Stokes intensity ratio calculated showed that the calculated silicon temperature was 30-35% lower than the heater chamber temperature. Since SiC is an excellent thermal conductor, these results were not expected. Thus, no acceptable silicon temperature measurement was available. As stated previously, the portion of the Raman mean wavenumber shift due to stress cannot be calculated without an accurate silicon temperature measurement.

Modifications to the *in-situ* Raman spectroscopy system to change the Raman excitation wavelength from 532 nm to a ultra-violet (UV) excitation source should allow the acquisition of SiC Raman spectra from the thin film. Given this change to the *in-situ* Raman spectroscopy system and the associated Raman spectra from the SiC thin film, a SiC film stress estimate can be calculated. The research presented in this appendix details the capabilities and limitation of the visible *in-situ* Raman spectroscopy system, as it applies to SiC and YSZ. In addition, the methods, experiments, and equipment apply directly to future *in-situ* UV Raman spectroscopy research.

A.2 Theory

Although a rigorous theoretical background of Raman spectroscopy is not necessary to understand and apply Raman spectroscopy techniques to pulsed laser deposition (PLD) experiments, a general overview of the Raman effect and its origin is

beneficial. The remainder of this section presents an overview of Raman spectroscopy, as well as typical Raman spectroscopy system components, benefits of Raman spectroscopy, Raman spectra for silicon and silicon carbide materials, material stress calculation from Raman spectroscopy measurements, and material temperature calculations from Raman spectroscopy measurements.

A.2.1 Raman Effect Phenomenon

When monochromatic light is incident upon a material, some of the light is absorbed, some is reflected, some is transmitted, and some is scattered [2; 3]. Reflection, absorption, and transmission are dependent on the angle of incidence and as such are specified by the rules of classic optical theory [4]. However as the term "scattered" implies, the scattered light is not directionally limited and is the result of the interaction between the sample molecules and the incident light. As a result of this interaction, the sample molecules may absorb energy from the incident light as vibrational, rotational, or electronic energy [5]. Raman spectroscopy measures the vibrational energy absorption or emission through changes in the spectra of the scattered optical emissions. Figure A-1 illustrates the interaction between the light and the molecular system that are relevant to Raman spectroscopy. Monochromatic excitation light is incident upon a sample material, and the sample material both reflects and scatters the incident light. Some of the absorbed incident light results in vibrational energy changes in the sample material, as shown in Figure A-1 [2; 3].

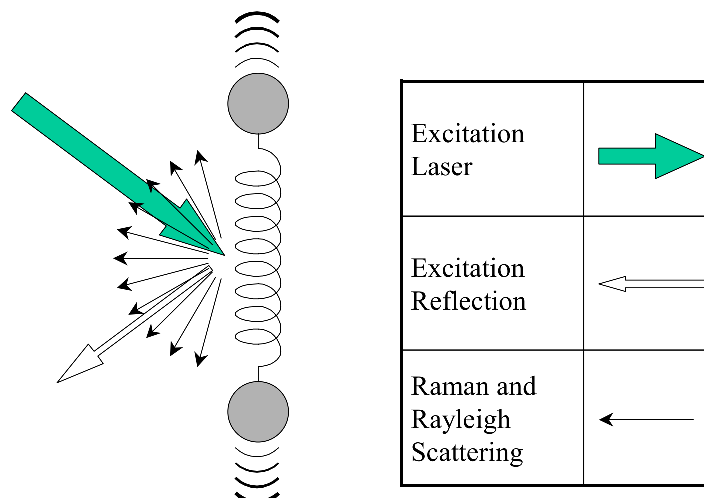

Figure A-1. Schematic Representation of Molecular Motion and Raman Scattering

The scattered portion of light can be divided into two types: Rayleigh and Raman. Rayleigh scattering denotes the condition in which both the incident and scattered light occur at the same frequency. Raman scattering refers to the condition in which the scattered light occurs at a different frequency than the incident light. Scattering occurs when a photon collides, either elastically or inelastically, with a sample molecule [2; 5]. The molecule has some initial energy E_i before the collision and some final energy E_f after the collision. Through the photon absorption, the molecule gains energy $E_{absorbed} = h \cdot v_0$ where h is *Planck's constant* and v_0 is *absorbed photon frequency*. After the collision, the molecule may transition to a lower energy level by emitting a photon with energy $E_{emitted} = h \cdot v$ where v is *emitted photon frequency*. Figure A-2 illustrates the process of photon absorption and emission by a molecule.

Thus, the molecule possesses some final energy $E_f = E_i + E_{absorbed} - E_{emitted}$. If E_i equals E_f the collision is said to be elastic, and $E_{absorbed}$ must equal $E_{emitted}$. In an elastic collision, the emitted photon has the same frequency as the absorbed photon, which is defined as Rayleigh scattering.

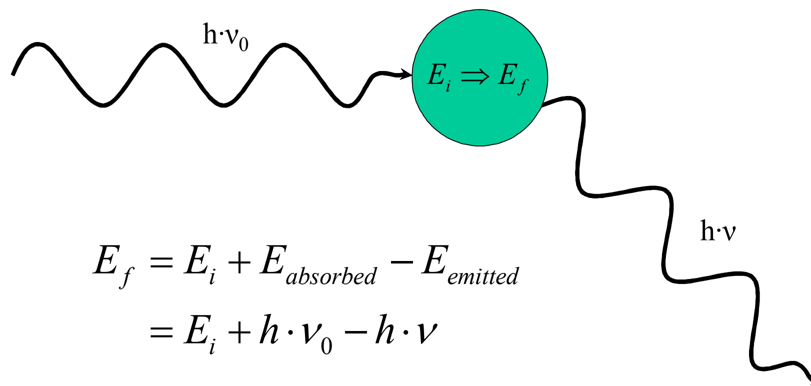

Figure A-2. Interaction Between a Molecule and a Photon Diagram

However, when E_f is not equal to than E_i, the collision is said to be inelastic, and the photon is emitted at a different frequency than the incident photon. Inelastic collisions produce Raman scattering. Raman scattering can be subdivided into two types: Stokes and anti-Stokes Raman scattering. If E_f is greater than E_i, then the emitted photon's frequency is shorter than the absorbed photon's frequency, and the scattering process is defined as Stokes Raman scattering. If E_f is less than E_i, then the emitted photon's frequency is longer than the absorbed photon's frequency, and the scattering process is defined as anti-Stokes Raman scattering. Figure A-3 illustrates the energy band diagram and relevant energy transitions for light scattering. E_0 and E_1 are electronic states, while v and v' are vibrational states. In addition, the abbreviations *IR*, *R*, *S*, and *A* denote infrared absorption, Rayleigh scattering, Stokes Raman scattering, and anti-Stokes Raman scattering, respectively. The dotted lines depict "virtual energy levels." Virtual energy level refer to energy level are not "real" and therefore cannot be populated. Since the virtual energy levels are not allowed, a photon must be quickly re-emitted.

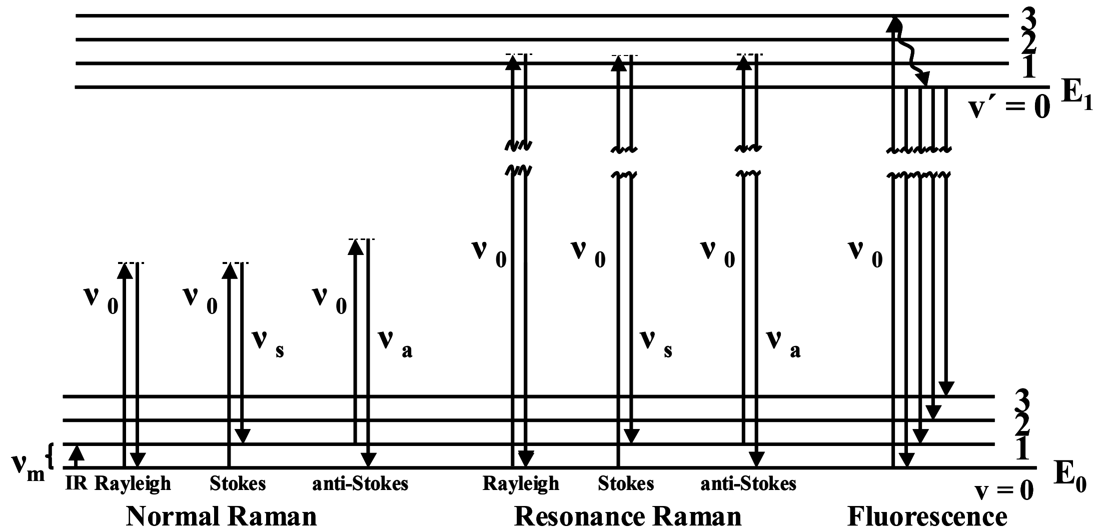

Figure A-3. Energy Levels for Normal Raman, Resonance Raman, and Fluorescence Spectra

The Stokes and anti-Stokes Raman frequency shifts are independent of the incident light frequency. As shown in Figure A-3, the difference between the excitation frequency and the Stokes/anti-Stokes scattering frequencies equals the vibrational frequency ν_m, as shown in Equation (A-1) [2; 3; 5]:

$$\nu_m = \nu_0 - \nu_s = \nu_a - \nu_0 \qquad \text{(A-1)}$$

where ν_s is *Stokes Raman frequency* and ν_a is *anti-Stokes Raman frequency*. Both the Stokes and anti-Stokes Raman frequency shifts provide the same information about the vibrational frequency ν_m. Under normal atmospheric conditions and temperatures, Stokes Raman scattering signals are stronger than anti-Stokes scattering signals [2; 3]. As such, Raman frequencies in current literature are often specified in terms of relative frequency, which implies the absolute value of the shift in frequency from the incident light frequency to Stokes Raman scattered frequency [3].

A special case of Raman scattering, denoted "Resonance Raman" scattering, is also illustrated in Figure A-3. Resonance Raman scattering differs from normal Raman scattering in that the virtual energy level coincides with the electronic energy level. Conditions corresponding to Resonance Raman enhance the Raman effect by a factor of 10^3 to 10^5, as compared to normal Raman scattering [2].

In addition to resonant Raman scattering, Figure A-3 illustrates two other effects: infrared absorption and fluorescence. The vibrational frequency v_m can also be measured using infrared spectroscopy, which measures the absorption of light as a function of frequency. Infrared spectroscopy typically reports the percentage transmission in terms of incident light frequency. Incident light frequencies corresponding to the vibrational frequency v_m are more strongly absorbed and appear as sharply defined attenuations in the percentage transmission [2]. Fluorescence describes the transition of an excited state molecule to the lowest excited vibrational state via thermal decay, followed by a photon emission during the transition to one of the ground vibrational states. The molecule is typically placed in the excited state by the absorption of an excitation photon. Fluorescence appears as an increase in the background spectra, which can significantly decrease the signal to noise ratio (SNR) of the Raman spectral acquisition [2; 3].

A.2.2 Raman Spectroscopy Instrumentation

Typical Raman spectroscopy instrumentation consists of five basic elements: excitation source, illumination and collection optics, sample holder, monochromator or spectrometer, and detection system [2]. The remainder of this section describes some of

these elements in more detail. The specific instrumentation used in this research is described in Section 3.10.

A.2.2.1 Excitation Source

The most common excitation source in use at this time is the laser. Several characteristics of current laser technology enhance the benefits of Raman spectroscopy. These beneficial characteristics include: high power, highly monochromatic beams, small beam diameters, linear polarization, and a wide range of available wavelengths. Many continuous wave (CW) lasers are available with output power ranging from tens of milliWatts up to several Watts. In addition, pulsed lasers, which are used for time-resolved and UV resonance Raman spectroscopy, are currently capable of producing 10-100 megaWatts [2]. Since the Raman phenomenon is a relatively weak effect, a high-power incident light source, such as a laser, greatly enhances the acquired Raman spectra's SNR. The second advantage of using a laser as the excitation source is the highly monochromatic beam. For example, an argon-ion laser produces beams with an approximately 0.1 cm^{-1} bandwidth. Also, most extraneous laser lines are much weaker than the primary beam, which enables most unwanted lines to be removed using optical filters or premonochromators. Next, the small spot size of the laser beam enables small samples to be studies. Utilizing Raman microscopy, samples as small as two micrometers in diameter can be studied. Lasers are almost completely linearly polarized, which is the fourth desirable characteristic. Linear polarization enables the symmetry properties of Raman-active vibrations, which are required for band assignment information, to be investigated using Raman spectroscopy. Lastly, lasers are available in

a wide range of wavelengths from UV to IR. IR Carbon dioxide lasers, near–IR Nd:YAG lasers, HeNe red lasers, argon-ion green lasers, and UV excimer lasers exemplify a small subset of the available wavelengths [2].

A.2.2.2 Illumination and Collection Optics

The Raman effect is a relatively weak phenomenon. Approximately one out of every 10^6 photons that are incident on the sample will produce Raman scattering. Thus, the laser beam should be focused onto the sample. In addition, the resulting Raman scattering must be efficiently collected, typically using both a collection lens and a focusing lens. The light gathering power of the collection lens, expressed in terms of F number, is of particular importance to the efficiency of the optical system. The F number is described by Equation (A-2) [2]:

$$F = \frac{f}{D} \quad \left(\mathrm{mm}/\mathrm{mm} \right) \tag{A-2}$$

where F is the *F number* (mm/mm), f is the *focal length of the lens* (mm), and D is the *lens diameter* (mm). Lower F numbers correspond to a greater light-gathering power of the lens [2].

In addition to a collection lens and a focusing lens, many optical systems include optical filters to attenuate unwanted light frequencies. Holographic notch filters are capable of blocking the Rayleigh scattered light and reflected light by attenuating a contiguous range of frequencies near the excitation frequency. Holographic notch filters can reduce the unwanted frequencies by up to six orders of magnitude, as compared to the frequencies that the filter passes [3].

A.2.2.3 Monochromator or Spectrometer

Monochromators limit the spectral components of the scattered light to be analyzed, typically by diffraction. Diffractive elements, usually gratings, angularly disperse the collected light according to frequency. However, undiffracted light scattered from the face of the grating inside the monochromator reduces the signal to noise ratio (SNR) of the Raman signal. Arranging two or more monochromators in tandem, so that the output of a preceding monochromator is coupled to the input of a subsequent monochromator, can reduce this undiffracted light. Thus, the monochromator is typically defined in terms of the number of gratings, such as a single, double, or triple monochromator. Figure A-4 shows the schematic of a double monochromator. The mirrors M1 through M5 image the entrance slit onto a focal plate near the exit slit. The exit slit limits the optical output of the monochromator to a narrow spectral window. This narrow spectral window is swept across the spectrum by varying the angular orientation of the gratings [2; 5].

The gratings are typically moved using either a gearbox driven by a motor or directly with a stepper motor and electronic angular decoder. The direct-drive stepper motor and electronic angular decoder system eliminates gear backlash and provides more accurate angular positioning of the gratings. Thus, the monochromator acquires the spectra sequentially, rather than simultaneously, by recording the optical intensities at the exit slit in terms of angular orientations of the gratings. A spectrometer is a special type of monochromator that replaces the exit slit with a multichannel detector to acquire a block of the spectrum simultaneously. The multichannel detector behaves like an array

of exit slits and multiple single channel detectors [2; 5]. Single channel and multichannel detectors are described further in Section A.2.2.4.

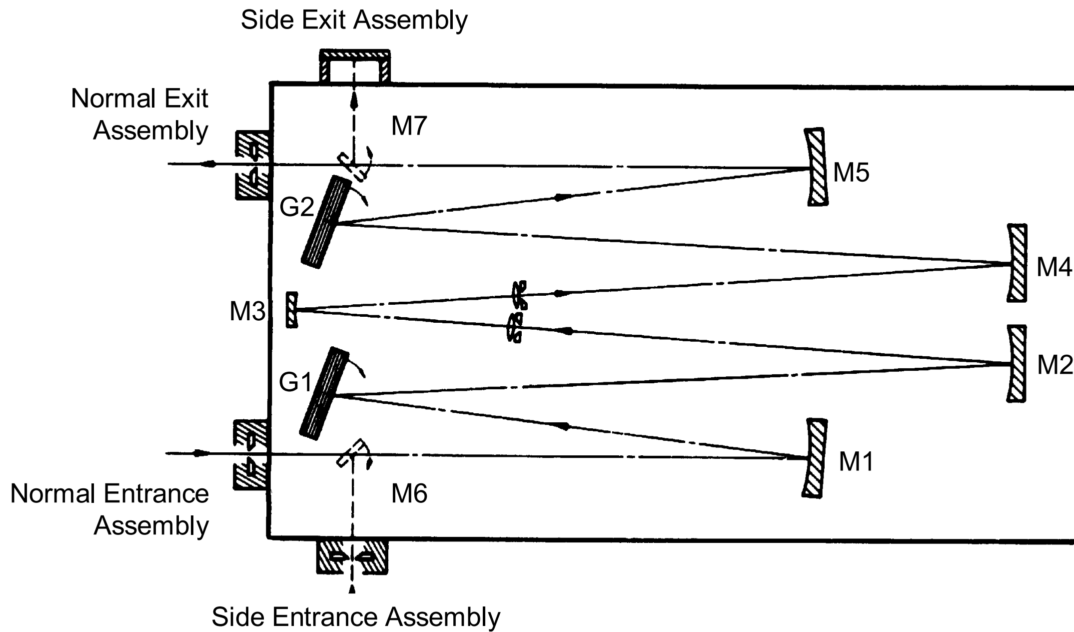

Figure A-4. Double Monochromator Schematic [2]

A.2.2.4 Detection

A photomultiplier tube (PMT) typically performs the function of single channel detector that monitors the output at the exit slit of the monochromator, as described in Section A.2.2.3. The PMT's electrical output is processed to produce either photon counts per second or amplified and averaged over time to produce DC current measurements. The photon count method provides maximum sensitivity from the PMT, by more than a factor of ten over the DC current detection method. The photon counting method has a disadvantage in that the maximum photon arrival rate is limited. However, this limitation is generally not applicable to the relatively weak Raman signals [2].

Early spectroscopy employed photographic plates as multichannel detectors. Photographic plates were placed at the output of the spectrometer and recorded the photon intensity over long integration periods. The time to develop and analyze the photographic plates limited the applicability of Raman spectroscopy as a diagnostic technique [2].

Currently, most multichannel detectors are charge-coupled devices (CCDs). CCDs have many advantages over the detection systems described previously, which include the following [2]:

- CCDs are available with a large number of pixels, typically numbering into the millions of pixels per device.
- CCD arrays are tightly spaced with pixel sizes on the order of 6 to 30 micrometers.
- CCDs have relatively low readout noise compared to most other multichannel detectors
- CCDs have high quantum efficiencies.
- CCDs detect over wide wavelength detection ranges.

A.2.3 Benefits of Raman Spectroscopy

Molecules vibrate only along the chemical bond connecting the nuclei. The vibrational frequency measured using Raman spectroscopy depends upon the strength of these bonds and the mass of the nuclei. As such, Raman spectroscopy can be used to identify the composition of a sample as well as other information, such as stress (see Section A.2.4 and A.2.5) and material polytype (see Section A.2.5). In addition, Raman

spectroscopy has several benefits over other analytical techniques, which include the following:

- Raman spectroscopy is non-destructive and does not require any special sample preparation, such as thinning or patterning [3].
- Only small quantities of a sample are required for analysis [2].
- Raman spectroscopy may be compatible with *in-situ* stress monitoring [3].
- The technique is fast and relatively simple [3].

A.2.4 Silicon Raman Spectroscopy and Stress

As stated previously, the Raman spectrum is unique to each sample material. In addition, samples containing more than one constituent produce Raman spectra containing a number of peaks. Thus, Raman-active materials may be identified and/or characterized by their associated Raman spectra. For example, Raman spectroscopy has been successfully applied to the effective measurement of mechanical stress in silicon [3; 6; 7; 8]. The technique depends on the type of stress, such as uniaxial or biaxial, and the direction in which the Raman spectra is acquired relative to the sample surface, such as normal or parallel to the sample surface [3]. The calculation for stress involves a comparison between the Raman frequency shift of unstressed silicon and the Raman frequency shift from the sample being measured. The Raman spectrum of silicon has one peak located 520 cm^{-1} from the excitation frequency. Figure A-5 shows a typical Raman spectrum for bulk silicon acquired using a Renishaw model 2000 Raman spectrometer equipped with a Leica microscope and a 514.5 nm argon-ion laser.

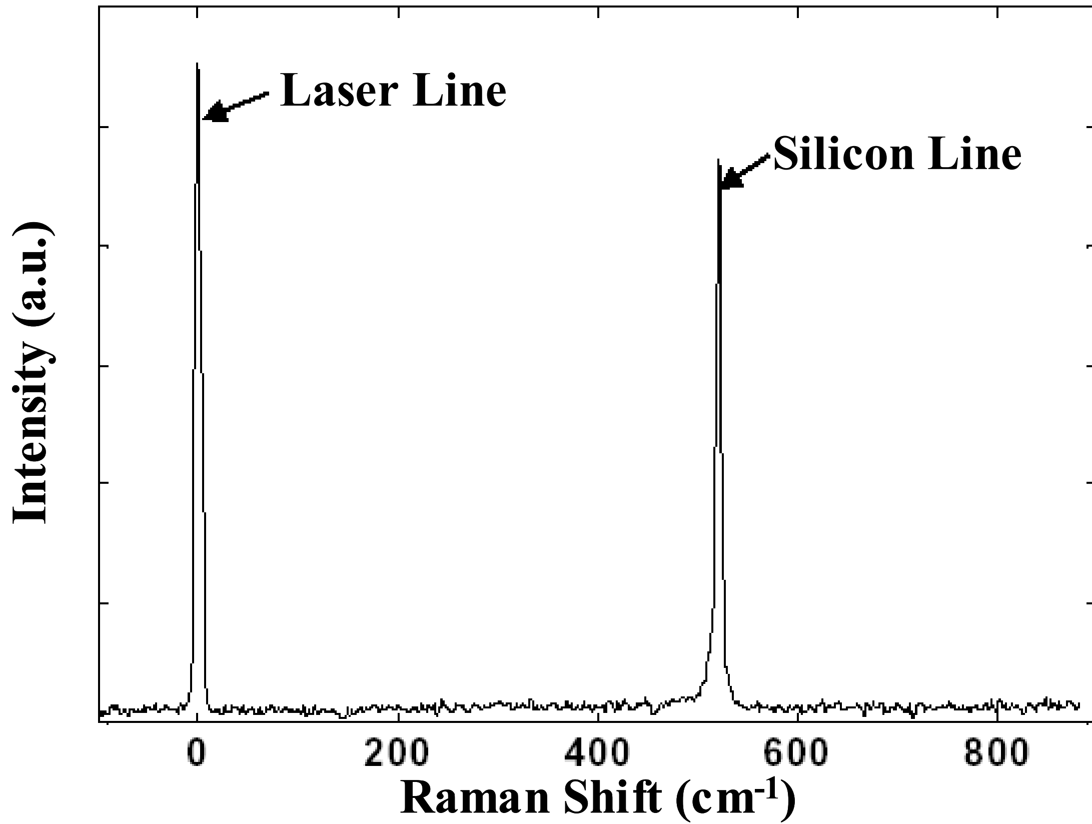

Figure A-5. Typical Raman Spectrum for Bulk Crystalline Silicon Using a 514.5 nm Argon-Ion Laser Excitation Source

A.2.5 Silicon Carbide Raman Spectroscopy and Stress

In addition to silicon, silicon carbide has been well characterized by Raman spectroscopy. An understanding of the crystalline nature of silicon carbide is necessary in order to discuss its material properties. Unlike silicon, crystalline silicon carbide exhibits a one-dimensional polymorphism called polytypism. All the polytypes of silicon carbide can be described using a hexagonal coordinate system, where the a and b axis are separated by 120 degrees and the c axis is normal to both the a and b axis. Although all

silicon carbide has the same atomic composition of silicon and carbon, the stacking order in the c-axis is used to specify the polytype, as shown in Figure A-6 [9; 10; 11; 12].

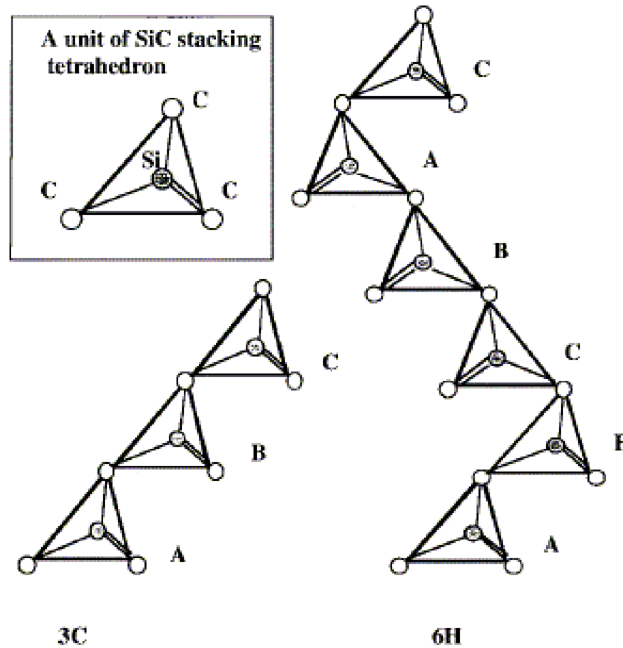

Figure A-6. Stacking Order of 3C and 6H Silicon Carbide [11]

Disorder in simple stacking sequences creates unique polytypes. Over 250 polytypes have been identified. However, only a few polytypes are common and can be described as cubic, hexagonal, or rhombohedral. Some common polytypes of silicon carbide and the associated stacking order are listed in Table A-1 and illustrated in Figure A-7 [9; 10; 11; 12].

Table A-1. Stacking Order of Common Silicon Carbide Polytypes

Nomenclature	Stacking Order	Description
3C	ABC	Cubic or zinc blende
2H	AB	Hexagonal or wurtzite
6H	ABCACB	Hexagonal or wurtzite
15R	ABCACBCABACABCB	Rhombohedral

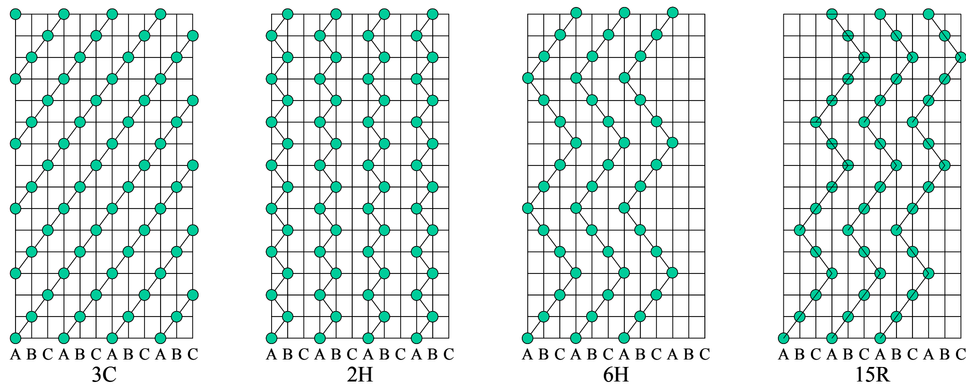

Figure A-7. Stacking Order of Common Silicon Carbide Polytypes.

Like silicon, silicon carbide exists in three degrees of crystallinity: amorphous, polycrystalline, and monocrystalline. Amorphous silicon carbide is randomly oriented silicon and carbon, which has no polytype. Material that is a single crystal composed entirely of one polytype is defined as monocrystalline. Material that has many local areas of single crystal material is defined as polycrystalline. The average size of the local area is defined as the grain size. Polycrystalline silicon carbide may be composed of more than one polytype. Silicon carbide has been well characterized by Raman spectroscopy in a number of sources. The predominant polytype of silicon carbide determines the number of peaks and the location of these peaks in the Raman spectra, as shown for some common polytypes in Figure A-8. Table A-2 summarizes the dominant peak locations. The Raman spectrum of a sample, in conjunction with the appropriate database, provides easy identification of a target as silicon carbide, as well as a means of determining the specific polytype. One or more vibrational modes may result in Raman scattering. Each vibrational mode may produce a separate Raman signal peak or be degenerate, having the same Raman signal peak. Some of the more common of these vibrational modes are transverse optical (TO), longitudinal optical (LO), transverse acoustic (TA), and

longitudinal acoustic (LA). [13; 14; 15]. Nakashima and Harima discuss each of the vibrational mode in more detail [15]. The vibrational modes are commonly used to denote one or more Raman signal peaks, as shown in Figure A-8.

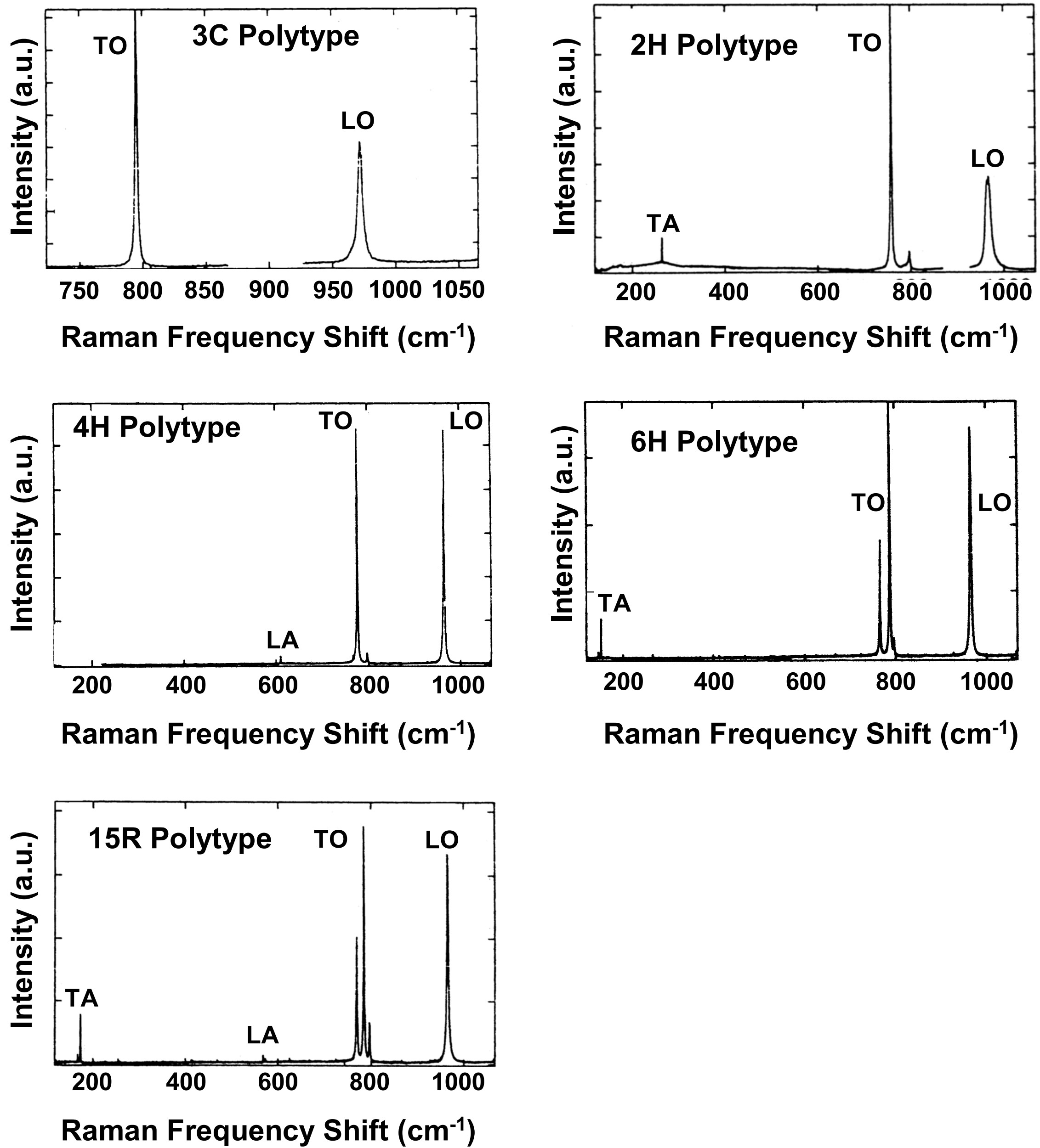

Figure A-8. Raman Spectra of Several Silicon Carbide Polytypes [15]

Table A-2. Raman Spectral Peaks for Common Polytypes of Silicon Carbide [15; 16]

	Frequency (cm^{-1})			
	TA	TO	LA	LO
3C (β)	-	796	-	972
2H	264	799 764	-	968
4H	204	796 776	610	964
6H	145	797 767	504 514	965
15R	167 173	797 785 769	569 577	965

As described in Section A.2.1, Raman scattering can occur after a sample material absorbs the excitation light. Figure A-9 shows the absorption coefficient of two common polytypes of SiC as a function of wavelength. The excitation source is a 532-nm Nd:YAG laser. The corresponding absorption coefficients are approximately 48 cm^{-1} and 2.6 cm^{-1} for 3C and 6H SiC, respectively [17]. Thus, the penetration depth for 3C and 6H SiC thin film at 532 nm is approximately 208.3 μm and 3.85 mm, respectively. The absorption coefficient for silicon near 532 nm is 14,400 cm^{-1} , which corresponds to an optical penetration depth of 680 nm [14]. Thus, for the SiC thin films grown for this research, the silicon substrate should always be visible. In addition, the silicon Raman spectra is scattered from the silicon at a depth of less than 1 μm from the silicon-SiC interface. Thus, even if the SiC Raman spectra is not apparent, the silicon Raman spectra should be present. Since the silicon Raman spectra corresponds to a shallow depth from the SiC-silicon interface, a stressed SiC layer on top of the silicon substrate should produce a shift in the silicon Raman spectra's mean wavenumber. Finally, Figure A-9 shows that the absorption coefficient increases with a decrease in wavenumber, which

shows that using a UV Raman excitation source will increase the SiC thin film optical absorption and increase the Raman spectra intensities.

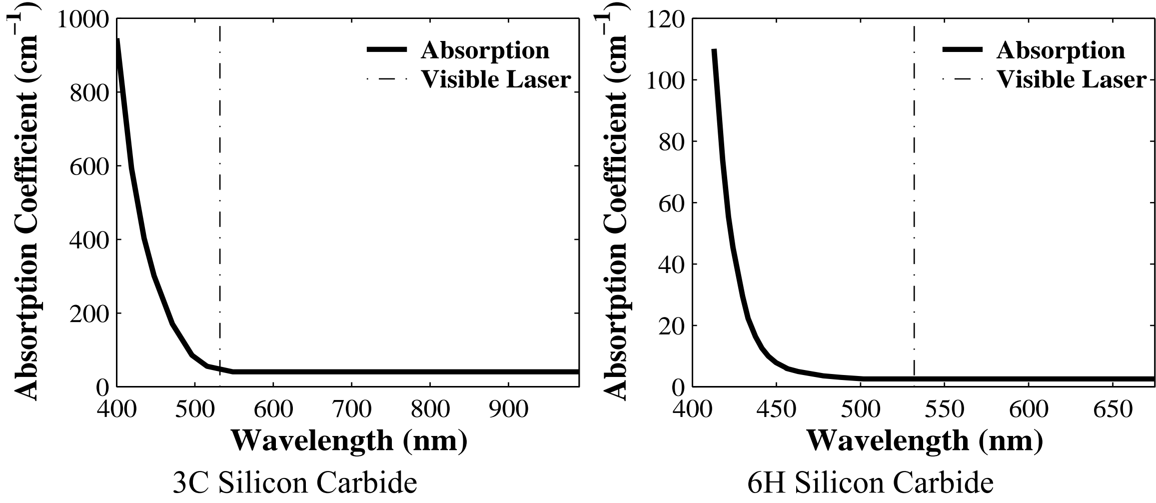

Figure A-9. Absorption Coefficients as a Function of Wavelength for Bulk 3C and 6H Silicon Carbide [17]

Mechanical strain in the sample shifts the peak frequency locations of the silicon carbide Raman spectrum. Thin films deposited on a substrate are usually under biaxial stress [18]. The source of this stress may be lattice mismatch, thermal expansion coefficient mismatch, or intrinsic stress caused by the deposition process. The TO and LO frequency peaks of a cubic material under two-dimensional stress (biaxial) are given by Equations (A-3) through (A-8) [19; 20; 21]:

$$\nu^{TO} - \nu_0^{TO} = -\left(2\eta_H^{TO} - \tfrac{1}{3}\eta_s^{TO}\right)\cdot X \quad \left(\text{cm}^{-1}\right) \tag{A-3}$$

$$\nu^{LO} - \nu_0^{LO} = -\left(2\eta_H^{LO} + \tfrac{2}{3}\eta_s^{LO}\right)\cdot X \quad \left(\text{cm}^{-1}\right) \tag{A-4}$$

$$\eta_H^{TO,LO} = -\frac{\left(p^{TO,LO} + 2q^{TO,LO}\right)\left(S_{11} + 2S_{12}\right)}{6\cdot\left(\nu_0^{TO,LO}\right)} \quad \left(\text{cm}^{-1}\cdot\text{Pa}^{-1}\right) \tag{A-5}$$

$$\eta_S^{TO,LO} = -\frac{\left(p^{TO,LO} - q^{TO,LO}\right)\left(S_{11} - S_{12}\right)}{2\cdot\left(\nu_0^{TO,LO}\right)} \quad \left(\text{cm}^{-1}\cdot\text{Pa}^{-1}\right) \tag{A-6}$$

$$\varepsilon_{ll} = \varepsilon_{xx} = \varepsilon_{yy} = \left(S_{11} + S_{12}\right)X \quad \left(\text{unitless}\right) \tag{A-7}$$

$$\varepsilon_{\perp} = \varepsilon_{zz} = 2S_{12}X \quad \left(\text{unitless}\right) \tag{A-8}$$

where ν_0^{TO} is *stress-free TO frequency* (cm^{-1}), ν_0^{LO} is *stress-free LO frequency* (cm^{-1}), ν^{TO} is *measured TO frequency* (cm^{-1}), ν^{LO} is *measured LO frequency* (cm^{-1}), X is *strain of the material* (Pa), $p^{TO,LO}$ and $q^{TO,LO}$ are *phonon deformation potentials for the TO or LO frequencies* (cm^{-2}), S_{11} and S_{12} are *elastic compliance constants* (Pa^{-1}), ε is *strain in the subscript axis* (unitless), and η_H and η_S are *stress coefficients* ($cm^{-1}Pa^{-1}$).

Substituting Equations (A-5) and (A-6) into Equations (A-3) and (A-4) results in two values for the strain X. The in-plane stress and the normal to the plane stress are calculated by averaging the two X values and substituting this averaged value into Equations (A-7) and (A-8) [19; 20; 21]. Although Equations (A-3) through (A-8) were derived for cubic SiC, the methods and equations apply equally well to other polytypes [19].

A.2.6 Vibrational Temperature from Raman Spectra

The temperature of the sample volume being measured using Raman spectroscopy may be of interest in many experiments. The vibrational temperature of the sample can be calculated using Raman spectroscopy if more than one Raman scattered frequency can be acquired. An example of multiple Raman scattered frequencies is illustrated in the Raman spectra of silicon carbide, as shown in Figure A-8. In addition, the Stokes and

anti-Stokes Raman scattered signal can be used to calculate vibrational temperature. The Stokes to anti-Stokes Raman scattered intensity ratio is sensitive to temperature, as illustrated in Equation (A-9) [22]:

$$\exp\left(-hc\nu/kT\right) = \frac{I_a\left(\mu+\nu\right)/\left(\mu+\nu\right)^4}{I_s\left(\mu-\nu\right)/\left(\mu-\nu\right)^4} \quad \left(\text{unitless}\right) \tag{A-9}$$

where h is *Planck's constant* (J·s), c is *speed of light* (cm/s), k is *Boltzmann's constant* (J/K), T is *vibrational temperature* (K), μ is *wavenumber of the excitation source* (cm^{-1}), ν is *Raman shift* (cm^{-1}), and $I_s(\mu-\nu)$ and $I_a(\mu+\nu)$ are the *Stokes* and *anti-Stokes Raman intensities* (counts) respectively, at the Raman peak wavenumbers.

Equation (A-9) references the Stokes and anti-Stokes Raman scattered intensities, $I_s(\mu-\nu)$ and $I_a(\mu+\nu)$. These intensities are not available for the calculation of the vibrational temperature. However, the acquired Raman spectra are related to these Raman scattered intensities through an instrument spectral response function, as shown in Equation (A-10) [22]:

$$I\left(\nu\right)\cdot S\left(\nu\right) = N(\nu) \quad \left(\text{counts}\right) \tag{A-10}$$

where $S(\nu)$ is the *instrument spectral response function* (unitless) at the Raman wavenumber ν and $N(\nu)$ is the *acquired Raman signal intensity* (counts). A Raman spectral acquisition system must be calibrated to determine its instrument spectral response function $S(\nu)$. Applying the instrument spectral response function $S(\nu)$ and the acquired Raman signal intensity $N(\nu)$ to Equation (A-9) produces Equation (A-11) [22]:

$$\exp\left(-hc\nu/kT\right)=\frac{N_a\left(\mu+\nu\right)\cdot\left(\mu-\nu\right)^4}{N_s\left(\mu-\nu\right)\cdot\left(\mu+\nu\right)^4}\cdot\frac{S(\mu+\nu)}{S(\mu-\nu)}\quad\left(\text{unitless}\right)\qquad\text{(A-11)}$$

Spectral lamps provide one method of spectral calibration. The light intensity output of the lamps is calculated as a function of the lamp color temperature. The color temperatures of the lamps are determined by the ohmic power loss across the filament of the lamp. However, previous research shows that the light output of the lamps decreases with lamp usage, even though the ohmic power loss remains constant. Also, the geometry of the lamp-spectrometer test setup greatly influenced the calibration results [22].

Due to the problems associated with the calibration lamps, previous research has shown that the relative instrument spectral response can be calculated directly from the acquired Raman spectra, if the temperature of a reference sample is known. This method is initiated by computing a raw temperature function from the acquired Raman spectra, as shown in Equation (A-12) [22]:

$$\exp\left[-hc\nu/kT_r\left(\mu,\nu\right)\right]=\frac{N_a\left(\mu+\nu\right)/\left(\mu+\nu\right)^4}{N_s\left(\mu-\nu\right)/\left(\mu-\nu\right)^4}\quad\left(\text{unitless}\right)\qquad\text{(A-12)}$$

where $T_r(\mu,\nu)$ is r*aw temperature function* (K), and $N_a(\nu)$ and $N_s(\nu)$ are *Stokes and anti-Stokes Raman photon count measurements* (s^{-1}) at the Raman wavenumbers $\mu\pm\nu$. Dividing Equation (A-12) by Equation (A-9) produces the relative instrument response function for two wavenumbers symmetrically located about the excitation source, as shown in Equation (A-13) [22]:

$$\exp\left[-\frac{hc\nu}{k}\cdot\left(\frac{1}{T_r(\mu,\nu)}-\frac{1}{T}\right)\right]=\frac{S(\mu+\nu)}{S(\mu-\nu)} \quad (\text{unitless}) \tag{A-13}$$

Thus, the absolute instrument response function is not necessary to calibrate the Raman acquisition system for temperature measurements. However, Equation requires an accurate temperature measurement from a reference sample. Given this sample temperature measurement, a correction to the raw temperature function, as shown in Equation (A-14) can be computed [22]:

$$\frac{1}{T}=\frac{1}{T_r(\mu,\nu)}+\xi(\mu,\nu) \quad (\text{K}^{-1}) \tag{A-14}$$

where $\xi(\mu,\nu)$ is *temperature response function* (K^{-1}) at the Raman wavenumber ν. Thus, a simple additive correction to the raw temperature determined *ex-situ* can be use to calculate the temperature *in-situ*. However, the temperature response function is only valid for Raman measurements at the wavenumbers $\mu\pm\nu$. Other research has assumed that the ratio involving the peak Stokes and anti-Stokes Raman signal intensities is linearly related to the inverse of temperature, as shown in Equation (A-15) [23; 24]:

$$\ln\left(\frac{N_S(\mu-\nu)}{N_A(\mu+\nu)}\right)=A\cdot\frac{1}{T}+B \quad (\text{unitless}) \tag{A-15}$$

where *A* and *B* are *linear fit constants*. However, Equation (A-15) implicitly assumes that the symmetric instrument spectral response function ratio $S(\mu+\nu)/S(\mu-\nu)$ is sufficiently flat over the wavenumber range of $\mu-\nu$ to $\mu+\nu$. In addition, both the Stokes and the anti-Stokes wavenumber vary with temperature. Figure A-10 shows an example

of the slight shift in wavenumber with temperature for GaSb (100) substrates [23]. Although the symmetric instrument spectral response function ratio may vary, Figure A-11 shows that any such variation is not significant to the results for this specific instrument, sample material, and temperature range. However, this assumption should be verified for each new experiment.

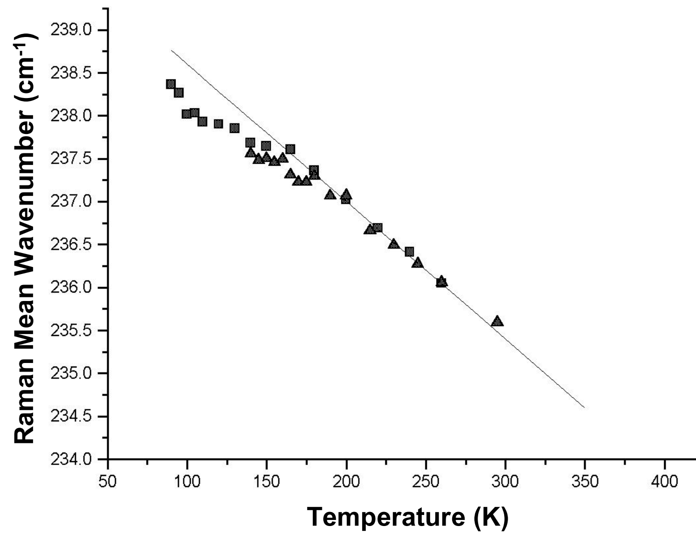

Figure A-10. Variation in Raman Wavenumber with Temperature [23]

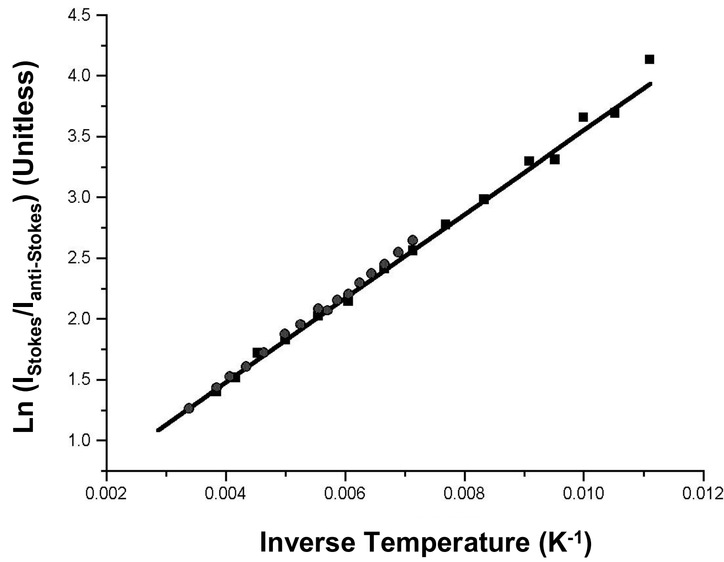

Figure A-11. Relationship Between the Stokes/anti-Stokes Raman Peak Intensity Ratio and Temperature [23]

A.3 Experiment

Three sets of experiments were performed: simulated *in-situ* Raman spectral acquisition of existing silicon carbide, *in-situ* Raman spectral acquisition of silicon carbide during deposition, and *in-situ* temperature extract from Raman spectral acquisition during deposition. The remainder of this section describes the Raman spectroscopy system calibration procedures and the experimental procedures for each of the experiments listed above. The results from these three sets of experiments are presented in Section A.4.

A.3.1 Raman Spectroscopy System Spectral Calibration

The Raman spectroscopy system, described in Section 3.10, required spectral calibration. This spectral calibration mapped pixels of the Andor CCD to wavenumbers. The EIC Laboratories VIS500 Echelle spectrometer segmented the spectra into thirteen horizontal tracks that are spread vertically across the CCD array. Since proprietary software mapped horizontal pixel location to wavenumber using a binomial expression, each track required four spectral lines for calibration. Three spectral lines were sufficient to calculate the three coefficients for each binomial mapping. However, the fourth spectral line over-specified the equation and provided a goodness-of-fit measure. The spectral calibration was performed using spectral lines from argon, krypton, mercury, and xenon lamps. These lamps emitted light at multiple known wavelengths. The spectra from each lamp were acquired in terms of photon counts per pixel horizontal position. A least square error fitting algorithm is used to generate the binomial coefficients to map the horizontal pixel locations to the correct wavenumbers. Since the Echelle

spectrometer contained no moving parts, except the shutter at the entrance slit, verification of the acquired spectra against the spectral lamps was performed on a semi-annual basis. During the more than two-year time span of this research, the Echelle spectrometer required recalibration only once. This calibration was due to a change in the setup of the Echelle spectrometer to capture a different spectral region of interest.

A.3.2 Raman Probe Focusing

As described in Section 3.10, the Raman spectroscopy system acquired the spectra through a retractable probe that placed the focusing lens near the substrate. The entire probe assembly was inserted by a positioning stage external to the deposition chamber. The positioning stage was commanded to move the probe toward the substrate at the maximum rate until an optical position sensor indicated that the positioning stage had reached the "home" position. The positioning stage was then slowed to a halt at a location past the home position and subsequently repositioned back to the home position. Thus, the stage assembly was inserted to a known position relative to the deposition chamber. However, the stainless steel tubing that comprised the business end of the Raman probe expanded when heated. The stainless steel substrate rotation shaft described in Section 3.5 also expanded when heated. The expansion of both the Raman probe and the substrate rotation shaft complicated the focusing of the Raman probe. If there were no expansion, the Raman probe would have been inserted up to a predetermined position that focused the excitation source onto the substrate. However, as the distance from the focusing lens to the substrate surface varied with temperature, the Raman probe was positioned such that the acquired Raman signal amplitude was

maximized. This position of maximum acquired Raman signal amplitude was assumed to place the focusing lens at the proper focal distance away from the substrate surface. The Raman spectra were acquired at multiple Raman probe positions. Since the acquired Raman signal background was non-zero and non-linear, the Raman spectra were fitted to a Gaussian equation with a quadratic baseline in order to extract the Raman signal amplitude. The Raman probe was then repositioned to the location that corresponded to the maximum Raman signal amplitude. Since this focusing process was tedious and time consuming, the process was automated using LabVIEW® from National Instruments [25]. For (100) silicon substrates, the Raman signal amplitude was approximately zero unless the Raman probe was within 10,000 motor steps (~2.5 mm) from the position of maximum Raman signal amplitude. The Raman signal amplitude was relatively insensitive to the Raman probe position when the Raman probe was position within 1500 motor steps (~0.38 mm) from the position of maximum Raman signal amplitude. In order to minimize the time required to focus the Raman probe, the stage positioning was performed in a two-step iterative process. The rough positioning procedure located the Raman probe near the maximum Raman signal focal distance by stepping through a set of fifteen locations uniformly spaced 7,500 motor steps (~1.91 mm) apart. The Raman spectra was acquired and fitted, as previously described, at each of the fifteen locations. A new set of fifteen locations uniformly spaced 1,500 motor steps (~0.38 mm) apart, and centered about the positioning stage location that corresponded to maximum Raman signal, were created. The fine positioning procedure located the final Raman probe position by sequencing through the new set of stage locations. Again, the Raman spectra was acquired and fitted, as described previously. The Raman probe was repositioned to

the stage location that corresponded to maximum Raman signal amplitude. The acquisition time varied between 5 seconds to 60 seconds per Raman spectra capture. As the temperature was increased, the Raman spectra SNR decreased. Longer acquisition times were required to compensate for this SNR decrease. These Raman probe positioning procedures were repeated for each temperature change and/or Raman probe insertion.

A.3.3 Simulated *In-situ* Raman Spectral Acquisition for Silicon Carbide

The first experiment simulated an *in-situ* Raman spectral acquisition by recording the Raman spectra of a silicon carbide sample. A sample labeled "SiC," which is the compound symbol for silicon carbide, was found in a sample storage rack at the Air Force Research Laboratory Materials Directorate (AFRL/ML), Wright-Patterson Air Force Base Building 651 Room 193. The sample was approximately 500 micrometers thick, as measured with a dial caliper. The sample was semi-transparent and greenish-gray in color. No other information about the sample was known before acquiring a Raman spectrum. The sample was analyzed *ex-situ* using Raman spectroscopy. The Raman spectrum verified that the sample was silicon carbide and that the polytype was 6H. The silicon carbide sample was mounted on the substrate holder and placed in the PLD chamber. Raman spectra of the silicon carbide sample were recorded at room temperature under normal atmosphere and under vacuum, as well as at elevated temperatures under a vacuum of less than 50 μTorr. The temperature was varied from room temperature up to 900ºC. The purpose of this test was to determine if silicon

carbide could be measured using Raman spectroscopy under *in-situ*-like conditions. The results of this experiment are presented in Section A.4.1.

A.3.4 *In-situ* Raman Spectral Acquisition for Silicon Carbide

The second experiment utilized Raman spectroscopy to monitor the deposition of silicon carbide on a (100) silicon substrate by PLD. The goal of the experiment was to extract as much information as possible about the formation of the silicon carbide thin film. An approximately 2 cm by 2 cm square piece of (100) silicon was mounted to the substrate holder using a substrate mask. The substrate mask exposed an approximately 1 cm by 1cm square area of the silicon substrate. Raman spectra were taken at room temperature under normal atmospheric pressure. Under a vacuum of less than 25 μTorr, the temperature was ramped from room temperature to 800ºC. Raman spectra were acquired at every 100ºC increment. A silicon carbide thin film was deposited by PLD on the silicon substrate. Table A-3 lists the parameters used during this deposition. The deposition was interrupted every 15 minutes to acquire Raman spectra. After deposition,

Table A-3. Growth Parameters for Silicon Carbide Thin Films on (100) Silicon Substrates

Parameter	Value
Laser Fluence	2.25 J/cm^2
Laser Repetition Rate	10 Hz
Ambient Pressure	< 25 μTorr
Target-to-substrate Distance	65.0 mm
Substrate Bias	-250 V
Target Rotation Rate	15 rpm
Substrate Rotation Rate	15 rpm
Deposition Length	120 minutes/72000 pulses

the sample was cooled to room temperature from 800ºC. Raman spectra were acquired at every 100ºC increment. The results of this experiment are presented in Section A.4.2.

A.3.5 *In-situ* Raman Spectra Vibrational Temperature Extraction for Silicon Carbide

The third experiment investigated the ability to extract the temperature of the sample. The purpose of this experiment was to determine if *in-situ* Raman spectroscopy could be used to calculate the local temperature of the sample. An Omega® model OS48H4K optical pyrometer was installed onto the bottom of the deposition chamber. The output of the optical pyrometer was monitored using an Omega® model CN8500 Temperature and Process Controller. The pyrometer viewed a limited area of the substrate through a zinc selenide window. Since the Omega® optical pyrometer was a single color pyrometer, both the emissivity setting of the optical pyrometer and the linear coefficients of the Omega® model CN8500 were calibrated. As described in Sections 3.5 and 3.7, the substrate temperature was typically monitored by a thermocouple located inside the inner heater chamber. However due to the rotation of the substrate, the thermocouple did not contact the substrate. To calibrate the optical pyrometer and associated temperature controller, a Chromel-Alumel K-type thermocouple was mounting onto a (100) silicon substrate. The thermocouple was then connected to the input of the Eurotherm temperature controller, which controlled the lamp power. Thus, the power of the heating lamps was adjusted to ensure the surface temperature of the silicon was equal to the commanded temperature. An emissivity dial on the back of the pyrometer (which was graduated based upon the assumption that the sample would fill the entire viewing

area of the pyrometer without any optical absorption between the pyrometer and the sample) was adjusted. Unfortunately, the inclusion of the zinc selenide window and the apertured viewing area visible to the optical pyrometer prevented setting the emissivity as marked on the dial to published emissivity references. In addition, the linearity coefficients of the Omega® temperature controller were adjusted. These adjustments were iteratively made by varying the surface temperature of the silicon substrate between room temperature (~25ºC) and 900ºC. After final adjustment, the optical pyrometer agreed with the output of the thermocouple within ±2ºC. After calibration of the optical pyrometer system was completed, the second experiment, described in Section A.3.4, was repeated.

A.4 Data and Analysis

This section presents the results of the experiments described in Section A.3. All Raman spectra presented in this section represent the difference between the Stokes Raman signal wavenumber and the excitation wavenumber.

A.4.1 Simulated *In-situ* Raman Spectral Acquisition for Silicon Carbide

As stated in Section A.3.3, the purpose of this experiment was to determine if silicon carbide could be measured using Raman spectroscopy under *in-situ* conditions. Figure A-12 shows the raw Raman spectrum for the 6H silicon carbide sample, as well as fitted data. The data was fit to the sum of three Gaussian-Lorentzian Sum distributions and a linear background using a software analysis package called TableCurve 2D [26]. The peaks of the three distributions agree well with the 6H silicon carbide Raman spectra

displayed in Figure A-8 and listed in Table A-2. The data displayed in Figure A-12 has a data resolution of approximately 4 cm^{-1}. This data resolution is not sufficient to determine the stress in the material. In addition, the fitting becomes increasing erroneous as the width of the Raman signals decrease relative to the data resolution. The Raman peak centered at 791 cm^{-1} is approximately 6 cm^{-1} less than the expected value of 797 cm^{-1}. Much of this error arises from the fitting of the sparsely spaced data.

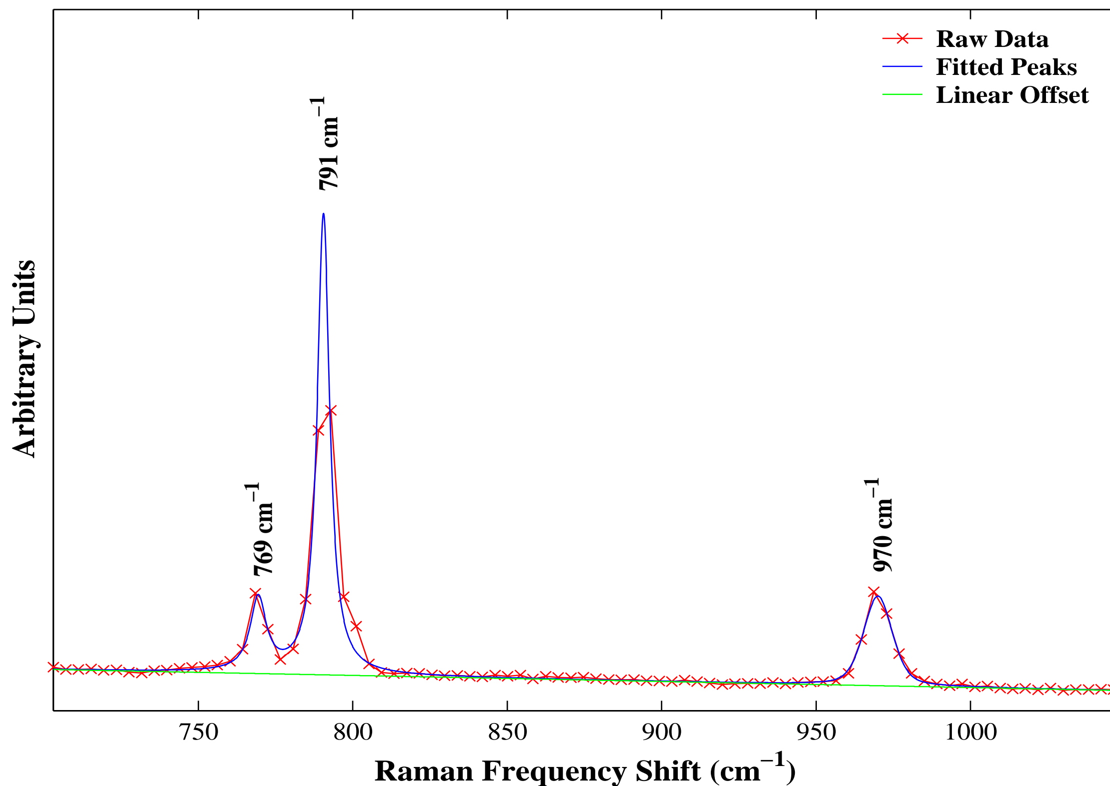

Figure A-12. Typical 6H Silicon Carbide Raman Spectra and Fitted Parameters

Figure A-13 displays the temperature and pressure dependence of the Raman spectra for the same 6H silicon carbide sample presented in Figure A-12. The center wavenumber for all three Raman signal peaks shift to a lower wavenumber, broaden in

width, and decrease in amplitude with an increase in temperature, as expected. Also, all three Raman signals are visible for all temperatures and pressures.

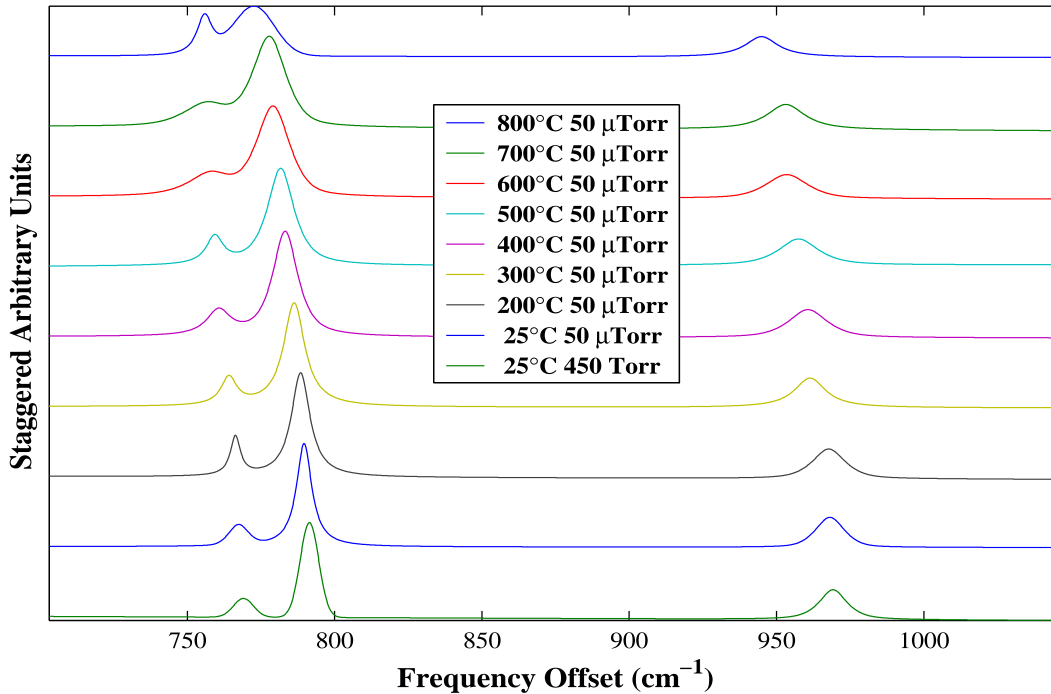

Figure A-13. Silicon Carbide Raman Spectra from Room Temperature to 800°C

A.4.2 *In-situ* Raman Spectral Acquisition for Silicon Carbide

The purpose of this experiment was to derive as much information as possible about the formation of the silicon carbide layer using Raman spectroscopy, as described in Section A.3.4. Unfortunately, a Raman spectrum corresponding to the silicon carbide thin film was never observed. However, the Raman spectrum from the silicon substrate was visible throughout the experiment. Twenty-five Raman spectra were acquired during the heating up to deposition temperature phase, the pulse laser ablation deposition phase,

and cooling down to room temperature phase. The Raman spectra were fitted in real time to a Gaussian distribution with a linear baseline. In addition, the Raman spectra were fitted offline to a variety of distributions and baselines, typically a Gaussian-Lorentzian sum with quadratic baseline. Both the raw spectra and the relevant fitted parameters were recorded. Figure A-14 shows the downward shift in the mean wavenumber during the pre-deposition phase (labeled as "Scan Number 1" through "Scan Number 9") when the temperature increased from room temperature to 800°C, a downward shift in mean wavenumber with laser ablation growth time (i.e. an increase in silicon carbide film thickness during the PLD growth process labeled "Scan Number 10" through "Scan Number 17"), and a upward shift in mean wavenumber as the temperature was decreased down to room temperature (labeled "Scan Number 18" through "Scan Number 25").

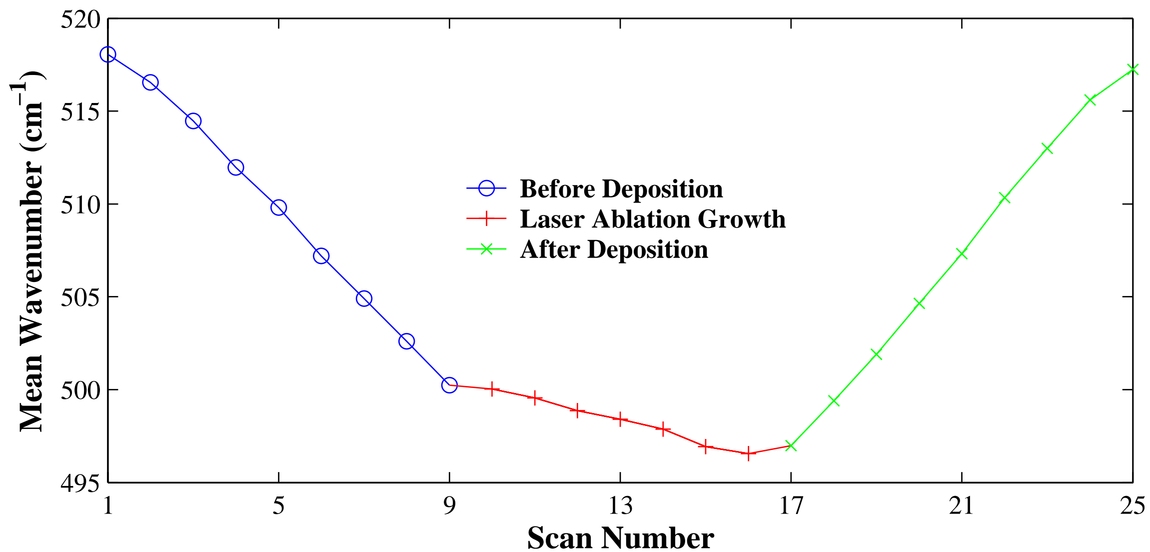

Figure A-14. Chronological *In-Situ* Silicon Raman Peak Wavenumber during Silicon Carbide Deposition During the PLD Growth of Silicon Carbide

Figure A-15 presents the same data; however, the x-axis is represented in terms of temperature rather than scan number. Using temperature as the x-axis directly compares the below SiC growth Raman mean wavenumber to the after SiC growth Raman mean wavenumber. This type of comparison is important since the stress is calculated by subtracting the shifted Raman mean wavenumber (after SiC growth) from the reference Raman mean wavenumber (before growth).

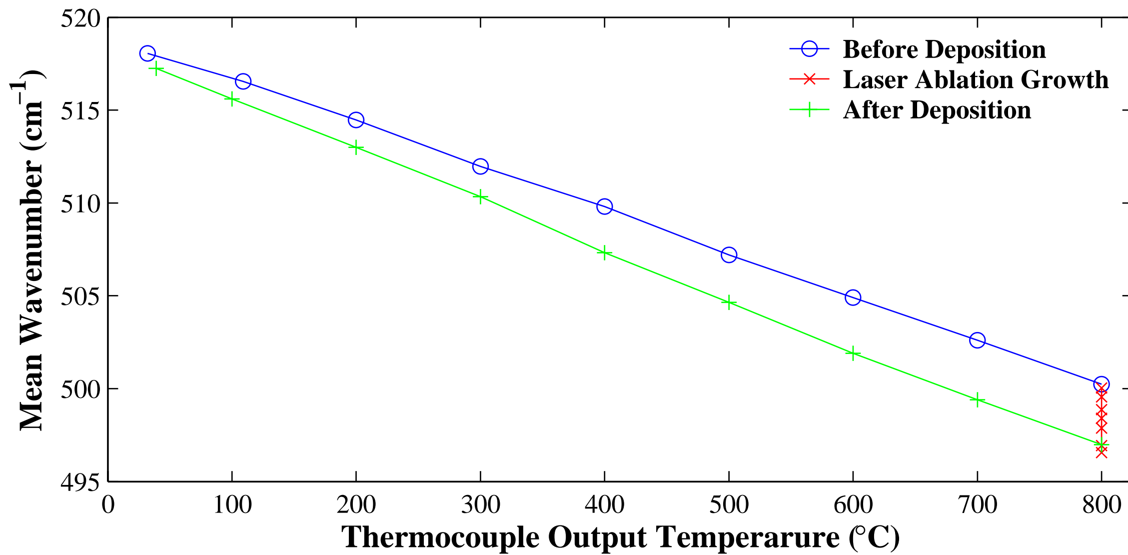

Figure A-15. *In-Situ* Silicon Raman Peak Wavenumber as a Function of Thermocouple Output Temperature During the PLD Growth of Silicon Carbide

It should be noted that the temperatures referenced in Figure A-15 are thermocouple readout temperatures. As described in Sections 3.5 and 3.7, the thermocouple that controls the temperature of the inner heater chamber is not in contact with the substrate. Therefore, the temperature of the inner chamber may not equal the substrate surface temperature. This possible discrepancy is discussed in Section A.4.3. Research has shown that the localized mechanical stress of silicon and polysilicon devices can be

calculated based on the relative shift in the Stokes Raman mean wavenumber. The measured Stokes Raman mean wavenumber is subtracted from the Stokes Raman mean wavenumber measured from bulk/unstressed material. For a given material, the Stokes Raman mean wavenumber varies only due to stress and temperature [3]. Figure A-16shows the Stokes Raman mean wavenumber shift due to stress at each temperature, assuming that the silicon substrate surface temperatures before, during, and after the laser ablation deposition are equal for equivalent thermocouple output reading. As stated previously, the possible discrepancy between silicon substrate surface temperature and thermocouple output temperature is discussed in Section A.4.3.

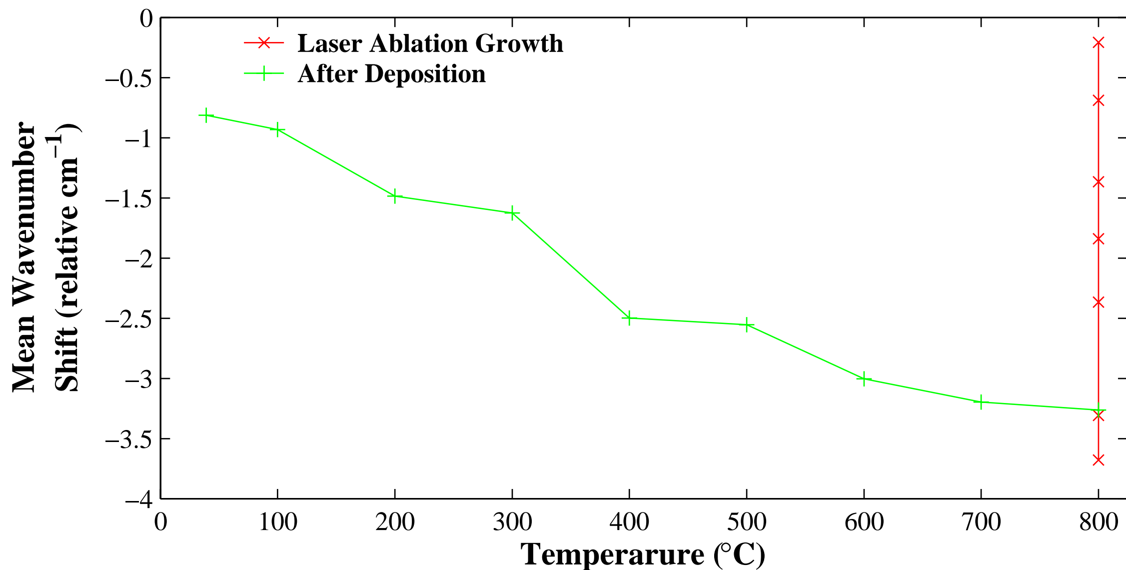

Figure A-16. *In-Situ* Silicon Raman Peak Wavenumber Shift as a Function of Thermocouple Output Temperature

In silicon the relationship between material stress and the difference in the Stokes Raman mean wavenumbers is linear with a 1.88±0.05 rcm^{-1}/GPa slope, where rcm^{-1} denotes relative cm^{-1} [3]. Thus, the maximum stress shown in Figure A-16 is

approximately 7 GPa of tensile strain [3], a much higher than expected value. However, without validation of the equivalence between the silicon substrate surface temperature and the thermocouple output temperature, no conclusions can be inferred.

A.4.3 *In-situ* Raman Spectra Vibrational Temperature Extraction for Silicon Carbide

The purpose of this experiment was to determine if the temperature of the sample could be calculated using Raman spectroscopy. Although the deposition chamber was equipped with an optical pyrometer, the emissivity of the sample being viewed by the pyrometer changed during the deposition. Initially, the pyrometer measured the surface temperature of the silicon sample. However, as the silicon carbide thin film was grown on the silicon substrate, the emissivity varied between the emissivity of silicon and the emissivity of silicon carbide. Given a sufficiently long deposition (i.e. a sufficiently thick silicon carbide layer), the pyrometer would measure only the temperature based on the emissivity of silicon carbide. However, the deposition durations necessary to grow such a sufficiently thick silicon carbide layer (on the order of many centimeters thick) are not feasible for PLD, or any other thin film deposition technique. Thus, the temperature measurements output by the optical pyrometer were not valid once the laser ablation deposition started. In addition, the thermocouples that were used to measure the temperature of the chamber were not in contact with the silicon substrate. Due to the rotating nature of the substrate during the deposition, a thermocouple could not be made to remain in contact with the silicon substrate. Therefore, an emissivity-independent optical temperature measurement technique was needed.

Section A.2.6 described a method to calculate the sample temperature using Raman spectroscopy. In fact, the temperature calculated is a localized aggregate temperature of the sample volume that is being illuminated by the excitation source. This is the same volume that produces Raman scattered light. Section A.3.5 details an optical pyrometer system calibration procedure, which was performed. Following the calibration, a silicon substrate was mounted in the PLD chamber. The temperature was ramped from room temperature up to 900°C in approximately 10°C increments. The temperature was controlled using the Eurotherm temperature controller, which measured the temperature using a thermocouple that was not in contact with the substrate holder. However, the temperature was recorded from the Omega® temperature controller and optical pyrometer. Once each target temperature was reach, no deposition parameter changes were made during a five-minute temperature stabilization period. The Raman probe was refocused after every 30°C to 40°C change. The Raman spectra were recorded for every 10°C temperature change. Section A.2.6 theorized that the symmetric relative instrument response function ratio could be used to calculate a temperature response function. It has already been shown with silicon and silicon carbide that the Stokes Raman mean wavenumbers down shift to lower wavenumbers with an increase in temperature. If the symmetric relative instrument response function ratio was sufficiently constant over the range of wavenumber shifts, then the temperature extraction problem would reduce to a simple linear fit, as predicted in Equation (A-15). If the fit to Equation (A-15) showed significant variations, then the symmetric relative instrument response function ratio would have to be calculated for each Raman mean wavenumber in the range. Figure A-17 shows the Stokes Raman mean wavenumber shift with temperature,

which is linear as expected. The slope of –0.024 $cm^{-1}/°C$ is useful for estimating the uncertainty in both the Stokes and anti-Stokes mean wavenumber. Thus, the total uncertainty in the mean wavenumbers results from both data fitting variance estimates and temperature uncertainty estimates. Figure A-17 displays a linear fit, as described in Equation (A-15). The fit is adequate enough to eliminate the symmetric relative instrument response function ratio computation at each temperature.

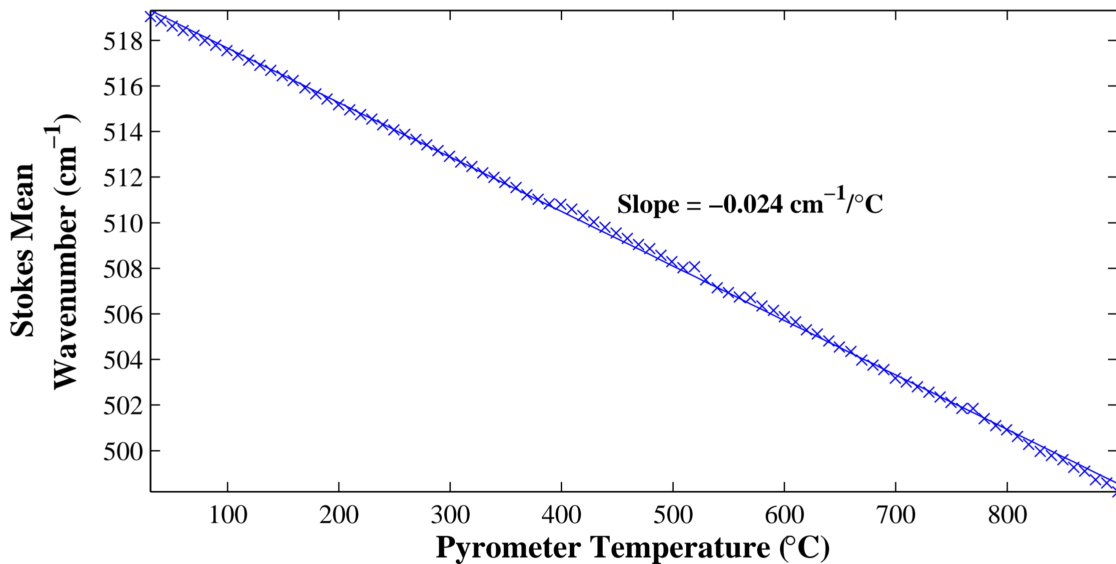

Figure A-17. Stokes Raman Mean Wavenumber Dependence on Temperature

The pyrometer system calibration procedure described in Section A.3.5 calibrated the pyrometer to with ±2/°C difference from a thermocouple mounted adjacent to the area being measured by the pyrometer. This ±2/°C is comparable to the measurement error of the thermocouple measurement system. Figure A-19 presents a comparison between the thermocouple that controls the temperature of the inner heater chamber and the pyrometer. Again the results are within the measurement error of the thermocouple

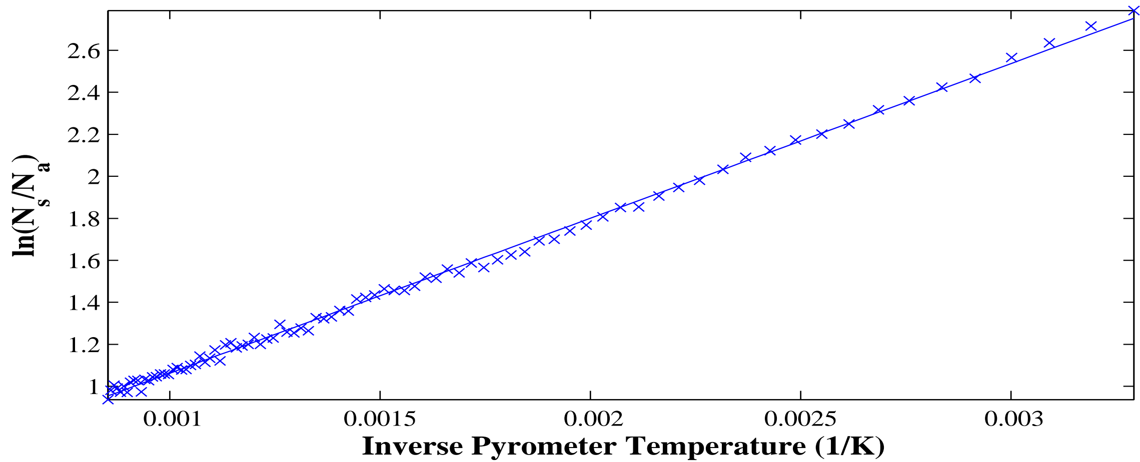

Figure A-18. Silicon Vibrational Temperature as a Function of Optical Pyrometer Output Temperature

measurement systems. Thus, the non-contact thermocouple measurement method used to control the temperature of the silicon substrate by controlling the temperature at a predetermined location inside the inner heater chamber is accurate to within ±2ºC.

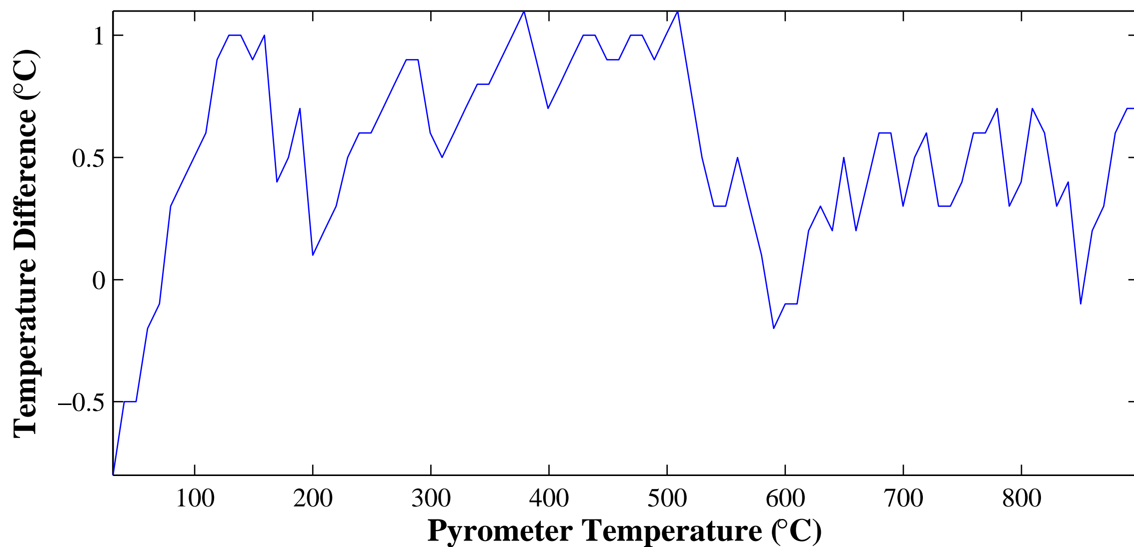

Figure A-19. Difference between Optical Pyrometer Temperature and Thermocouple Temperature.

However, no conclusion about the assumption that the non-contact thermocouple adequately estimates the substrate surface temperature can be made during the deposition process or after a thin film has been deposited on the surface of the substrate. During the deposition process, the laser plume can and typically does increase the surface temperature. Yet, the non-contact thermocouple is shielded from the laser plume by the substrate and may not indicate that a surface temperature increase has occurred. In addition, the substrate is optically heated from both top and bottom. Therefore, any changes in reflectivity caused by growing a thin film on the substrate surface can change the substrate surface temperature.

Since this section shows that Raman spectroscopy can provide an emissivity-independent temperature measurement, the technique was applied to the growth of silicon carbide on silicon substrates. The experiment described in Section A.3.4 was repeated. However, no Raman spectra were acquired during the laser ablation deposition process. Thus, the deposition was not interrupted during the 120 minute laser ablation time. The Raman spectroscopy data mirrored that presented in Figure A-14, Figure A-15, and Figure A-16. However, when the Raman spectra were examined offline and the temperatures were calculated, the calculated temperatures were 30-35% lower than the thermocouple output temperature. Since SiC is an excellent thermal conductor, this lower calculated silicon temperature was unexpected, which suggested some error in the Raman intensity measurements. Since both the Stokes and anti-Stokes Raman signal from the silicon were transmitted through the SiC thin film, it is possible that the SiC thin film attenuated the Stokes and anti-Stokes wavelengths differently, which would invalidate the intensity ratio-based temperature calculation. Also, any Fabry-Perot

interference modulation of the Stokes and anti-Stokes intensities could invalid the ratio measurements. However, no conclusion about the validity of the temperature calculations or the possible sources of error can be made with a means to verify the temperature of the silicon under the SiC thin film layer.

A.4.4 Other Data and Results

Several other experiments were conducted other than those described previously. The *in-situ* Raman spectroscopy monitoring of silicon carbide on silicon was conducted numerous times and under various deposition conditions. EDS, XPS, AES, and XRD analysis verified that the thin films were polycrystalline silicon carbide. Section 2.5 lists the capabilities and limitations of each of these thin film analysis techniques. In addition, the thickness of the silicon carbide films was varied between 500 nanometers and 3 micrometers. No silicon Raman spectra were acquired for SiC thin films with thickness greater than 3 μm. These samples were also measured *ex-situ* using a Renishaw model 2000 Raman spectrometer equipped with a Leica microscope and a 514.5 nanometer argon ion laser. The results from the *ex-situ* Raman spectrometer agree with the *in-situ* Raman spectrometer: no silicon carbide Raman spectra could be acquired.

In addition to silicon carbide, yttria stabilized zirconia (YSZ) on both CP1 polymer substrates and silicon substrates were measured *in-situ* and *ex-situ* using Raman spectroscopy. The CP1 polymer substrate fluoresced intolerably. No Raman signal could be acquired. YSZ thin films between 250 nanometers and 5 micrometers were grown on silicon substrates. The Raman spectra from the silicon substrates were evident for all samples within this YSZ film thickness range. Yet, no Raman spectra

corresponding to YSZ was present. The YSZ on silicon samples were verified using XRD analysis to be polycrystalline YSZ.

A.5 Conclusion

Raman spectroscopy has the potential to be employed *in-situ* to measure the stress in the growth of silicon carbide thin films. However, the silicon carbide thin film is not visible when using a green 514.5 or 532 nanometer excitation source. Thus, the Raman spectra from the silicon substrate is acquired and used for analysis. The silicon Raman spectra can be recorded throughout the PLD process. The silicon Raman mean wavenumber shifts with temperature and stress. However, the difficulty arises when attempting to separate the portion of the Raman wavenumber shift due to stress from the portion due to temperature change. Without an accurate estimate of temperature, no estimate of the stress in the silicon carbide thin film can be made *in-situ*. Yet, given an accurate temperature estimate, Raman spectroscopy can be used as an *in-situ* diagnostic sensor for thin film stress. Raman spectra acquisition times are on the order of a few minutes, compared to deposition times on the order of a few hundred minutes. Thus, multiple acquisitions could be made discretely during the PLD growth process and the deposition parameters varied to achieve the desired stress at the conclusion of the deposition process.

In addition to applicability as a stress monitor (if given an accurate temperature measurement), Raman spectroscopy can provide an emissivity-independent temperature measurement for the top layer of a sample. Thermocouple-based temperature sensors are limited in that contact with the sample is necessary. Optical pyrometers are limited in that the emissivity of the sample must be known. With spectral intensity calibration

(either the full instrument spectral response function ratio or the symmetric instrument spectral response function ratio), Raman spectroscopy can provide the temperature using simple calculation. However, the technique is limited to the top layer of material, which is not visible for either YSZ or silicon carbide.

The dominant hurdle preventing Raman spectroscopy from being fully utilized as a stress and temperature sensor for PLD is the inability to "see" the thin films using visible Raman spectroscopy with a green excitation source. Further investigations are ongoing to modify the PLD chamber and associated Raman spectroscopy system used in this research to change the excitation wavelength from green to ultra violet (UV). In addition to changing the excitation source, the holographic notch filter, spectrometer, and CCD must be replaced with components that are compatible with the UV excitation source. Personnel at the Air Force Research Laboratory, Materials and Manufacturing Directorate are currently active pursuing these proposed modifications and the associated extension of this research to UV Raman spectroscopy for *in-situ* PLD diagnostic sensors.

Bibliography

1. Busbee, J. D., Team Lead, Air Force Research Laboratory, Materials and Manufacturing Directorate, Manufacturing Technology Division, Wright-Patterson AFB OH. Personal Correspondence. 1 April 2001.

2. Ferraro, J. R. and K. Nakamoto. *Introductory Raman Spectroscopy*. New York: Academic Press, 1994.

3. Starman, L. A. *Characterization of* Residual *Stress in MicroElectroMechanical Systems (MEMS) Devices Using Raman Spectroscopy*. Ph.D. Dissertation, Air Force Institute of Technology (AU), Wright-Patterson AFB OH, April 2002 (AD-A402559)(AAT 3047611).

4. Hecht, E., *Optics* (2nd Edition). Massachusetts: Addison-Wesley Publishing Company, 1990.

5. Demtröder, W. *Laser Spectroscopy: Basic Concepts and Instrumentation* (2nd Edition). New York: Springer-Verlag, 1998.

6. Anastassakis, E. M., A. Pinczuk, E. Burstein, F. H. Pollak, and M. Cardona. "Effect of static uniaxial stress on the Raman spectrum of silicon," *Solid State Communications*, 8(2):133-138, 1970.

7. De Wolf, I. "Micro-Raman spectroscopy to study local mechanical stress in silicon integrated circuits," *Semiconductor Science Technology*, 11:139-154, 1996.

8. Siakavellas, M., E. Anastassikis, G. Kaltsas, and A. G. Nassiopoulos. "Micro-Raman Characterization Of Stress Distribution Within Free Standing Mono- And Poly-Crystalline Silicon Membranes," *Microelectronic Engineering*, 41/42:469-472, 1998.

9. Knippenberg, W. F. *Philips Research Reports*, 18, 1963.

10. Mehregany, M. and C. A. Zorman. "SiC MEMS: Opportunities and Challenges for Applications in Harsh Environments," *Thin Solid Films*, 355-356: 518-524, November 1996.

11. Mehregany, M., C. A. Zorman, N. Rajan, and C. H. Wu. "Silicon Carbide MEMS for Harsh Environments," Proceedings of the IEEE, 86:1594-1609, August 1998.

12. Sarro, P. M. "Silicon Carbide as a New MEMS Technology," Sensors and Actuators, 82: 210-218, 2000.

13. Tong, L. and Mehran M. "Silicon Carbide as a New Micromechanics Material," *IEEE Solid-State Sensor and Actuator Workshop* Technical Digest, Hilton Head Island, SC, 21-25 June, 198-201. 1992, IEEE: New York, 1992.

14. Freitas, J. A. Jr., S. G. Bishop, A. Addamiano, and P. H. Klein. "Photoluminescence and Raman Spectroscopy of Cubic SiC Grown by Chemical Vapor Deposition on Si Substrates," *Materials Research Society Symposia Proceedings*, 46:581-586, 1985.

15. Nakashima, S. and H. Harima. "Raman Investigation of SiC Polytypes," *Physica Status Solidi A*, 162:39-64, 1997.

16. Yamanaka, M., K. Ikoma, M. Ohtsuka, T. Ishizama, and Y. Shichi. "Raman Scattering Spectroscopy of 3C-SiC (111) Heteroepitaxial Films," *Japanese Journal of Applied Physics*, 33(1):997-998, February 1994.

17. Levinshtein, M. E., S. L. Rumyantsev, and M. S. Shur. *Properties of Advanced Semiconductor Materials*. New York: John Wiley & Sons, 2001.

18. Choo, A. G., S. Tlali, and H. E. Jackson. "Raman Scattering Characterization of Ultrathin Films of β-SiC," *Materials Research Society Symposia Proceedings*, 324:367-371, 1994.

19. Feng, Z. C., W. J. Choke, and J. A. Powell. "Raman Determination of Layer Stresses and Strains for Heterostructures and Its Application to the Cubic SiC/Si System," *Journal of Applied Physics*, 64(12):6827-6835, 15 December 1988.

20. Feng, Z. C. and A. J. Mascarenhas. "Raman Scattering Studies of Chemical Vapor Deposited Cubic SiC Films of (100) Si," *Journal of Applied Physics*, 64(6):3176-3186, 15 September 1988.

21. Rohmfeld, S., M. Hundhausen, L. Ley, C.A. Zorman, and M. Mehregany. "Raman Spectroscopy on Biaxially Strained Epitaxial Layers of 3C-SiC on Si," *Materials Science Forum*, 338-342(1):595-598, 2000.

22. MalyJ, M. and J. E. Griffiths. "Stokes/Anti-Stokes Raman Vibrational Temperatures: Reference Materials, Standards Lamps, and Spectrophotometric Calibrations," *Applied Spectroscopy*, 37(4):315-333, 1983.

23. Swan, Anna, M. Lande, S. Ünlü, and B. Goldberg. "Measuring Temperature With Scattered Light- Raman Spectroscopy." n. pag. http://ultra.bu.edu/projpages/tram/Raman.html. 22 January 2003.

24. Schamlott, A. "Background of the investigations of SiC." n. pag. http://www.fz-rossendorf.de/FWK/fel/sic.html. 22 January 2003.

25. *LabVIEW*®. Version 6.0, IBM, CD-ROM. Computer Software. National Instruments, Austin, TX, 2000.

26. *TableCurve 2D*. Version 5.1, IBM, CD-ROM. Computer Software, SYSTAT Software Inc., Richmond CA, 2001.

Vita

Captain Paul C. Rounsavall graduated from Southern Baptist Educational Center in Memphis, Tennessee. He entered undergraduate studies at Mississippi State University in Starkville, Mississippi where he graduated with a Bachelor of Science degree in Electrical Engineering in December 1993. He was commissioned through the Detachment 425 AFROTC at Mississippi State University.

His first assignment was in Norman, Oklahoma as a developmental engineer at the Next Generation Weather Radar Operational Support Facility in April 1994. While stationed in Norman, Oklahoma, he earned a Masters of Business Administration from Oklahoma City University in May 1997. In September 1997, he entered the Graduate School of Engineering and Management, Air Force Institute of Technology (AFIT). He graduated with a Masters of Science in Electrical Engineering from AFIT in April 1999. In October 2002, he was assigned to the Air Force Research Laboratories, Materials and Manufacturing Directorate. He is a member of Tau Beta Pi and Et Kappa Nu.

REPORT DOCUMENTATION PAGE

Form Approved
OMB No. 0704-0188

The public reporting burden for this collection of information is estimated to average 1 hour per response, including the time for reviewing instructions, searching existing data sources, gathering and maintaining the data needed, and completing and reviewing the collection of information. Send comments regarding this burden estimate or any other aspect of this collection of information, including suggestions for reducing the burden, to Department of Defense, Washington Headquarters Services, Directorate for Information Operations and Reports (0704-0188), 1215 Jefferson Davis Highway, Suite 1204, Arlington, VA 22202-4302. Respondents should be aware that notwithstanding any other provision of law, no person shall be subject to any penalty for failing to comply with a collection of information if it does not display a currently valid OMB control number.
PLEASE DO NOT RETURN YOUR FORM TO THE ABOVE ADDRESS.

1. REPORT DATE *(DD-MM-YYYY)*	2. REPORT TYPE	3. DATES COVERED *(From - To)*
01-08-2003	Doctoral Dissertation	Mar 1999 - Aug 2003

4. TITLE AND SUBTITLE
CONTROLLED-STRESS LARGE-AREA PULSED LASER DEPOSITION OF YTTRIA STABILIZED ZIRCONIA

5a. CONTRACT NUMBER

5b. GRANT NUMBER

5c. PROGRAM ELEMENT NUMBER

6. AUTHOR(S)
Rounsavall, Paul C., Major (select), USAF

5d. PROJECT NUMBER

5e. TASK NUMBER

5f. WORK UNIT NUMBER

7. PERFORMING ORGANIZATION NAME(S) AND ADDRESS(ES)
Air Force Institute of Technology
Graduate School of Engineering and Management (AFIT/EN)
2950 P Streeet, Building 640
WPAFB OH 45433-7765

8. PERFORMING ORGANIZATION REPORT NUMBER
AFIT/DS/ENG/03-06

9. SPONSORING/MONITORING AGENCY NAME(S) AND ADDRESS(ES)
AFRL/MLMR
Attn: Mr. John D. Busbee
2977 P Street Rm 215
WPAFB OH 45433-7746
DSN: 674-4323
e-mail: John.Busbee@wpafb.af.mil

10. SPONSOR/MONITOR'S ACRONYM(S)

11. SPONSOR/MONITOR'S REPORT NUMBER(S)

12. DISTRIBUTION/AVAILABILITY STATEMENT
APPROVED FOR PUBLIC RELEASE; DISTRIBUTION UNLIMITED.

13. SUPPLEMENTARY NOTES

14. ABSTRACT
The US Air Force has need of parabolic-shaped membrane mirrors for surveillance satellites. The current polymer membrane technology has been unable to overcome shape deformation problems caused by intrinsic stresses from the membrane casting and mounting processes. One proposed solution was to coat the membrane mirrors with a stressed coating to compensate for shape deformations. Thus, the research presented in this dissertation produced controlled-stress large-area pulsed laser deposition (PLD) grown thin films on polymer substrates and investigated optical time-of-flight (TOF) sensor systems and Raman spectroscopy for control of the PLD process with respect to thin film stress. Initially, the PLD-grown film stress was controlled using a constant combination of deposition parameters. Also, the velocity was extracted from the optical TOF data and indicated film stress. As such, the velocity was used to control the laser fluence in order to compensate for slight variations in deposition conditions, which improved the film stress run-to-run stability. Additionally, iterative and theoretical experiments produced large-area YSZ films with less than ten percent total thickness variations. Combining the controlled-stress and large-area aspects produced desirable compensations in shape to the polymer substrates. Finally, Raman spectroscopy was shown to be compatible with the PLD

15. SUBJECT TERMS
Pulsed Laser Deposition, Residual Stress, Thin Films, Rasters, Scanning, Large Area PLD, Raman Spectroscopy, Time of Flight

16. SECURITY CLASSIFICATION OF: a. REPORT	b. ABSTRACT	c. THIS PAGE	17. LIMITATION OF ABSTRACT	18. NUMBER OF PAGES	19a. NAME OF RESPONSIBLE PERSON
U	U	U	UU	258	Mikel M. Miller, Ph.D, Lt. Col USAF (Ret)

19b. TELEPHONE NUMBER *(Include area code)*
(937) 255-6127 ext 4274